ASEAN
Journal of Scientific and Technological Reports

Online ISSN:2773-8752

Vol. 27 No. 4, July - August 2024

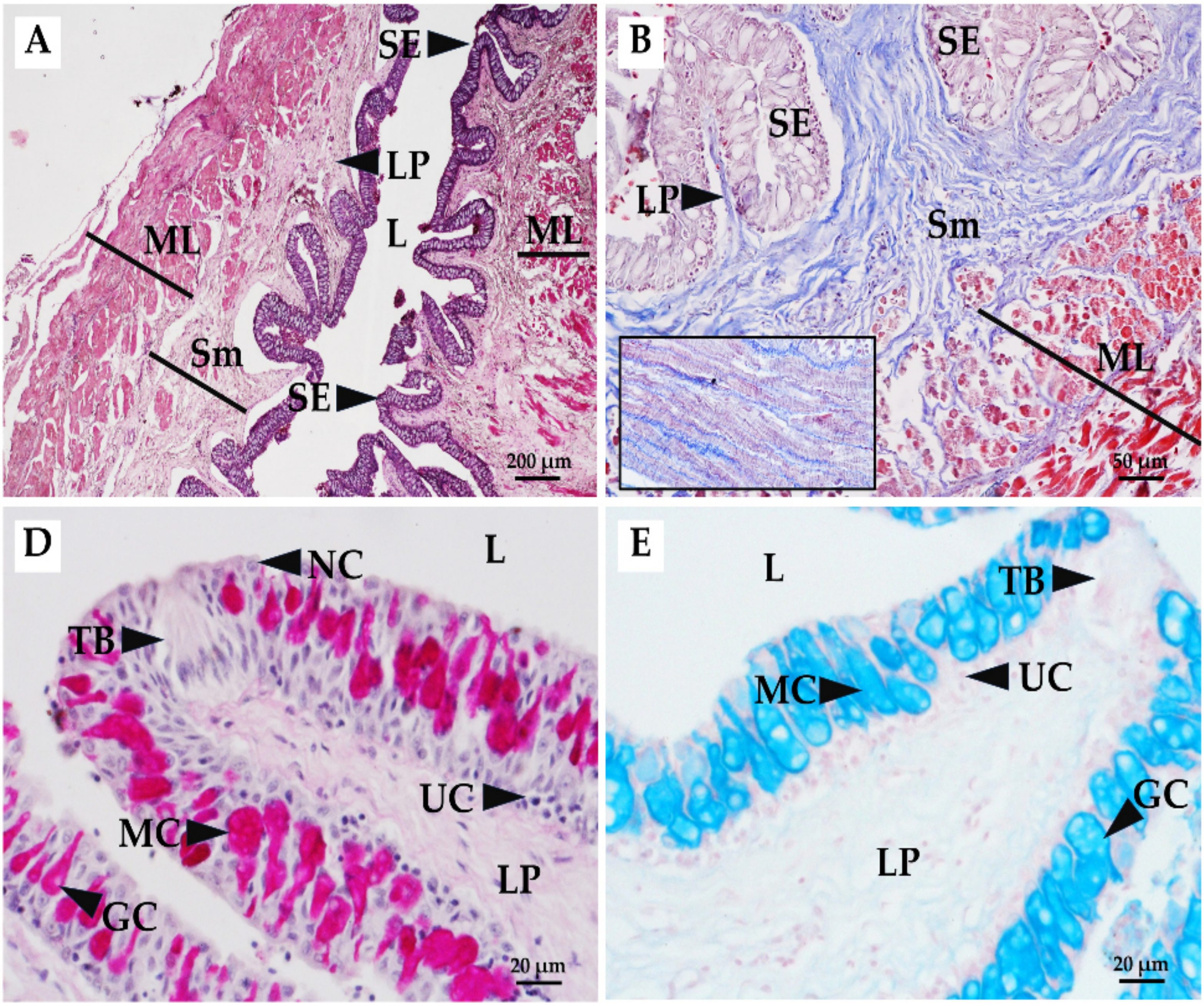

ISSN 2773-8752 (online)

https://ph02.tci-thaijo.org/index.php/tsujournal/issue/view/17079

ASEAN
Journal of Scientific and Technological Reports
Online ISSN:2773-8752

ASEAN Journal of Scientific and Technological Reports (AJSTR)

Name	ASEAN Journal of Scientific and Technological Reports (AJSTR)
Owner	Thaksin University

Advisory Board	Assoc. Prof. Dr. Nathapong Chitniratna (President of Thaksin University, Thailand) Assoc. Prof. Dr. Samak Kaewsuksaeng (Vice President for Reserach and Innovation, Thaksin University, Thailand) Assoc. Prof. Dr. Suttiporn Bunmak (Vice President for Academic Affairs and Learning, Thaksin University, Thailand) Assoc. Prof. Dr. Samak Kaewsuksaeng (Acting Director of Reserach and Innovation, Thaksin University, Thailand) Asst. Prof. Dr. Prasong Kessaratikoon (Dean of the Graduate School, Thaksin University, Thailand)
Editor-in-Chief	Assoc. Prof. Dr. Sompong O-Thong, Mahidol University, Thailand

Session Editors

1. Assoc. Prof. Dr. Jatuporn Kaew-On, Thaksin University, Thailand
2. Assoc. Prof. Dr. Samak Kaewsuksaeng, Thaksin University, Thailand
3. Assoc. Prof. Dr. Rattana Jariyaboon, Prince of Songkla University, Thailand
4. Asst. Prof. Dr. Noppamas Pukkhem, Thaksin University, Thailand
5. Asst. Prof. Dr. Komkrich Chokprasombat, Thaksin University, Thailand

Editorial Board Members

1. Prof. Dr. Hidenari Yasui, University of Kitakyushu, Japan
2. Prof. Dr. Jose Antonio Alvarez Bermejo, University of Almeria, Spain
3. Prof. Dr. Tjokorda Gde Tirta Nindhia, Udayana University in Bali, Indonesia
4. Prof. Dr. Tsuyoshi Imai, Yamaguchi University, Japan
5. Prof. Dr. Ullah Mazhar, The University of Agriculture, Peshawar, Pakistan
6. Prof. Dr. Win Win Myo, University of Information Technology, Myanmar
7. Prof. Dr. Yves Gagnon, University of Moncton, Canada
8. Assoc. Prof. Dr. Chen-Yeon Chu, Feng Chia University, Taiwan
9. Assoc. Prof. Dr. Gulam Murtaza, Government College University Lahore, Lahore, Pakistan
10. Assoc. Prof. Dr. Jompob Waewsak, Thaksin University, Thailand
11. Assoc. Prof. Dr. Khan Amir Sada, American University of Sharjah, Sarjah, United Arab Emirates.
12. Assoc. Prof. Dr. Sappasith Klomklao, Thaksin Univerrsity, Thailand
13. Asst. Prof. Dr. Dariusz Jakobczak, National University, Pakistan
14. Asst. Prof. Dr. Prawit Kongjan, Prince of Songkla University, Thailand
15. Asst. Prof. Dr. Shahrul Isamail, Universiti Malaysia Terengganu, Malaysia
16. Asst. Prof. Dr. Sureewan Sittijunda, Mahidol University, Thailand
17. Dr. Nasser Ahmed, Kyushu University, Fukuoka, Japan
18. Dr. Peer Mohamed Abdul, Universiti Kebangsaan Malaysia, Malaysia
19. Dr. Sriv Tharith, Royal University of Phnom Penh, Cambodia
20. Dr. Zairi Ismael Rizman, Universiti Teknologi MARA, Malaysia
21. Dr. Khwanchit Suwannoppharat, Thaksin University, Thailand

Staff: Journal Management Division

1. Miss Kanyanat Liadrak, Thaksin University, Thailand
2. Miss Ornkamon Kraiwong, Thaksin University, Thailand

Contact Us
Institute of Research and Innovation, Thaksin University
222 M. 2 Ban-Prao sub-district, Pa-Pra-Yom district, Phatthalung province, Thailand
Tel. 0 7460 9600 # 7242 , E-mail: aseanjstr@tsu.ac.th

List of Contents

ASEAN
Journal of Scientific and Technological Reports
Online ISSN:2773-8752

ASEAN
Journal of Scientific and Technological Reports
Online ISSN:2773-8752

Research article

Enhancing Methane Production from Empty Fruit Bunches by Augmented *Thermoanaerobacterium thermosaccharolyticum* PSU-2

Sittikorn Saelor[1], Chonticha Mamimin[2], and Nantharat Phruksaphithak[3*]

[1] Biotechnology Program, Faculty of Science, Thaksin University, Phatthalung, 93210, Thailand
[2] Bio4gas (Thailand) Company Limited, Phatthalung, 93210, Thailand
[3] Department of Chemistry, Faculty of Science and Digital Innovation, Thaksin University, Phatthalung, 93210, Thailand
* Correspondence: katenant@gmail.com

Citation:
Saelor, S., Mamimin, C, Phruksaphithak, N. Enhancing methane production from empty fruit bunches through augmented *Thermoanaerobacterium thermosaccharolyticum* PSU-2. *ASEAN J. Sci. Tech. Report.* **2024**, 27(4), e253700. https://doi.org/10.55164/ajstr.v27i4.253700.

Article history:
Received: April 16, 2024
Revised: May 4, 2024
Accepted: May 16, 2024
Available online: 30 June, 2024

Publisher's Note:
This article has been published and distributed under the terms of Thaksin University.

Abstract: The recalcitrant nature of the substrate often limits the anaerobic digestion of Empty Fruit Bunches (EFB). This study investigates the effectiveness of augmenting *Thermoanaerobacterium thermosaccharolyticum* PSU-2 for the pretreatment of EFB in mono-digestion and co-digestion with Palm Oil Mill Effluent (POME) to enhance biogas production. The augmented *T. thermosaccharolyticum* PSU-2 demonstrated enhanced cellulolytic and hemicellulolytic capabilities, resulting in improved biogas yield, methane content, and substrate degradation efficiency compared to the control without augmentation. Mono-digestion of EFB with the augmented strain at an S:I ratio of 15:1 achieved a methane yield of 35.13 ± 1.05 m^3 CH_4/tonne, representing a 64.31 ± 1.17% improvement over the control. Co-digestion of EFB with POME using the augmented strain further enhanced the methane yield to 46.67 ± 1.40 m^3 CH_4/tonne at an S:I ratio of 15:1, representing a 103.00 ± 2.81% improvement over the control. Kinetic analysis revealed improved hydrolysis rates and reduced lag phases in mono-digestion and co-digestion processes. Comparison with other pretreatment methods and energy balance and economic analysis indicated that co-digestion of EFB with POME using the augmented *T. thermosaccharolyticum* PSU-2 pretreatment is a promising, energy-efficient, and profitable approach for enhancing biogas production from EFB. This study highlights the potential of biological pretreatment using augmented bacterial strains to improve the valorization of agricultural waste streams through anaerobic digestion.

Keywords: Anaerobic digestion; Bioaugmentation; Empty fruit bunches; Palm oil mill effluent; *Thermoanaerobacterium thermosaccharolyticum* PSU-2; Pretreatment

1. Introduction

The growing demand for renewable energy and the need to mitigate greenhouse gas emissions have increased interest in valorizing organic waste streams through anaerobic digestion (AD) [1]. AD is a sustainable technology that converts organic matter into biogas, a renewable energy source while reducing waste and generating nutrient-rich digestate [2]. However, the efficiency of AD processes is often limited by the recalcitrant nature of lignocellulosic biomass, such as agricultural residues and agro-industrial waste [3]. EFB, a major byproduct of the palm oil industry, has been identified as a promising feedstock for biogas production due to its abundant availability and high organic content [4]. However, the complex lignocellulosic structure of EFB, consisting of cellulose, hemicellulose, and lignin, hinders its biodegradability and limits the efficiency of AD processes [5]. Pretreatment methods, such as physical, chemical, and biological approaches, have enhanced the digestibility of lignocellulosic biomass and improved biogas yields [6]. Biological pretreatment using cellulolytic and hemicellulolytic microorganisms has gained attention as an eco-friendly and low-cost approach to enhance the hydrolysis of lignocellulosic biomass [7]. *T. thermosaccharolyticum* PSU-2, a thermophilic anaerobic bacterium, has been reported to possess high cellulolytic and hemicellulolytic activities, making it a promising candidate for the biological pretreatment of lignocellulosic substrates [8]. Bioaugmentation, the inoculation of specific microbial strains or consortia into AD systems, has enhanced the hydrolysis and biodegradation of complex substrates [9]. Co-digestion, the simultaneous digestion of two or more substrates, has improved biogas yields and process stability compared to mono-digestion [10]. POME, another major waste stream from the palm oil industry, has been successfully co-digested with EFB to enhance biogas production [4]. The synergistic effects of co-digestion, such as improved nutrient balance, increased buffering capacity, and the presence of trace elements, contribute to the enhanced performance of AD processes [11].

Despite the potential of biological pretreatment and co-digestion strategies, limited research has been conducted on the application of augmented cellulolytic and hemicellulolytic bacterial strains for the pretreatment of EFB in mono-digestion and co-digestion with POME. This study aims to investigate the effectiveness of augmenting *T. thermosaccharolyticum* PSU-2 for the pretreatment of EFB in mono-digestion and co-digestion with POME to enhance biogas production. The specific objectives of this study are to evaluate the performance of the augmented strain in the mono-digestion of EFB and co-digestion of EFB with POME in terms of biogas yield, methane content, and substrate degradation efficiency, determine the optimal substrate-to-inoculum (S:I) ratio for the mono-digestion and co-digestion processes, compare the performance of the augmented strain pretreatment with other pretreatment methods reported in the literature, and assess the energy balance and economic viability of the augmented strain pretreatment in mono-digestion and co-digestion processes. The findings of this study are expected to contribute to developing efficient and sustainable strategies for valorizing agricultural waste streams, such as EFB and POME, through AD. The application of augmented cellulolytic and hemicellulolytic bacterial strains for the pretreatment of lignocellulosic biomass has the potential to enhance the economic viability and environmental sustainability of biogas production, thereby promoting the transition towards a circular economy and renewable energy generation.

2. Materials and Methods

2.1 Substrate preparation

EFB was collected from a palm oil factory in Krabi province, Thailand. Upon collection, the EFB samples were immediately transported to the laboratory and stored at 4°C until further use. Before the digestion experiments, the EFB was subjected to the following pretreatment steps. The EFB was first cut into smaller pieces, approximately 2-3 cm long, using a mechanical cutter to increase the surface area for microbial action. The chopped EFB was washed thoroughly with tap water to remove dirt or debris and rinsed with distilled water. The washed EFB was oven-dried at 60°C for 48 hours to remove moisture and gain a constant weight. The dried EFB was ground using a laboratory mill to obtain a particle size of 1-2 mm to enhance the surface area for further microbial degradation. The ground EFB was stored in airtight containers at room temperature until used in the digestion experiments. POME was collected from the same palm oil factory in Krabi province, Thailand. The POME was collected from the outlet of the oil clarification tank and stored at 4°C to minimize biological activity before its use in the co-digestion experiments. Before use, the POME was characterized for pH, chemical oxygen demand (COD), TS, volatile solids (VS), and oil and grease content. The characterization of POME was performed according to standard methods [12]. POME was used as a co-substrate in the digestion experiments without further pretreatment.

2.2 Methane-producing inoculum preparation.

The methane-producing inoculum used in this study was obtained from an anaerobic digester treating POME at a palm oil mill in Krabi province, Thailand. The inoculum was collected from the digester outlet and immediately transported to the laboratory in airtight containers to maintain anaerobic conditions. The inoculum was characterized for pH, TS, VS, Total Suspended Solids (TSS), Volatile Suspended Solids (VSS), Alkalinity, and Volatile Fatty Acids (VFA). The characterization was performed according to standard methods [12] to ensure the suitability of the inoculum for digestion experiments. The inoculum was passed through a 2 mm sieve to remove large particles and debris. The sieved inoculum was then washed with an anaerobic medium to remove residual substrates and maintain the anaerobic conditions. The anaerobic medium was prepared according to the composition described by Hiligsmann et al. [13]. Before the digestion experiments, the inoculum was acclimatized to the experimental conditions to minimize the lag phase and ensure optimal performance. The acclimatization was carried out in batch reactors with a working volume of 1 L. The reactors were fed a mixture of EFB and POME at a ratio similar to that used in the co-digestion experiments. The reactors were incubated at 55°C (thermophilic conditions) and maintained under anaerobic conditions by sparging with nitrogen gas. The acclimatization process was monitored by measuring biogas production and composition. Once the biogas production rate and methane content stabilized, the inoculum was considered acclimatized and ready for use in digestion experiments.

2.3 *T. thermosaccharolyticum* PSU-2 cultivation and inoculum preparation

The stock culture of *T. thermosaccharolyticum* PSU-2 was maintained on BA medium containing the following components (per liter): yeast extract 2.0 g, peptone 2.0 g, beef extract 1.0 g, glucose 10.0 g, and agar 15.0 g. The medium was prepared anaerobically under an N_2 atmosphere and sterilized by autoclaving at 121°C for 15 minutes. The stock culture was maintained at 55°C and subcultured every two weeks to ensure viability. The inoculum of *T. thermosaccharolyticum* PSU-2 was prepared in a liquid BA medium. The composition of the liquid medium was the same as the stock culture medium, excluding the agar. The medium was prepared anaerobically under an N_2 atmosphere in serum bottles and sterilized by autoclaving at 121°C for 15 minutes. A 10% (v/v) inoculum from the stock culture was transferred anaerobically using a sterile syringe into the liquid BA medium. The inoculated bottles were incubated at 55°C for approximately 48 hours until the optical density at 600 nm (OD600) reached 0.5 ± 0.05, indicating the mid-exponential growth phase [14].

2.4 Bioaugmentation of mono-digestion and co-digestion

The desired OD_{600} was achieved, and the *T. thermosaccharolyticum* PSU-2 culture was used as an inoculum for augmenting the mono-digestion of EFB and co-digestion of EFB with POME. The inoculum was transferred anaerobically using sterile syringes into the digestion bottles at various substrate-to-inoculum (S:I) ratios of 15:1, 10:1, 5:1, 4:1, 3:1, 2:1, and 1:1. The mono-digestion bottles contained only EFB as the substrate. In contrast, the co-digestion bottles contained a mixture of EFB and POME. The total working volume in each digestion bottle was maintained at 500 mL, and the bottles were incubated at 55°C under anaerobic conditions. The performance of *T. thermosaccharolyticum* PSU-2 in enhancing the digestion process was evaluated by monitoring the biogas production, methane content, and substrate degradation efficiency.

2.5 Biochemical methane potential assay

The biochemical methane potential (BMP) assay was carried out to evaluate the effect of bioaugmentation with *T. thermosaccharolyticum* PSU-2 on the AD EFB and co-digestion of EFB with POME. The EFB:POME ratio was maintained at 1:1.4, corresponding to 20% TS of EFB at a particle size of 3.25 mm, based on the findings of previous studies. The BMP tests were conducted in 500 mL serum bottles with a working volume of 400 mL. The substrate-to-inoculum (S:I) ratios were investigated at 2:1 for both mono-digestion of EFB and co-digestion of EFB with POME. The inoculum was the methanogenic sludge obtained from an anaerobic digester treating POME, as described in Section 2.2. The required substrates (EFB and POME) and inoculum were added to the serum bottles according to the respective S:I ratios. The bottles were then purged with a mixture of N_2:CO_2 (80:20) for 5 minutes to ensure anaerobic conditions. After purging, the bottles were immediately sealed with butyl rubber stoppers and aluminum crimp caps to maintain anaerobic conditions. Bottles containing only inoculum and water, without any substrate, account for the background methane production from the inoculum. Bottles containing only water, without any inoculum or substrate, should be checked for contamination or leakage. The sealed bottles were incubated at 55°C for 45 days in a temperature-controlled incubator. All the BMP tests were carried out in triplicate to ensure reproducibility. The biogas production was monitored periodically by measuring the pressure in the headspace of the bottles using a pressure transducer. The biogas composition, particularly methane content, was analyzed using a gas chromatograph. The net methane production from the substrates was calculated by subtracting the methane production in the positive control bottles from the methane production in the sample bottles. The cumulative methane yield was expressed as mL CH_4 per gram of VS added (mL CH_4/gVS). Scanning electron microscopy (SEM) was employed to observe the morphological changes and degradation of EFB fibers during the anaerobic digestion.

2.6 Analytical Methods and Calculations

The biogas composition produced during the AD was analyzed using a gas chromatograph (GC-8A, Shimadzu, Japan) equipped with a thermal conductivity detector (TCD). The GC-TCD was calibrated using standard gas mixtures of known composition. Gas samples were collected from the headspace of the digestion bottles using a gas-tight syringe and injected into the GC-TCD for analysis. The percentages of methane (CH_4) and carbon dioxide (CO_2) in the biogas were determined based on the peak areas and the calibration curves obtained from the standard gas mixtures. Total alkalinity (TA) was measured according to standard methods [12]. A sample of the digestate was centrifuged, and the supernatant was titrated with a standardized sulfuric acid solution to a pH endpoint of 4.5. The total alkalinity was calculated based on the volume of acid consumed and expressed as mg $CaCO_3$/L. VFA concentrations in the digestate were determined using a gas chromatograph (GC-17A, Shimadzu, Japan) with a flame ionization detector (FID). The digestate samples were centrifuged, and the supernatant was filtered through a 0.45 μm membrane filter. The filtrate was then acidified with formic acid and injected into the GC-FID for analysis. The individual VFA concentrations (acetic, propionic, butyric, and valeric acids) were quantified based on the peak areas and the calibration curves obtained from standard VFA solutions. The kinetics of biogas production were described using a first-order kinetic model proposed by Angelidaki et al. [15]. The first-order kinetic model is given by Equation 1:

$$\ln (B\infty - B) = \ln(B_\infty) - Kt \quad (1)$$

Where K is the constant biogas rate (d^{-1}), B∞ is the value of the final methane production, B is the methane produced at a given time, and t is the production time. The hydrolysis constant (K) was determined by plotting ln (B∞ - B) against time (t) and calculating the slope of the linear regression line. The lag phase before the start of methane production was determined using the modified Gompertz equation, as described by Trzcinski & Stuckey[16]. The modified Gompertz equation is given by Equation 2:

$$M = P \times \exp [-\exp (((R_{max} \times e/P)\times (\lambda - t)) + 1)] \quad (2)$$

Where M is the cumulative methane production, P is the methane production potential, Rmax is the maximum methane production rate, λ is the lag phase, t is time, and e is exp (1) = 2.7183. The parameters P, Rmax, and λ were estimated by fitting the experimental data to the modified Gompertz equation using non-linear regression analysis in SigmaPlot ® 11.0 software [17]. The biodegradability of the substrate can be calculated using the following biodegradability (%) = (Experimental Methane Yield / Theoretical Methane Yield) × 100.

3. Results and Discussion

3.1 Characterization of the augmented *T. thermosaccharolyticum* PSU-2

The successful genetic modification of *T. thermosaccharolyticum* PSU-2 was confirmed by evaluating the enzymatic activities of key cellulolytic and hemicellulolytic enzymes in both the wild-type and augmented strains. As presented in Table 1, the augmented strain exhibited significantly higher activities of endoglucanase, exoglucanase, β-glucosidase, xylanase, and β-xylosidase compared to the wild-type strain. Endoglucanase activity increased 4-fold in the augmented strain, reaching 3.2 U/mg protein compared to 0.8 U/mg protein in the normal flora strain. Similarly, exoglucanase activity showed a 5-fold increase, from 0.3 U/mg protein in the normal flora to 1.5 U/mg protein in the augmented strain. The activity of β-glucosidase, an essential enzyme for the complete hydrolysis of cellobiose to glucose, increased by 4-fold, from 1.2 U/mg protein in the normal flora to 4.8 U/mg protein in the augmented strain. The augmented *T. thermosaccharolyticum* PSU-2 also demonstrated enhanced hemicellulolytic capabilities, with xylanase activity increasing by 5-fold (from 1.0 to 5.0 U/mg protein) and β-xylosidase activity increasing by 5-fold (from 0.6 to 3.0 U/mg protein) compared to the normal flora strain. These increased enzymatic activities indicate that the genetic modifications successfully enhanced the strain's ability to degrade the cellulose and hemicellulose components of lignocellulosic biomass. Its growth performance on different substrates further confirmed the improved cellulolytic and hemicellulolytic capabilities of the augmented strain. The augmented strain exhibited faster growth and higher cell densities when cultivated on cellulosic substrates (e.g., Avicel or filter paper), hemicellulosic substrates (e.g., xylan), and lignocellulosic biomass (e.g., acid pretreated EFB) compared to the normal flora strain. This improved growth performance can be attributed to the enhanced enzymatic machinery of the augmented strain, which enables more efficient hydrolysis and utilization of the complex polysaccharides present in these substrates. Furthermore, the augmented *T. thermosaccharolyticum* PSU-2 demonstrated superior hydrolytic efficiency when incubated with lignocellulosic biomass. Higher concentrations of glucose, xylose, and other reducing sugars were detected in the culture supernatant of the augmented strain compared to the normal flora strain, indicating more effective biomass hydrolysis. SEM images of EFB before and after hydrolysis by the augmented strain provided visual evidence of the extensive degradation of the biomass structure, further confirming the enhanced hydrolytic capabilities of the augmented strain (Fig.1).

Table 1. Enzymatic activities of normal flora and augmented *T. thermosaccharolyticum* PSU-2

Enzyme	Normal flora (U/mg protein)	Augmented (U/mg protein)	Fold increase
Endoglucanase	0.8	3.2	4.0
Exoglucanase	0.3	1.5	5.0
β-glucosidase	1.2	4.8	4.0
Xylanase	1.0	5.0	5.0
β-xylosidase	0.6	3.0	5.0

3.2 Performance of augmented *T. thermosaccharolyticum* PSU-2 in EFB mono-digestion

The mono-digestion of EFB using the augmented *T. thermosaccharolyticum* PSU-2 showed significant improvements in biogas yield and methane content compared to the control without augmentation. As presented in Table 2, the highest methane production of 35.13 ± 1.05 m^3 CH_4/ tonne-substrate was achieved at an S:I ratio of 15:1, representing a 64.31 ± 1.17% improvement over the control (21.38 ± 0.64 m^3 CH_4/tonne-substrate). The enhanced methane yield can be attributed to the increased cellulolytic and hemicellulolytic activities of the augmented strain, which facilitated the effective hydrolysis of EFB [18]. The methane yield improvement ranged from 25.26 ± 0.88% to 113.9 ± 1.60% across the different S:I ratios, with the highest improvement observed at the 4:1 ratio. This finding suggests that the augmented *T. thermosaccharolyticum* PSU-2 can significantly enhance methane production from EFB, even at higher substrate concentrations [19].

The biodegradability and removal of VS from EFB were also positively influenced by the augmentation with *T. thermosaccharolyticum* PSU-2. The highest biodegradability of 47.31 ± 1.42% and VS removal of 58.91 ± 1.77% were observed at the S:I ratio 15:1, indicating efficient degradation of the lignocellulosic components of EFB. The enhanced degradation efficiency can be attributed to the improved enzymatic machinery of the augmented strain, which enables the effective breakdown of the complex polysaccharides in EFB [20]. The volatile fatty acid (VFA) concentrations remained relatively low (0.046 ± 0.00 to 0.093 ± 0.00 g/L) across all S:I ratios, suggesting a well-balanced AD process with efficient conversion of the hydrolyzed products to biogas [21]. The alkalinity levels (12.9 ± 0.39 to 17.5 ± 0.53 g$CaCO_3$/L) were within the optimal range for stable AD, indicating sufficient buffering capacity to maintain a suitable pH for the methanogenic community [22]. Interestingly, the highest methane yield improvement (113.9 ± 1.60%) was observed at the 4:1 S:I ratio, while the highest biodegradability and VS removal were achieved at the 15:1 ratio. This discrepancy suggests that factors other than substrate degradation efficiency, such as the balance between hydrolysis and methanogenesis rates, may influence the overall methane production [23]. The augmented *T. thermosaccharolyticum* PSU-2 demonstrates superior performance in the mono-digestion of EFB, enhancing biogas yield, methane content, and substrate degradation efficiency. The improved hydrolytic capabilities of the augmented strain facilitate the effective breakdown of the lignocellulosic components of EFB, leading to higher methane production and better substrate utilization. These findings highlight the potential of using augmented cellulolytic and hemicellulolytic bacteria to optimize the AD of lignocellulosic biomass for biogas production.

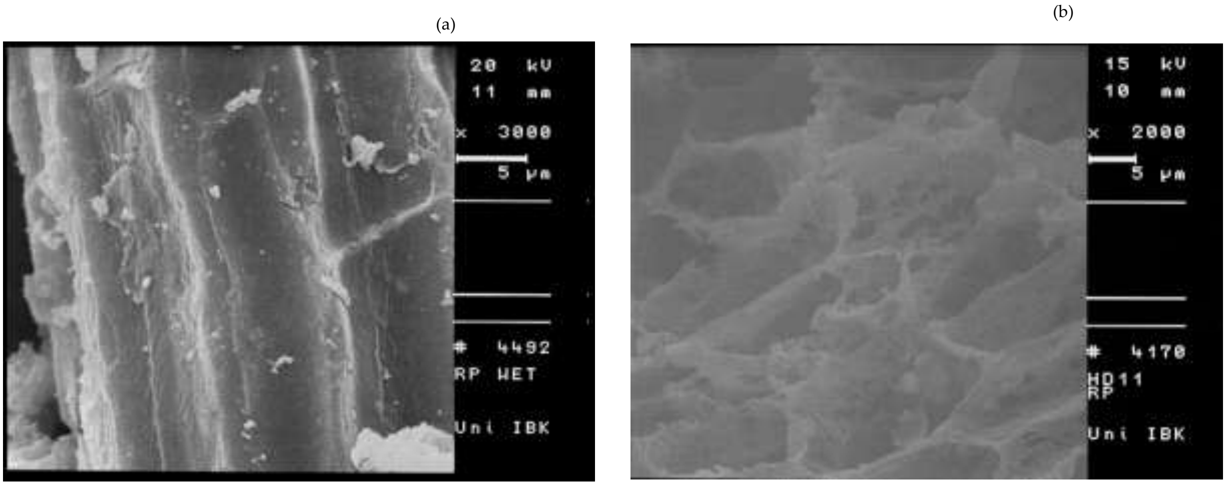

Figure 1. SEM images of EFB before (a) and after hydrolysis (b) by the augmented *T. thermosaccharolyticum* PSU-2

Figure 1 illustrates the cumulative methane yield of mono-digestion EFB augmented with *T. thermosaccharolyticum* PSU-2 at various substrate-to-inoculum (S:I) ratios. The results demonstrate that the augmentation of *T. thermosaccharolyticum* PSU-2 significantly enhances the methane yield compared to the control without augmentation across all S:I ratios tested. The highest cumulative methane yield was achieved at an S:I ratio of 15:1, indicating that this ratio provides the optimal balance between substrate availability and inoculum concentration for effective methane production. This finding is consistent with the results reported by Suksong et al. [24], who observed improved methane yields from the mono-digestion of EFB using a cellulolytic bacterial consortium. The enhanced methane yield can be attributed to the increased hydrolytic capabilities of the augmented *T. thermosaccharolyticum* PSU-2, which facilitates the effective breakdown of the lignocellulosic components in EFB [25]. The cumulative methane yield curves for the augmented digestions exhibit a steeper slope than the control, indicating faster methane production rates. This observation suggests that the augmented *T. thermosaccharolyticum* PSU-2 accelerates the hydrolysis step, which is often considered the rate-limiting step in the AD of lignocellulosic biomass [26]. The improved hydrolysis rate can be attributed to the augmented strain's enhanced cellulolytic and hemicellulolytic activities, as demonstrated in previous studies [19,20]. Interestingly, the cumulative methane yield curves for the augmented digestions at different S:I ratios show similar trends, with only minor variations in the final methane yields. This finding indicates that the augmented *T. thermosaccharolyticum* PSU-2 can maintain its hydrolytic efficiency even at higher substrate concentrations, which is crucial for the practical application of this augmentation strategy in industrial-scale biogas plants [27]. The control digestion without augmentation exhibited a lower methane yield and a more gradual increase in cumulative methane production over time. This slower methane production rate can be attributed to the limited hydrolytic capabilities of the indigenous microbial community present in the inoculum [10]. The limited hydrolysis rate in the control digestion highlights the need for augmentation strategies to enhance the AD performance of lignocellulosic biomass, such as EFB. The cumulative methane yield curves presented in Figure 2 demonstrate the effectiveness of augmenting the mono-digestion of EFB with *T. thermosaccharolyticum* PSU-2. The enhanced methane yields and faster methane production rates observed across various S:I ratios underscore the potential of this augmentation strategy to optimize the AD process and improve the overall biogas production from lignocellulosic biomass.

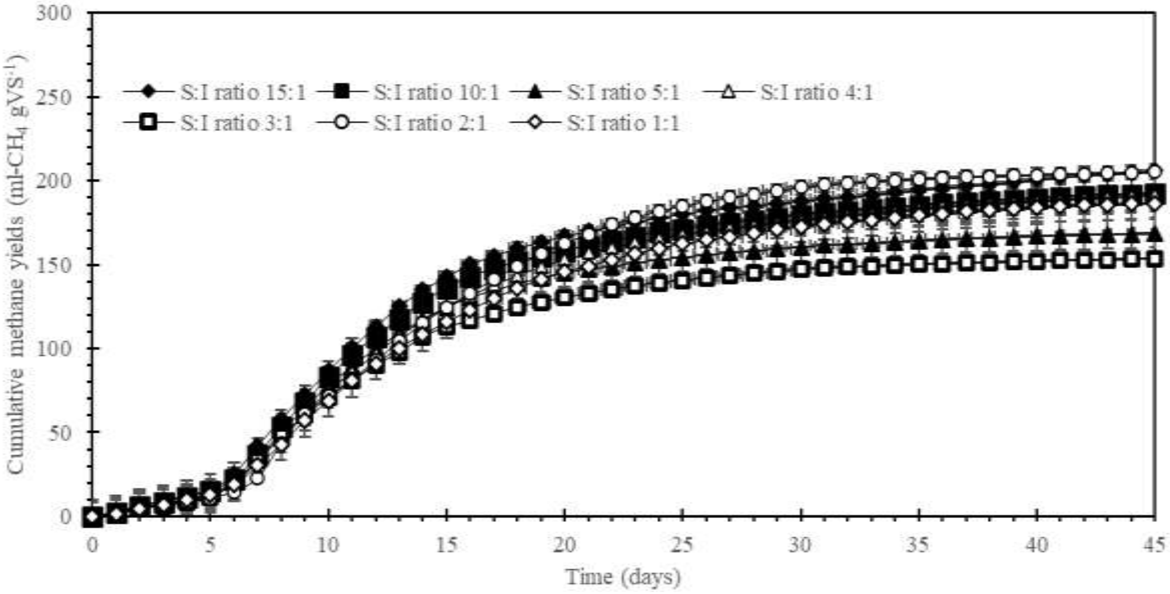

Figure 2. Cumulative methane yield of mono-digestion EFB with *T. thermosaccharolyticum* PSU-2 augmentation at various S:I ratio

3.3 Performance of augmented *T. thermosaccharolyticum* PSU-2 in EFB co-digestion with POME

The co-digestion of EFB with POME using the augmented *T. thermosaccharolyticum* PSU-2 demonstrated significant improvements in biogas yield and methane content compared to the control without augmentation. As shown in Table 2, the highest methane production of 46.67 ± 1.40 m^3 CH_4/tonne-substrate was achieved at an S:I ratio of 15:1, representing a 103.00 ± 2.81% improvement over the control (22.99 ± 0.09 m^3 CH_4/tonne- substrate). The enhanced methane yield can be attributed to the synergistic effect of co-digesting EFB with POME, which provides a more balanced nutrient profile and improves the overall biodegradability of the substrate [4]. The methane yield improvement ranged from 48.54 ± 2.84% to 103.00 ± 2.81% across the different S:I ratios, indicating that the augmented *T. thermosaccharolyticum* PSU-2 can significantly enhance the methane production from EFB co-digested with POME. This finding is consistent with the results reported by [28], who observed improved biogas yields from the co-digestion of EFB with POME using a thermophilic bacterial consortium. The biodegradability and removal of VS from EFB and POME were also positively influenced by the augmentation with *T. thermosaccharolyticum* PSU-2. The highest biodegradability of 55.44 ± 1.66% and VS removal of 66.53 ± 2.00% were observed at the S:I ratio of 15:1, indicating efficient degradation of the lignocellulosic components of EFB and the organic matter present in POME [5]. The enhanced degradation efficiency can be attributed to the improved hydrolytic capabilities of the augmented strain, which enable the effective breakdown of the complex substrates in the co-digestion mixture [20]. The volatile fatty acid (VFA) concentrations remained relatively low (0.035 ± 0.00 to 0.048 ± 0.00 g/L) across all S:I ratios, suggesting a well-balanced AD process with efficient conversion of the hydrolyzed products to biogas [21] . The alkalinity levels (14.9 ± 0.45 to 15.65 ± 0.47 $gCaCO_3/L$) were within the optimal range for stable AD, indicating sufficient buffering capacity to maintain a suitable pH for the methanogenic community [22]. Interestingly, the methane yield improvement and degradation efficiency were higher in the co-digestion experiments compared to the mono-digestion of EFB (Table 2). This observation highlights the benefits of co-digesting EFB with POME, which include improved nutrient balance, increased buffering capacity, and the presence of readily biodegradable organic matter in POME that stimulates the growth of the anaerobic microbial community [29]. The augmented *T. thermosaccharolyticum* PSU-2 demonstrates superior performance in the co-digestion of EFB with POME, enhancing biogas yield, methane content, and substrate degradation efficiency. The improved hydrolytic capabilities of the augmented strain, coupled with the synergistic effects of co-digestion, facilitate the effective breakdown and conversion of the complex substrates into biogas. These findings underscore the potential of using augmented cellulolytic and hemicellulolytic bacteria in conjunction with co-digestion strategies to optimize the AD of lignocellulosic biomass and POME for enhanced biogas production.

Figure 2 illustrates the cumulative methane yield of co-digestion of EFB with POME augmented with *T. thermosaccharolyticum* PSU-2 at various substrate-to-inoculum (S:I) ratios. The results demonstrate that the augmentation of T. thermosaccharolyticum PSU-2 significantly enhances the methane yield compared to the control without augmentation across all S:I ratios tested. The highest cumulative methane yield was achieved at an S:I ratio of 15:1, indicating that this ratio provides the optimal balance between substrate availability and inoculum concentration for effective methane production in the co-digestion system. This finding is consistent with the results reported by Saelor et al. [28], who observed improved biogas yields from the co-digestion of EFB with POME using a thermophilic bacterial consortium. The enhanced methane yield can be attributed to the increased hydrolytic capabilities of the augmented *T. thermosaccharolyticum* PSU-2, which facilitates the effective breakdown of the lignocellulosic components in EFB and the organic matter present in POME. The cumulative methane yield curves for the augmented co-digestions exhibit a steeper slope than the control, indicating faster methane production rates. This observation suggests that the augmented *T. thermosaccharolyticum* PSU-2 accelerates hydrolysis, often considered the rate-limiting step in the AD of lignocellulosic biomass and POME [29]. The improved hydrolysis rate can be attributed to the enhanced cellulolytic and hemicellulolytic activities of the augmented strain and the synergistic effects of co-digesting EFB with POME [5]. Interestingly, the cumulative methane yield curves for the augmented co-digestions at different S:I ratios show similar trends, with only minor variations in the final methane yields. This finding indicates that the augmented *T. thermosaccharolyticum* PSU-2 can maintain its hydrolytic efficiency even at higher substrate concentrations in the co-digestion system. It is crucial to practically apply this augmentation strategy in industrial-scale biogas plants [27]. The control co-digestion without augmentation exhibited a lower methane yield and a more gradual increase in cumulative methane production over time than the augmented co-digestions. This slower methane production rate can be attributed to the limited hydrolytic capabilities of the indigenous microbial community present in the inoculum [10]. The limited hydrolysis rate in the control co-digestion highlights the need for augmentation strategies to enhance the AD performance of lignocellulosic biomass and POME. The cumulative methane yield curves presented in Figure 3 demonstrate the effectiveness of augmenting the co-digestion of EFB with POME using *T. thermosaccharolyticum* PSU-2. The enhanced methane yields and faster methane production rates observed across various S:I ratios underscore the potential of this augmentation strategy to optimize the anaerobic co-digestion process and improve the overall biogas production from lignocellulosic biomass and POME.

Table 2. Summary parameter from biogas production by bio-augmentation *T. thermosaccharolyticum* PSU-2

S:I ratio	**Methane production (m^3 CH_4/tonne-substrate)**		**Improvement (%)**	**biodegradability (%)**	**VS removal (%)**	**VFA (g· L^{-1})**	**Alkalinity (g$CaCO_3$/L)**
	Augmentation	Control					
Mono digestion of EFB							
15:1	35.13 ± 1.05	21.38 ± 0.64	64.31 ± 1.17	47.31 ± 1.42	58.91 ± 1.77	0.058 ± 0.00	17.5 ± 0.53
10:1	32.81 ± 0.98	16.63 ± 0.50	97.29 ± 1.48	44.17 ± 1.33	55.01 ± 1.65	0.072 ± 0.00	16 ± 0.47
5:1	28.82 ± 0.86	19.74 ± 0.59	45.99 ± 0.95	38.81 ± 1.16	48.32 ± 1.45	0.05 ± 0.00	15.5 ± 0.45
4:1	32.65 ± 0.97	15.26 ± 0.46	113.9 ± 1.60	43.97 ± 1.32	54.75 ± 1.64	0.082 ± 0.00	14.9 ± 0.45
3:1	26.2 ± 0.77	18.51 ± 0.56	25.26 ± 0.88	35.28 ± 1.06	43.93 ± 1.32	0.046 ± 0.00	12.9 ± 0.39
2:1	34.97 ± 1.05	22.3 ± 0.67	56.24 ± 0.99	47.09 ± 1.41	58.64 ± 1.76	0.093 ± 0.00	14.85 ± 0.45
1:1	31.81± 0.95	22.41 ± 0.67	49.54 ± 0.89	42.84 ± 1.29	53.34 ± 1.60	0.059 ± 0.00	12.95 ± 0.39
Co-digestion of EFB with POME							
15:1	46.67 ± 1.40	22.99 ± 0.09	103.00 ± 2.81	55.44 ± 1.66	66.53 ± 2.00	0.048 ± 0.00	14.9 ± 0.45
10:1	45.4 ± 1.36	22.95 ± 0.09	97.82 ± 2.81	53.94 ± 1.62	64.73 ± 1.94	0.04 ± 0.00	15.6 ± 0.47
5:1	40.26 ± 1.20	23.2 ± 0.10	73.53 ± 2.76	47.84 ± 1.44	57.4 ± 1.72	0.043 ± 0.00	15.4 ± 0.46
4:1	37.1 ± 1.11	23.22 ± 0.10	59.77 ± 2.74	44.08 ± 1.32	52.9 ± 1.59	0.035 ± 0.00	15.5 ± 0.47
3:1	38.86 ± 1.17	22.81 ± 0.08	67.36 ± 2.78	46.17 ± 1.39	55.4 ± 1.66	0.042 ± 0.00	15.65 ± 0.47
2:1	32.22 ± 0.97	21.69 ± 0.05	48.54 ± 2.84	38.28 ± 1.15	45.94 ± 1.38	0.038 ± 0.00	15.55 ± 0.47
1:1	38.04 ± 1.14	22.43 ± 0.07	69.59 ± 2.81	45.2 ± 1.36	54.24 ± 1.63	0.042 ± 0.00	15.5 ± 0.47

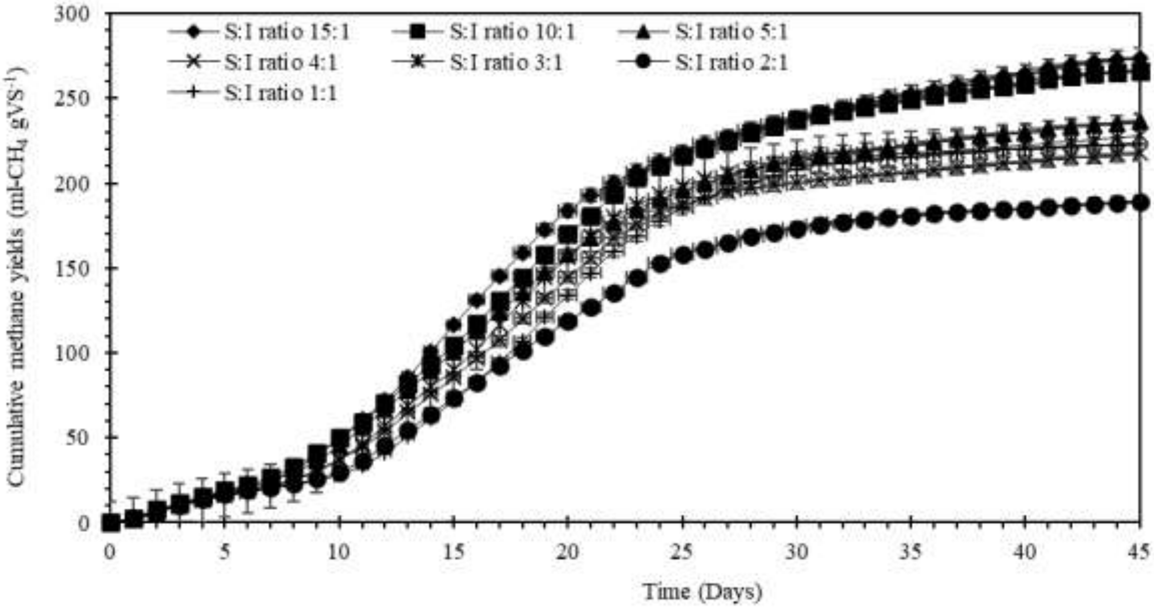

Figure 3. Cumulative methane yield of co-digestion EFB with POME and *T. thermosaccharolyticum* PSU-2 augmentation at various S:I ratio

3.4 Comparison of mono-digestion and co-digestion performance

The kinetic parameters obtained from the biogas production experiments using bioaugmentation with *T. thermosaccharolyticum* PSU-2 at various S:I ratios for both mono-digestion of EFB and co-digestion of EFB with POME are presented in Table 3. The table allows for a direct comparison of the digestion performance between the two processes. The methane production rate was higher in the co-digestion process compared to mono-digestion at all S:I ratios, with the highest rate of 13.34 ± 0.40 mL-CH_4/gVS/d observed at the 15:1 ratio in co-digestion. This finding is consistent with the results reported by [30], who observed enhanced methane production rates in the co-digestion of POME with EFB compared to the mono-digestion of EFB. The improved methane production rate in co-digestion can be attributed to the synergistic effects of the two substrates, which provide a more balanced nutrient profile and support the growth of a diverse microbial community [29]. Interestingly, the lag time was generally longer in the co-digestion process compared to mono-digestion, ranging from 6.09 ± 0.18 to 8.68 ± 0.26 days in co-digestion and 3.62 ± 0.11 to 4.68 ± 0.14 days in mono-digestion. This observation suggests that adapting the microbial community to the co-digestion substrate mixture may require more time than the mono-digestion of EFB [28]. However, the longer lag time in co-digestion did not negatively impact the overall methane yield and production rate, as evidenced by the higher values observed in co-digestion compared to mono-digestion. The hydrolysis constant (k_h) was similar in mono-digestion and co-digestion processes, ranging from 0.07 to 0.11 d^{-1}. This finding indicates that the hydrolysis rate of the substrates was not significantly affected by the co-digestion process [25]. However, the slightly lower hydrolysis constants observed in co-digestion at some S:I ratios may be attributed to the higher complexity of the substrate mixture, which could potentially slow down the hydrolysis process [5]. The methane yield and methane production per tonne of mixed waste were consistently higher in the co-digestion process compared to mono-digestion at all S:I ratios. The highest methane yield of 232.87 ± 6.99 mL-CH_4/gVS and methane production of 46.67 ± 1.46 m^3/tonne were observed at the 15:1 ratio in co-digestion, representing a 12.9% and 32.9% increase, respectively, compared to mono-digestion at the same ratio. These findings highlight the benefits of co-digesting EFB with POME, which includes improved methane yield and production due to the complementary characteristics of the substrates

[27]. The coefficient of determination (R^2) values were consistently high (0.99) for all the kinetic models fitted to the experimental data, indicating that the first-order kinetic model adequately described the methane production in both mono-digestion and co-digestion processes [24]. The comparison of mono-digestion and co-digestion performance using bioaugmentation with *T. thermosaccharolyticum* PSU-2 demonstrates the superiority of the co-digestion process in terms of methane production rate, methane yield, and methane production per tonne of mixed waste. The synergistic effects of co-digesting EFB with POME, coupled with the enhanced hydrolytic capabilities of the augmented strain, result in improved digestion performance and higher energy recovery from the substrates.

Table 3. Kinetic parameter from biogas production by bio-augmentation

S:I ratio	Methane production rate (mL-CH_4/gVS/d)	Lag time (d)	R^2	k_h (d^{-1})	Methane yield (mL-CH_4 /gVS)	Methane production (m^3 /$tonne_{mixwaste}$)
Mono digestion of EFB						
15:1	13.11 ± 0.39	3.62 ± 0.11	0.99	0.1 ± 0.00	206.18 ± 6.19	35.13 ± 1.05
10:1	12.64 ± 0.38	3.77 ± 0.11	0.99	0.1 ± 0.00	192.52 ± 5.78	32.81 ± 0.98
5:1	12.25 ± 0.37	3.95 ± 0.12	0.99	0.11 ± 0.00	169.13 ± 5.07	28.82 ± 0.86
4:1	11.57 ± 0.35	3.94 ± 0.12	0.99	0.1 ± 0.00	191.62 ± 5.75	32.65 ± 0.98
3:1	10.78 ± 0.32	3.77 ± 0.11	0.99	0.11 ± 0.00	153.74 ± 4.61	26.2 ± 0.79
2:1	12.4 ± 0.37	4.68 ± 0.14	0.99	0.1 ± 0.00	205.24 ± 6.16	34.97 ± 1.05
1:1	10.56 ± 0.32	3.86 ± 0.12	0.99	0.09 ± 0.00	186.7 ± 5.60	31.81 ± 0.95
Co-digestion of EFB with POME						
15:1	13.34 ± 0.40	6.17 ± 0.19	0.99	0.07 ± 0.00	232.87 ± 6.99	46.67 ± 1.46
10:1	12.67 ± 0.38	6.25 ± 0.19	0.99	0.07 ± 0.00	226.54 ± 6.80	45.4 ± 1.36
5:1	11.76 ± 0.35	6.09 ± 0.18	0.99	0.07 ± 0.00	200.92 ± 6.03	40.26 ± 1.21
4:1	11.77 ± 0.35	7.12 ± 0.21	0.99	0.08 ± 0.00	185.14 ± 5.55	37.1 ± 1.11
3:1	13.1 ± 0.39	7.48 ± 0.22	0.99	0.08 ± 0.00	193.91 ± 5.82	38.86 ± 1.17
2:1	9.46 ± 0.28	6.84 ± 0.21	0.99	0.07 ± 0.00	160.77 ± 4.82	32.22 ± 0.97
1:1	12.37 ± 0.37	8.68 ± 0.26	0.99	0.07 ± 0.00	189.84 ± 5.70	38.04 ± 1.14

The performance of mono-digestion and co-digestion at the optimal substrate-to-inoculum (S:I) ratio of 15:1 is compared in Table 4. The results demonstrate that the co-digestion of EFB with POME significantly enhances the methane yield, biodegradability, and VS removal compared to the mono-digestion of EFB. The methane yield in co-digestion (46.67 ± 1.40 m^3 CH_4/tonne-substrate) was 32.9% higher than in mono-digestion (35.13 ± 1.05 m^3 CH_4/tonne-substrate). This finding is consistent with the results reported by [30], who observed a significant increase in methane yield when co-digesting POME with EFB compared to the mono-digestion of EFB. The improved methane yield in co-digestion can be attributed to the synergistic effects of the two substrates, which provide a more balanced nutrient profile and support the growth of a diverse microbial community [29]. The methane yield improvement over the control (without augmentation) was also higher in co-digestion (103.00 ± 2.81%) compared to mono-digestion (64.31 ± 1.17%). This finding highlights the effectiveness of the augmented *T. thermosaccharolyticum* PSU-2 in enhancing methane production in both digestion processes, with a more pronounced effect in co-digestion [28]. Biodegradability and VS removal were also higher in co-digestion (55.44 ± 1.66% and 66.53 ± 2.00%, respectively) compared to mono-digestion (47.31 ± 1.42% and 58.91 ± 1.77%, respectively). These results indicate that co-digestion of EFB with POME improves the overall substrate utilization and degradation efficiency, which can be attributed to the complementary characteristics of the substrates and the enhanced hydrolytic capabilities of the augmented strain [5,27]. The volatile fatty acid (VFA) concentration was lower in co-digestion (0.048 ± 0.00 g/L) compared to mono-digestion (0.058 ± 0.00 g/L), suggesting a more efficient conversion of the hydrolyzed products to biogas in the co-digestion process [21]. The alkalinity was also slightly lower in co-digestion (14.9 ± 0.45 $gCaCO_3/L$) compared to mono-digestion (17.5 ± 0.53 $gCaCO_3/L$), but both values were within the optimal range for stable AD [22]. The comparison of mono-digestion and co-digestion performance at the optimal S:I ratio of 15:1 demonstrates the co-digestion process's superiority in methane yield, biodegradability, and VS removal. The synergistic effects of co-digesting EFB with POME, coupled with the enhanced hydrolytic capabilities of the augmented *T. thermosaccharolyticum* PSU-2, result in improved digestion performance and higher energy recovery from the substrates. These findings highlight the potential of co-digestion as a promising strategy to optimize the AD of lignocellulosic biomass and POME for biogas production.

Table 4. Comparison of mono-digestion and co-digestion performance at the optimal S:I ratio (15:1)

Parameter	Mono-digestion	Co-digestion
Methane yield (m^3 CH_4/tonne-substrate)	35.13 ± 1.05	46.67 ± 1.40
Methane yield improvement (%)	64.31 ± 1.17	103.00 ± 2.81
Biodegradability (%)	47.31 ± 1.42	55.44 ± 1.66
VS removal (%)	58.91 ± 1.77	66.53 ± 2.00
VFA (g/L)	0.058 ± 0.00	0.048 ± 0.00
Alkalinity ($gCaCO_3/L$)	17.5 ± 0.53	14.9 ± 0.45

3.5 Comparison with other pretreatment methods

Table 5 compares the performance of the augmented *T. thermosaccharolyticum* PSU-2 pretreatment method with other pretreatment methods applied to various lignocellulosic biomass substrates. The comparison includes alkaline pretreatment, hydrothermal pretreatment, fungal pretreatment, ionic liquid pretreatment, microwave-alkaline pretreatment, and steam explosion pretreatment. The methane yield obtained from the mono-digestion of EFB pretreated with augmented *T. thermosaccharolyticum* PSU-2 (35.13 ± 1.05 m^3 CH_4/tonne) is lower than the yields reported for other pretreatment methods. However, it is essential to consider the nature of the substrate and the specific experimental conditions when comparing the effectiveness of different pretreatment methods [3]. Interestingly, the co-digestion of EFB and POME pretreated with augmented *T. thermosaccharolyticum* PSU-2 resulted in a significantly higher methane yield (46.67 ± 1.40 m^3 CH_4/tonne) and improvement (103.00 ± 2.81%) compared to the mono-digestion of pretreated EFB. This finding highlights the synergistic effects of co-digestion and the importance of substrate combinations in enhancing biogas production [30]. Among the other pretreatment methods, ionic liquid pretreatment of corn stover resulted in the highest methane yield (304.0 m^3 CH_4/tonne) and improvement (39.6%) [31]. Ionic liquids have shown great potential in solubilizing and fractionating lignocellulosic biomass, making it more accessible to microbial degradation [32]. However, ionic liquids' high cost and potential environmental concerns may limit their large-scale application [33]. Hydrothermal and microwave-alkaline pretreatments also resulted in high methane yields (257.4 and 260.0 m^3 CH_4/tonne, respectively) and improvements (35.0% and 28.0%, respectively) [34,35]. These pretreatment methods employ a combination of high temperature, pressure, and alkaline conditions to disrupt the lignocellulosic structure and enhance biodegradability [36]. Fungal pretreatment using *Phanerochaete chrysosporium* resulted in a lower methane yield (120.6 m^3 CH_4/tonne) and improvement (33.0%) compared to the other pretreatment methods [37]. However, biological pretreatments are generally considered more environmentally friendly and less energy-intensive than physicochemical methods [38]. Steam explosion pretreatment of corn stovers resulted in the lowest improvement (18.8%) among the compared methods [39]. Although steam explosion is effective for lignocellulosic biomass pretreatment, its performance may vary depending on substrate characteristics and conditions [40]. The augmented *T. thermosaccharolyticum* PSU-2 pretreatment method, particularly when applied to the co-digestion of EFB and POME, demonstrated a significant improvement in methane yield compared to the mono-digestion of pretreated EFB. While the methane yields obtained in this study are lower than the other pretreatment methods, it is important to consider each method specific substrate characteristics, experimental conditions, and potential economic and environmental implications. Future research should optimize the pretreatment conditions and explore the synergistic effects of combining biological pretreatment with other methods to maximize biogas production from lignocellulosic biomass.

Table 5. Comparison of different pretreatment methods for AD of lignocellulosic biomass

Pretreatment Method	**Substrate**	**Methane Yield (m^3 CH_4/tonne)**	**Improvement (%)**	**Reference**
Augmented *T. thermosaccharolyticum* PSU-2	EFB	35.13 ± 1.05	64.31 ± 1.17	This study
Augmented *T. thermosaccharolyticum* PSU-2 (co-digestion)	EFB + POME	46.67 ± 1.40	103.00 ± 2.81	This study
Alkaline pretreatment	Rice straw	220.0	57.1	[41]
Hydrothermal pretreatment	Sugarcane bagasse	257.4	35.0	[34]
Fungal pretreatment (*Phanerochaete chrysosporium*)	Rice straw	120.6	33.0	[37]
Ionic liquid pretreatment	Corn stover	304.0	39.6	[31]
Microwave-alkaline pretreatment	Wheat straw	260.0	28.0	[35]
Steam explosion pretreatment	Corn stover	190.0	18.8	[39]

3.6 Energy balance and economic analysis

The energy balance and economic analysis of the augmented *T. thermosaccharolyticum* PSU-2 pretreatment method for both mono-digestion of EFB and co-digestion of EFB with POME are presented in Table 6. The energy input, including the pretreatment and AD processes, was considered 350 MJ/tonne for mono-digestion and co-digestion. Energy output was calculated based on the methane yield and lower heating value (35.8 MJ/m^3) [42]. The co-digestion of EFB with POME resulted in a higher net energy yield (1,320.79 MJ/tonne) compared to the mono-digestion of EFB (907.65 MJ/tonne). This can be attributed to the higher methane yield obtained from co-digestion (46.67 m^3 CH_4/tonne) than mono-digestion (35.13 m^3 CH_4/tonne). The energy output to input ratio was also higher for co-digestion (4.77) than for mono-digestion (3.59). These findings suggest that co-digestion of EFB with POME is more energy-efficient than mono-digestion of EFB [43]. The economic analysis considered the pretreatment and AD costs and the revenue generated from the produced methane. The total production cost was approximately 25 USD/tonne for mono-digestion and co-digestion. Revenue from methane was calculated based on a selling price of 1 USD/m^3 [43]. Co-digestion of EFB with POME generated a higher revenue (46.67 USD/tonne) than mono-digestion of EFB (35.13 USD/tonne) due to the higher methane yield obtained from co-digestion. The net profit, calculated by subtracting the total production cost from the revenue generated from methane, was higher for co-digestion (21.67 USD/tonne) than mono-digestion (10.13 USD/tonne). This indicates that co-digestion of EFB with POME is a more profitable approach than mono-digestion of EFB. The payback period, the time required to recover the initial investment, was shorter for co-digestion (1.15 years) than for mono-digestion (2.47 years). This suggests that co-digestion of EFB with POME can lead to a faster return on investment than EFB mono-digestion. It is important to note that the values provided in the table are hypothetical and may vary depending on the specific project conditions, scale, and location. A more detailed economic analysis should consider factors such as capital costs, operating costs, maintenance costs, and potential revenue from digestate utilization [44]. Furthermore, the availability and cost of feedstocks and the market demand for biogas should be considered when assessing the economic feasibility of the pretreatment method [45]. The energy balance and economic analysis suggest that the augmented *T. thermosaccharolyticum* PSU-2 pretreatment method, particularly when applied to the co-digestion of EFB with POME, is a promising approach for enhancing biogas production from lignocellulosic biomass. Co-digestion of EFB with POME results in higher energy efficiency, profitability, and shorter payback periods than mono-digestion of EFB. However, further research is needed to optimize the pretreatment conditions and assess the scalability and long-term performance of the augmented pretreatment method at both pilot and full-scale levels.

Table 6. Energy balance and economic analysis of the augmented *T. thermosaccharolyticum* PSU-2 pretreatment method for AD of EFB and co-digestion of EFB with POME

Parameter	**Mono-digestion (EFB)**	**Co-digestion (EFB + POME)**
Methane yield (m^3 CH_4/tonne)	35.13	46.67
Energy input (MJ/tonne)		
- Pretreatment	150	150
- AD	200	200
Total energy input (MJ/tonne)	350	350
Energy output (MJ/tonne)		
- Methane (Lower heating value: 35.8 MJ/m^3)	1,257.65	1,670.79
Net energy yield (MJ/tonne)	907.65	1,320.79
Energy ratio (Output/Input)	3.59	4.77
Economic analysis		
- Pretreatment cost (USD/tonne)	10	10
- AD cost (USD/tonne)	15	15
- Total production cost (USD/tonne)	25	25
- Revenue from methane (USD/tonne)	35.13	46.67
- Net profit (USD/tonne)	10.13	21.67
- Payback period (years)	2.47	1.15

4. Conclusions

This study investigated the effectiveness of augmenting *T. thermosaccharolyticum* PSU-2 for the pretreatment of EFB in mono-digestion and co-digestion with POME. The augmented *T. thermosaccharolyticum* PSU-2 demonstrated enhanced cellulolytic and hemicellulolytic capabilities, as evidenced by the increased enzymatic activities, improved growth performance on lignocellulosic substrates, and higher yields of hydrolysis products compared to the wild-type strain. Mono-digestion of EFB with the augmented *T. thermosaccharolyticum* PSU-2 improved biogas yield, methane content, and substrate degradation efficiency compared to the control without augmentation. The highest methane yield of 35.13 ± 1.05 m^3 CH_4/tonne was achieved at an S:I ratio of 15:1, representing a 64.31 ± 1.17% improvement over the control. Co-digestion of EFB with POME using the augmented *T. thermosaccharolyticum* PSU-2 further enhanced the biogas yield, methane content, and substrate degradation efficiency compared to mono-digestion. The highest methane yield of 46.67 ± 1.40 m^3 CH_4/tonne was achieved at an S:I ratio of 15:1, representing a 103.00 ± 2.81% improvement over the control. Kinetic analysis revealed that the augmented *T. thermosaccharolyticum* PSU-2 improved the hydrolysis rate and reduced the lag phase in mono-digestion and co-digestion processes. Co-digestion of EFB with POME exhibited higher methane production potential and biodegradability than mono-digestion of EFB. Comparison with other pretreatment methods suggested that the augmented *T. thermosaccharolyticum* PSU-2 pretreatment, particularly when applied to the co-digestion of EFB with POME, is a promising approach for enhancing biogas production from lignocellulosic biomass. However, further optimization and comparison with other pretreatment methods are needed to assess its full potential. Energy balance and economic analysis indicated that co-digestion of EFB with POME using the augmented *T. thermosaccharolyticum* PSU-2 pretreatment is more energy-efficient and profitable than mono-digestion of EFB. Co-digestion resulted in higher net energy yields, higher net profits, and shorter payback periods. The augmented *T. thermosaccharolyticum* PSU-2 pretreatment method, particularly when applied to the co-digestion of EFB with POME, has demonstrated significant potential for enhancing biogas production from lignocellulosic biomass. The improved hydrolytic capabilities of the augmented strain, coupled with the synergistic effects of co-digestion, result in higher methane yields, better substrate degradation efficiency, and enhanced process kinetics. However, further research is needed to optimize the pretreatment conditions, assess the long-term stability and performance of the augmented strain, and evaluate the scalability and economic feasibility of the pretreatment method in pilot and full-scale applications. Additionally, the potential for combining biological pretreatment with other methods should be explored to maximize the biogas production potential from lignocellulosic biomass. The findings of this study contribute to developing efficient and sustainable strategies for valorizing agricultural waste streams, such as EFB and POME, through AD. The augmented *T. thermosaccharolyticum* PSU-2 pretreatment method can enhance biogas production's economic viability and environmental sustainability from lignocellulosic biomass, promoting the transition towards a circular economy and renewable energy generation.

5. Acknowledgements

The authors thank the Thailand Research Fund through grant number (RRI_PHD60I0009) National Research Council of Thailand (NRCT) for the financial support.

Author Contributions: Conceptualization, experimental design, S.S., C.M., N.P., carrying out experiment and data acquisition, S.S., C.M., N.P. writing and editing, S.S., N.P.

Funding: This research was funded by the Thailand Research Fund through grant number (RRI_PHD60I0009) National Research Council of Thailand (NRCT)

Conflicts of Interest: The authors declare no conflict of interest.

References

[1] Surendra, K. C.; Sawatdeenarunat, C.; Shrestha, S.; Sung, S.; Khanal, S. K. Anaerobic digestion-based biorefinery for bioenergy and biobased products. *Industrial Biotechnology* **2015**, *11*(2), 103–112. doi:10.1089/ind.2015.0001.

[2] Aragaw, T.; Andargie, M.; Gessesse, A. Co-digestion of cattle manure with organic kitchen waste to increase biogas production using rumen fluid as inoculums. *International Journal of Physical Sciences* **2013**, *8*(11), 443–450. doi:10.5897/IJPS2013.3863.

[3] Carrere, H.; Antonopoulou, G.; Affes, R.; Passos, F.; Battimelli, A.; Lyberatos, G.; et al. Review of feedstock pretreatment strategies for improved anaerobic digestion: From lab-scale research to full-scale application. Bioresource Technology **2016**, *199*, 386–397. doi:10.1016/j.biortech.2015.09.007.

[4] Krishnan, S.; Singh, L.; Sakinah, M.; Thakur, S.; Wahid, Z. A.; Sohaili, J. Effect of organic loading rate on hydrogen (H_2) and methane (CH_4) production in two-stage fermentation under thermophilic conditions using palm oil mill effluent (POME). *Energy for Sustainable Development* **2016**, *34*, 130–138. doi:10.1016/j.esd.2016.07.002.

[5] Nieves, D. C.; Karimi, K.; Horváth, I. S. Improvement of biogas production from oil palm empty fruit bunches (OPEFB). *Industrial Crops and Products* **2011**, *34*(1), 1097–1101. doi:10.1016/j.indcrop.2011.03.022.

[6] Amin, F. R.; Khalid, H.; Zhang, H.; Rahman, S.; Zhang, R.; Liu, G.; et al. Pretreatment methods of lignocellulosic biomass for anaerobic digestion. *AMB Express* **2017**, 7(1). doi:10.1186/s13568-017-0375-4.

[7] Paudel, S. R.; Banjara, S. P.; Choi, O. K.; Park, K. Y.; Kim, Y. M.; Lee, J. W. Pretreatment of agricultural biomass for anaerobic digestion: Current state and challenges. *Bioresource Technology* **2017**, *245*, 1194–1205. doi:10.1016/j.biortech.2017.08.182.

[8] Ren, N.; Wang, A.; Cao, G.; Xu, J.; Gao, L. Bioconversion of lignocellulosic biomass to hydrogen: Potential and challenges. *Biotechnology Advances* **2009**, *27*(6), 1051–1060. doi:10.1016/j.biotechadv.2009.05.007.

[9] Tsapekos, P.; Kougias, P. G.; Treu, L.; Campanaro, S.; Angelidaki, I. Process performance and comparative metagenomic analysis during co-digestion of manure and lignocellulosic biomass for biogas production. *Applied Energy* **2017**, *185*, 126–135. doi:10.1016/j.apenergy.2016.10.081.

[10] Rabii, A.; Aldin, S.; Dahman, Y.; Elbeshbishy, E. A review on anaerobic co-digestion with a focus on the microbial populations and the effect of multi-stage digester configuration. *Energies* **2019**, *12*(6). doi:10.3390/en12061106.

[11] Hagos, K.; Zong, J.; Li, D.; Liu, C.; Lu, X. Anaerobic co-digestion process for biogas production: Progress, challenges and perspectives. **Renewable and Sustainable Energy Reviews 2017**, *76*(September), 1485–1496. doi:10.1016/j.rser.2016.11.184.

[12] APHA, AWWA, W. Standard Methods for Examination of Water and Wastewater (22ND ED); Eugene W. Rice , Rodger B. Baird, Andrew D.Eaton, L. S. C., Ed.; washington, DC,USA 20001-3710, **2012**. doi:ISBN 9780875532356.

[13] Hiligsmann, S.; Masset, J.; Hamilton, C.; Beckers, L.; Thonart, P. Comparative study of biological hydrogen production by pure strains and consortia of facultative and strict anaerobic bacteria. *Bioresource Technology* **2011**, *102*(4), 3810–3818. doi:10.1016/j.biortech.2010.11.094.

[14] O-Thong, S.; Prasertsan, P.; Birkeland, N. K. Evaluation of methods for preparing hydrogen-producing seed inocula under thermophilic condition by process performance and microbial community analysis. *Bioresource Technology* **2009**, *100*(2), 909–918. doi:10.1016/j.biortech.2008.07.036.

[15] Angelidaki, I.; Alves, M.; Bolzonella, D.; Borzacconi, L.; Campos, J. L.; Guwy, A. J.; et al. Defining the biomethane potential (BMP) of solid organic wastes and energy crops: A proposed protocol for batch assays. *Water Science and Technology* **2009**, *59*(5), 927–934. doi:10.2166/wst.2009.040.

[16] Trzcinski, A. P.; Stuckey, D. C. Determination of the Hydrolysis Constant in the Biochemical Methane Potential Test of Municipal Solid Waste. *Environmental Engineering Science* **2012**, *29*(9), 848–854. doi:10.1089/ees.2011.0105.

[17] Morris, D. L. Quantitative Determination of Carbohydrates with Dreywood’s Anthrone Reagen; **1948**. doi:10.1007/978-94-007-0753-5_100521.

[18] Sitorus, B.; Sukandar; Panjaitan, S. D. Biogas recovery from anaerobic digestion process of mixed fruit -vegetable wastes. *Energy Procedia* **2013**, *32*, 176–182. doi:10.1016/j.egypro.2013.05.023.

[19] Merklein, K.; Fong, S. S.; Deng, Y. Production of butyric acid by a cellulolytic actinobacterium Thermobifida fusca on cellulose. *Biochemical Engineering Journal* **2014**, *90*, 239–244. doi:10.1016/j.bej.2014.06.012.

[20] Lü, F.; Bize, A.; Guillot, A.; Monnet, V.; Madigou, C.; Chapleur, O.; et al. Metaproteomics of cellulose methanisation under thermophilic conditions reveals a surprisingly high proteolytic activity. *ISME Journal* **2014**, *8*(1), 88–102. doi:10.1038/ismej.2013.120.

[21] Wang, S.; Ma, Z.; Zhang, T.; Bao, M.; Su, H. Optimization and modeling of biohydrogen production by mixed bacterial cultures from raw cassava starch. *Frontiers of Chemical Science and Engineering* **2017**, *11*(1), 100–106. doi:10.1007/s11705-017-1617-3.

[22] Holliger, C.; Alves, M.; Andrade, D.; Angelidaki, I.; Astals, S.; Baier, U.; et al. Towards a standardization of biomethane potential tests. *Water Science and Technology* **2016**, *74*(11), 2515–2522. doi:10.2166/wst.2016.336.

[23] Shi, X.; Lin, J.; Zuo, J.; Li, P.; Li, X.; Guo, X. Effects of free ammonia on volatile fatty acid accumulation and process performance in the anaerobic digestion of two typical bio-wastes. *Journal of Environmental Sciences (China)* **2017**, *55*, 49–57. doi:10.1016/j.jes.2016.07.006.

[24] Suksong, W.; Kongjan, P.; Prasertsan, P.; O-Thong, S. Thermotolerant cellulolytic Clostridiaceae and Lachnospiraceae rich consortium enhanced biogas production from oil palm empty fruit bunches by solid-state anaerobic digestion. *Bioresource Technology* **2019**, *291*(July), 121851. doi:10.1016/j.biortech.2019.121851.

[25] Prapinagsorn, W.; Sittijunda, S.; Reungsang, A. Co-digestion of napier grass and its silage with cow dung for methane production. *Energies* **2017**, *10*(10), 1–20. doi:10.3390/en10101654.

[26] Muñoz, C.; Hidalgo, C.; Zapata, M.; Jeison, D.; Riquelme, C.; Rivas, M. Use of cellulolytic marine bacteria for enzymatic pretreatment in microalgal biogas production. *Applied and Environmental Microbiology* **2014**, *80*(14), 4199–4206. doi:10.1128/AEM.00827-14.

[27] Mustafa, A. M.; Poulsen, T. G.; Sheng, K. Fungal pretreatment of rice straw with Pleurotus ostreatus and Trichoderma reesei to enhance methane production under solid-state anaerobic digestion. *Applied Energy* **2016**, *180*, 661–671. doi:10.1016/j.apenergy.2016.07.135.

[28] Saelor, S.; Kongjan, P.; O-Thong, S. Biogas Production from Anaerobic Co-digestion of Palm Oil Mill Effluent and Empty Fruit Bunches. *Energy Procedia* **2017**, *138*, 717–722. doi:10.1016/j.egypro.2017.10.206.

[29] Chaikitkaew, S.; Kongjan, P.; O-Thong, S. Biogas Production from Biomass Residues of Palm Oil Mill by Solid State Anaerobic Digestion, *Elsevier B.V.*, **2015**, *79*. doi:10.1016/j.egypro.2015.11.575.

[30] Krishnan, Y.; Bong, C. P. C.; Azman, N. F.; Zakaria, Z.; Othman, N.; Abdullah, N.; et al. Co-composting of palm empty fruit bunch and palm oil mill effluent: Microbial diversity and potential mitigation of greenhouse gas emission. *Journal of Cleaner Production* **2017**, *146*, 94–100. doi:10.1016/j.jclepro.2016.08.118.

[31] Li, Q.; Gao, Y.; Wang, H.; Li, B.; Liu, C.; Yu, G.; et al. Comparison of different alkali-based pretreatments of corn stover for improving enzymatic saccharification. *Bioresource Technology* **2012**, *125*, 193–199. doi:10.1016/j.biortech.2012.08.095.

[32] Tadesse, H.; Luque, R. Advances on biomass pretreatment using ionic liquids: An overview. *Energy and Environmental Science* **2011**, 4(10), 3913–3929. doi:10.1039/c0ee00667j.

[33] Brandt, A.; Gräsvik, J.; Hallett, J. P.; Welton, T. Deconstruction of lignocellulosic biomass with ionic liquids. *Green Chemistry* **2013**, *15*(3), 550–583. doi:10.1039/c2gc36364j.

[34] Costa, A. G.; Pinheiro, G. C.; Pinheiro, F. G. C.; Dos Santos, A. B.; Santaella, S. T.; Leitão, R. C. The use of thermochemical pretreatments to improve the anaerobic biodegradability and biochemical methane potential of the sugarcane bagasse. *Chemical Engineering Journal* **2014**, *248*, 363–372. doi:10.1016/j.cej.2014.03.060.

[35] Jackowiak, D.; Bassard, D.; Pauss, A.; Ribeiro, T. Optimisation of a microwave pretreatment of wheat straw for methane production. *Bioresource Technology* **2011**, *102*(12), 6750–6756. doi:10.1016/j.biortech.2011.03.107.

[36] Chandra, R.; Takeuchi, H.; Hasegawa, T. Methane production from lignocellulosic agricultural crop wastes: A review in context to second generation of biofuel production. *Renewable and Sustainable Energy Reviews* **2012**, 16(3), 1462–1476. doi:10.1016/j.rser.2011.11.035.

[37] Zhao, J.; Ge, X.; Vasco-Correa, J.; Li, Y. Fungal pretreatment of unsterilized yard trimmings for enhanced methane production by solid-state anaerobic digestion. *Bioresource Technology* **2014**, *158*, 248–252. doi:10.1016/j.biortech.2014.02.029.

[38] Sindhu, R.; Binod, P.; Pandey, A. Biological pretreatment of lignocellulosic biomass - An overview. *Bioresource Technology* **2016**, *199*, 76–82. doi:10.1016/j.biortech.2015.08.030.

[39] Lizasoain, J.; Trulea, A.; Gittinger, J.; Kral, I.; Piringer, G.; Schedl, A.; et al. Corn stover for biogas production: Effect of steam explosion pretreatment on the gas yields and on the biodegradation kinetics of the primary structural compounds. *Bioresource Technology* **2017**, *244*(June), 949–956. doi:10.1016/j.biortech.2017.08.042.

[40] Baruah, J.; Nath, B. K.; Sharma, R.; Kumar, S.; Deka, R. C.; Baruah, D. C.; et al. Recent trends in the pretreatment of lignocellulosic biomass for value-added products. *Frontiers in Energy Research* **2018**, *6*(DEC), 1–19. doi:10.3389/fenrg.2018.00141.

[41] He, Y.; Pang, Y.; Liu, Y.; Li, X.; Wang, K. Physicochemical characterization of rice straw pretreated with sodium hydroxide in the solid state for enhancing biogas production. *Energy and Fuels* **2008**, *22*(4), 2775–2781. doi:10.1021/ef8000967.

[42] Angelidaki, I.; Treu, L.; Tsapekos, P.; Luo, G.; Campanaro, S.; Wenzel, H.; et al. Biogas upgrading and utilization: Current status and perspectives. Biotechnology Advances **2018**, *36*(2), 452–466. doi:10.1016/j.biotechadv.2018.01.011.

[43] Siddique, M. N. I.; Wahid, Z. A. Achievements and perspectives of anaerobic co-digestion: A review. *Journal of Cleaner Production* **2018**, *194*, 359–371. doi:10.1016/j.jclepro.2018.05.155.

[44] Ullah Khan, I.; Hafiz Dzarfan Othman, M.; Hashim, H.; Matsuura, T.; Ismail, A. F.; Rezaei-DashtArzhandi, M.; et al. Biogas as a renewable energy fuel – A review of biogas upgrading, utilisation and storage. *Energy Conversion and Management* **2017**, *150*(May), 277–294. doi:10.1016/j.enconman.2017.08.035.

[45] Li, W.; Khalid, H.; Zhu, Z.; Zhang, R.; Liu, G.; Chen, C.; et al. Methane production through anaerobic digestion: Participation and digestion characteristics of cellulose, hemicellulose and lignin. *Applied Energy* **2018**, *226*(May), 1219–1228. doi:10.1016/j.apenergy.2018.05.055.

ASEAN
Journal of Scientific and Technological Reports
Online ISSN:2773-8752

Research article

Effects of Rearing Black Soldier Fly Larvae *(Hermetia Illucens)* from Organic Wastes

Piyaruk Pradabphetrat[1*], Sidthipong Sathawong[2] and Montakarn Pimsen[3]

[1] Program in Public Health, Faculty of Science Technology and Agriculture, Yala Rajabhat University, Yala, 95000, Thailand
[2] Program in Food Science and Technology, Faculty of Science Technology and Agriculture, Yala Rajabhat University, Yala, 95000, Thailand
[3] Program in Applied Biology, Faculty of Science and Technology, Princess of Naradhiwas University, Narathiwat, 96000, Thailand
[*] Correspondence: piyaruk.p@yru.ac.th

Citation:
Pradabphatrat, P.; Sathawong, S.; Pimsen, M. Effects of rearing black soldier fly larvae (*Hermetia illucens*) from organic wastes. *ASEAN J. Sci. Tech. Report.* **2024**, *27*(4), e252644. https://doi.org/10.55164/ajstr.v27i4.252644

Article history:
Received: February 1, 2024
Revised: May 3, 2024
Accepted: May 16, 2024
Available online: June 30, 2024

Abstract: Organic waste is one of the major environmental problems, and the black soldier fly (*Hermetia illucens*) larvae can help decompose organic waste. Therefore, this research is interested in studying organic fertilizers' growth, nutritional value, and nutrient contents from the residue of black soldier fly larvae. Four experimental sets of plastic buckets containing organic wastes, i.e., pineapple peels, banana peels, durian peels, and vegetable scraps, were used to trap the black soldier flies and observe the spawning and the number of egg clusters. After that, the 4-day-old black soldier fly larvae were incubated in plastic boxes using different foods for the same duration. Three replicates of the experiment were performed, recording the growth period and size of the soldier fly larvae. The study found that the life cycle of the black soldier fly was divided into 5 stages: egg, larval, prepupal, pupal, and adult stages, in 47–67 days. The black soldier fly larvae fed pineapple peels both in the larval and prepupal stages were the largest, while the larvae fed with durian peels entered the larval stage the fastest. Subsequently, 100 g of fresh black soldier fly larvae samples from four experimental sets were analyzed for nutritional value. It was found that fresh black soldier fly larvae had protein contents of 9.25–10.69 g/100 g and a fat content of 3.29–15.90 g/100 g, which were suitable for use as an ingredient in animal feed to reduce production costs. Then, 100 g of the frass of the black soldier fly larvae fed with durian peels was collected for analysis of the essential nutrients for plants, i.e., nitrogen, phosphorus, and potassium, at about 2.46%, 2.77%, and 3.14%, respectively, which are suitable for use as organic fertilizers for soil amendments.

Keywords: Black soldier fly larvae; Organic waste; Alternative protein source

1. Introduction

Solid waste, especially organic waste, is an important problem that is increasing in volume yearly due to the increasing population, economic expansion, and changes in people's consumption behavior. However, proper waste management by local administrative organizations is still insufficient to cope with the amount of waste that tends to increase yearly [1]. Moreover, unclean waste management results in various problems, such as being a source of germs, disturbing odors, leachate contaminating surfaces and groundwater, and environmental impacts [2]. If people separate and reuse solid waste, especially organic waste such as vegetable scraps and various types of fruit peels, such as banana peels, pineapple peels, and durian peels, etc., which are agricultural waste from consumption and processing industries that are in large quantities in the three southern border provinces. This will reduce the amount of solid waste and pollution in various areas and promote and support the use of natural resources as new raw materials [3].

The black soldier fly has the scientific name of *Hermetia illucens*. It can decompose animal manure, food scraps, and leftover parts from various processing operations with a low risk of causing harm to animals and humans. Additionally, the larvae have high protein and fat benefits compared to current animal feed raw materials [4, 5]. Currently, small animal farmers often face problems with the expensive cost of ready-made feed, which affects their livelihood. Therefore, farmers must find alternative protein sources for animal feed, such as soybean meal, fish meal, etc. [5, 6]. Hence, the black soldier fly larvae can be used as a high-quality protein source for animals, especially economic animals such as carp fish, ornamental fish, grouper fish, giant freshwater prawns, lobsters, organic chickens, fighting cocks, etc. In the United States, black soldier fly larvae are also used to raise trout, salmon, Nile Tilapia fish, and shrimp [7]. Furthermore, the black soldier fly larvae frass can make compost or organic fertilizer [2].

Organic waste management at the source with the black soldier flies larvae is a biotechnological method that is simple, safe, environmentally friendly and doesn't take long. The black soldier fly larvae can digest food scraps faster than composting them. It can also reduce contamination by pathogenic microorganisms from the decay of organic waste, help prevent being a source of breeding vectors for bluebottle flies, house flies, and fruit flies, as well as reduce the transmission of disturbing odors in the area [8]. This has led to using organic wastes to create various benefits, such as organic fertilizer and a source of high-protein raw materials. The black soldier fly larvae can digest food scraps up to 20 times their body weight, or 40 kilograms per square meter, within 24 hours, they can digest organic waste 5 times faster than earthworms, which reduces greenhouse gas emissions and low levels of ammonia. This may be because microorganisms within the intestinal tract of the black soldier fly larvae decompose quickly. In addition, it can add value to animal manure, reduce animal manure pollution by more than 60%, be used to produce compost for growing plants and nourishing the soil, reduce bad odors, and the movement of larvae helps inhibit the growth of bacteria that produce bad smell gas [9, 10].

However, the cultivation of black soldier fly larvae in households has not been widely studied. The foods used for growing the black soldier fly larvae are household leftovers, organic waste, and animal manure. The nutritional value and quality of the black soldier fly larvae depends on the nature and quality of the food used for raising them, which is a restriction on its use as a raw material in animal feed. Thus, if you choose to use food or formula suitable for the black soldier fly larvae, you will be able to control the quality of the larvae to a constant level. This includes expanding the results of raising black soldier fly larvae to be used as raw material to replace protein sources in the animal feed industry more efficiently [11]. This research is therefore interested in studying the management of organic waste using black soldier fly larvae. The objectives are (1) to study the life cycle and growth of black soldier fly larvae fed on different types of organic waste, including pineapple peels, banana peels, durian peels, and vegetable scraps; (2) to compare the nutritional value of the black soldier fly larvae; and (3) to analyze the amount of macronutrients in organic fertilizer from the frass of the black soldier fly larvae.

2. Materials and Methods

2.1 Trapping black soldiers fly to lay eggs

A completely randomized design (CRD) was applied to 4 experimental sets (4 types of organic waste), each consisting of fruit peels and vegetable scraps from fruit and vegetable shops. Then place 2 kilograms each of pineapple peels, banana peels, durian peels, and vegetable scraps into a 10-liter plastic bucket with a diameter of 25 centimeters and a height of 30 centimeters, with a tight lid and a triangular slit at the top edge and 10 centimeters on each side, so that the soldier fly can easily lay their eggs. The plastic buckets were placed 30 centimeters below the eaves in soft sunlight for 7 days. The egglaying and number of ovaries were observed and surveyed every day. The black soldier flies were found laying eggs around the edge of the inner tank. When the food ran out, 500 grams were added as new food at a time for every experimental set. Record the number of egg groups by counting the number of eggs per group and averaging the number of eggs in each group of each experimental set. Finally, collect the egg groups that have been raised for further cultivation.

2.2 Cultivation of black soldier fly larvae

Conducting research by adapting the process of breeding the black soldier fly larvae of the Department of Environmental Quality Promotion [8] by preparing a container for the nursery of the black soldier fly larvae, width 45 centimeters and height 16 centimeters, adding 500 grams of chicken feed, and laying eggs 10 grams of the black soldier fly larvae on the cardboard, 1 centimeter wide and 1 centimeter long, were placed above chicken feed. Then, observe the changes and hatching rate. After the black soldier fly larvae hatch from the eggs, 500 grams of food are added to the larvae until they have grown for 16 days, which is the stage when the larvae can be separated for use in test rearing. The experiment was planned to be completely randomized, with 4 experiment sets (4 organic waste types) and 3 replicates. In each experimental set, 100 grams of the black soldier fly larvae were placed in a rectangular box measuring 21.5 centimeters in width, 21.5 centimeters in length, and 18 centimeters in height. Afterward, the larvae are fed by adding fruit peels and vegetable scraps obtained from fruit and vegetable shops by chopping them into small pieces, including 100 grams of pineapple peel, banana peel, durian peel, and vegetable scraps. Each rectangular box was covered with a thin white cloth. Make observations every day, and food was added to all sets of black soldier fly larvae equally every 2 days or until food was gone. The new food was added 50 grams at a time to every experimental set. Record the growth period of the black soldier fly larvae from the egg stage to the adult stage, and the survival rate of the black soldier fly larvae in each experimental set.

2.3 Nutritional analysis

The samples of the prepupal stage of black soldier fly larvae were taken from 4 types of organic waste, including pineapple peels, banana peels, durian peels, and vegetable scraps, 100 grams per experimental set, placed in ziplock bags and refrigerated at a temperature of approximately 10°Celsius to prepare for nutritional analysis in the laboratory by proximate analysis according to the method of AOAC (2019) to analyze the values of moisture, ash, protein, fat, fiber, carbohydrates, and total energy. All data were analyzed for variance (Analysis of Variance: ANOVA), and the differences between the means were compared using Duncan's New Multiple Range Test (DMRT) at a confidence level of 95% ($P < 0.05$).

2.4 Analysis of macronutrient contents from black soldier fly larvae

At the end of the organic fertilizer process, the frass of the black soldier fly larvae obtained from the decomposition of organic waste in all four experimental sets observed that the fertilizer had the appearance of fine, crumbly pellets, was blackish-brown, and was lightweight. Therefore, samples of the black soldier fly larvae frass were collected in each experimental set. The fertilizer from the black soldier fly larvae frass was mixed evenly throughout the pile and spread out. Then, 100 grams of fertilizer samples were collected from each experimental set, and the samples were stored in separate plastic bags for each experimental set to analyze the amount of essential nutrients for plants, including nitrogen, phosphorus, and potassium.

3. Results and Discussion

3.1 Study of the life cycle and growth period of black soldier fly fed with different types of organic waste

From the study of the egg-laying behavior of the black soldier flies, it was found that the black soldier fly hovers around 30 centimeters above the food source and then approaches the food source. It takes approximately 5-10 minutes to lay eggs. The newly laid egg clusters are soft white and have a sticky consistency that makes the eggs stick together in groups and stick well to the material. The groups of eggs will be found under the surface of the food, which is dry, and on the inside edges of food containers. The counting the number of eggs study laid by five adult black soldier flies found that each one laid only one group of eggs, which had an average number of eggs of 483.00 ± 134.30 eggs per group. The experiment set fed with pineapple peels had the highest mean number of eggs, which was 517 ± 110.15 eggs per group, and the experiment set fed with banana peels had the lowest, 383 ± 175.13 eggs per group. This is consistent with a previous study [12], which documented that female black soldier flies prefer to lay their eggs over organic waste in dry areas, small openings, and sheltered areas. There are 400 to 800 eggs per egg group. The male and female breeders will die after mating and laying eggs. Furthermore, a study of the culture of the black soldier fly by using organic wastes as food found that the life cycle of the black soldier fly can be divided into 5 stages (Figure 1), including the egg stage, in which the eggs are oval-shaped, approximately 0.5-1 millimeters in length, and challenging to observe with the naked eye. During the first 1-2 days, they will be so cloudy white that the eggs will hatch into larvae and crawl into the culture medium for approximately 3-4 days. The average hatching rate from 4 experimental sets is 98.5 ± 0.58%. In addition, the study results found that the larval stage is where they eat a lot of organic waste as food. Therefore, it is an appropriate time to dispose of organic waste.

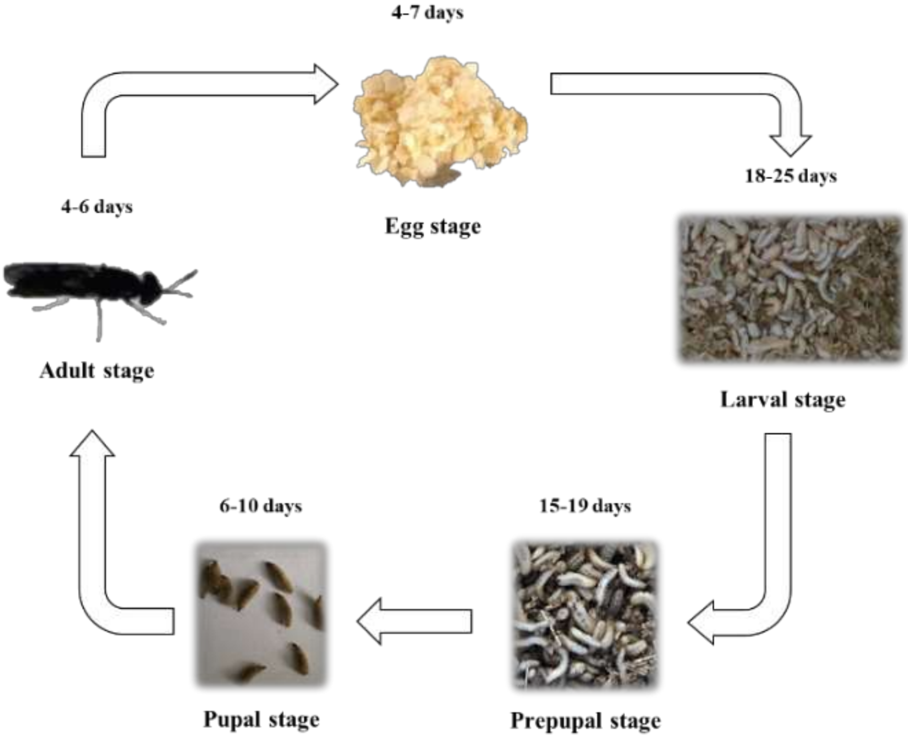

Figure 1. The life cycle of the black soldier flies.

This study also found that black soldier fly larvae are plump, flat, and creamy white (Figure 2). Nevertheless, if the larvae have a brown body, they will eat less food to prepare before entering the pupal stage. Food should not be added at this stage because the larvae will molt for the last time to pupate [8].

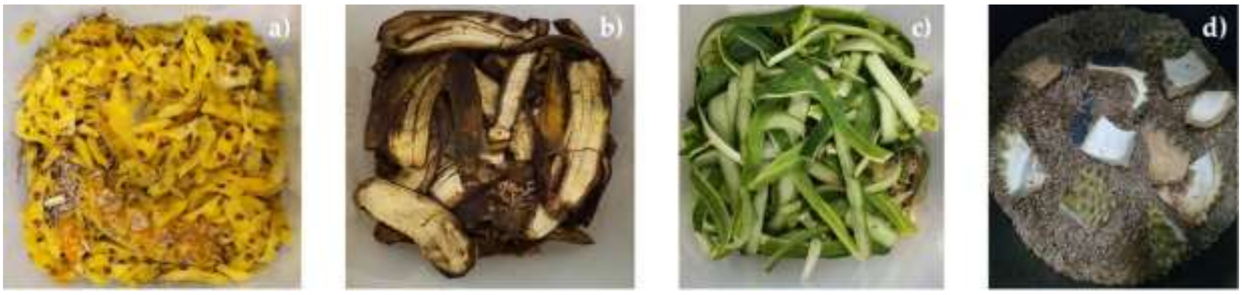

Figure 2. The black soldier flies larvae fed on different types of organic waste: a) pineapple peels, b) banana peels, c) vegetable scraps, and d) durian peels.

It was found that the type of food used to feed the black soldier fly larvae affects their growth and survival rate [10, 13]. The black soldier fly larvae fed with pineapple peels were the largest, with an average size of approximately 10.6 ± 0.2 millimeters. In contrast, the black soldier fly larvae fed with durian peels were the smallest, with an average size of roughly 7.3 ± 0.3 millimeters (Table 1). The moisture content and type of food waste that is the medium of larval growth significantly affect larval development [14]. The study by Muenmee and Prasertboonyai [15] found that durian peel has a moisture content of 78.64 ± 0.38%, while pineapple peel has a moisture content of 85.09 ± 0.07%. This could also explain why the larvae that consumed durian peels had the lowest size. In the prepupal stage, the larvae were light brown to dark brown, and their body size ranged from 13 to 20 millimeters in length. The prepupal larvae can climb up from the rearing area at an angle of 40-65°Celsius and move as far as 100 meters. The black soldier fly larvae fed with pineapple peels were the largest, with an average size of approximately 15.2 ± 0.4 millimeters. In contrast, the black soldier fly larvae fed with durian peels were the smallest, with an average size of approximately 11.4 ± 0.1 millimeters (Table 1). Moreover, it was found that the black soldier fly larvae fed with durian peels could enter the pupal stage the fastest, at 15 days, followed by the larvae fed with pineapple peels and banana peels. As for the larvae fed with vegetable scraps were able to enter the pupal stage the slowest, at 19 days, with an average survival rate of 85.5 ± 1.15%. For the pupal stage, when the larvae have a dark black body and dry, hard skin. It is about 7 days old and has a complete pupation rate of 30.5 ± 0.18% because most of the pupae atrophy, but the rate of hatching into adults is 90.04 ± 0.29%. In the adult stage, the survival rate from egg to adult was 25.25 ± 0.11%. The black soldier fly larvae fed with pineapple peel had a higher rate of hatching eggs, the prepupal stage, and hatching into adults, but the pupation rate was low.

Table 1. The size of the black soldier fly larvae fed on different types of organic waste.

Types of organic waste	The average size of the larval stage of the black soldier fly larvae (mm.)	The average size of the prepupal stage of the black soldier fly larvae (mm.)
Pineapple peels	10.6 ± 0.2	15.2 ± 0.4
Durian peels	7.3 ± 0.3	11.4 ± 0.1
Banana peels	9.4 ± 0.3	13.3 ± 0.2
Vegetable scraps	9.1 ± 0.1	12.1 ± 0.2

3.2 Study of the nutritional value of black soldier fly larvae fed with different types of organic waste

The prepupal stage black soldier fly larvae samples were taken from 4 different types of organic waste, i.e., pineapple peels, banana peels, durian peels, and vegetable scraps, to be analyzed for chemical composition by estimation methods in the laboratory. It was found that the total protein, carbohydrate, and total energy contents in every experimental set were not statistically different. The black soldier fly larvae fed with durian peels had the highest amount of fiber, ash, and moisture, which were 10.69%, 0.32%, 2.54%, and 82.21%, respectively. In contrast, the black soldier flies larvae fed banana peels had the highest amount of fat, which was 15.90%, as in Table 2, because banana peels are high in fat [16]. It could be stated that the type of food affects the nutritional value of the black soldier fly larvae, especially their protein and fat content [17].

Table 2. The nutritional value of fresh black soldier fly larvae.

Types of organic waste	nutritional value (%)						
	Protein	Fat	Fiber	Ash	Moisture	Carbohydrate	Total energy
Pineapple peels	9.25	7.20a	0.08a	2.18a	79.65a	1.72	108.63
Durian peels	10.69	3.29b	0.32ab	2.54b	82.21b	1.28	77.49
Banana peels	10.10	15.90c	0.10b	1.83a	71.92a	0.25	184.54
Vegetable scraps	10.50	8.02d	0.12c	2.24c	79.11c	0.13	114.71
F-test	ns	*	*	*	*	ns	ns

Calculate the protein value by using a protein conversion factor of 6.25 for the black soldier fly larvae.
Means with the same letters in the same column are not statistically different at the 95% confidence level, compared using Duncan's multiple range test (DMRT).
* = There was a statistically significant difference ($P < 0.05$)
ns = There was no statistical difference ($P > 0.05$)

In a previous study [18], pineapple peels contained soluble carbohydrates in the form of reducing sugars, including sucrose (70%), glucose (20%), and fructose (10%), which microorganisms living in animal stomachs can use for fermentation as an important source of energy, and this energy is transferred to herbivorous animals. The black soldier fly larvae are highly nutritious, and the nutrients that accumulate in the bodies of adults and pupal stages contain 44.96-50.56% protein, 16.84-28.89% fat, and 5,520-6,480 kilocalories of energy per kilogram [19]. In the larval and pupal stages of the black soldier fly, protein and fat accumulate within the body when eating food. This is beneficial to adults when mating and laying eggs [20]. A previous study of the use of black soldier fly larvae fed with soy waste powder in a broiler diet [21] showed that the black soldier fly larvae powder had 94.28% dry matter, 45.68% protein, 34.53% fat, 1.22% calcium, 0.8% phosphorus, and a total energy of 6,235 kilocalories per kilogram. Furthermore, testing of the nutritional value of black soldier fly larvae fed on general food scraps and vegetable wastes from the market found that fresh black soldier fly larvae, dried black soldier fly larvae, pupa casings, and black soldier fly carcasses had protein values of 15.23, 33.38, 45.04, and 59.07 grams per 100 grams, respectively, as well as lipid values of 17.64, 39.08, 19.32, and 4.75 grams per 100 grams, respectively [10]. Thus, the black soldier fly larvae can be an alternative source of protein that can be used as a dietary supplement to feed local chickens, organic chickens, fighting cocks, carp fish, ornamental fish, grouper fish, trout, salmon, Nile Tilapia fish, giant freshwater prawns, lobster, pigs, and frogs [7, 19, 22]. Subsequently, it is suggested that agricultural waste has the potential to be used as an ingredient in food for growing black soldier fly larvae.

3.3 Analysis of macronutrient contents of organic fertilizer from the frass of black soldier fly larvae fed with different types of organic waste

At the end of the organic fertilizer process, the black soldier flies larvae frass was obtained from the decomposed organic waste in 4 experimental sets: pineapple peels, banana peels, durian peels, and vegetable scraps. The result of the study revealed that the black soldier fly larvae were always eating food. When organic waste or food scraps are decomposed, they can be turned into organic fertilizer. So, the black soldier fly larvae frass was analyzed for physical and chemical properties to compare with the standard values of organic fertilizer (Table 3). It was found that pineapple peels, banana peels, and vegetable scraps contained a lot of water because these foods have a high moisture content. As a result, the remains of the black soldier fly larvae frass dissolve in the remaining food scraps into a liquid that cannot be used to test the macronutrient contents. Nevertheless, the frass of black soldier fly larvae obtained from the decomposition of durian peels has a moisture content, total nitrogen, total phosphorus, and total potassium that meet the standards for organic fertilizers set by the Department of Agriculture [23], which can be used as a soil amendment material.

Table 3. The quality of the frass of the black soldier fly larvae obtained from the decomposition of organic wastes.

The quality of the frass of the black soldier fly larvae	Durian peels	Criteria*
Moisture content	39.41	Not more than 35%
Total nitrogen	2.46	Not less than 1%
Total phosphorus	2.77	Not less than 0.5%
Total potassium	3.14	Not less than 0.5%

*Announcement of the Department of Agriculture: Organic Fertilizer Standard B.E. 2548 [23]

In addition, it can be used in various ways, such as covering the base of durian trees or making compost, which is the proper management of agricultural residues and helps improve soil, add organic matter, and create a balance of nutrients in the soil. This may be because durian peels are high in potassium and an easily decomposed organic material. The element potassium helps promote the growth of strong roots and stems, promote flowering in plants, and increase quality production [24]. Durian peels are a material that easily decomposes and contains carbon elements. Hence, it is a source of organic matter and plant nutrients, including 1.70% nitrogen, 0.44% phosphorus, and 2.13% potassium [25]. Moreover, a study by the Department of Science Service found that durian peels contain nutrients that plants need, especially potassium and phosphorus, and when mixed with soil in vegetable plots, they can help improve and restore soil health very well, as well as store nutrients and absorb some toxins [26]. Our study is consistent with the previous study [10] that the black soldier flies larvae frass contains essential nutrients for plants, including nitrogen, phosphorus, and potassium, with values equal to 6%, 3.9%, and 5.9%, respectively. This result suggests that the frass of the black soldier fly larva is suitable for use as organic fertilizer and is a soil amendment for growing vegetables in the kitchen garden.

Based on these findings, evaluating the nutritional components of the black soldier fly fed on other types of organic waste at different life stages is necessary. This will help create a database of suitable substrates for producing black soldier fly larvae and improve the economic level of inclusion in animal feeds [27]. Additionally, the black soldier fly could also serve as a model biorefinery for valorizing various organic resources into biodiesel and other high-value products such as chitin and its derivative (chitosan), a binder (in dyes), edible films, industrial membranes, biodegradable surgical thread, a fining agent (in winemaking), protein hydrolysates, bioplastic, natural pigments (e.g., melanin and ommochromes), a potential source of industrially important enzymes (e.g., trypsin, chymotrypsin, ligninase, and cellulase), and antimicrobial peptides [28, 29].

4. Conclusions

The results of this study indicate that the life cycle of the black soldier fly can be divided into 5 stages: egg stage, larval stage, prepupal stage, pupal stage, and adult stage. When the prepupal stage of black soldier fly larvae fed with different types of organic waste was analyzed for nutritional value, it was found that fresh black soldier fly larvae had protein and fat contents in the range of 9.25-10.69 grams per 100 grams and 3.29-15.90 grams per 100 grams, respectively. This revealed that agricultural waste has the potential to be used as an ingredient in food for raising black soldier fly larvae and as an ingredient in animal feed to reduce the cost of producing animal feed. The frass of the black soldier fly larvae obtained from the decomposition of durian peels contains macronutrient contents for plants, including nitrogen, phosphorus, and potassium, with values equal to 2.46%, 2.77%, and 3.14%, respectively. The quality met the organic fertilizer standard BE 2548 of the Department of Agriculture, Thailand. Accordingly, it can be concluded that the black soldier fly larvae frass can be used as a soil improvement material and for other agricultural purposes. This will help reduce the problem of organic waste management in the community, reduce costs in purchasing fertilizer and animal feed, add value to agricultural wastes, increase income for people in the community and farmers in the area, and be a way to use natural resources with maximum sustainable efficiency.

5. Acknowledgements

The researchers would like to thank the Faculty of Science, Technology and Agriculture, Yala Rajabhat University, for the research grant for the year 2022, as well as for supporting the laboratory facilities and equipment to complete this research.

Author Contributions: Conceptualization, P.P. and S.S.; methodology, P.P. and S.S.; formal analysis, P.P. and S.S.; investigation, P.P., S.S., and M.P.; resources, P.P. and S.S.; data curation, P.P. and S.S.; writing—original draft preparation, P.P.; writing—review and editing, S.S. and M.P.; supervision, P.P; project administration, P.P. and S.S.; funding acquisition, P.P., S.S., and M.P. All authors have read and agreed to the published version of the manuscript.

Funding: This research was funded by the Faculty of Science, Technology and Agriculture, Yala Rajabhat University, grant number 003-2565.

Conflicts of Interest: The authors declare no conflict of interest.

References

[1] Silapasuwan, P. *Municipal solid waste: The significant problem of Thailand*. Bangkok: Academic Office, The Secretariat of The Senate. **2014**.

[2] Suttibak, S.; Sukthanapirat, R.; Photharin, S.; Chansakhatana, N.; Setmat, A.; Sriyoha, R.; Suttibak, P. *Community organic waste management development project by using appropriate innovations and technologies according to the sufficiency economy philosophy for sustainable community development*. **2019**. https://ppi.psu.ac.th/project/564.

[3] Nili, A.; Chearwae, H.; Tipmanae, O. Extraction of cellulose from Mon Thong durian rind and Saba banana rind by using local natural extract for cosmetic application: body scrub cream. *Proceedings of the 7th National Science and Technology Conference (NSCIC 2022),*. March 10-11, 2022 (pp. 113-122). Suratthani: Suratthani Rajabhat University. **2022**.

[4] Wang, Y.S.; Shelomi, M. Review of black soldier fly (*Hermetia illucens*) as animal feed and human food. *Foods* **2017**, *6*(91), 1-23.

[5] Jaichansukkit, T.; Sittigool, P.; Pulmar, C.; Boonpro, P.; Jaraturaitham, D. *A raise of black soldier fly (Hermetia illucens) larvae feed by animal manure for use as alternative protein source in animal feed* [Research report]. Phranakhon Si Ayutthaya: Rajamangala University of Technology Suvarnabhumi, Phranakhon Si Ayutthaya Huntra campus. **2020**.

[6] Anankware P.J., Ayizanga R.A., Opoku O., & Obeng-Ofori D. (**2018**). Potential of the black soldier fly (*Hermetia illuscens*) as a replacement for fish/soybean meal in the diet of broilers. *Global Advanced Research Journal of Agricultural Science*, *7*(8), 272-280.

[7] Munkit, J. Using black soldier fly larval meal as ingredients in common climbing perch (*Anabas testudineus* Bloch) dietary. *Journal of Vocational Institute of Agriculture* **2020**. *4*(2), 15-25.

[8] Department of Environmental Quality Promotion. *Handbook for raising black soldier fly (Hermetia illucens) larvae for the public*. Bangkok: Environmental Research and Training Center. **2022**.

[9] Tancho, A. Black soldier fly. https://www.nstda.or.th/agritec/wp-content/uploads/2020/06/20180913-leaflet-maejo-fly_compressed.pdf. **2020**.

[10] Laoleam, J.; Narongsak, S.; Yindee, R.; Wongpan, P.; Chaiyong, S.; Photharin, S. Organic waste management using the black soldier fly larvae (Hermetia illucens). *Proceedings of the 5th CRU-National Conference in Science and Technology Chandrakasem Rajabhat University*, July 16, 2022 (pp. 194-200). Bangkok: Chandrakasem Rajabhat University. **2022**.

[11] Tiabching, T. *Study the optimal of carbon-to-nitrogen ratio for black soldier fly and the nutrient utilization of black soldier fly when used as a dietary protein source for Korat chickens* [Thesis proposal]. Nakhon Ratchasima: Suranaree University of Technology. **2021**.

[12] Dortmans, B.M.A.; Diener, S.; Verstappen, B.M.; Zurbrügg, C. *Black soldier fly biowaste processing: a step-by-step guide*. Switzerland: Eawag - Swiss Federal Institute of Aquatic Science and Technology. **2017**.

[13] Jaichansukkit, T.; Sittigool, P.; Pulmar, C.; Boonpro, P.; Jaraturaitham, D. *A raise of black soldier fly (Hermetia illucens) larvae feed by animal manure for use as alternative protein source in animal feed* [Research report]. Phranakhon Si Ayutthaya: Rajamangala University of Technology Suvarnabhumi, Phranakhon Si Ayutthaya Huntra campus. **2020**.

[14] Khairuddin, D.; Ghafar, S.N.A.; Hassan, S.N.F. Food waste type and moisture content influence on the *Hermetia illucens* (L.), (Diptera: Stratiomyidae) Larval Development and Survival. *IOP Conference Series: Earth and Environmental Science* **2022**. *1022*(1), doi:10.1088/1755-1315/1022/1/012076.

[15] Muenmee, S.; Prasertboonyai, K. Potential biogas production generated by mono-and co-digestion of food waste and fruit waste (durian shell, dragon fruit and pineapple peel) in different mixture ratio under anaerobic condition. *Environmental Research, Engineering and Management* **2021**, *77*(1), 25-35.

[16] Bakri, N.F.M.; Ishak, Z.; Jusoh, A.Z.; Hadijah, H. Quantification of nutritional composition and some antinutrient factors of banana peels and pineapple skins. *Asian Food Science Journal* **2020**, *18*(4), 1-10.

[17] Nyakeri, E. M. *Optimization of production of black soldier fly larvae (Hermetia illucens, L) for fish feed formulation* [Doctoral Dissertation]. Kenya: Jaramogi Oginga Odinga University of Science and Technology. **2018**.

[18] Chaokaur, A.; Laikhonburi, Y.; Kunmee, C.; Santhong, C.; Chimthong, S. Evaluation of nutritive value and sugar soluble carbohydrate of pineapple residue. *Khon Kaen Agriculture Journal* **2014**, *42*(Supplement 1), 301-306.

[19] Photharin, S.; Lokaewmanee, K.; Ponphang-Nga, P.; Suttibak, S.; Sukthanapirat, R.; Baotong, S.; Setmat, A.; Chansakhatana, N.; Wongnarat, W.; Thaoyabut, P.; Kraisornwong, K.; Prapun, S.; Panphojan, T. *Promoting and potential development of farmer by management environmental innovation* [Research report]. Sakon Nakhon: Kasetsart University Chalermphrakiat Sakon Nakhon Province campus. **2020**.

[20] Timcharoensombut, P.; Boonsri, C.; Sripontan, Y. Effects of fruit type on larval growth and egg-laying of black soldier fly, *Hermetia illucens* (L.). *Khon Kaen Agriculture Journal* **2018**, *46*(5), 1001-1008.

[21] Malamaneerat, J.; Maneewan, B.; Chukiatsiri, K.; Panatuk, J. (Use of black soldier fly larvae (BSFL) fed with soy waste powder in broiler diet on growth performance, carcass composition and meat quality. *Khon Kaen Agriculture Journal* **2020**, *48*(5), 942-953.

[22] Barragán-Fonseca, K.B.; Dicke, M.; van Loon, J.J. Nutritional value of the black soldier fly (*Hermetia illucens* L.) and its suitability as animal feed–a review. *Journal of Insects as Food and Feed* **2017**, *3*(2), 105-120.

[23] Department of Agriculture. *Announcement of the Department of Agriculture on organic fertilizer standards B.E. 2548*. http://www.ratchakitcha.soc.go.th/ DATA/PDF/2548/00172707.PDF. **2005**.

[24] Siritrakulsak, T.; Tikheaw, K. Influence of durian peel compost application on growth and flowering of marigold var. Sara Orange. *Proceedings of the 4th Rajamangala University of Technology Suvarnabhumi Conference (RUSCON 4)*, July 15-16, 2020 (pp. 640-647). Phranakhon Si Ayutthaya: Rajamangala University of Technology Suvarnabhumi, Phranakhon Si Ayutthaya Huntra campus. **2020**.

[25] Land Develop Department. *Quality compost from durian husks formulated by the Land Develop Department*. https://www.ldd.go.th/WEB_Download/Data/E-Leaflets/L03.pdf. **n.d**.

[26] Thai PBS. *Environmentalist recommended to process durian peels into charcoal briquettes-fertilizers*. https://news.thaipbs.or.th/content/263572. **2017**.

[27] Adebayo, H.A.; Kemabonta, K.A.; Ogbogu, S.S.; Elechi, M.C.; Obe, M.T. Comparative assessment of developmental parameters, proximate analysis and mineral compositions of black soldier fly (*Hermetia illucens*) prepupae reared on organic waste substrates. *International Journal of Tropical Insect Science* **2021** *41*, 1953-1959.

[28] Surendra, K.C.; Tomberlin, J.K.; van Huis, A.; Cammack, J.A.; Heckmann, L.H.L.; Khanal, S.K. Rethinking organic wastes bioconversion: Evaluating the potential of the black soldier fly (*Hermetia illucens* (L.))(Diptera: Stratiomyidae)(BSF). *Waste Management* **2020**, *117*, 58-80.

[29] Amrul, N.F.; Kabir Ahmad, I.; Ahmad Basri, N.E.; Suja, F.; Abdul Jalil, N.A.; Azman, N.A. A review of organic waste treatment using black soldier fly (*Hermetia illucens*). *Sustainability* **2022**, *14*(8), 4565.

ASEAN
Journal of Scientific and Technological Reports
Online ISSN:2773-8752

Research article

Thailand's Maize Prices Forecasting Using Ensemble Technique

Sararith Mao[1] and Nuanwan Soonthornphisaj[2*]

[1] Department of Computer Science, Faculty of Science, Kasetsart University, Bangkok, 10900, Thailand
[2] Department of Computer Science, Faculty of Science, Kasetsart University, Bangkok, 10900, Thailand
* Correspondence: nuanwan.s@ku.th

Citation:
Mao, S.; Sooonthornphisaj, N. Thailand's Maize prices forecasting using ensemble technique. *ASEAN J. Sci. Tech. Report.* **2024**, *27*(4), e252279. https://doi.org/10.55164/ajstr.v27i4.252279

Article history:
Received: January 4, 2024
Revised: May 16, 2024
Accepted: June 18, 2024
Available online: June 30, 2024

Abstract: Crop price forecasting is crucial for farmers, policymakers, and investors. This paper aims to propose suitable machine learning models for forecasting Thailand's maize prices by implementing and comparing various machine learning algorithms, including regression trees (RT), support vector regression (SVR), ensemble bagging with RT and SVR as the base learner (Bag-RT and Bag-SVR), and random forest (RF). The dataset used in this study is collected from two main sources: the Office of Agricultural Economics in Thailand (OAE) and the investing.com website from January 2002 to August 2023, consisting of 260 records and 53 features. Given the dataset's numerous independent variables, we applied the recursive feature elimination combined with the Pearson correlation feature selection method to reduce feature dimensions by focusing on the most relevant features. The prediction models were trained using 10-fold cross-validation and evaluated using three metrics: R-squared (R^2), mean absolute error (MAE), and root mean square error (RMSE). The top-performing model, Bag-SVR, achieved the best R^2 value of 0.961, MAE of 0.234, and RMSE of 0.315, followed by the SVR model with R^2 value of 0.959, MAE of 0.251, and RMSE of 0.333. In contrast, the RT model demonstrated the lowest performance scores with an R^2 value of 0.846, MAE of 0.44, and RMSE of 0.617. In conclusion, our study emphasizes the influence of feature selection on model performance and showcases the potential of machine learning models for accurate maize price forecasting in Thailand.

Keywords: Price Prediction; Feature Selection; Regression Problem; Ensemble Technique

1. Introduction

The agricultural sector is important for global economic stability and food security. The cultivation and trade of agricultural crops are particularly crucial, as they substantially impact international markets and complex food supply networks [1]. Thailand is among the Southeast Asian nations whose economies are still heavily dependent on agriculture. In 2020, it significantly contributed THB 1.36 trillion to the country's gross domestic product (GDP), representing 8.65% of the overall GDP [2]. Additionally, around 30% of the total labor force, which includes 6.4 million households, is involved in agricultural activities, emphasizing its role in providing rural employment and generating income [3]. Thailand is known for its diverse agricultural landscape and substantial maize production. Maize is one of the most widely cultivated crops in Thailand. It serves two important roles as feed livestock and as a resource for food and industrial applications. Forecasting maize prices is a complex and challenging task due to the volatile nature of agricultural markets and the influence of various factors such as weather patterns, supply and demand, import and export, and other economic conditions. Therefore, accurate maize prices forecasting is not just an economic concern but also an urgent task.

Traditionally, forecasting maize prices in Thailand relies on farmers' experience, historical data, and expert opinion, which often fail to capture the complex patterns and non-linear relationships that define the country's current agricultural markets. But with the advance of modern technology like artificial intelligence and machine learning, along with the power to analyze vast datasets using high-performance computing, this limitation has led to a growing interest in utilizing machine learning algorithms to enhance the accuracy and timely agricultural price predictions [4, 5].

This research paper aims to tackle this issue by investigating the utilization of machine learning algorithms to construct predictive models that can improve the accuracy of maize price forecasts in Thailand. These models could benefit more than farmers and agribusinesses but also make food more secure, assist the government in creating better policies, and maintain market stability. The following two main objectives drive this paper:

1) Utilize the feature selection method to identify the most relevant features. This process helps to reduce the dataset's dimensionality, leading to improved computational efficiency and enhancing the effectiveness of the prediction models.
2) Employ various regression machine learning models to determine the one that demonstrates the most robust and effective performance in predicting maize prices in Thailand.

This section reviews the literature relevant to our machine learning-based maize price forecasting research. We aim to situate our work within the broader context of previous studies while highlighting the gaps and opportunities that motivate our research.

In the study related to the agricultural landscape, understanding factors influencing maize prices is really important. Exploring different studies helps us see how weather patterns, trade dynamics, and other factors contribute to the prediction and comprehension of maize pricing. Climate variables like temperature and rainfall were used to forecast the yield and price of corn and soybeans for Hancock County in Illinois, United States [6]. Significant information concerning how fluctuations in the prices of rice and wheat can influence corn prices, even though these crops can be used interchangeably as essential food sources for various needs [7]. The correlations between production and consumption, import and export volume, and supply and demand were examined to identify the main factors influencing maize prices in Chinese markets [8]. In addition to economic and environmental factors, currency rate fluctuations were used to impact agricultural goods trade between China and Africa [9]. These collective studies highlight the necessity of economic and environmental data to provide a complete understanding of the factors influencing maize prices.

The process of selecting key factors holds significant importance, directly impacting the precision of crop price prediction. Several studies have explored different feature selection methods, showcasing their effectiveness in finding the most important features from large datasets to enhance the accuracy of predicting crop prices and market trends. The variables that affect agricultural prices in India, including total area for planting, supply forecasts, government regulations, consumer needs, and producer supply for products derived from agriculture, were investigated. With many features in the dataset, the author employed the feature concatenation approach to select only the feature representative from weather data, data quality, and Agmarknet data [10]. A modified recursive feature elimination (MRFE) technique was introduced, proving highly effective in selecting relevant features. Combined with the bagging ensemble technique, this approach achieved an impressive 95% accuracy rate in predicting land suitability for crop cultivation [11]. The effectiveness of combining the recursive feature elimination (RFE) technique with the adaptive bagging classifier for precise crop suitability prediction was emphasized in the study by [12]. Various factors, including plant population, planting dates, environmental elements, and partial in-season weather knowledge, were analyzed to forecast corn yield in three US Corn Belt states: Illinois, Indiana, and Iowa. The study employed a three-stage feature selection process involving consultation with domain experts, utilization of random forest feature importance, and Pearson correlation analysis, effectively reducing the initial set of 597 features to 72. An optimized weighted ensemble technique was also applied to those selected features, achieving the best performance with a relative root mean square error (RRMSE) of 9.5% [13]. Leave One Out Cross-Validation (LOOCV) was employed on a relatively small dataset consisting of 168 samples and 10 variables, utilizing principal component analysis (PCA) to reduce the feature set from 10 to 7. This study found that the ensemble models with two, three, or four base learners outperformed individual models for predicting future corn prices [14]. These approaches highlight feature selection's crucial role in improving crop price-prediction models.

Agricultural price forecasting is a vibrant field of research that encompasses diverse scenarios, including stock price prediction [15], energy load forecasting [16], traffic forecasting [17], and crop yield prediction [18]. Within the scope of time series prediction, numerous traditional machine learning models have been introduced, such as Ridge and LASSO regression [19, 20], Gaussian processes [21], support vector regression [22], as well as modern deep learning techniques like LSTMs [23]. Beyond these single models, various ensemble models were proposed to improve prediction accuracy by combining the strengths of multiple base learners [24, 25]. Recent studies have explored traditional and ensemble machine learning models to predict commodity prices. These investigations highlight the effectiveness of diverse techniques in accurately forecasting prices within different agricultural markets. A combination of econometrics and ensemble machine learning models was employed to predict corn and sugar price in Brazil. Their findings revealed that the SVR model outperformed other models because of the small dataset with a remarkable R2 of 0.99 and 0.979 and a low MAE of 0.287 and 0.430 for corn and sugar, respectively [26]. Multiple linear, Ridge, and Lasso regression models were implemented to predict maize prices in Thailand. The authors introduced Pearson correlation analysis and stepAIC function, reducing the initial feature set from 47 to 27. Utilizing the selected features, the multiple linear regression model outperformed other models, achieving an R^2 value of 0.94, MAE of 0.31, and RMSE of 0.50 [20].

From a literature review, our study explores the complex landscape of maize prices forecasting in Thailand, considering multiple factors. We aim to fill these research gaps by underscoring the significance of feature selection, emphasizing its capacity to improve accuracy while reducing the number of features. Furthermore, we explore various machine learning algorithms, including individual models and ensemble bagging techniques, to effectively address the challenges of constructing maize price-prediction models. The structure of this paper is as follows: In Section 2, we provide detailed data used in this study and explain the key theories supporting our research. The results and discussion are presented in Section 3. Finally, in Section 4, we conclude.

2. Materials and Methods

2.1 Dataset

The dataset is essential to our study since it provides insightful information and ensures our research findings' robustness. We present an overview of the dataset used in our study, which was collected from two primary sources.

2.1.1 Office of Agricultural Economics Dataset

We acquired historical data on maize prices in Thailand from January 2002 to August 2023 through the Office of Agricultural Economics (OAE). This dataset includes a wide array of monthly historical data encompassing numerous variables. This study focuses on the dependent variable, which is the price of maize sold by Thai farmers in Thai baht per kilogram. The independent variables cover various aspects of maize and cassava, such as the total planting land area, crop price, crop yield, rainfall, import and export volumes, import and export values, and the price change of both crops. Overall, this dataset contains 48 variables and 260 observations.

2.1.2 Investing.com Dataset

The dataset from the Investing website (https://www.investing.com) is a comprehensive repository containing various crop prices and additional relevant data. It offers records at hourly, daily, and monthly intervals, making it suitable for our research needs. In the existing literature, [7] have examined the correlation among agricultural commodity prices, such as wheat, rice, and corn, which can serve as alternative crops. Our study aims to identify potential factors influencing maize prices, explicitly looking at soy and sugar prices. Additionally, the exchange rate of USD and Thai Baht data was collected, considering its relevance to import and export activities in the global market [9]. This dataset has 260 records and 5 independent variables, covering January 2002 to August 2023.

The descriptive measure of the target variable (maize prices) alongside the prices of alternative crops is shown in Table 1. In contrast, Figure 1 illustrates the trend of monthly maize prices in Thailand over the entire period covered by the dataset.

Figure 1. Graph of monthly maize prices in Thailand

Table 1. Descriptive measure of maize prices and alternative crop's price

Descriptive Measure	Maize	Cassava	Wheat	Soy	Sugar	Rice
Count	260	260	260	260	260	260
Min	3.88	0.74	261.75	430.25	5.67	3.50
Q1	5.99	1.23	427.06	848.87	10.94	9.83
Q3	8.31	2.18	667.97	1305.37	18.66	14.82
Max	11.60	3.15	1088	1754.37	33.97	21.48
Mean	7.15	1.77	555	1026.92	15.14	11.97
Std	1.71	0.57	177.55	316.56	5.85	3.65

2.2 Methodology

Investigating and using methods that improve forecasting accuracy become highly relevant in this setting. To enhance the clarity and dependability of decision-making, increasing forecasting precision is a key focus in our study. As such, this section will explore the key theories crucial to understanding how this research has developed.

2.2.1 Data Preprocessing

The data preprocessing step is a key component of getting data ready for training the machine learning model. First, due to the diverse scale of values among numerous independent variables, we applied the standard scaler technique to normalize and rescale all input variables to a range between 0 and 1. Second, we employed recursive feature elimination using a random forest model to select only the most significant features to maximize overall accuracy. Finally, Pearson correlation was applied to select only the strong linear relationship between input features and target variables. All these data preprocessing steps help to enhance the efficiency and effectiveness of machine learning algorithms and reduce the computational workload for building the prediction model.

1) Standard Scaler: Standard Scaler is a technique used for feature scaling, specifically mean centering and variance scaling. This process does not change the shape of the feature's distribution but ensures that they all have the same scale to avoid potential issues where the magnitudes of certain features could mislead the machine learning models. This operation is performed independently for each feature in the dataset. As a result, the mean of each feature becomes 0, and the standard deviation becomes 1. The formula of the Standard Scaler function for each feature is shown in equation (1).

$$Z = \frac{x - \mu}{\sigma} \tag{1}$$

- x is the input feature
- μ is Mean
- σ is the Standard Deviation.

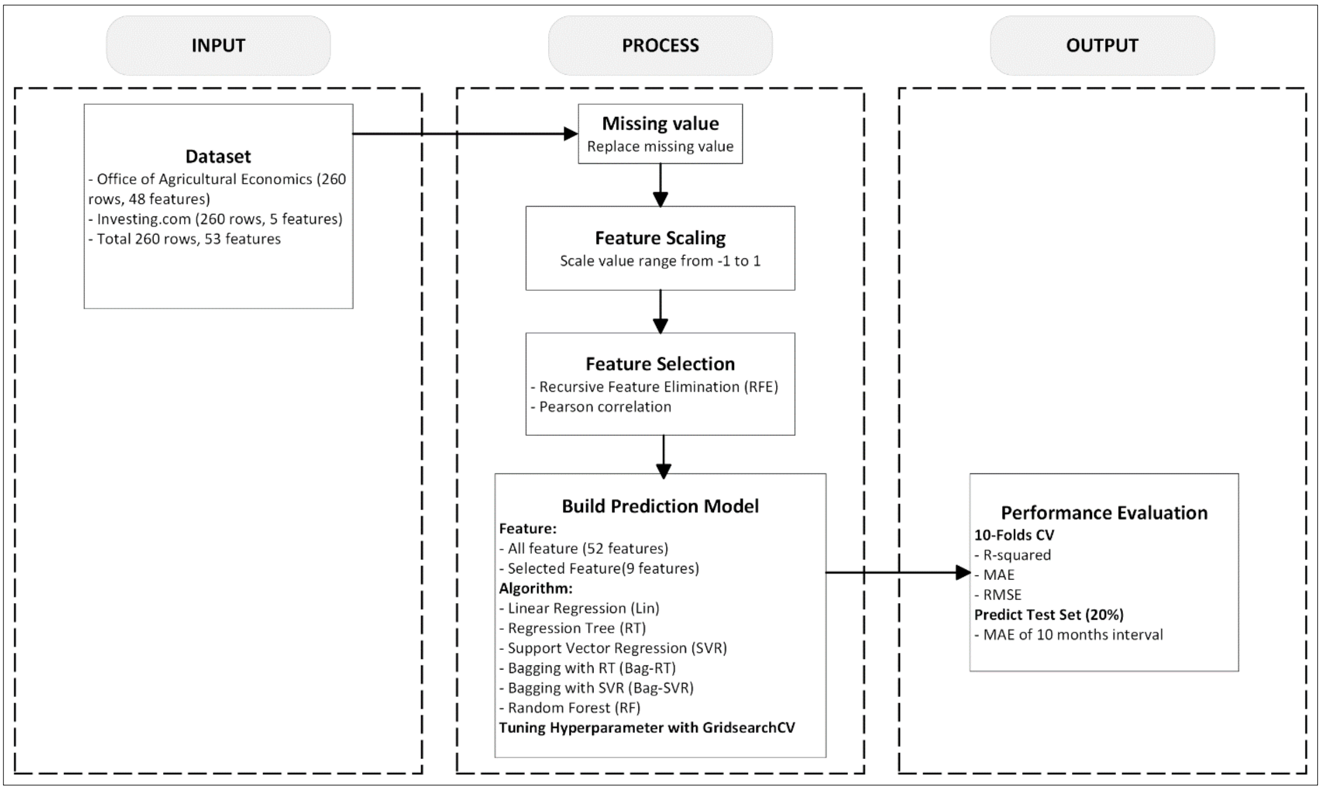

Figure 2. Conceptual framework in this study

2) Feature Selection: As discussed in the dataset description, the presence of numerous variables in the dataset can potentially lead to overfitting, reducing the ability of the predictive model to generalize to new observations. To solve this problem, we proposed two feature selection methods to reduce dataset dimensionality and ensure only the most relevant variables were selected for building the prediction model. The recursive feature elimination (RFE) method based on Random Forest was implemented in the initial stage. The RFE technique systematically evaluates the significance of each feature. It eliminates those that contribute the least to model performance, meaning to keep the feature set that leads to achieving the highest accuracy [11]. In the second stage, we applied a filter-based feature selection method called Pearson correlation, specifically when the input and target variables are quantitative. Pearson correlation is a statistical measure designed to quantify the strength and direction of a linear relationship between two continuous variables. It produces a correlation coefficient, represented by the letter "r" with values between -1 and 1. An "r" value close to 0 denotes a weak or nonexistent linear relationship, whereas an "r" value close to 1 or -1 indicates a strong positive or strong negative linear relationship. The formula produces a number between -1 and 1 by dividing the covariance of the two variables (the numerator) by the product of their standard deviations (the denominator), as shown in equation (2).

$$r = \frac{\sum (X_i - \bar{X})(Y_i - \bar{Y})}{\sqrt{\sum (X_i - \bar{X})^2 (Y_i - \bar{Y})^2}} \tag{2}$$

- r represents the Pearson correlation coefficient.
- X_i and Y_i are data points from the two variables being correlated.
- $\bar{X}$ and $\bar{Y}$ represent the mean of the respective variables.

2.2.2 Regression Trees

Regression trees are a type of machine learning model employed in regression tasks. They operate by recursively partitioning the dataset into subsets based on input features, with each split chosen to minimize the variance of the target variable within each subset. Predictions are made at the tree's leaf nodes, typically by calculating the mean or median value of the target variable for the data points in that node. One of the key advantages of Regression Trees is their interpretability and visualizability, which allows for a clear understanding of how input features relate to the target variable. However, they are prone to overfitting, particularly when the tree becomes too deep [27].

2.2.3 Support Vector Regression

Initially, support vector machines (SVMs) were introduced to solve classification problems and were later extended to support vector regression (SVR) to address the regression issue. The core concept behind this methodology involves identifying data points close to a hyperplane (known as support vectors) that maximize the margin between two classes of data points – those above and below the target variable. The difference between the target value and a certain threshold is used to calculate this margin. This approach aims to reduce structural risk in regression problems by minimizing the upper bound of generalization error rather than focusing on lowering training error [28]. Recognizing that many real-world problems exhibit non-linear characteristics, SVMs can incorporate the concept of Kernel functions, which enable the transformation of data into a higher-dimensional space and capture its inherent features. Various kernel functions are available, including Gaussian, Polynomial, Linear, and radial basis function (RBF) kernels. Support vector regression (SVR) offers advantages in this study when the dataset consists of several samples. However, a notable drawback when choosing the wrong kernel function can potentially lead to misleading or incorrect conclusions [29].

2.2.4 Ensemble Bagging Regressor

In machine learning, the ensemble bagging regressor is a robust and adaptable approach frequently used with various base learners to significantly boost the performance of regression tasks. The key concept behind ensemble bagging is the creation of multiple base learners that collectively outperform the individual base model [30]. In our research, we take advantage of the power of ensemble bagging by combining it with two base learners named regression trees and support vector regression.

1) **RT as a base learner (Bag-RT):** Regression Trees are a foundational and widely used base learner in machine learning. They excel at capturing nonlinear relationships between features and target variables, making them well-suited for cases where data exhibits intricate and non-obvious patterns. By integrating ensemble bagging with Regression Trees, we aim to harness the advantages of both techniques. Ensemble bagging lowers the risk of overfitting and model variance by using diverse subsets of the training data (bootstrap samples) to train several instances of Regression Trees. The combination of these methods not only enhances model stability but also enables our model to generalize unseen data more effectively. The adaptability of ensemble bagging with regression trees is valuable when dealing with diverse and complex datasets, ultimately contributing to more accurate results.

2) **SVR as a base learner (Bag-SVR):** SVR is a robust and versatile base learner known for its capability to model linear and nonlinear relationships between features and target variables. This versatility makes SVR an excellent choice when dealing with datasets with a wide range of complexities. Ensemble bagging with SVR is particularly effective in scenarios characterized by noisy data, complex feature interactions, and challenges in feature selection. The ensemble bagging technique mitigates the pitfalls of overfitting and variance associated with individual models. At the same time, SVR's ability to adapt to various data patterns ensures that our model remains adaptable and resilient.

The combination of ensemble bagging that integrates regression trees and support vector regression as the base learner illustrates our commitment to a comprehensive approach to predicting maize prices. Our goal is to maximize the predictive model's performance through ensemble bagging techniques combined with two strong base learners. Our model generates remarkably accurate forecasts through this strategy while effortlessly capturing complex data patterns. This creates a model that maintains adaptability and robustness, improving accuracy in making predictions for our research.

3) Random Forest (RF): Random Forest Regressor is a robust ensemble machine learning algorithm for regression tasks. It leverages an ensemble of decision trees, each trained on a random subset of the data and features. Aggregating predictions from these trees provides robust and accurate predictions while also handling noisy data and overfitting. It's widely used across various domains and offers the benefit of feature importance analysis to understand the data [31] better.

2.2.5 Hyperparameter Tuning

Hyperparameter tuning is a vital step in developing robust machine-learning models. The choice of hyperparameters can significantly impact the performance and generalizability of the models. In our study, we employed Gridsearch CV, a popular optimization technique, to systematically explore hyperparameter combinations available from each machine learning model. In addition, K subsets (or "folds") with approximately the same size were created within the dataset using K-fold cross-validation. A different fold is used as the validation set, and the remaining K-1 folds are used for each iteration's training set. This process ensures that every data point is used for validation exactly once. The results from each fold are averaged to obtain a more robust performance and reduce the risk of overfitting. Typical values for K include 5, 10, and 20, depending on the size of the dataset and the computational resources available. In our study, the value of K was set to 10 to evaluate these hyperparameter combinations through the Gridsearch CV function as part of the cross-validation process. This method allowed us to identify and select the most effective hyperparameters to improve model performance and accuracy. All Grid values and the hyperparameters chosen for each model in this study are shown in **Table 8**.

2.2.6 Performance Measures

Performance measures are critical tools used to evaluate the effectiveness and quality of machine learning models. These measures provide insights into how well a model performs, how accurately it makes predictions, and its overall reliability. In this paper, the model's performance is assessed using three metrics: R-squared (R^2), mean absolute error (MAE), and root mean squared error (RMSE). The mathematical expressions for each of these metrics used for model performance evaluation are shown in the equation (3), (4), and (5).

$$R^2 = 1 - \frac{RSS}{TSS} \tag{3}$$

$$MAE = \frac{1}{n}\sum_{i=1}^{n} |y_i - \bar{y}_i| \tag{4}$$

$$RMSE = \sqrt{\frac{1}{n}\sum_{i=1}^{n} (y_i - \bar{y}_i)^2} \tag{5}$$

Where R^2 is the coefficient of determination, RSS represents the residual sum of squares, and TSS represents the total sum of squares. n is the number of total observations, y_i is the *i*th value observed for series and $\bar{y}_i$ is the *i*th value predicted for the model.

3. Results and Discussion

3.1. Feature Scaling

In the dataset in our study, due to the different scale of various features which make machine learning difficult for training, we apply Standard Scaler function, a standardized method to make all input data at the same scale. Figure 3 shows the data distribution plot of some independent variables after scaling with the standard scaler function.

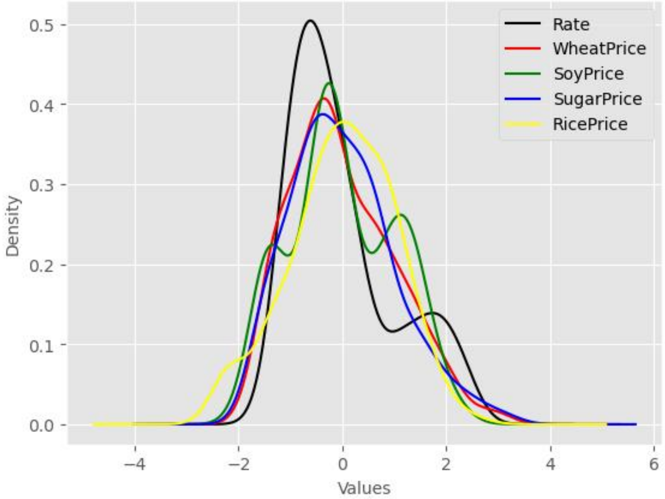

Figure 3. The data distribution after scaling process

3.2 Feature Selection

To the feature selection process discussed in Section 2, first, we applied the recursive feature elimination based on random forest to identify the optimal number of features required to achieve the highest score. Additionally, it has identified and selected the top 6 performing features from an initial set of 52 features, which form the appropriate datasets for training the machine learning models. The 6 chosen features by the RFE model include: 'MaiFutPrice,' 'CasPrice,' 'CasPlant,' 'MaiChg4', 'Rate,' and 'RicePrice.' Using these 6 features, the model achieved the highest R^2 score of 0.928, as shown in

Table **2**. Second, we applied the Pearson correlation feature selection technique, in which the input variable correlates with the target variable. In this case, features with a correlation coefficient (r) value more excellent than 0.6 or less than -0.7 were selected, and all p-values of those correlated features must be less than 0.05 to present a statistically significant linear relationship between the variables. This feature selection step resulted in the selection of 8 features considered strong positive and negative linear relationships with the target variable. Table *3* shows the Pearson correlation coefficient value and the p-value between target variable with strong linear relationship variables selected through this technique.

Figure 4. Graph of R^2 score by number of features using RFE feature selection method

Table 2. R^2 score of RFE method by number of features

#	**R^2**	#	**R^2**	#	**R^2**	#	**R^2**
52	0.913	39	0.913	26	0.915	13	0.919
51	0.915	38	0.914	25	0.914	12	0.918
50	0.912	37	0.912	24	0.915	11	0.919
49	0.913	36	0.913	23	0.915	10	0.922
48	0.913	35	0.913	22	0.915	9	0.921
47	0.913	34	0.912	21	0.915	8	0.924
46	0.913	33	0.912	20	0.915	7	0.924
45	0.913	32	0.913	19	0.915	**6**	**0.928**
44	0.912	31	0.916	18	0.916	5	0.9
43	0.913	30	0.914	17	0.918	4	0.888
42	0.912	29	0.914	16	0.917	3	0.877
41	0.912	28	0.914	15	0.918	2	0.814
40	0.913	27	0.916	14	0.918	1	0.649

Table 3. Correlation value and p-value of selected feature by Pearson correlation

No	**Feature**	**Corr Value**	**p-value**
1	CasPrice	0.85	2e^{-74}
2	MaiFutPrice	0.81	6e^{-62}
3	SoyPrice	0.80	8e^{-59}
4	RicePrice	0.79	7e^{-56}
5	WheatPrice	0.74	3e^{-47}
6	CasPlant	0.73	2e^{-45}
7	SugarPrice	0.60	1e^{-24}
8	Rate	-0.70	6e^{-40}

By integrating the RFE and Pearson correlation feature selection stages, we aim to optimize the dataset by keeping only the most relevant features for building the prediction model. We combine the features selected by those two methods together, resulting in 9 variables such as 'MaiFutPrice,' 'CasPrice,' 'CasPlant,' 'MaiChg4', 'Rate,' 'RicePrice,' 'SoyPrice,' 'WheatPrice,' and 'SugarPrice.' This approach reduces dataset dimensions, prevents the model from overfitting, and strengthens the model's ability to generate accurate forecasts while managing a concise set of features.

3.3 Experiment #1

In the first experiment, we employed various machine learning algorithms, including individual models like regression trees (RT) and support vector regression (SVR), as well as the ensemble bagging regressor (Bag-RT and Bag-SVR), and random forest (RF). We also utilized a multiple linear regression model (Lin), the proposed model by recent study of [20] on the same OAE dataset, to compare the performance with our proposed models. Our study utilized 260 complete records from the dataset and training using 10-fold cross-validation to ensure each fold was used as a test set exactly once. Each model was trained using the parameters outlined in Table 8 and tuned through the GridSearch CV function to achieve the best score. This table summarizes the results of hyperparameter tuning performed using the GridSearchCV function. It includes columns for the Model, Hyperparameter, Parameter List, and Best Parameter. Each row represents a different model, and the corresponding hyperparameters are tuned to enhance model performance. By systematically testing various hyperparameter configurations and selecting the ones that maximize performance metrics, GridSearchCV helps fine-tune models for better predictive accuracy and generalization.

Furthermore, we compared the performance of each model using "All Features" against "Selected Features" set to see the difference between these selections. Evaluation metrics, including R^2, MAE, and RMSE, were used to compare the model's performance, as shown in Table 4.

Table 4. Performance score comparison by each model on "All feature" and "Selected feature."

Feature	Model	R^2	MAE	RMSE
All Feature	Lin	0.865	0.456	0.599
	RT	0.822	0.476	0.638
	SVR	0.918	0.360	0.475
	Bag-RT	0.927	0.318	0.426
	Bag-SVR	0.926	0.344	0.459
	RF	0.91	0.375	0.487
Selected Feature	Lin	0.893	0.423	0.537
	RT	0.846	0.44	0.617
	SVR	**0.959**	**0.251**	**0.333**
	Bag-RT	0.94	0.292	0.396
	Bag-SVR	**0.961**	**0.234**	**0.315**
	RF	0.932	0.309	0.421

From a comparison of performance between using the "Selected Feature" set and a complete set of 52 features in Table 4, the "Selected Feature" set consistently demonstrates superior performance across all models. This suggests improved predictive accuracy and efficiency with the smaller feature set. The Bag-SVR and SVR model within the "Selected Feature" achieved the highest R^2 value of 0.961 and 0.959 as well as the lowest MAE value of 0.234 and 0.251 and RMSE value of 0.315 and 0.333, respectively, compared to all other models applied on the "All Feature" set.

3.4 Experiment #2

The second experiment involved dividing the data into different training sizes (70%, 75%, 80%, 85%, 90%, and 95%) to assess the model's predictive capability for each division aim to find the best training and testing set ratio which make the model achieved the best R^2 score to predict the future maize prices in the unseen data. The samples of each training size were trained using 10-fold cross-validation, and the rest were kept as a test set for future prediction. The outcomes of this analysis are illustrated in Table 5, and the graph of the prediction accuracy of each model in different training sizes is shown in Figure *5*.

Table 5. R^2 score by different training sets from 70 to 95 percent

Training		Lin	RT	SVR	Bag-RT	Bag-SVR	RF
%	Records						
70	182	0.898	0.899	0.942	0.901	0.951	0.9
75	195	0.894	0.863	0.938	0.931	0.95	0.91
80	208	0.895	0.870	**0.947**	0.927	**0.956**	0.921
85	221	0.894	0.863	0.941	0.932	0.953	0.927
90	234	0.869	0.856	0.909	0.916	0.929	0.903
95	247	0.858	0.863	0.847	0.863	0.868	0.871

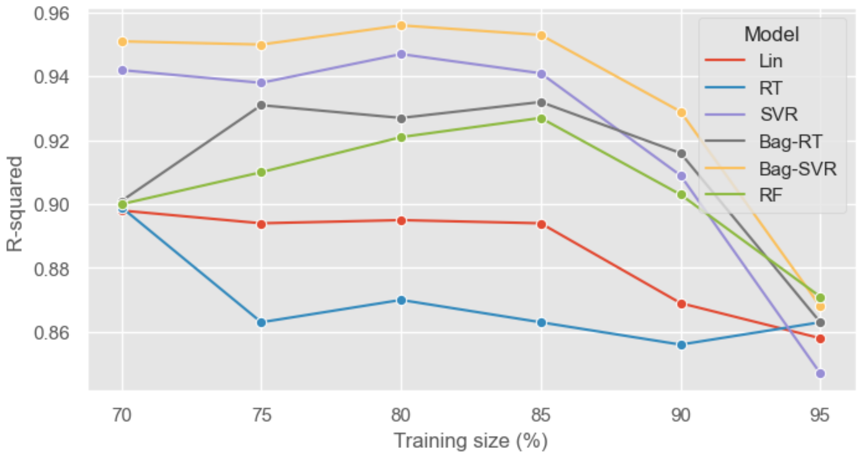

Figure 5. R^2 score of test set from different training size

The experiment's result in Table 5 and Figure 5 revealed that the Bag-SVR model using the "Selected Feature" set consistently demonstrated superior performance expressly when the training size was set to 80%, resulting in the highest R^2 score value of 0.956, followed by SVR model with R^2 value of 0.947. Based on this conclusion, we conducted 80% of the dataset as a training set using 10-fold cross-validation while allocating 20% in the most recent months for the testing set. This approach was employed to evaluate the mean absolute error (MAE) score, aiming to see the average price difference between the actual and predicted prices generated by each model and find the model that accurately forecasts the future price of maize. Figure 6 displays a graph visualizing the correlation between actual and predicted prices. This analysis incorporates all machine learning models applied to the "Selected Feature" by using each model's best hyperparameters obtained from the Gridsearch CV function. These models were utilized to predict the 20% of unseen data (test set), covering a range from May 2019 to August 2023, totaling 52 months.

Based on the graph in Figure 6, the models have superior predictive capabilities compared to the actual values within the first 10-month period of the test set. So, we segmented the test set into 10-month intervals and computed the MAE score, as outlined in Table 6. The first segment, from May 2019 to February 2020, notably stands out for its consistently low MAE values across multiple models. During this period, the SVR model demonstrated superior predictive capabilities with an impressive MAE score of 0.23, closely followed by the Bag-RT and Bag-SVR models, which had MAE values of 0.25 and 0.26, respectively. This exceptional performance is due to the fact that the test data is closely aligned with the previous training set. However, as we progress beyond this initial phase into the period from March 2020 to December 2020, while some models maintain relatively low MAE scores (e.g., RT and Bag-RT), for others, the MAE scores go up a bit, suggesting that maybe the data is changing or the models need a little fine-tuning. Moving further along the timeline, the MAE scores exhibit a gradual upward trend, particularly in the intervals from January 2021 to October 2021 and November 2021 to August 2022. During these periods, the models encountered more significant challenges in accurately predicting outcomes, as reflected in the higher MAE values recorded across all models. By the final segment, spanning from September 2022 to August 2023, the MAE scores peak, suggesting a significant divergence between the test data and the original training set, posing considerable challenges for the models in making accurate predictions.

Table 6. The MAE score of the test set split by 10 months range

Date Range	Lin	RT	SVR	Bag-RT	Bag-SVR	RF
May 19 - Feb 20	0.41	0.36	**0.23**	**0.25**	**0.26**	0.42
Mar 20 - Dec 20	0.34	0.26	0.40	0.25	0.62	0.32
Jan 21 - Oct 21	1.21	0.47	1.12	0.51	1.57	0.49
Nov 21- Aug 22	0.96	0.78	1.30	0.65	1.08	0.91
Sep 22 - Aug 23	1.49	2.08	3.24	2.05	3.02	2.22

Furthermore, we conducted training using all the observations while reserving only the most recent month, August 2023, with a value of 9.56 Baht per kilogram as a test set. This approach allowed us to observe and compare the predictions made by each model. Table 7 provides an analysis of different models' performance in predicting maize prices one month ahead by displaying the prices, along with the price difference between the predicted and actual values.

Table 7. The predicted price and price difference of each model on the test set of the last month

Model	Lin	RT	SVR	Bag-RT	Bag-SVR	RF
Predicted	8.71	7.73	9.9	8.68	9.8	9.12
Different	0.85	1.83	**0.34**	0.88	**0.24**	0.44

From the result of Table *7*, both the Bag-SVR and SVR models exhibited notable predictive accuracy in the last month of the test set. The Bag-SVR model showcased a closer estimation of the actual price, differing by only 0.24 baht/kg, followed by the SVR model, which demonstrated differing by 0.34 baht/kg.

4. Conclusions

This study aimed to enhance maize price forecasts in Thailand using various machine learning algorithms, targeting benefits for farmers, agribusinesses, and governmental policies. The Recursive Feature Elimination (RFE) combined with Pearson correlation successfully identified 9 key variables for training the machine learning models for feature selection. In building the prediction models, individual and ensemble techniques were employed to compare their accuracy in predicting maize prices. Notably, the Bag-SVR demonstrated superior predictive accuracy with an R^2 score of 0.961, MAE of 0.234, and RMSE of 0.315, followed closely by the SVR model with an R^2 score of 0.959, MAE of 0.251, and RMSE of 0.333. In contrast, the RT model achieved the lowest score, with an R^2 score of 0.846, MAE of 0.44, and RMSE of 0.617. In conclusion, this research underscores the importance of feature selection in refining model efficiency and emphasizes the potential of machine learning in enhancing maize price forecasts in Thailand.

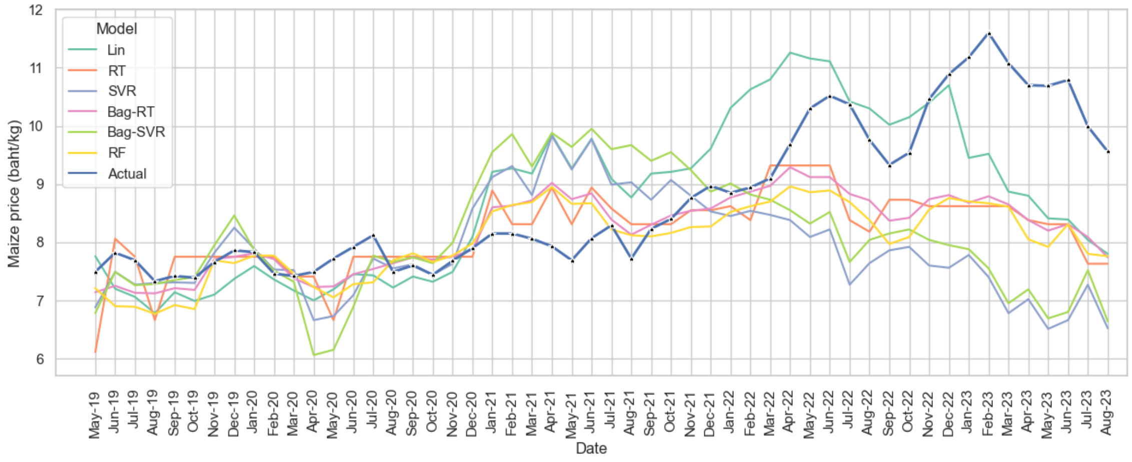

Figure 6. Actual maize price and predicted price by each model on test set

Table 8. The details of hyperparameter tuning of each model

Model	Hyperparameter	Parameter List	Best Parameter
RT	max_depth	[2, 5, 10, 20, 30, 40, None]	20
	min_samples_split	[1,2,3,4,5,6,7,8,9,10]	1
	min_samples_leaf	[1,2,3,4,5,6,7,8,9,10]	5
SVR	C	[10,20,30,40,50,60,70,80,90,100]	20
	gamma	['scale', 'auto']	scale
	kernel	['rbf','linear','poly']	'rbf'
Bag-RT	Bootstrap	[True, False]	False
	bootstrap_features	[True, False]	True
	max_features	[0.5, 0.6, 0.7, 0.8, 0.9, 1.0]	0.9
	max_samples	[0.5, 0.6, 0.7, 0.8, 0.9, 1.0]	0.9
	n_estimators	[10, 50, 100, 200]	50
Bag-SVR	Bootstrap	[True, False]	False
	bootstrap_features	[True, False]	False
	max_features	[0.5, 0.6, 0.7, 0.8, 0.9, 1.0]	0.8
	max_samples	[0.5, 0.6, 0.7, 0.8, 0.9, 1.0]	0.9
	n_estimators	[10, 50, 100, 200]	200
RF	max_features	[' sqrt', 'log2']	'sqrt'
	max_depth	[10, 20, 30, 40, None]	20
	min_samples_split	[1,2,3,4,5,6,7,8,9,10]	2
	min_samples_leaf	[1,2,3,4,5,6,7,8,9,10]	1
	n_estimators	[10, 50, 100, 200]	100

5. Acknowledgement

This work has been supported by the Royal Scholarship under Her Royal Highness Princess Maha Chakri Sirindhorn Education Project to the Kingdom of Cambodia.

Author Contributions: Conceptualization, N.S.; methodology, N.S, S.M.; software, S.M.; validation, N.S., S.M. data curation, N.S.; writing—original draft preparation, S.M.; writing—review and editing, N.S.; visualization, S.M.; supervision, N.S. All authors have read and agreed to the published version of the manuscript."

Funding: The APC was funded by Department of Computer Science, Faculty of Science, Kasetsart University.

Conflicts of Interest: The authors declare no conflict of interest. The funders had no role in the design of the study; in the collection, analyses, or interpretation of data; in the writing of the manuscript, or in the decision to publish the results.

References

[1] Sjah, T.; Zainuri, Z. Agricultural supply chain and food security. In *Zero Hunger*, Springer, **2020**, pp 79-88.

[2] Warr, P.; Suphannachart, W. Agricultural productivity growth and poverty reduction: Evidence from Thailand. *Journal of Agricultural Economics* **2021**, *72*(2), 525-546.

[3] Jaipong, P.; Sriboonruang, P.; Siripipattanakul, S.; Sitthipon, T.; Kaewpuang, P.; Auttawechasakoon, P. A review of intentions to use artificial intelligence in Big Data Analytics for Thailand agriculture. *Review of Advanced Multidisciplinary Science, Engineering & Innovation* **2022**, *1*(2), 1-8.

[4] Basso, B.; Liu, L. Seasonal crop yield forecast: Methods, applications, and accuracies. *advances in agronomy* **2019**, *154*, 201-255.

[5] Shahhosseini, M.; Hu, G.; Pham, H. Optimizing ensemble weights and hyperparameters of machine learning models for regression problems. *Machine Learning with Applications* **2022**, *7*, 100251.

[6] Kantanantha, N.; Serban, N.; Griffin, P. Yield and Price Forecasting for Stochastic Crop Decision Planning. *Journal of Agricultural, Biological, and Environmental Statistics* **2010**, *15*(3), 362-380. DOI: 10.1007/s13253-010-0025-7.

[7] Wang, L.; Duan, W.; Qu, D.; Wang, S. What matters for global food price volatility? *Empirical Economics* **2018**, *54*, 1549-1572.

[8] Ge, Y.; Wu, H. Prediction of corn price fluctuation based on multiple linear regression analysis model under big data. *Neural Computing and Applications* **2020**, *32*, 16843-16855.

[9] Ya, Z.; Pei, K. Factors influencing agricultural products trade between China and Africa. *Sustainability* **2022**, *14* (9), 5589.

[10] Jain, A.; Marvaniya, S.; Godbole, S.; Munigala, V. A framework for crop price forecasting in emerging economies by analyzing the quality of time-series data. *arXiv preprint arXiv:2009.04171* **2020**.

[11] Mariammal, G.; Suruliandi, A.; Raja, S.; Poongothai, E. Prediction of land suitability for crop cultivation based on soil and environmental characteristics using modified recursive feature elimination technique with various classifiers. *IEEE Transactions on Computational Social Systems* **2021**, *8*(5), 1132-1142.

[12] Suruliandi, A.; Mariammal, G.; Raja, S. Crop prediction based on soil and environmental characteristics using feature selection techniques. *Mathematical and Computer Modelling of Dynamical Systems* **2021**, *27* (1), 117-140.

[13] Shahhosseini, M.; Hu, G.; Archontoulis, S. V. Forecasting corn yield with machine learning ensembles. *Frontiers in Plant Science* **2020**, *11*, 1120.

[14] Ribeiro, M. H. D. M.; Ribeiro, V. H. A.; Reynoso-Meza, G.; dos Santos Coelho, L. Multi-objective ensemble model for short-term price forecasting in corn price time series. In *2019 International Joint Conference on Neural Networks (IJCNN)*, **2019**, pp 1-8.

[15] Nikou, M.; Mansourfar, G.; Bagherzadeh, J. Stock price prediction using DEEP learning algorithm and its comparison with machine learning algorithms. *Intelligent Systems in Accounting, Finance and Management* **2019**, *26*(4), 164-174.

[16] Khwaja, A. S.; Anpalagan, A.; Naeem, M.; Venkatesh, B. Joint bagged-boosted artificial neural networks: Using ensemble machine learning to improve short-term electricity load forecasting. *Electric Power Systems Research* **2020**, *179*, 106080.

[17] Li, Y.; Yu, R.; Shahabi, C.; Liu, Y. Diffusion convolutional recurrent neural network: Data-driven traffic forecasting. *arXiv preprint arXiv:1707.01926*, **2017**.

[18] Paudel, D.; Boogaard, H.; de Wit, A.; Janssen, S.; Osinga, S.; Pylianidis, C.; Athanasiadis, I. N. Machine learning for large-scale crop yield forecasting. *Agricultural Systems* **2021**, *187*, 103016.

[19] Li, J.; Chen, W. Forecasting macroeconomic time series: LASSO-based approaches and their forecast combinations with dynamic factor models. *International Journal of Forecasting* **2014**, *30*(4), 996-1015.

[20] Jantankaew, P.; Soonthornphisaj, N. Data Analytics for Maize Price Prediction using Regression Algorithms. *KKU Research Journal (Graduate Studies)* **2023**, *23*(2), 92-106.

[21] Roberts, S.; Osborne, M.; Ebden, M.; Reece, S.; Gibson, N.; Aigrain, S. Gaussian processes for time-series modelling. *Philosophical Transactions of the Royal Society A: Mathematical, Physical and Engineering Sciences* **2013**, *371*(1984), 20110550.

[22] Kim, K.-j. Financial time series forecasting using support vector machines. *Neurocomputing* **2003**, *55* (1-2), 307-319.

[23] Ouyang, H.; Wei, X.; Wu, Q. Agricultural commodity futures prices prediction via long-and short-term time series network. *Journal of Applied Economics* **2019**, *22*(1), 468-483.

[24] Cerqueira, V.; Torgo, L.; Pinto, F.; Soares, C. Arbitrated ensemble for time series forecasting. In *Machine Learning and Knowledge Discovery in Databases: European Conference, ECML PKDD 2017, Skopje, Macedonia, September 18–22, 2017, Proceedings, Part II 10*, **2017**, pp 478-494.

[25] Oliveira, M.; Torgo, L. Ensembles for time series forecasting. In *Asian Conference on Machine Learning*, **2015**, PMLR: pp 360-370.

[26] Silva, R. F.; Barreira, B. L.; Cugnasca, C. E. Prediction of Corn and Sugar Prices Using Machine Learning, Econometrics, and Ensemble Models. *Engineering Proceedings* **2021**, *9*(1), 31.

[27] Breiman, L. *Classification and regression trees*; Routledge, 2017.

[28] Chen, R.; Liang, C.-Y.; Hong, W.-C.; Gu, D.-X. Forecasting holiday daily tourist flow based on seasonal support vector regression with adaptive genetic algorithm. *Applied Soft Computing* **2015**, *26*, 435-443.

[29] Cortes, C.; Vapnik, V. Support-vector networks. *Machine learning* **1995**, *20*, 273-297.

[30] Dietterich, T. G. Ensemble methods in machine learning. In *International workshop on multiple classifier systems*, **2000**, pp 1-15.

[31] Breiman, L. Random forests. *Machine learning* **2001**, *45*, 5-32.

ASEAN
Journal of Scientific and Technological Reports
Online ISSN:2773-8752

Research article

Histological Structure and Histochemistry of the Digestive Tract of the Striped Tiger Nandid Fish, *Pristolepis fasciata*

Akkanee Pewhom[1*] and Akapon Vanikasampanna[2]

[1] Department of Biology, Faculty of Science and Digital Innovation, Thaksin University, Phatthalung, 93210 Thailand,
[2] Innovative Learning Center, Srinakharinwirot University, 10110, Thailand
* Correspondence: pewhomakkanee@gmail.com

Abstract: The striped tiger nandid fish, *Pristolepis fasciata*, is widely distributed in Thailand. However, its diet composition has been intensively investigated. The histological profile remains an exciting and challenging issue. Therefore, the objectives of this study are to describe the histological structure and histochemistry of the digestive tract of the striped tiger nandid fish. Fifteen adult fish were collected from Songkhla province, Thailand. The digestive tract was fixed in Bouin's solution, followed by basic paraffin techniques. The 5 µm sections were stained with hematoxylin and eosin (H&E), periodic acid Schiff's (PAS), alcian blue (AB) pH 2.5 and pH 1.0, and Masson's trichrome (MT). The results revealed that the digestive tract wall comprised four layers: mucosa, submucosa, muscularis, and serosa. The mucous and goblet cells in the esophagus exhibited positive staining with PAS, AB pH 2.5, and pH 1.0. The stomach was divided into three parts: cardiac, fundic, and pyloric stomach. The epithelium of the cardiac stomach showed positive staining with PAS and weak staining with AB pH 1.0. The fundic cells showed strong positive staining with PAS but weak staining with AB pH 2.5 and 1.0. In contrast, the cells lining the fundic and cardiac glands showed positive staining with PAS. The pyloric epithelium revealed positive staining with PAS but did not contain a gland. In the anterior, middle, and posterior intestines, glands were absent. Goblet cells exhibited intense labeling with PAS and AB pH 2.5 and 1.0 in each portion. The intestinal coefficient was 0.62±0.01, indicating an omnivorous fish.

Keywords: Gastrointestinal tract; gastric gland; histology; histochemical study; intestinal coefficient

Citation:
Pewhom, A.; Vanikasampanna, A. Histological structure and histochemistry of the digestive tract of the striped tiger nandid fish, *Pristolepis fasciata ASEAN J. Sci. Tech. Report.* **2024**, *27*(4), e253044. https://doi.org/10.55164/ajstr.v27i4.253044

Article history:
Received: March 7, 2024
Revised: May 27, 2024
Accepted: June 4, 2024
Available online: June 30, 2024

1. Introduction

The digestive tract is one of the largest systems in fish, which is related to their feeding habitat, environment [1, 2], type of food, and behavior [3]. Additionally, the digestive tract plays an important role in growth and nutrition [1, 2]. Al-Abdulhadi [4] mentioned that the digestive tract exhibits a diversity of morphology and function. The digestive tract of many teleosts has been studied through gross anatomy, histology, and histochemical analysis, such as the South American catfish *Rhamdia quelen* [5], short mackerel *Rastrelliger brachysoma* [6], spotted snakehead fish *Channa punctata*, striped snakehead fish *C. striata* [7], pebbly fish *Alestes baremoze* [8], large yellow croaker *Larimichthys crocea* [9], lizardfish *Synodus variegatus* [10] and banded tilapia *Tilapia sparrmanii* [2]. However, the gastrointestinal tract in these fish exhibits a marked difference in characteristics, reflecting their evolution, diet, and environment [2, 11]. Herbivorous fish primarily consume plants and have a small stomach and a long intestine. Omnivorous fish, feeding on animals and plants, exhibits a large stomach and a long intestine [2, 12]. On the other hand, carnivorous fish, specializing in animal consumption, possess a distensible stomach and the shortest intestine [13].

In categorizing feeding habits, numerous studies utilize the intestinal coefficient (IC) to identify fish feeding types [14]. Omnivorous fish typically have an IC ranging from 0.6 to 8.0, while carnivorous fish exhibit an IC in the range of 0.2 to 2.5. Additionally, herbivorous fish generally have an IC between 0.8 and 15.0. Notably, some herbivorous fish species may have a shorter intestine and a lower IC [9]. Despite the fish having various diets, the digestive wall's characteristics consist of four tunics when considering histology. These are arranged from the innermost to the outermost tunic, i.e., (I) the mucosa, including the layer of epithelial tissue, lamina propria, and muscularis mucosae, (II) the submucosa being the layer of connective tissue, blood vessels, and nerve plexus, (III) the muscular tunic that subdivided into two layers (inner circular and outer longitudinal layers), and (IV) the layer of connective tissue that known as the serosa [6].

The striped tiger nandid fish, *Pristolepis fasciata* is a member of the family Nandidae. This species is distributed widely from Burma to Indonesia, inhabiting areas with aquatic or emergent plants in marshes, lakes, swamps, and rivers, typically slow-running or still water [15]. In the previous study, Sangpradub and Chutima [16] investigated the diet composition of striped tiger nandid fish in Kaeng Lawa, Thailand, identifying as the significant groups of prey (in the phylum Arthropoda and Mollusca) and other foods (plants, algae, and Euglenozoa). Furthermore, several studies on the diet of striped tiger nandid fish yield consistent results. The striped tiger nandid fish is reported to feed on aquatic insects, crustaceans, filamentous algae, submerged plants [15], fish fry, and aquatic insects [17]. Despite numerous studies on the diet of striped tiger nandid fish, there remains a scarcity of information on the histology and histochemical analysis of the digestive tract.

The information about the structure and characteristics of the digestive tract in fish is important because it can serve as a guideline for understanding the pathology, culture, conservation, and management and gaining insights into the structure and physiology of the fish's digestive system. In the present work, the histological structure and histochemistry of the digestive tract of the striped tiger nandid fish were deeply investigated.

2. Materials and Methods

Fifteen adult striped tiger nandid fish were collected by trawling from Pak Ro subdistrict, Singhanakhon district, Songkhla province, Thailand (7°15'05.3"N 100°26'24.0" E) from February to November 2023. The sampling was collected every two months. Fifteen specimens (mean snout-vent length approximately 15.91±0.82 cm (Table 1)) were anesthetized with fish anesthesia (tricaine methanesulfonate, MS 222, and solution by using a dosage of 100 mg/L). The digestive tract was removed for photography after a longitudinal incision in the abdominal wall. The intestinal length, with a mean total length of 9.79±0.59 cm (Table 1), was measured to calculate the IC [14].

$$\mathrm{IC} = \frac{\text{Intestinal length}}{\text{Snout} - \text{vent length}}$$

The digestive tract was cut into small pieces, which were fixed in Bouin's solution for 48 hours and placed in 70% alcohol. Subsequently, they underwent basic paraffin techniques, including dehydration using a graded series of ethyl alcohol (70%, 80%, 95%, and absolute alcohol), clearing with xylene, infiltration, and embedding with Paraplast Plus® (Sigma-Aldrich, USA), and sectioning was performed with a rotary microtome. The 5 µm serial sections were stained with hematoxylin and eosin (H&E) for general characteristics, periodic acid Schiff's – hematoxylin (PAS) for neutral glycoproteins/mucopolysaccharides, alcian blue (AB) pH 2.5 – nuclear fast red (NF) for carboxylated acid glycoproteins/mucopolysaccharides, AB pH 1.0 – NF for sulphated acid glycoproteins/mucopolysaccharides and Masson's trichrome (MT) for the connective tissue and muscle [18]. The sections were observed under a light microscope. This research was approved by the Animal Ethics Screening Committee, Thaksin University (Permit number: TSU 2022-008. IACUC No. 0008).

3. Results and Discussion

3.1 Gross morphology

The gross morphology of the digestive tract of striped tiger nandid fish is shown in Figure 1, and the length of the digestive tract is presented in Table 1. The esophagus was found to be a short, straight, muscular tube connecting to the white J-shaped stomach. At the end of the stomach, it curved and connected to the intestine. Meanwhile, the intestine exhibited a marked decrease in size from the anterior to posterior portions, according to other fish species [2, 19, 20].

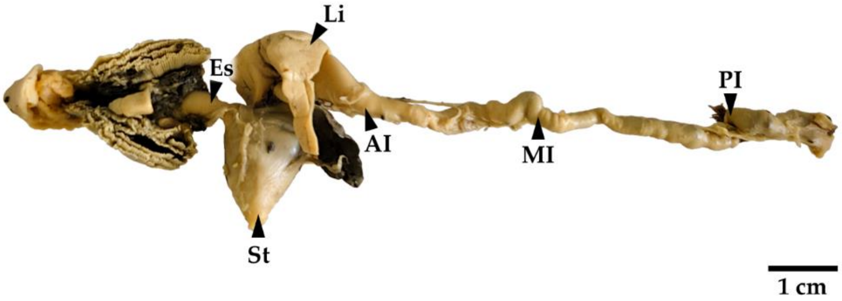

Figure 1. Photograph showing the components of the digestive tract and liver (Li), consisting of the esophagus (Es), stomach (St), and intestinal part. The intestine was divided into three parts: the anterior intestine (AI), the mid-intestine (MI), and the posterior intestine (PI).

Table 1. Mean and standard deviation of snout-vent length, gastrointestinal tract length, intestinal length, and intestinal coefficient (IC) (N=15).

	Snout-vent length (cm)	**Gastrointestinal tract length (cm)**	**Intestinal length (cm)**	**Intestinal coefficient (IC)**
Mean ± standard deviation	15.91 ± 0.82	13.43 ± 0.67	9.79 ± 0.59	0.62 ± 0.01

3.2 Histological structures and histochemistry

The histological structure of the digestive tract in striped tiger nandid fish revealed general characteristics similar to those found in other fish and vertebrates, with the wall comprising four layers: the mucosa (epithelium, lamina propria, and muscularis mucosae), submucosa, muscularis, and serosa, whereas some portions lacked muscularis mucosae. However, the characteristics of the four tunics displayed no discernible difference in each fish corresponding to those observed in spotted pimelodid *Pimelodus maculatus* [21] large yellow croaker *L. crocea* [9] and banded tilapia *T. sparrmanii* [2]. However, some species lacked muscularis mucosae in all parts, such as pike characin *Oligosarcus hepsetus* [22]. In addition, the muscular layers of all portions in striped tiger nandid fish were involved in the motility of food, mixing food with digestive enzymes [22], and transporting food.

3.2.1 Esophagus

The mucosa exhibited numerous longitudinal folds (Figure 2A) with a mean fold height of 313.84±36.46 µm and a fold width of 236.36±51.56 µm (Table 2). The longitudinal fold of the esophagus in striped tiger nandid fish helped to increase the luminal diameter and distension during the food transported to the stomach, similar to other fish species [2, 21]. Furthermore, Okuthe and Bongile [2] stated that the number of folds was related to the digestive capacity, with more folds leading to the increased efficiency. The epithelium of the esophagus was lined by non-keratinized stratified columnar epithelium. These consisted of four cell types: non-mucous, mucous, undifferentiated, and goblet cells (Figures 2C-2F). The stratified epithelium was similar to the esophagus of many fish such as sea bream *Mylio cuvieri* [4], pike characin *O. hepsetus* [22], killifish *Anablepsoides urophthalmus* [23], and banded tilapia *T. sparrmanii* [2]. However, the epithelium of the esophagus of striped tiger nandid fish was columnar, which differed from the large yellow croaker *L. crocea* [9]. In contrast, the esophagus of a large yellow croaker, *L. crocea*, was divided into two regions: the frontward part with stratified squamous epithelium and the hindmost region with stratified columnar epithelium [9]. Additionally, the esophagus of striped tiger nandid fish differed from pike characin, *O. hepsetus*, which had stratified squamous epithelium [22], and from Asian seabass, *Lates calcarifer* [24], which had simple columnar epithelium. The present study and previous reports indicated the variability in esophageal epithelium types. The stratified epithelium, as observed in the esophagus of striped tiger nandid fish, was suggested to have a role in the renewal and protection of the surface from abrasion or abrasion resistance to protect the epithelium from injury [4]. Furthermore, the stratified epithelium was believed to protect the esophagus from pathogens [4, 25].

The non-mucous cells of the esophagus were low-columnar to columnar with round nuclei. The cytoplasm showed positive staining with eosin but negative staining with PAS (Figure 2D), AB pH 2.5 (Figure 2E), and AB pH 1.0 (Figure 2F). The mucous cells interspersed between non-mucous cells had round nuclei and a columnar shape. The cytoplasm showed strongly positive staining with PAS (Figure 2D), AB pH 2.5 (Figure 2E), and AB pH 1.0 (Figure 2F). These results demonstrated the secretion of neutral, carboxylated, and sulphated acid mucins, respectively. These results were consistent with the previous reports suggesting that neutral mucous with low viscosity functioned in lubricating the luminal epithelium [22] and helped to protect the esophageal epithelium from chemical and mechanical injury [24, 26]. Reifel and Anthony [27] stated that numerous mucous cells in the esophagus were mostly found in carnivorous and omnivorous fish but decreased in herbivorous fish, functioning similarly to salivary glands in mammals [28]. Meanwhile, acid mucous with high viscosity was believed to have the function of trapping particles to enter the esophagus [29].

Near the basement membrane, undifferentiated cells were found, characterized by clear cytoplasm and round nuclei (Figure 2C). These cells showed negative staining with PAS (Figure 2D), AB pH 2.5 (Figure 2E), and AB pH 1.0 (Figure 2F). Between the mucous cells, the goblet cells showed strongly positive staining for PAS (Figure 2D), AB pH 2.5 (Figure 2E), and AB pH 1.0 (Figure 2F). Goblet cells showed positivity to AB pH 2.5, indicating the synthesis of carboxylated acid mucins. The benefit of acid mucins was the increase in the viscosity of mucus for the lubrication of food during swallowing and protecting the epithelium from bacterial invasion, as noted in other studies [2, 30]. Meanwhile, neutral mucins secreted from goblet cells might be involved in transporting food from the esophagus to the stomach, protecting the wall from mechanical damage [2, 9]. Furthermore, the striped tiger nandid fish's anterior esophagus had taste buds between the epithelial cells. The taste buds were round-shaped and comprised of columnar taste cells with basal nuclei and supporting cells (Figures 2C-2F). The discovery of taste buds indicated that striped tiger nandid fish could perceive taste and reject unswallowed food.

The thick muscular layer consisted of striated muscle (Figures 2A-2B). These results were similar to damsel fish *Stegastes fuscus* [31], Pantanal eartheater *Satanoperca pappaterra* [32], pike characin *O. hepsetus* [22], Asian seabass *L. calcarifer* [24], large yellow croaker *L. crocea* [9], and killifish *A. urophthalmus* [23]. The striated muscle might be useful for controlling the swallowing of food. Furthermore, Kalhoro *et al.* [9] stated that the striated muscle might help in luminal expansion or assist the fish in ejecting unswallowed food [33].

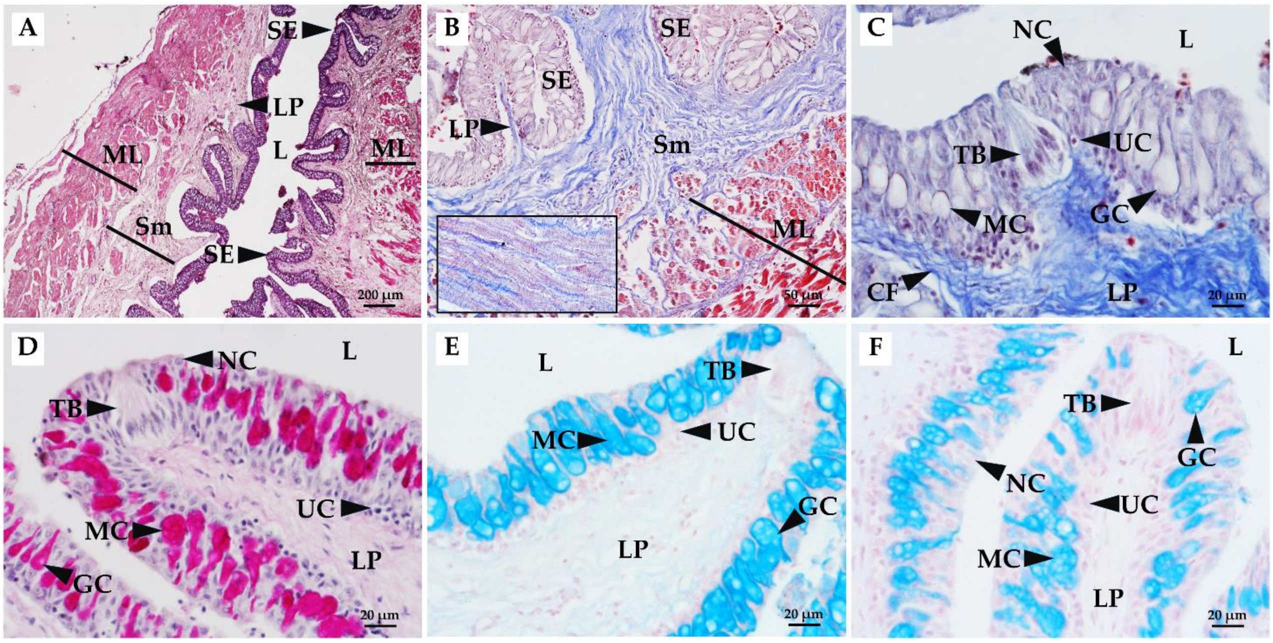

Figure 2. A-F: Photograph of the esophagus of *P. fasciata*. A: Photograph showing distinct layers, including stratified epithelium (SE), lamina propria (LP), submucosa (Sm), and the muscularis layer (ML). B: An enlarged picture of the muscularis and submucosa layers, depicting inner circular and outer longitudinal muscles and loose connective tissue in the submucosa. The box highlights the striated muscle of the esophagus. C: An enlarged view of the mucosa, consisting of epithelium and lamina propria. The epithelium comprises non-mucus cells (NC), mucus cells (MC), undifferentiated cells (UC), and goblet cells (GC). Taste buds (TB) were visible between the epithelial cells. Beneath the epithelium, positive staining with aniline blue of Masson's trichrome reveals collagen fibers (CF). D: Photograph illustrating mucus cells and goblet cells containing neutral mucins. E: Photograph illustrating mucus cells and goblet cells containing carboxylated acid mucins. F: Photograph illustrating mucus cells and goblet cells containing sulphated acid mucins. Lumen (L). A: H&E, B-C: MT, D: PAS-H, E: AB pH 2.5-NF, F: AB pH 1.0-NF.

3.2.2 Stomach

The stomach of striped tiger nandid fish had basic morphology similar to many teleosts [22]. In the present study, the stomach appeared to be a J-shape, similar to omnivorous fish [34], such as characin *Astyanax bimaculatus* [35]. However, it differed from the U-shaped stomach of armored catfish *Hypostomus pusarum* [36], gangetic mystus *Mystus cavasius* [19], whitemouth croaker *Micropogonias furnieri* [37], and large yellow croaker *L. crocea* [9], which was the characteristic of carnivorous fish. Other reports mentioned that the morphological differences in the stomach of teleosts could indicate the food, feeding habits, body shape, and environment [19]. The mucosal fold (Figure 3A) of the stomach of striped tiger nandid fish increased the surface area for digestion and food storage [2, 38]. Okuthe and Bongile [2] also suggested that the mucosal folds might delay food during transport through the stomach and facilitate the mixing with digestive enzymes.

The stomach was divided by histological characteristics into three parts: cardiac, fundic, and pyloric stomach. The epithelium of the three portions was simple columnar epithelium (Figures 3, 4, 5). These results were similar to other fish species [4, 8, 19, 22, 24]. Beneath the laminar propria, the muscularis mucosae, the smooth muscle band was found (Figures 3B, 4B-4D, 5A-5B). The muscularis mucosae aided in the elimination and generated the force for the compression of gastric glands. The submucosa was loose connective tissue of collagen fibers and blood vessels (Figures 3B, 4B, 5B). Surrounding the submucosa, two muscular layers were observed: inner circular and outer longitudinal layers. The muscular layer of the stomach of striped tiger nandid fish was similar to other fish species [19, 21, 22, 32, 35].

The stomach could be divided into three portions, with two portions having glands (cardiac and fundic stomach), also called the glandular stomach (Figures 3, 4), and another portion not having glands (pyloric stomach) or the non-glandular stomach (Figure 5). The first portion was the cardiac stomach, which connected to the esophagus. The mean mucosal fold height was 1,744.94±226.06 μm, and the mucosal fold width was 1,301.16±284.60 μm (Table 2). Beneath the epithelium, the lamina propria contained gastric glands that were simple tubular glands. The cardiac glands were surrounded by thin connective tissue. The cells lining the glands were simple cuboidal epithelium with a central nucleus (Figure 3). The gland cells secreted the content to the lumen through the gastric crypts (pits). The epithelium of the cardiac stomach showed positive staining with PAS (Figure 3D) and weak staining to AB pH 1.0 (Figure 3F). The cardiac glands showed positive staining with PAS (Figure 3D) but were negative to AB pH 2.5 (Figure 3E) and AB pH 1.0 (Figure 3F). The thickness of the cardiac glands was 408.24±72.89 μm and the cardiac stomach had a mean muscle tissue layer thickness of 918.25±49.81 μm (Table 2).

The fundic stomach had fundic glands in the lamina propria, which were simple tubular glands lined by simple cuboidal to low columnar epithelium (Figures 4A-4E). The fundic glands open to the lumen by secreting granules through gastric pits. The epithelial cells showed strong positive staining with PAS (Figure 4D) but showed weak staining to AB pH 2.5 (Figure 4E) and AB pH 1.0 (Figure 4F). The cells lining the fundic glands showed positive staining with PAS (Figure 4D) but were negative to AB pH 2.5 (Figure 4E) and AB pH 1.0 (Figure 4F). In contrast, the gastric pits showed weakly positive staining with PAS (Figure 4D) and AB pH 1.0 (Figure 4F). The thickness of the fundic glands was 159.36±12.12 μm, the mean mucosal thickness was 240.88±10.96 μm, and the mean muscle tissue layer thickness of the fundic stomach was 86.30±5.15 μm (Table 2).

The pyloric stomach had a simple columnar epithelium; the submucosa had rich blood vessels and loose connective tissue. The muscular layer comprises inner circular and outer longitudinal smooth muscle (Figures 5A-5D). The results of histochemistry revealed positive staining with PAS (Figure 5D) but showed weak staining to AB pH 2.5 (Figure 5E) and AB pH 1.0 (Figure 5F). However, any gland was invisible, increasing the width of the lumen. This led to the assumption that the pyloric region served as the site for food storage [24]. This configuration increased the lumen's diameter and helped extend digestion time [24]. The pyloric stomach had a mean mucosal thickness of 126.60±19.19 μm and a mean muscle tissue layer thickness of 170.08±13.95 μm (Table 2).

The cardiac and fundic glands were simple tubular glands, similar to tilapia fish *T. spilurus* [4], but different from European eel *Anguilla anguilla* [39], stripped weakfish *Cynoscion guatucupa* [30], and pike characin *O. hepsetus* [22]. Rotta [40] suggested that branched tubular glands were found in carnivorous fish. In this study, we found cardiac and fundic glands in the cardia and fundus, respectively, indicating that these portions played a role in gastric digestion, corresponding to other studies [2, 19]. Vieira-Lopes *et al.* [22] stated that the gastric glands consisted of oxynticopeptic cells, which played a role in hydrochloric acid (HCl) and pepsinogen secretion. These cells were similar to principal and parietal cells in mammals, respectively. Both cardiac and fundic glands found in this study were common features of carnivorous and omnivorous fish, correlating with protein digestion [26]. Similarly, based on the previous research, striped tiger nandid fish were omnivorous, sometimes consuming invertebrate animals. Therefore, the presence of gastric glands might be related to their feeding habits.

The simple columnar epithelium of the cardiac stomach showed weak staining to AB pH 1.0 (Figure 3F). In contrast, the fundic and pyloric stomach showed weak staining to AB pH 2.5 (Figures 4E, 5E, respectively) and AB pH 1.0 (Figures 4F, 5F, respectively). These findings demonstrated that the epithelium primarily secreted neutral mucins, protecting the epithelium from stomach enzymes and HCl [19, 24] and promoting food transport to the intestine [22]. Meanwhile, acid mucins might be a barrier against microorganisms [41]. The cardiac and fundic glands of striped tiger nandid fish showed a positive reaction only with PAS, similar to tilapia fish *T. spilurus* [4], Gangetic mystus *M. cavasius*, nile tilapia *Oreochromis niloticus* [19]. Meanwhile, the gastric pits in the cardiac and fundic stomachs reacted to AB pH 1.0, demonstrating that the gastric pit cells secreted sulphated mucopolysaccharides, as observed in banded tilapia *T. sparrmanii* [2].

Table 2. Mean and standard deviation of musosal fold height (MFH), musosal fold width (MFW) of the esophagus and stomach, cardiac gland thickness (CGT), muscular layer thickness (MLT), mucosal thickness (MuT) and fundic gland thickness (FGT) of the stomach (µm) (N=15).

	Esophagus		**Stomach**								
			Cardiac				**Fundic**			**Pyloric**	
	MFH	**MFW**	**MFH**	**MFW**	**CGT**	**MLT**	**MuT**	**FGT**	**MLT**	**MuT**	**MLT**
Mean ± standard deviation	313.84 ± 36.46	236.36 ± 51.56	1,744.94 ± 226.06	1,301.16 ± 284.60	408.24 ± 72.89	918.25 ± 49.81	240.88 ± 10.96	159.36 ± 12.12	86.30 ± 5.15	126.60 ± 19.19	170.08 ± 13.95

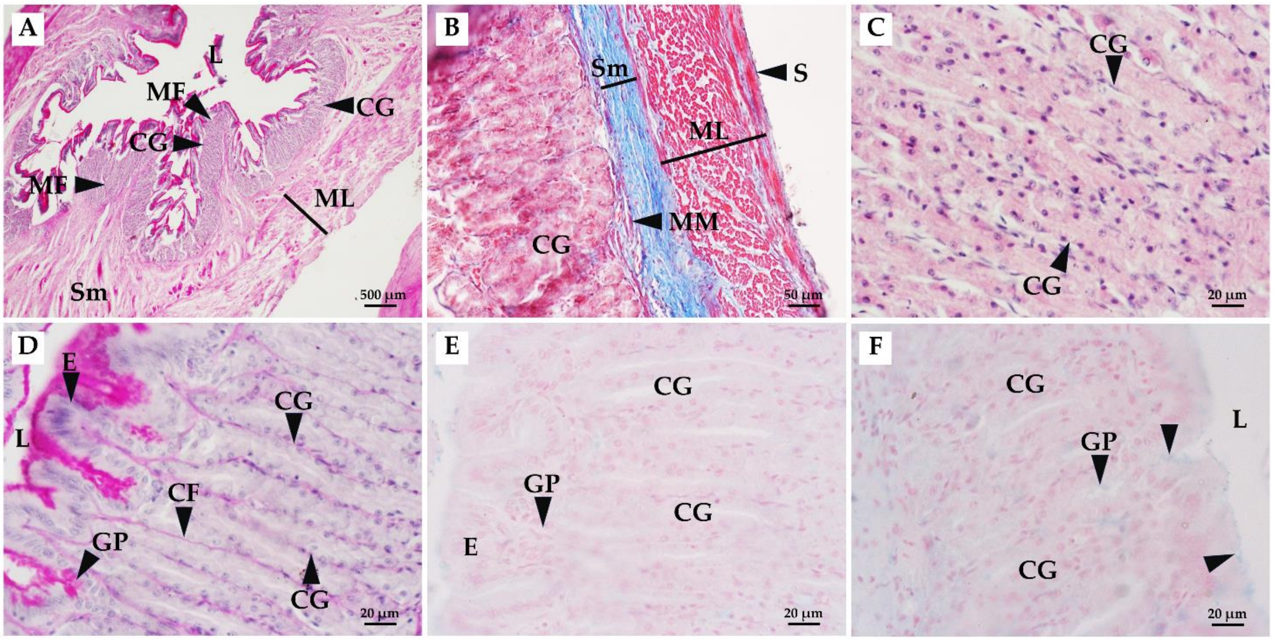

Figure 3. A-F: Photograph of the cardiac stomach of *P. fasciata.* A: Photograph showing distinct layers and mucosal folds (MF) consisting of cardiac glands (CG) in the lamina propria and muscularis layer (ML). B. A picture highlighting the muscularis mucosae (MM), submucosa (Sm), muscularis layer and serosa (S). C: An enlarged picture of cardiac glands, revealing a simple cuboidal-low columnar epithelium. The gland cells exhibit eosin-positive granules. D: An enlarged view of PAS-positive cuboidal-columnar cells and a PAS-positive gastric pit (GP). The cardiac gland displays weak PAS-positive cells. E: Photograph illustrating the negative staining with AB pH 2.5 of cardiac gland cells and gastric pit. F: Photograph illustrating AB pH 1.0-positive epithelial cells (arrowhead) and gastric pit. Collagen fiber (CF), epithelium (E), lumen (L). A, D: PAS-H , B: MT, C: H&E, E: AB pH 2.5-NF, F: AB pH 1.0-NF.

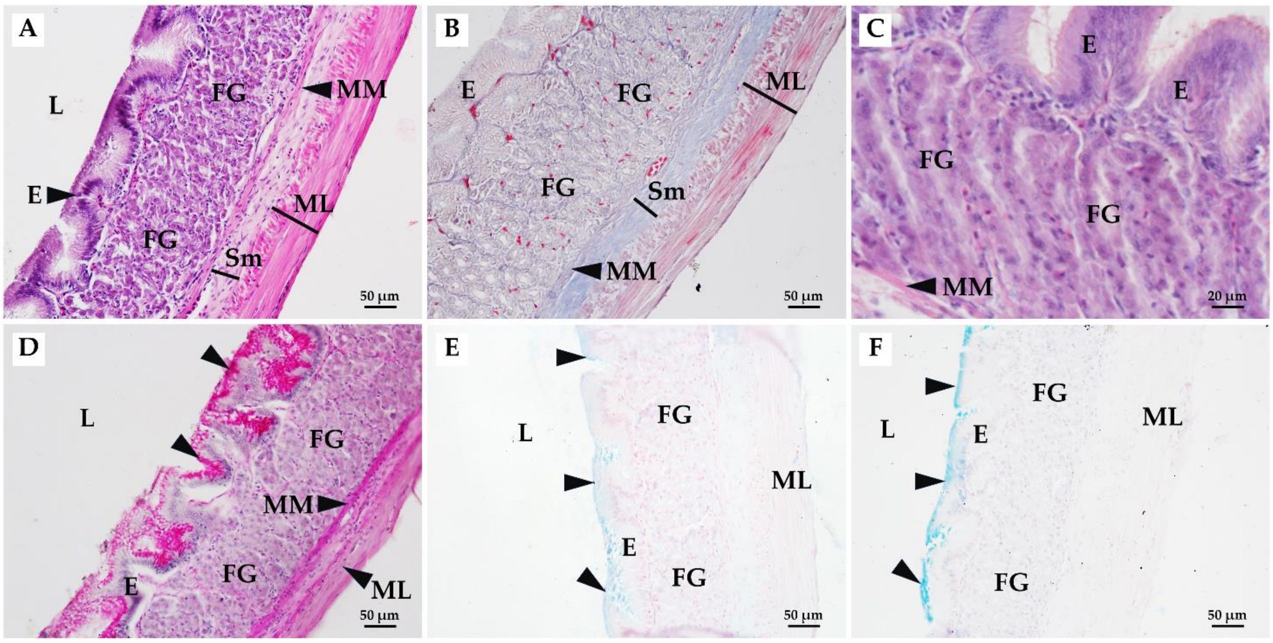

Figure 4. A-F: Photographs of the fundic stomach of *P. fasciata*. A-B: Photographs showing distinct layers of mucosa, consisting of epithelium (E), and fundic glands (FG), as well as the muscularis mucosae (MM). These pictures represent the two distinct muscularis layer (ML) layers, consisting of inner circular and outer longitudinal smooth muscle bundles. C: An enlarged picture of the mucosa showing simple columnar epithelium (E). The fundic gland cells exhibit eosin-positive granules and thin muscularis mucosae. D: Photograph showing PAS-positive columnar epithelial cells (arrowheads) and a PAS-positive gastric pit. The fundic glands show weak PAS-positive cells. E-F: Photographs illustrating the representation of AB pH 2.5 and AB pH 1.0 positive fundic epithelial cells, respectively (arrowheads). Lumen (L), Sm (submucosa). A, C: H&E, B: MT, D: PAS-H, E: AB pH 2.5-NF, F: AB pH 1.0-NF.

3.2.3 Intestine

The IC of striped tiger nandid fish was 0.62±0.01 (Table 1), indicating an omnivorous fish. The intestine could be divided into three portions (Figure 6): anterior, middle, and posterior intestines. The intestine wall had four layers, similar to other digestive tract regions. The epithelium was lined by a simple columnar epithelium consisting of absorptive cells (enterocytes) and goblet cells (Figure 6). The enterocyte had a brush border at the apical domain. The nucleus of the goblet cell was found at the basal portion of the cell, while the mucus was found in the cytoplasm (Figure 6). In some sections, exocytosis released content from the goblet cell's apical domain. This was similar to other teleosts [2, 9, 22, 23, 24, 32, 35]. The enterocytes showed positive staining with PAS (Figures 6B, 6F, 6J), similar to Asian seabass *L. calcarifer* [24]. The submucosal layer comprises loose connective tissue with collagen fibers and blood vessels. All three parts of the intestine had no glands (Figures 6A, 6E, 6I), the similarity observed in Asian seabass *L. calcarifer* [24], large yellow croaker *L. crocea* [9], and killifish *A. urophthalmus* [23]. The muscularis layer consisted of the inner circular layer and the outer longitudinal layer. The outermost layer was the mesothelium and loose connective tissue (Figures 6A, 6E, 6I).

The mucosal fold of the intestine, also known as the villi, consists of the epithelium and the lamina propria. Differences between each portion were defined by mucosal fold height, width, and muscular thickness. The anterior intestine had a mean fold height of 1,046.15±75.08 µm, a mean fold width of 157.28±16.34 µm, and a mean muscular layer thickness of 96.22±18.11 µm. The mid-intestine had a mean mucosal fold height of 814.22±95.15 µm, a mean fold width of 95.42±15.42 µm, and a mean muscular layer thickness of 17.82±3.33 µm. The posterior intestine had a mean fold height of 753.11±64.44 µm, a mean fold width of 74.16±6.13 µm, and a mean muscular layer thickness of 99.93±5.56 µm (Table 3). The results showed that the anterior intestine's mucosal fold/villi were the tallest than the middle and posterior intestine. This finding was similar to pike characin *O. hepsetus* [22], pebbly fish *A. baremoze* [8], and killifish *A. urophthalmus* [23], leading to the suggestion that the anterior and middle intestine of striped tiger nandid fish were the main regions for digestion and absorption [23, 35]. The mucosal folds/villi reduced food speed as it flowed through the intestine for absorption. These folds could promote an increase in absorptive efficiency due to the presence of numerous enterocytes or absorptive cells [2].

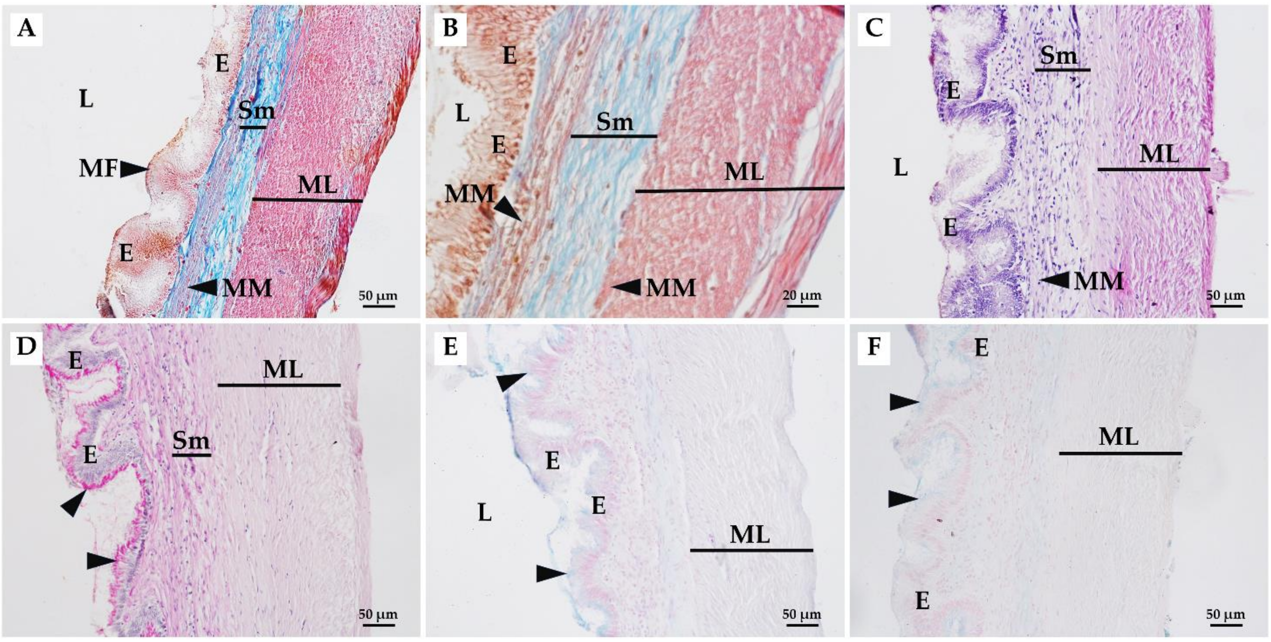

Figure 5. A-F: Photograph of the pyloric stomach of *P. fasciata*. A-C: Photograph showing distinct mucosa layers consisting of simple columnar epithelium (E), lamina propria, and muscularis mucosae (MM). Pictures A and B represent the distinct muscularis layer layers (ML). D: Photograph showing PAS-positive columnar epithelial cells (arrowheads). E-F: Photograph illustrating the representation of AB pH 2.5 and AB pH 1.0 positive epithelial cells, respectively (arrowheads). Lumen (L), mucosal fold (MF), submucosa (Sm). A-B: MT, C: H&E, D: PAS-H, E: AB pH 2.5-NF, F: AB pH 1.0-NF.

Additionally, the goblet cells were numerous in the posterior intestine of striped tiger nandid fish, similar to flower fish *Pseudophoxinus antalyae* [1], characin *A. bimaculatus* [35], Asian seabass *L. calcarifer* [24], pebbly fish *A. baremoze* [8] and large yellow croaker *L. crocea* [9]. Machado *et al.* [26] suggested mucous from goblet cells helped defend the intestine lining and support waste or feces inclusion. The goblet cells in each portion revealed intense labeling with both PAS (Figures 6B, 6F, 6J) and AB pH 2.5 (Figures 6C, 6G, 6K) but weak reaction to AB pH 1.0 (Figures 6D, 6H, 6L). This finding was also found in other species, such as flower fish *P. antalyae* [1], common dentex *Dentex dentex* [42], characin *A. bimaculatus* [35], and Asian seabass *L. calcarifer* [24]. These results indicated they secreted mainly neutral and carboxylated acid glycoproteins/mucopolysaccharides. The neutral mucous from goblet cells might function in protecting the epithelium from gastric juices from the stomach, providing co-factors useful to nutrient enzymatic breakdown [43], emulsification of nutrients [44], absorption [45], and protection of the intestinal epithelium from HCl [40]. In addition, Carrassón *et al.* [42] stated that neutral mucous had a lubrication function for transporting nutrients. Meanwhile, carboxylated acid mucins shielded the luminal surface from glucosidase deprivation [42]. This work also found sulphated acid mucins secreted from goblet cells. These mucins might help prevent microorganism invasion or infection, similar to large yellow croaker *L. crocea* [9], and trapping particles.

However, the co-secretion of neutral and acidic mucins probably represented the sequential steps of mucous synthesis [24].

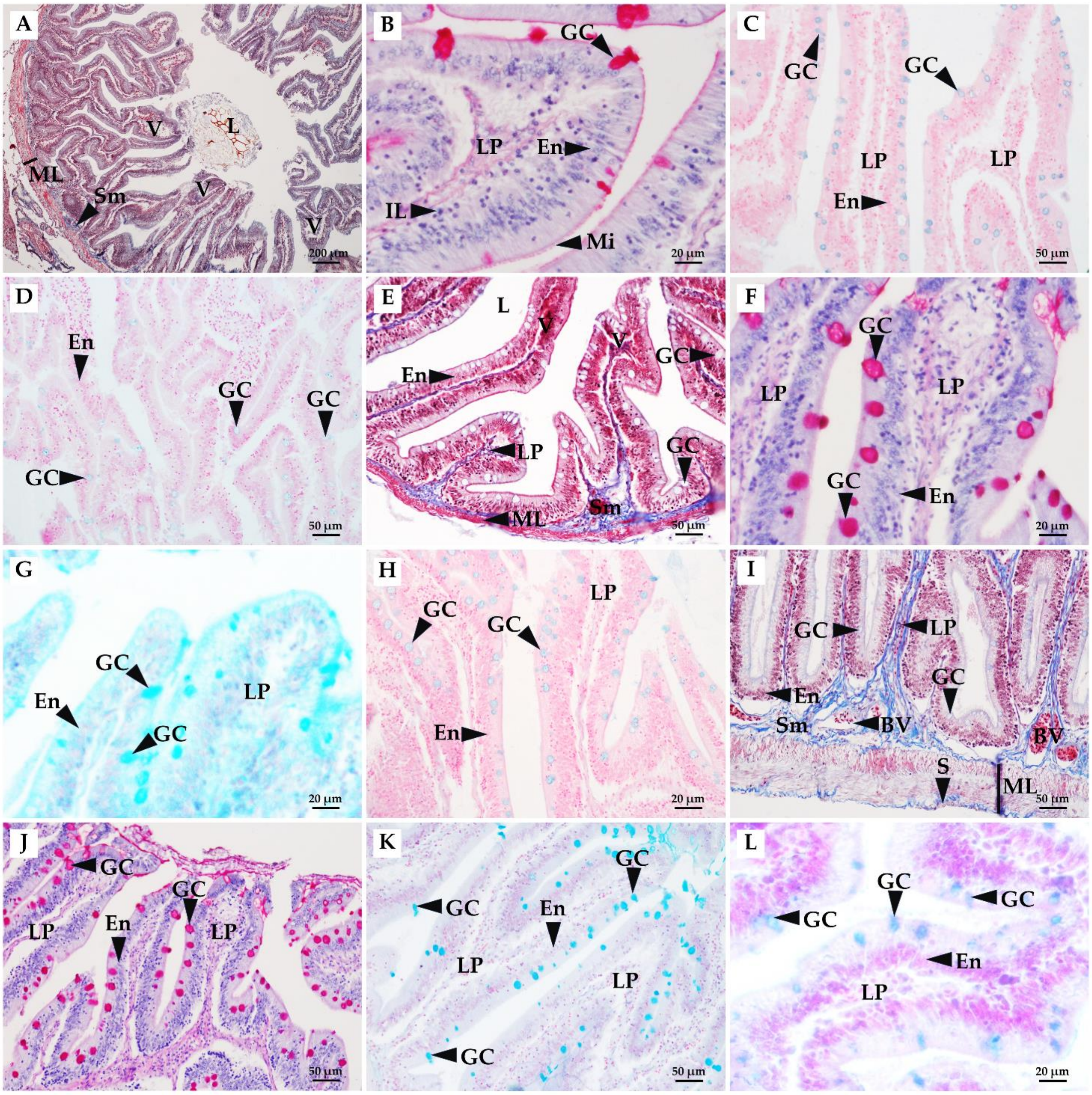

Figure 6. A-D: Photograph of the anterior intestine of *P. fasciata*. E-H: Photograph of the mid-intestine. I-L: Photograph of the posterior intestine. Pictures A, E, and I show distinct layers of mucosa, consisting of simple columnar epithelium with enterocytes (En) and goblet cells (GC), lamina propria (LP), and also the submucosa (Sm) with blood vessels (BV). Underneath the submucosa, circular and longitudinal smooth muscles were observed. Pictures B, C, and D show villi (V) of the anterior intestine, with PAS-positive, AB pH 2.5-positive, and AB pH 1.0-positive goblet cells, respectively. Pictures F, G, and H depict the presence of PAS-positive, AB pH 2.5-positive, and AB pH 1.0-positive goblet cells, respectively. Pictures J, K, L: Photograph illustrating the representation of PAS-positive, AB pH 2.5-positive, and AB pH 1.0-positive goblet cells, respectively. Intraepithelial leukocytes (IL), lumen (L), microvilli (Mi), muscularis layer (ML), and serosa (S). A, E, I: MT, B, F, J: PAS-H, C, G, K: AB pH 2.5-NF, D, H, L: AB pH 1.0-NF.

Table 3. Mean and standard deviation of musosal fold height (MFH), musosal fold width (MFW) and muscular layer thickness (MLT) of the intestines (μm) (N=15).

	Anterior intestine			**Mid-intestine**			**Posterior intestine**		
	MFH	**MFW**	**MLT**	**MFH**	**MFW**	**MLT**	**MFH**	**MFW**	**MLT**
Mean ± standard deviation	1,046.15 ± 75.08	157.28 ± 16.34	96.22 ± 18.11	814.22 ± 95.15	95.42 ± 15.42	17.82 ± 3.33	753.11 ± 64.44	74.16 ± 6.13	99.93 ± 5.56

4. Conclusions

This research represented the first description and report on the histology and histochemistry of the gastrointestinal tract of the striped tiger nandid fish. The histological characteristics of their gastrointestinal tract were consistent with those of fish consuming both plants and animals (omnivore). The short esophagus was the muscular tube connecting to the stomach, the sac containing fundic and cardiac glands. In the pylorus of the stomach, no glandular structures were found. Similarly, glandular structures were not found in any of the three parts of the intestine; however, the enterocyte and goblet cells were present. In the future, this research may be used to develop food and farm management strategies, as the morphology of the gastrointestinal tract is closely related to feeding habits. Furthermore, it can aid in distinguishing abnormal tissue from normal tissue.

5. Acknowledgements

This work was financially supported by Thaksin University Research Fund and the Department of Biology, Faculty of Science and Digital Innovation, Thaksin University, for the opportunity to use the laboratory to do this research.

Author Contributions: Conceptualization, A.P.; methodology, A.P and A.V.; formal analysis, A.P.; investigation, A.P. and A.V.; resources, A.P.; writing—original draft preparation, A.P. and A.V.; writing—review and editing, A.P.; supervision, A.P.; funding acquisition, A.P. and A.V. All authors have read and agreed to the published version of the manuscript.

Funding: This work was supported by the Thaksin University Research Fund, grant number TSU66-NR010.

Conflicts of Interest: The authors declare no conflict of interest.

References

[1] Cinar, K.; Nurgül, S. Histological and histochemical characterization of the mucosa of the digestive tract in flower fish (*Pseudophoxinus antalyae*). *Anat. Histol. Embryol.* **2006**, *35*, 147–151.

[2] Okuthe, G.E.; Bongile, B. Morphology, histology and histochemistry of the digestive tract of the banded tilapia, *Tilapia sparrmanii* (Perciformes: Cichlidae). *Zoologia* **2020**, *37*, 1-14.

[3] Wainwright, P.C.; Richard, B.A. Predicting patterns of prey use from morphology of fishes. *Environ. Biol. Fishes*. **1995**, *44*, 97-113.

[4] Al-Abdulhadi, H.A. Some comparative histological studies on alimentary tract of tilapia fish (*Tilapia spilurus*) and sea bream (*Mylio cuvieri*). *Egypt. J. Aquat. Res.* **2005**, *31*, 387-39.

[5] Hernández, D.R.; Pérez Gianeselli, M.; Domitrovic, H.A. Morphology, histology and histochemistry of the digestive system of south American catfish (*Rhamdia quelen*). *Int. J. Morphol.* **2009**, *27*, 105-111.

[6] Senarat, S.; Jes, K.; Wannee, J.; Niwat, K. Structural classifications in the digestive tract of short mackerel, *Rastrelliger brachysoma* (Bleeker, 1851) from upper gulf of Thailand. *Songklanakarin J. Sci. Technol.* **2015**, *37*, 561-567.

[7] Borman, M.; Ismot, A.; Mohammad, K.; Md Rafiqun, N. Histo-morphology of the alimentary canal in two freshwater snakehead fish *Channa punctata* and *Channa striata*. *J. Fish.* **2015**, *3*, 297-300.

[8] Kasozi, N.; Gerald, I.D.; Julius, M.; Charles, D.K.; Majid, K.; Akisoferi, O.W.; Godfrey, K.; Victoria, T.N. Histomorphological description of the digestive system of pebbly fish, *Alestes baremoze* (Joannis, 1835). *Sci. World J.* **2017**, https://doi.org/10.1155/2017/8591249.

[9] Kalhoro, H.; Shengli, T.; Lei, W.; Ying, H.; Josie, A.V.; Qingjun, S. Morphological study of the gastrointestinal tract of *Larimichthys crocea* (Acanthopterygii: Perciformes). *Zoologia* **2018**, *35,* 1-9.

[10] Alabssawy, A.N.; Hassan, M.M.K.; Ahmed, A.G. Anatomical and histological adaptations of digestive tract in relation to food and feeding habits of lizardfish, *Synodus variegatus* (Lacepède, 1803). *Egypt. J. Aquat. Res.* **2019**, *45*, 159–165.

[11] Santos, M.L.D.; Fábio, P.A.; Tiago, C.P.; José, E.S. Morphological, histological and histochemical analysis of the digestive tract of *Trachelyopterus striatulus* (Siluriformes: Auchenipteridae). *Zoologia* **2015**, *32*, 296–305.

[12] Smith, L.S. *Introduction to Fish Physiology*, Argent Laboratories Press: Washington, DC., The United States of America, **1991**.

[13] Qu, M.; Shaoxiong, D.; Xiaojing, X.; Minghui, S.; Yingzhe, Y.; Yongquan, S. Ontogenetic development of the digestive system and growth in coral trout (*Plectropomus leopardus*). *Aquaculture* **2012**, *334*, 132–141.

[14] Angelescu, V.; Franscisco, S.G. Adaptaciones del aparato digestivo al régimen alimenticio en algunos peces del Río Uruguay y Río de La Plata. *Rev. Inst. Nac. Invest. Nat.* **1949**, *1*, 161-281.

[15] Rainboth, W.J. *Fishes of the Cambodian Mekong. FAO Species Identification Field Guide for Fishery Purposes*, FAO: Rome, Italy, **1996.**

[16] Sangpradub, N.; Chutima, H. Diet composition of *Pristolepis fasciata* (Bleeker, 1851) (Family Nandidae) and *Puntius brevis* (Bleeker, 1849) (Family Cyprinidae) in Kaeng Lawa, Thailand. *Chiang Mai J. Sci.* **2017**, *44*, 839-846.

[17] Uk-katawewat, S. *Illustration of Thai Fish and Aquatic animals*, Kdurusapa Ladprao Printing Press: Bangkok, Thailand, **2002**.

[18] Bancroft, J.D.; Marilyn, G. *Theory and practice of histological techniques*, Churchill Livingstone: London, U.K., **2002**.

[19] Ghosh, S.K.; Padmanabha, C. Histological and histochemical characterization on stomach of *Mystus cavasius* (Hamilton), *Oreochromis niloticus* (Linnaeus) and *Gudusia chapra* (Hamilton): comparative study. *The Journal of Basic and Applied Zoology* **2015**, *70*, 16–24.

[20] Smith, B.J.; Smith, S.A.; Bundit, T.; Terry, A.L. Gross morphology and topography of the adult intestinal tract of the tilapian fish, *Oreochromis niloticus* L. *Cells Tissues Organs* **2000**, *166*, 294–303.

[21] Santos, M.D.; Lima, C.L.P.; Sandra, R.; Carvalho, B.S.M. Metazoan parasite fauna of *Pimelodus maculatus* La Cépède, 1803 (Siluriformes, Pimelodidae) from the Guandu river, Rio de Janeiro Rio State, Brazil. *Acta Sci. Biol. Sci.* **2007**, *29*, 101-107.

[22] Vieira-Lopes, D.A.; Nadja, L.P.; Armando, S.; Adriana, V.; Francisco, G.A.; Iracema, D.G.; Aparecida, A.N. Immunohistochemical study of the digestive tract of *Oligosarcus hepsetus*. *World J. Gastroenterol.* **2013**, *19*, 1919-1929.

[23] Nascimento, W.S.; Glaucia, M.M.S.; Lenilda, T.T.; Naisandra, B.S.; Sathyabama, C. Histology of the digestive tract of *Anablepsoides urophthalmus* from Brazilian oriental Amazonia. *Journal of Aquaculture and Marine Biology* **2018**, *7*, 39-42.

[24] Purushothaman, K.; Doreen, L.; Jolly, M.S.; Syed, M.S.; Declan, P.L.; Shubha, V.; László, O. Morpho-histological characterisation of the alimentary canal of an important food fish, Asian seabass (*Lates calcarifer*). *PeerJ.* **2016**, DOI 10.7717/peerj.2377.

[25] Dias, A.C.M.I.; Castelo, B.C.W.; Lopes, V.G. Estudo da dieta natural de peixes no reservatório de Ribeirão das Lajes, Rio de Janeiro, Brasil. *Acta Sci. Biol. Sci.* **2005**, *7*, 355–364.

[26] Machado, M.R.F.; Helena, O.S.; Valderes, L.S.; Alexandre, A.; Roberto, G.; André, D.B. Morphological and anatomical characterization of the digestive tract of *Centropomus parallelus* and *C. undecimalis*. *Acta Sci. Biol. Sci.* **2013**, *35*, 467–474.

[27] Reifel, C.W.; Anthony, A.T. Structure and carbohydrate histochemistry of the stomach in eight species of teleosts. *J. Morphol* **1978**, *158*, 155–67.

[28] Pedini, V.; Cecilia, D.; Parillo, F.; Paola, S. A lectin histochemical study of the oesophagus of Shi Drum. *J. Fish. Biol.* **2004**, *64*, 625–631.

[29] Sibbing, F.A.; Uribe, R. Regional specialisation in the oro-pharyngeal wall and food processing in carp (*Cyprinus carpio* L.). *Neth. J. Zool.* **1985**, *35*, 377–422.

[30] Díaz, A.O.; Alocia, M.C.; Adriana, L.G. Glycoconjugates in the mucosa of the digestive tract of *Cynoscion guatucupa*: a histochemical study. *Acta Histochem*. **2008**, *110*, 76–85.

[31] Canan, B.; Wallace, S.N.; Naisandra, B.S.; Sathyabama, C. Morphohistology of the digestive tract of the damsel fish *Stegastes fuscus* (Osteichthyes: Pomacentridae). *The Scientific World Journal* **2012**, doi:10.1100/2012/787316.

[32] Rodrigues da Silva, M.; Maria, R.M.N.; Norma, S.H. Histology of the digestive tract of *Satanoperca pappaterra* (Osteichthyes, Cichlidae). *Acta Sci. Biol.* **2012**, *34*, 319-326.

[33] Cao, X.J.; Wang, W.M. Histology and mucin histochemistry of the digestive tract of yellow catfish, *Pelteobagrus fulvidraco*. *Anat Histol Embryol*. **2009**, *38*, 254-261.

[34] Eckert, R.; Randall, D.; Augustine, G. *Animal Physiology; Mechanisms and Adaptations,* WH Freeman and Company: New York, The United States, **1988**.

[35] Cardoso, N.N.; Enely, M.S.F.; Iracema, D.G.; Aparecida, A.N.; Armando, S.; Francisco, G.A. Histochemical and immunohistochemical study on endocrine cells (5HT, GAS, and SST) of the gastrointestinal tract of a teleost, the characin *Astyanax bimaculatus*. *Acta Histochem*. **2015**, *117*, 595-604.

[36] Pessoa, E.K.R.; Naisandra, B.S.; Naithirithi, T.C.; Arrilton, A.S.; Sathyabama, C. Morfologia comparativa do trato digestorio dos peixes *Hoplias malabaricus* e *Hypostomus pusarum* do acude Marechal Dutra, Rio Grande do Norte, Brasil. *Biota Amazôn.* **2013**, *3*, 48–57.

[37] Andrade, I.M.; Juliana, P.G.; Matheus, M.R.; Renata, B.M. Morphology of the digestive tract of the whitemouth croaker *Micropogonias furnieri* (Desmarest, 1823) (Perciformes: Sciaenidae). *Acta Zool.* **2016**, doi: 10.1111/azo.12156.

[38] Legler, J.M. Morphology and physiology of the Chelonia. *Australian Biological Recourses Study, Caberra* **1993**, 108–119.

[39] Domeneghini, C.; Silvana, A.; Giuseppe, R.; Giampaolo, B.; Veggetti A. Histochemical analysis of glycoconjugate secretion in the alimentary canal of *Anguilla anguilla* L. *Acta Histochem*. 2**005**, *106*, 477-87.

[40] Rotta, M.A. *Aspectos gerais da fisiologia e estrutura do sistema digestivo dos peixes relacionados à piscicultura*, Corumbá Embrapa: Brazil, **2003**.

[41] Ringø, E.; Reidar, M.; Terry, M.M.; Rolf, E.O. Bacterial translocation and pathogenesis in the digestive tract of larvae and fry. *Aquaculture* **2007**, *268*, 251–264.

[42] Carrassón, M.; Grau, A.; Dopazo, L.R.; Selena, C. A histological, histochemical and ultrastructural study of the digestive tract of *Dentex dentex* (Pisces, Sparidae). *Histol. Histopathol*. **2006**, *21*, 579-593.

[43] Anderson, T.A. Histological and cytological structure of the gastrointestinal tract of the luderick, *Girella tricuspidata* (Pisces, Kyphosidae), in relation to diet. *J. Morphol.* **1986**, *190*, 109–119.

[44] Clarke, A.J.; Witcomb, D.M. A study of the histology and morphology of the digestive tract of the common eel (*Anguilla anguilla*). *J. Fish. Biol.* **1980**, *16*, 159-170.

[45] Gartner, L.P.; Hiatt, J.L.; De Souza, L.F.; Sales, Md.G.F. *Atlas colorido de histologia*, Guanabara Koogan LTDA: Rio de Janeiro, Brazil, **2002**.

ASEAN
Journal of Scientific and Technological Reports
Online ISSN:2773-8752

Research article

Pharmacognostic Investigation, Optimization of Extraction Condition, and Determination of Piperine in Black Pepper Fruit

Lukman Sueree[1]*, Chaowalit Monton[2], Aurawan Boonyataeng[3] and Auttapong Pinthongpan[4]

[1] Faculty of Science and Technology, Hatyai University, Songkhla, 90110, Thailand
[2] Drug and Herbal Product Research and Development Center, College of Pharmacy, Rangsit University, Pathum Thani, 12000, Thailand
[2] Medicinal Cannabis Research Institute College of Pharmacy, Rangsit University, Pathum Thani, 12000, Thailand
[2] Department of Pharmacognosy, College of Pharmacy, Rangsit University, Pathum Thani, 12000, Thailand
[3] Faculty of Science and Technology, Hatyai University, Songkhla, 90110, Thailand
[4] Faculty of Science and Technology, Hatyai University, Songkhla, 90110, Thailand
* Correspondence: lukman.su@hu.ac.th

Citation:
Sueree, L.; Monton, C.; Boonyataeng, A.; Pinthongpan, A. Pharmacognstic investigation, optimization of extraction condition, and determination of piperine in black pepper fruit. *ASEAN J. Sci. Tech. Report.* **2024**, *27*(4), e253186. https://doi.org/10.55164/ajstr.v27i3.253186

Article history:
Received: March 13, 2024
Revised: May 21, 2024
Accepted: June 4 ,2024
Available online: June 30, 2024

Publisher's Note:
This article is published and distributed under the terms of the Thaksin University.

Abstract: This study investigated the standardization parameters of black pepper fruit (*Piper nigrum* Linn.) through qualitative analyses. Microscopic characteristics of the crude drug were examined. Various parameters were determined, including loss on drying (7.46 ± 0.16 %w/w), total ash (4.29 ± 0.12 %w/w), acid-insoluble ash (0.15 ± 0.03 %w/w), water-soluble extractives (8.35 ± 0.45 %w/w), ethanol-soluble extractives (4.30 ± 0.18 %w/w), and volatile oil content (1.60 ± 0.00 %w/w). Piperine content in the ethanol extract was evaluated using Thin Layer Chromatography (TLC) fingerprint analysis and validated High-Performance Liquid Chromatography (HPLC) analysis. The calibration curve for piperine showed good linearity ($R^2 = 0.9991$) in the range of 10-100 µg/ml. The limits of detection and quantification were 0.01 µg/ml and 0.04 µg/ml, respectively. Intra-day and inter-day precision were 0.01-0.12% RSD and 0.52-0.90% RSD, respectively. Recovery ranged from 95.85% to 101.85%. Optimal extraction conditions determined through experimental design were 70°C for 60 minutes, yielding a piperine content of 38.98 ± 0.05%. The study provides quantitative pharmacognostic specifications for the fundamental standardization of black pepper fruit.

Keywords: Pharmacognostic investigation; optimization; black pepper fruit

1. Introduction

Piper nigrum Linn., commonly known as black pepper (Piperaceae), is utilized as a spice in many countries worldwide, primarily due to the presence of piperine (Figure 1), which enhances its value as a food additive. The spicy heat of black pepper predominantly arises from piperine obtained from both the outer fruit and the seed. Traditionally, black pepper has been employed as an herbal remedy for alleviating various ailments such as pain, muscular aches, chills, rheumatism, influenza, and fever. Additionally, black pepper tea has been administered to relieve headaches, migraines, strep throat, and digestive issues [1]. It has also been used to address conditions like asthma, chronic indigestion, colon toxins, obesity, sinus congestion, fever, intermittent fever, cold extremities, colic, gastric ailments, and diarrhea. Moreover, black pepper exhibits potent antioxidant activity, aiding in relieving oxidative stress induced by a high-fat diet and acetaminophen-triggered liver damage in mice [2].

The major constituent of black pepper, piperine, possesses various pharmacological properties, including central nervous system depression, antipyretic, analgesic, antioxidant, and hepatoprotective effects. Piperine has also demonstrated anti-inflammatory properties by reducing inflammation in animal models [3]. In humans, piperine enhances the bioavailability of antitubercular drugs when administered together [4].

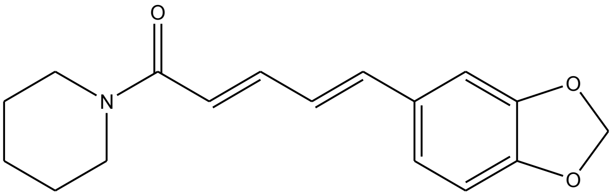

Figure 1. Structure of piperine

The concentration of piperine varies among different types of pepper. Its content in *P. nigrum* L. fruit and root ranges from 3,000 to 6,650 mg/100 g and 790 mg/100 g, respectively [5-9]. Black pepper typically contains between 4.6 and 9.7% piperine by mass [10]. Lee *et al.* (2021) determined the concentration of piperine in black pepper using high-performance liquid chromatography–ultraviolet detection, validating their findings through performance parameter measurements [11]. They observed that the concentration of piperine in black pepper was 4,418 mg/100 g. Bhardwaj *et al.* (2002) investigated the functional properties of piperine through human liver microsomal studies, revealing its inhibition of human P-glycoprotein [12].

Considering the beneficial properties of piperine, particularly its utility in drugs and preservatives, there is a need for its standardization and quality evaluation using a short, fast, reliable, and economical tool. Therefore, this study aimed to investigate the standardization parameters through qualitative analyses of black pepper fruit.

2. Materials and Methods

The pharmacognostic parameters were examined using standard methods outlined in the World Health Organization (WHO) guidelines, "Quality Control Methods for Medicinal Plant Materials."

2.1 Microscopic Characterization

The microscopic characteristics of the black pepper fruit were examined in cross-section. The tissue section was mounted onto a glass slide in water for microscopic observation.

2.2 Loss on Drying

Determination of Loss on Drying: The ground sample was weighed in a pre-weighed small beaker and dried with heat at 105 °C until a constant weight was achieved.

2.3 Determination of Total Ash

The ground sample of black pepper fruit powder was weighed in a pre-weighed crucible and incinerated for 5 hours at 500 °C until it turned white. The crucible was cooled at room temperature in a desiccator, and the total ash content was calculated as a percentage.

2.4 Determination of Acid Insoluble Ash

The crucible containing the total ash was treated with 25 mL of 10% hydrochloric acid, covered with a watch glass, and boiled gently for 5 minutes. The insoluble matter was filtered through ashless filter paper No. 40, dried on a hot plate, and then incinerated for 5 hours at 500 °C. The crucible was cooled at room temperature in a desiccator, and the acid-insoluble ash content was calculated as a percentage.

2.5 Determination of Volatile Oil Content

The ground sample was subjected to volatile oil distillation in a Clevenger apparatus for approximately 4-6 hours.

2.6 Determination of Water and Ethanol Soluble Extractive Value

The ground sample of dried black pepper fruit was macerated with either 100 mL of water or 95% ethanol in a closed conical flask for 6 hours, followed by standing for 18 hours. The extract was filtered rapidly, and 20 mL of the filtrate was evaporated to dryness in a water bath, then dried at 105 °C until a constant weight was achieved. The extractive value was calculated as a percentage.

2.7 Thin Layer Chromatographic Fingerprint

One gram of black pepper fruit dried powder was macerated in 20 mL of 95% ethanol, shaken for 6 hours, and left to stand for 18 hours at room temperature. The extract was then evaporated to dryness and dissolved in 1 mL of 95% ethanol. The resulting solution was applied to a TLC silica gel 60 GF254 plate, developed in a saturated TLC chamber with hexane: ethyl acetate (1:1), and observed under short wavelength (254 nm) and long wavelength (366 nm) ultraviolet light. The plate was then sprayed with anisaldehyde, developing a reagent.

2.8 Experimental Design and Plant Extraction

Extraction conditions, including temperature (X_1) and time (X_2), were designed based on a spherical composite design. X1 and X2 were varied from 45-95 °C and 10-60 minutes, respectively. The ground sample (10 g) of black pepper fruit powder was mixed with 50 mL of 95% ethanol in a closed Erlenmeyer flask. The flask was then placed in a water bath shaker and extracted under specific conditions. The mixture was filtered using Whatman No. 1 filter paper, and the residue was extracted twice before evaporating to dryness.

Table 1. Two-factor spherical composite experimental design.

Condition No.	Temperature (X_1)		Time (X_2)	
	Coded	Actual (°C)	Coded	Actual (min)
P1	-1	52.3	-1	17.3
P2	1	87.7	-1	17.3
P3	-1	52.3	1	52.7
P4	1	87.7	1	52.7
P5	$-\sqrt{2}$	45.0	0	35.0
P6	$\sqrt{2}$	95.0	0	35.0
P7	0	70.0	$-\sqrt{2}$	10.0
P8	0	70.0	$\sqrt{2}$	60.0
P9	0	70.0	0	35.0
P10	0	70.0	0	35.0

2.9 Chromatographic Conditions

The study utilized an HPLC instrument (Agilent 1260 Infinity) with a photodiode array detector coupled to a UV detector set at 342 nm. A ZORBAX Eclipse Plus C18 (4.6 x 5.5 mm, 3.5 µm) column was eluted using a mixture of methanol and water (70:30) as the mobile phase. The injection volume, flow rate, and column temperature were set at 10 µL, 1 mL/min, and 25 °C, respectively.

2.10 Preparation of Standard Piperine

A stock solution of piperine was dissolved in ultrapure water at a concentration of 1 mg/mL. From this solution, a series ranging from 10-100 µg/mL was prepared to construct a calibration curve.

2.11 Method Validation

Method validation was performed following the ICH Harmonised Tripartite Guideline 6, covering five topics: linearity and range, specificity, limit of detection (LOD) and limit of quantitation (LOQ), precision, and accuracy.

2.11.1 Linearity and Range

The standard solution was prepared at five concentrations (10, 25, 50, 75, and 100 µg/mL) and injected for analysis. The linearity was assessed by the coefficient of determination (R^2), and the relationship between peak areas and standard piperine concentrations was determined.

2.11.2 Specificity

Specificity was evaluated by scanning UV absorption spectra in the range of 190-400 nm. Similar UV spectra obtained across the interest peak's up-slope, apex, and down-slope indicated specificity.

2.11.3 Limit of Detection (LOD) and Limit of Quantitation (LOQ)

LOD represents the lowest concentration detectable but not necessarily quantifiable, while LOQ represents the lowest concentration detectable and measurable. Formulas were utilized based on the standard deviation of y-intercepts and the slope of the calibration curve.

$LOD = (3.3 \times \sigma)/S$, $LOQ = (10 \times \sigma)/S$

2.11.4 Precision

Precision was assessed at three standard solution levels (25, 50, and 75 μg/mL) by determining intra-day and inter-day precision. Percent relative standard deviation (% RSD) was calculated to quantify precision.

$\% RSD = SD \times 100/mean$

2.11.5 Accuracy

Accuracy was evaluated using the spike method, where different standard levels (low, medium, and high) were spiked into the sample. Recovery percentages were calculated based on adding standard piperine to the known amount of black pepper fruit extract.

3. Results and Discussion

The anatomical structure in the transverse section of the *Piper nigrum* Linn fruit reveals several key features. Anatomical characteristics include: a) Epidermis: Comprising an outer layer of polygonal cells with a distinct cuticle containing dark brown to blackish contents. b) Parenchyma: Consisting of two layers of thin-walled cells interspersed with considerably thickened isodiametric to radically elongated stone cells. c) Stone cells are considerably thickened and vary in shape from isodiametric to radially elongated. d) Oil cells: Larger oil cells with suberized walls are in a layer beneath the parenchyma cells. e) Starch grains: Certain starch grains are scattered among the parenchyma cells. f) Pericarp: The mesocarp, a comparatively broad zone, comprises most of the pericarp. The outer layers of cells are parenchymatous, and larger secretion sacs with suberized walls and oil contents may be observed. g) Perisperm: The inner zone of perisperm cells is radial and contains largely oleoresin starch and protein substances. The morphological characteristics observed in this study are similar to those reported in a previous study conducted in India. The epicarp has polygonal cells with a cuticle and dark contents, followed by 2-3 layers of parenchyma and thickened stone cells. The mesocarp is a broad zone with parenchymatous cells containing starch grains, secretion sacs, oil/resin, and fibrovascular bundles. The endocarp consists of stone cells with pronounced inner walls. The testa has compressed elongated cells and a pigment layer with tannin [13].

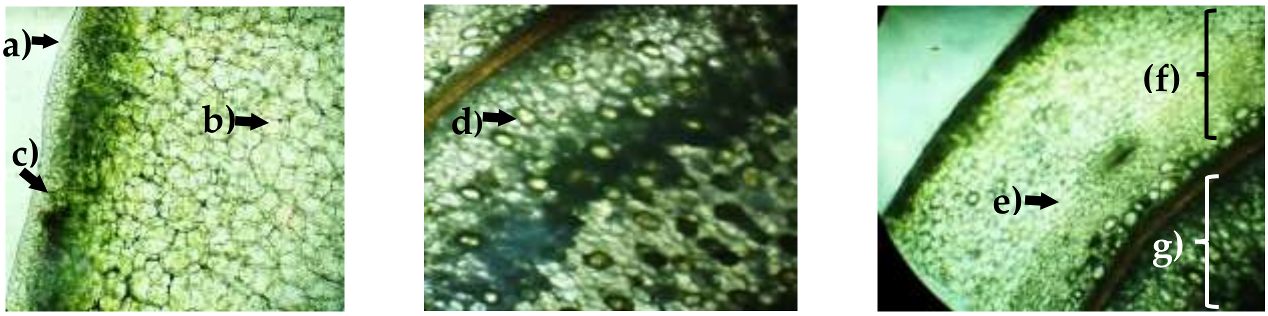

Figure 2. Transverse section of the fruit of *Piper nigrum* Linn.

Table 2. The pharmacognostic parameters of black pepper fruit

Parameters	**Content (%w/w)**
Loss on drying	7.46 ± 0.16
Total ash	4.29 ± 0.12
Acid-insoluble ash	0.15 ± 0.03
Water extractive value	8.35 ± 0.45
Ethanol extractive value	4.30 ± 0.18
Volatile oil	1.60 ± 0.00

The pharmacognostic parameters of black pepper fruit were determined, including loss on drying, total ash, acid-insoluble ash, water-soluble extractives, ethanol-soluble extractives, and volatile oil content. The results are as follows: 7.46 ± 0.16, 4.29 ± 0.12, 0.15 ± 0.03, 8.35 ± 0.45, 4.30 ± 0.18, and 1.60 ± 0.00 %w/w, respectively, as shown in Table 2.

A TLC fingerprint of the Piper nigrum Linn fruit was conducted using a TLC silica gel 60 GF254 plate as the stationary phase. The development was performed in a saturated TLC chamber with a hexane and ethyl acetate ratio of 1:1. The spots were observed using ultraviolet light under both short (254 nm) and long (366 nm). Subsequently, the plate was sprayed with anisaldehyde developing reagent and observed (Figure 3). Thin-layer chromatography is a simple, rapid, and inexpensive method with promising potential for analyzing and quantifying the constituents in herbal drugs [14].

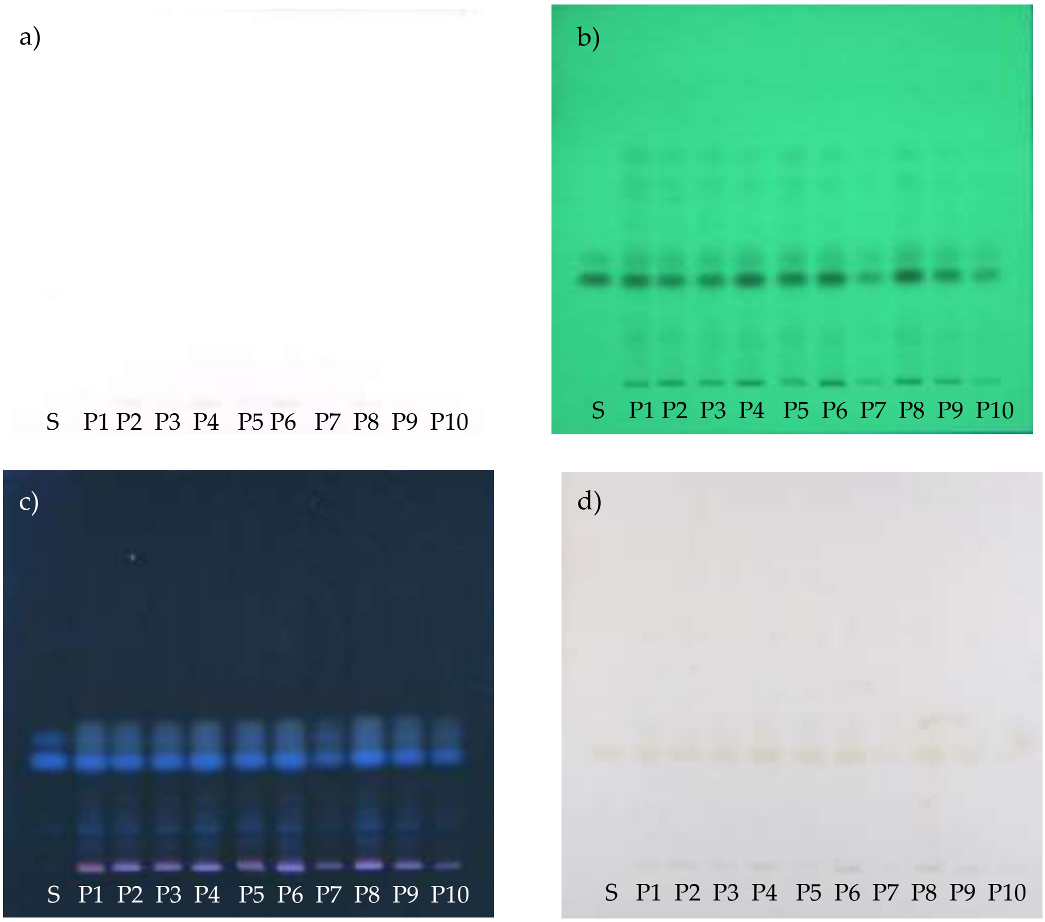

Figure 3. TLC fingerprint of *Piper nigrum* Linn. Fruit a) detection under daylight, b) detection under UV 254 nm, c) detection under UV 366 nm, d) detection with anisaldehyde reagent, (S) piperine standard and (P1-P10) extract of *Piper nigrum* Linn. Fruit

Table 3. HPLC validation of piperine content in black pepper fruit

Parameter	Piperine in black pepper fruit
Calibration curve	y = 137356x – 447800 (R^2 = 0.9991)
Range	10-100 µg/ml
Accuracy	95.85-101.85% recovery
Precision	
Intra-day	0.01-0.12 % RSD
Inter-day	0.52-0.90 %RSD
LOD	0.01 µg/ml
LOQ	0.04 µg/ml

The HPLC analysis utilized in this study for the quantitative determination of piperine was validated in terms of linearity, LOD (limit of detection), LOQ (limit of quantification), accuracy, precision, and specificity.

The regression line of the method demonstrated linearity in the range of 10-100 µg/ml, with a coefficient of determination (R^2) of 0.9991. The recovery of spiked known concentrations of standard piperine was assessed accurately. The percent recovery ranged from 95.85% to 101.85%, indicating the method's accuracy with a percent recovery between 80% and 120%.

Repeatability (intra-day precision) and intermediate (inter-day precision) were less than 2%. The precision of piperine quantitative analysis was determined by analyzing three concentrations on three different days.

The LOD and LOQ of the method were calculated using the residual standard deviation of the regression lines. The LOD was found to be 0.01 µg/ml, and the LOQ was 0.04 µg/ml (refer to Table 3).

The specificity of the method was validated through absorbance spectra within the range of 190-400 nm, comparing standard piperine with the extracts. The results revealed identical spectra obtained at the peak's up-slope, apex, and down-slope, indicating the piperine's chromatographic peak purity. The maximum absorption of piperine was observed at 342 nm, consistent with a previous study reporting an absorption peak at 343 nm [15].

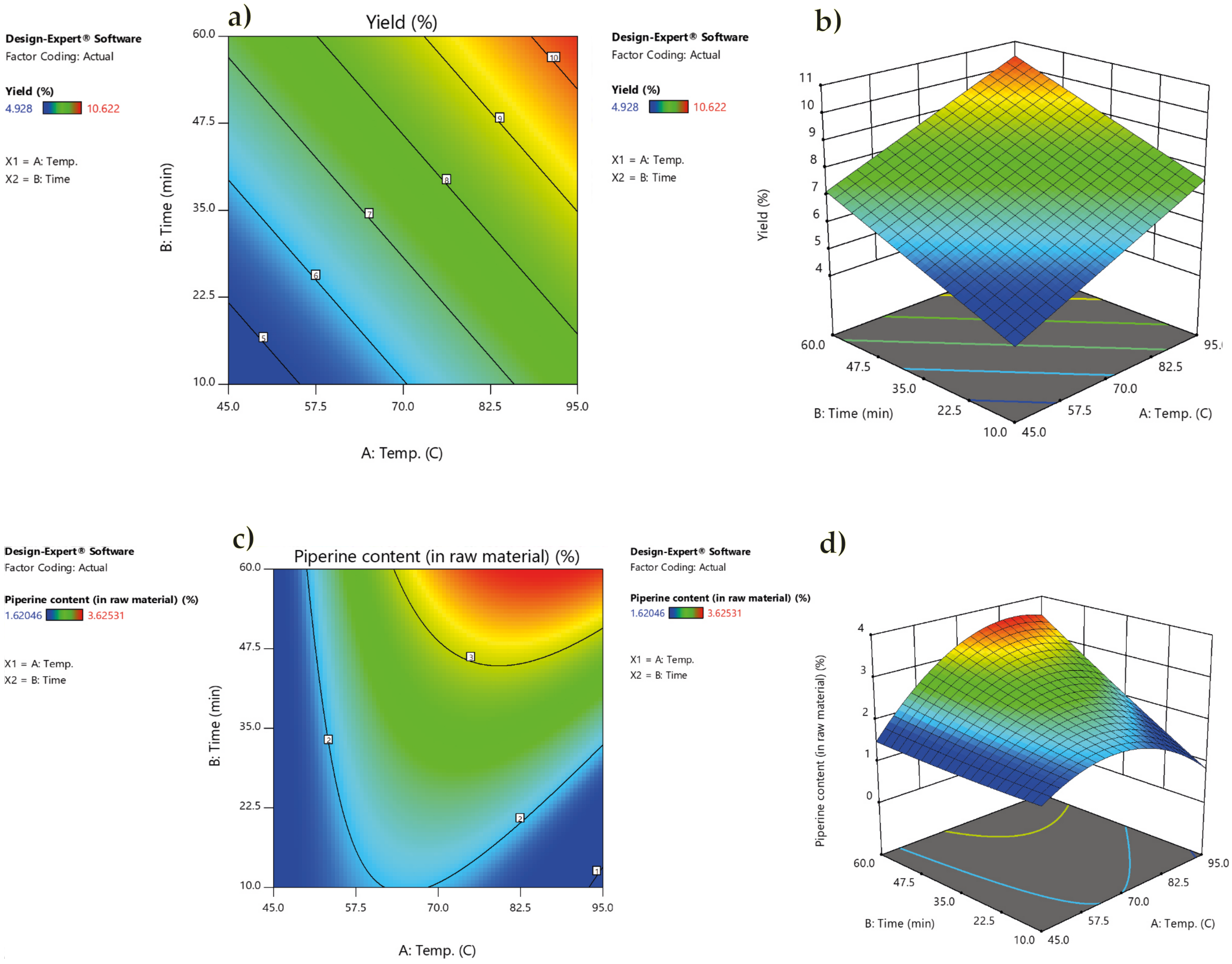

Figure 4. Contour plots of the model conditions of the content of (a-b) % yield and (c-d) piperine content

A two-factor spherical composite experimental design was conducted to estimate piperine content. The response surface analysis revealed the complex relationship between the causal factors (Xn) and their responses (Yn). Higher piperine content was observed at higher temperatures and longer extraction times. The optimal conditions for achieving the highest piperine content were a temperature of 70°C and an extraction time of 60 minutes. The result indicated that the extract's piperine content was 38.98±0.05% (as shown in Figure 4). Previous studies have suggested that piperine content's extraction yield was lower than ultrasound-assisted extraction (37.0 mg/g) at 50°C for 30 minutes. Extraction yields of piperine obtained from Soxhlet extraction and batch extraction methods were much lower than those obtained from ultrasound-assisted extraction. Utilizing ultrasound-assisted extraction for natural phytochemicals can mitigate the issues of lower extractability and longer extraction times associated with conventional methods [16].

4. Conclusion

The pharmacognostic properties identified in this study can contribute to the quality control of black pepper fruit. Physicochemical parameters are crucial for herbal drug identification and quality control. The findings of this study, including pharmacognostic specifications, quality control parameters, and prediction of piperine content, can facilitate drug development.

5. Acknowledgements

The authors acknowledge the support from the Faculty of Science and Technology, Hatyai University, Hatyai, Songkhla, Thailand, and the Herbal Medicinal Products Research and Development Center, Faculty of Pharmacy, Rangsit University, Thailand, for their material and equipment support.

Author Contributions: Conceptualization, L.S., and C.M.; methodology, L.S.; software, C.M.; validation, L.S., C.M., and A.B.; formal analysis, L.S.; investigation, L.S.; resources, A.P.; data curation, L.S.; writing-original draft preparation, L.S.; writing-review and editing, A.B.; visualization, A.P.; supervision, L.S. All authors have read and agreed to the published version of the manuscript.

Funding: This research received no external funding.

Conflicts of Interest: The authors declare no conflict of interest.

References

[1] Parthasarathy, V.A., Chempakam, B.; Zachariah, T.J. (eds.), *Chemistry of spices*. Cabi. **2008**.

[2] Vijayakumar, R.; Surya, D.; Nalini, N. Antioxidant efficacy of black pepper (*Piper nigrum* L.) and piperine in rats with high fat diet induced oxidative stress. *Redox Report* **2004**, *9*(2), 105-110.

[3] Bang, J.S.; Oh, D.H.; Choi, H.M.; Sur, B.J.; Lim, S.J.; Kim, J.Y.; Yang, H.I.; Yoo, M.C.; Hahm, D.H.; Kim, K.S. Anti-inflammatory and antiarthritic effects of piperine in human interleukin 1β-stimulated fibroblast-like synoviocytes and in rat arthritis models. *Arthritis research & therapy* **2009**, *11*, 1-9.

[4] Srinivasan, K. Black pepper and its pungent principle-piperine: a review of diverse physiological effects. *Critical reviews in food science and nutrition* **2007**, *47*(8), 735-748.

[5] Ko, J. M. A study on quantitative method of piperine in pure ground black pepper. *Journal of Food Hygiene and Safety* **1995**, *10*, 169-174.

[6] Hu ShiLin, H. S.; Ao Ping, A. P.; Liu Dai, L. D. Pharmacognostical studies on the roots of *Piper nigrum* L. *III: Determination of essential oil and piperine* **1996**, 179-182.

[7] Pradeep, C. R.; Kuttan, G. Effect of piperine on the inhibition of lung metastasis induced B16F-10 melanoma cells in mice. *Clinical & experimental metastasis* **2002**, *19*, 703-708.

[8] Sunila, E. S.; Kuttan, G. Immunomodulatory and antitumor activity of *Piper longum* Linn. and piperine. *Journal of ethnopharmacology* **2004**, *90*(2-3), 339-346.

[9] Lee, J. G.; Kim, A. Y.; Kim, D. W.; Kim, Y. J. Determination and risk characterization of bio-active piperine in black pepper and selected food containing black pepper consumed in Korea. *Food Science and Biotechnology* **2021**, *30*, 209-215.

[10] Lawless, H. T.; Heymann, H. Sensory evaluation of food: principles and practices. Springer Science & Business Media. **2010**.

[11] Lee, J. G.; Kim, Y. J. Comparison study of validation parameters and measurement uncertainty of rapid analytical methods for piperine in black pepper by ultraviolet spectroscopy and high-performance liquid chromatography. *Food Science and Biotechnology* **2022**, *31*(9), 1133-1143.

[12] Bhardwaj, R. K.; Glaeser, H.; Becquemont, L.; Klotz, U.; Gupta, S. K.; Fromm, M. F. Piperine, a major constituent of black pepper, inhibits human P-glycoprotein and CYP3A4. *Journal of Pharmacology and Experimental Therapeutics* **2002**, *302*(2), 645-650.

[13] Trivedi, M. N.; Khemani, A.; Vachhani, U. D.; Shah, C. P.; Santani, D. D. Pharmacognostic, phytochemical analysis and antimicrobial activity of two Piper species. *Pharmacie Globale* **2011**, *7*(05), 1-4.

[14] Sueree, L.; Ruangrungsi, N. Pharmacognostic Specification and Pinocembrin Content of *Boesenbergia rotunda* Root. RSU International Research Conference 2016, Rangsit University, Thailand, 29 April 2016.

[15] Saingam, W.; Monton, C.; Suksaeree, J.; Chankana, N.; Kittiwisut, S.; Charoenchai, L. Development and validation of RP-HPLC method for determination of piperine in maha-solos tablet formulation. *The Thai Journal of Pharmaceutical Sciences* **2013**, *38*, 133-136.

[16] Gorgani, L.; Mohammadi, M.; Najafpour, G. D.; Nikzad, M. Sequential microwave-ultrasound-assisted extraction for isolation of piperine from black pepper (*Piper nigrum* L.). *Food and Bioprocess Technology* **2017**, *10*, 2199-2207.

ASEAN
Journal of Scientific and Technological Reports
Online ISSN:2773-8752

Research article

Bacillus vietnamensis SF-1, a Promising Heterotrophic Nitrifier for Saline Wastewater Treatment

Sunipa Chankaew[1] and Yutthapong Sangnoi[2]*

[1] Faculty of Natural Resources, Prince of Songkla University, Songkhla, 90110, Thailand
[2] Faculty of Natural Resources, Prince of Songkla University, Songkhla, 90110, Thailand
* Correspondence: yutthapong.s@psu.ac.th

Citation:
Chankaew, S.; Sangnoi, Y. *Bacillus vietnamensis* SF-1, a promising heterotrophic nitrifier for saline wastewater teratment. *ASEAN J. Sci. Tech. Report.* **2024**, *27*(4), e253550. https://doi.org/10.55164/ajstr.v27i4.253550.

Article history:
Received: April 4, 2024
Revised: June 17, 2024
Accepted: June 19, 2024
Available online: June 30, 2024

Abstract: Shrimp farming wastewater regularly contains significant quantities of organic matter and inorganic nitrogen. Additionally, shrimp are extremely toxic to inorganic nitrogen, such as nitrite and ammonia. Ammonia removal is necessary for shrimp culture to improve water quality. Heterotrophic-nitrifying bacteria, genus *Bacillus*, are a kind of bacteria that effectively eliminate ammonia during the nitrification and aerobic denitrification processes. *Bacillus vietnamensis* SF-1 demonstrated 69.44% ammonium removal efficiency in a high ammonium medium. The nitrite production was 0.24 mg-N/L, and the nitrate concentration was 0.14 mg-N/L. The suitable carbon source of *B. vietnamensis* SF-1 was sucrose, which had ammonium removal at 57.39%, while a suitable nitrogen source was ammonium sulfate, which had ammonium removal at 46.15%. The C/N ratio at 8 showed the highest ammonium removal of 71.15%. An optimal salinity range for strain SF-1 growth was 2.0 to 4.0% NaCl (w/v). B. vietnamensis SF-1 was added to synthesis wastewater for 14 days to improve wastewater. The study found that the efficacy of ammonium removal of *B. vietnamensis* SF-1 was 94.77%. Nitrite and nitrate increased from 0.02-0.09 and 0.01-0.27 mg-N/L. The result showed considerable potential for the salt-tolerant *B. vietnamensis* SF-1 to improve water quality in coastal aquaculture.

Keywords: Heterotrophic nitrifying bacteria; ammonium removal; *Bacillus vietnamensis* SF-1; C/N ratio

1. Introduction

The wastewaters include significant quantities of nitrogenous organic compounds, including ammonia (NH_3), nitrite (NO_2^-), and nitrate (NO_3^-), which endanger the ecological balance and cause eutrophication in aquatic systems. For this reason, removing nitrogenous wastewater is essential for maintaining the aquaculture ecosystem [1]. Microbiological processing is one of the best techniques for eliminating nitrogen from wastewater. In principle, aerobic nitrification and anaerobic denitrification [2-4]. Microorganisms known as autotrophic nitrifying and heterotrophic denitrifying perform nitrification and denitrification, respectively, constituting traditional biological nitrogen removal processes [5]. Furthermore, autotrophic nitrifying bacteria have an extended life cycle and weak growth rates, which means that their biomass yields are sensitive to pH, heavy metals, toxic substances, and high ammonia concentrations. These factors make it difficult for traditional technology to use autotrophic nitrifying technology [6-7]. For this reason, there are practical limits to the conventional biological nitrogen removal approach.

According to a previous investigation, the autotrophic problem was less effective in removing ammonia than the heterotrophic nitrification process [8]. A new and efficient process for removing nitrogen from wastewater has been made possible by the heterotrophic nitrification-aerobic denitrification bacteria. These microorganisms have the potential for nitrification as well as denitrification at the same time [1, 9]. As a result of the higher phylogenetic variety relative to their autotrophic different versions, heterotrophic nitrifying bacteria are more adapted to their surroundings [10]. Investigation has demonstrated that *Bacillus* species can manage nitrogenous waste in aquaculture. Nitrate levels in catfish pond water treated by *B. velezensis* AP193 were found to have been reduced by 75% and total nitrogen levels by 43% in research conducted [11]. *Bacillus* treatment has reported a similar observation about decreasing toxic inorganic nitrogen compounds in synthetic water [12]. Both nitrite and nitrate have been found in relatively few concentrations. For example, *Bacillus* treatment resulted in increased nitrite and nitrate. *Bacillus* has reportedly been shown to improve the toxicity of ammonia. Specifically, studies on aquaculture have discovered that *B. subtilis, B. megaterium*, and *B. amyloliquefaciens* decreased ammonia levels [12-18]. *Bacillus* spp. is widely used in aquaculture. They have been developed to treat diseases, boost immune systems, improve growth rates, and improve water quality [11, 19-23]. Although coastal aquaculture is a significant sector, most of the current research on the microorganisms that contribute to heterotrophic nitrification and aerobic denitrification has been focused on freshwater sewage. There are few studies on the biological treatment of wastewater with high salinity. Therefore, if we can find a salt-tolerant heterotrophic nitrifier that can eliminate salty wastewater. It will increase the aquacultural efficiency and reduce the cost of coastal aquaculture.

This study aims to determine the optimization of carbon sources, nitrogen sources, and C/N ratio of salt-tolerant *B. vietnamensis* SF-1. Additionally, it will measure the efficiency of nitrogen removal in synthetic sewage.

2. Materials and Methods

2.1 Stock of heterotrophic nitrifying bacteria strain SF-1

The heterotrophic nitrifying bacterium, *Bacillus* strain SF-1, was obtained from the bottom sediment in the seabass cage in Songkhla Lake, Thailand, and was identified as *B. vietnamensis* SF-1 [24]. Bacterial cells were stored in a 25% glycerol at −20 °C, inoculated with a modified Pep-Beef-AOB medium, and incubated at 28 °C at 170 rpm for three days [25-27].

2.2 Ammonium removal efficiency of *B. vietnamensis* SF-1 in high ammonium level

A high ammonium medium was used to examine the efficiency of ammonium removal; 1.5 ml of *B. vietnamensis* SF-1 was inoculated in a flask containing 150 ml of medium. Then the flasks were shaked at 170 rpm at 28 °C. After 5 days of culturing, the supernatant was separated and collected by centrifugation at 3,500 rpm for 40 minutes [25, 26]. The concentrations of ammonium (NH_4^+), nitrite (NO_2^-), and nitrate (NO_3^-) were measured [28].

2.3 Optimization of carbon source, nitrogen source, C/N ratio, and salt-requirement

2.3.1 Carbon source

Five different carbon sources (glucose ($C_6H_{12}O_6$), sucrose ($C_{12}H_{22}O_{11}$), sodium acetate (CH_3COONa), sodium citrate ($C_6H_5Na_3O_7$) and sodium succinate ($C_4H_4Na_2O_4$)) were each added to the high-ammonium medium used for cultivating the isolate [5, 27]. The starting concentration of ammonia was around 790–880 mg-N/L, and ammonium sulfate was fixed as a nitrogen source. The 1.5 ml of *B. vietnamensis* SF-1 from the enrichment culture was inoculated into a 150 mL medium. The cultures were shaken in an incubator at 170 rpm, 28°C for 5 days. [27] To remove the bacterial cells, the suspension of cultures was centrifuged at 3,500 rpm for 40 minutes at the end of cultivation. Following standard methods, the concentrations of ammonium (NH_4^+), nitrite (NO_2^-), and nitrate (NO_3^-) in the supernatant were determined [28]. When a result was obtained, the carbon source with the highest effectiveness was suggested to study further.

2.3.2 Nitrogen source

Ammonium sulfate ($(NH_4)_2SO_4$) and ammonium chloride (NH_4Cl) were used as different sources of nitrogen. The initial ammonium concentration had been set to 800-820 mg-N/L, supplementing a suitable carbon source. The cultural conditions were followed as mentioned above. The supernatant was harvested and measured after 5 days of incubation. The optimum nitrogen source was recognized when the medium had the highest nitrogen removal efficiency [27, 28].

2.3.3 C/N ratio

The C/N ratio was studied using the optimal of carbon and nitrogen sources. By adjusting the ammonium concentration to around 820 to 840 mg-N/L. The level of C/N ratio was adjusted to 0, 2, 4, 8, and 16. The cultural condition, supernatant collection, and nitrogen removal determination were done above [27, 28].

2.3.4 Optimization of the salt requirement of B. vietnamensis **SF-1**

1% (v/v) of seed solution, *B. vietnamensis* SF-1 from the enrichment culture, was inoculated in modified Pep-Beef-AOB medium, which had 9 levels of NaCl concentrations as 0, 0.5, 1.0, 1.5, 2.0, 2.5, 3.0, 3.5, and 4.0% (w/v) for study. Then incubated at 28^{o}C, 170 rpm for 24 hours. A spectrophotometer was also used to measure the cell density at a wavelength of 600 nm using the supernatant after 24 hours of cultivation [27, 29].

2.4 The effectiveness of *B. vietnamiensis* SF-1 for nitrogen removal in the sterilizing of synthetic wastewater

Synthetic wastewater (a single usage), using 0.5% w/v shrimp feed for three days during fermentation, boosted the ammonium level in the salty wastewater. The synthetic wastewater was autoclaved at 121°C for 15 minutes after left for five days. Four liters of high synthetic wastewater were inoculated with 1% (v/v) of *B. vietnamensis* SF-1 cell suspension, and a control group received no bacterial inoculation. The experiment was extended to 14 days at room temperature, keeping aeration given during that period. Wastewater of 200 ml was kept every 7 days, ammonium, nitrite, and nitrate concentrations were analyzed [24, 25, 28].

2.5 Analytical methods

The concentration of ammonia and nitrite was analyzed using the colorimetric method. The nitrate concentration was determined by cadmium reduction column (ion chromatography) [28].

2.6 Statistical methods

The variance analysis (ANOVA) will be applied to water, ammonia, nitrite, and nitrate parameters. Duncan's new multiple range test (DMRT) method at 95% significance ($P < 0.05$) was used to analyze the difference in treatment using the R program.

3. Results and Discussion

3.1 Morphology of heterotrophic nitrifying bacterium *B. vietnamensis* SF-1

After re-streaking on modified Pep-Beef-AOB medium, *B. vietnamensis* SF-1 was obtained. The color of the colony on the solid medium was yellow-orange. *B. vietnamensis* SF-1 was rod-shaped, Gram-positive, and produced an endospore (Figure 1).

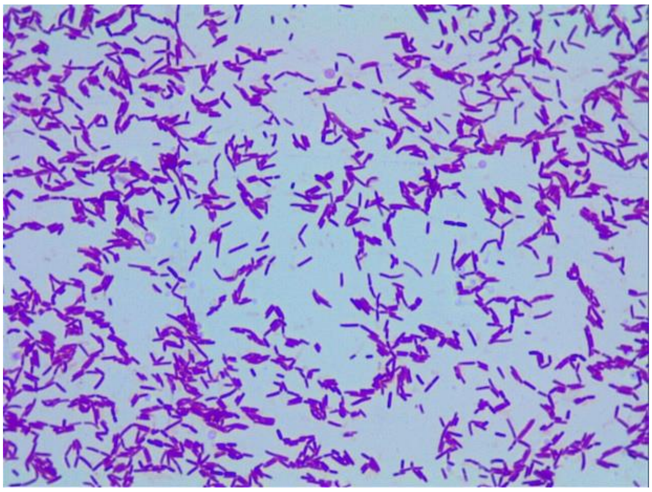

Figure 1. Cell morphology of *B. vietnamensis* SF-1.

3.2 Ammonium removal efficiency in high ammonium condition

The investigation of the nitrogen removal efficiency included ammonia, nitrite, and nitrate concentrations. According to the results, *B. vietnamensis* SF-1 demonstrated an ammonium removal efficiency of 69.44%, reducing the concentration from 825.16 ± 11.22 mg-N/L to 252.17 ± 8.00 mg-N/L. *B. vietnamensis* SF-1 can produce a nitrite concentration of 0.24 ± 0.01 mg-N/L and a nitrate concentration of 0.14 ± 0.03 mg-N/L (Figure 2). The result, which was consistent with additional previous studies, indicated that *B. subtilis* A1 had high ammonium removal abilities [30]. Furthermore, the study of Xioa et al. [31] shows that *B. subtilis* AYC's had effective nitrogen removal at an initial ammonium concentration of 10 mg-N/L. The ammonium concentration dropped rapidly after 10 minutes and steadily decreased after 30 minutes. The lowest ammonium removal efficiency was 43% at a high ammonium concentration of 2,000 mg-N/L. In another study, *Alcaligenes faecalis* no. 4 showed excellent ammonium removal efficiency at heavy ammonium concentrations (1,050 mg-N/L in 68 hours) [32].

3.3 Optimization of carbon source, nitrogen source, C/N ratio, and salt requirement

3.3.1 Optimal carbon and nitrogen sources

An essential component of heterotrophic nitrification capacity was thought to be the carbon supply. During the study, sucrose was used to determine the optimal carbon source for ammonium removal, exhibiting a statistically significant difference from the other four carbon sources ($p<0.05$). Ammonium removal was 57.39% (Figure 3). At the same time, other carbon sources, sodium citrate, sodium succinate, glucose, and sodium acetate, provided ammonium elimination of 52.99%, 47.32%, 42.60%, and 36.47%, respectively. The study was related to the efficiency of *B. oceanisediminis* Ba9 to remove ammonia when sucrose is the carbon source [27], and the red yeast, *Sporidiobolus pararoseus* Y1, demonstrated an ammonium removal rate of 62.08%, which has sucrose as a carbon source. Additionally, *B. subtilis* A1 was provided as acetate, glucose, citrate, and succinate as carbon sources; the percentages of ammonium removed were up to 50 percent within 60 hours (60.3 ± 1.2%, 60.8 ± 2.4%, 59.7 ± 1.0%, and 59.8 ± 2.3%, respectively) [30]. The various carbon sources have demonstrated the effectiveness of heterotrophic bacteria in eliminating ammonia well. According to the study, different carbon sources have the potential to be used by heterotrophic nitrifying bacteria, which might have an impact on the amount that nitrogen decreases throughout the nitrification process [30, 33, 34]. The other research results demonstrated that glucose and sodium succinate could effectively support the development of *B. methylotrophicus* L7, demonstrating effective nitrification capabilities. There was a 48.00% and 38.40% decrease in total ammonium, respectively [35]. Additionally, using citrate, glucose, and L-malate as the carbon source for 24 hours raised the ammonium removal efficiency of *Alcaligenes faecalis* strain NR to 98.9%, 94.9%, and 94.7%, respectively [34]. When succinate was used as a carbon source, *Acinetobacter junii* YB can remove ammonium entirely in 25 hours [36]. Consequently, sucrose was utilized in additional research as a suitable carbon source for *B. vietnamensis* SF-1.

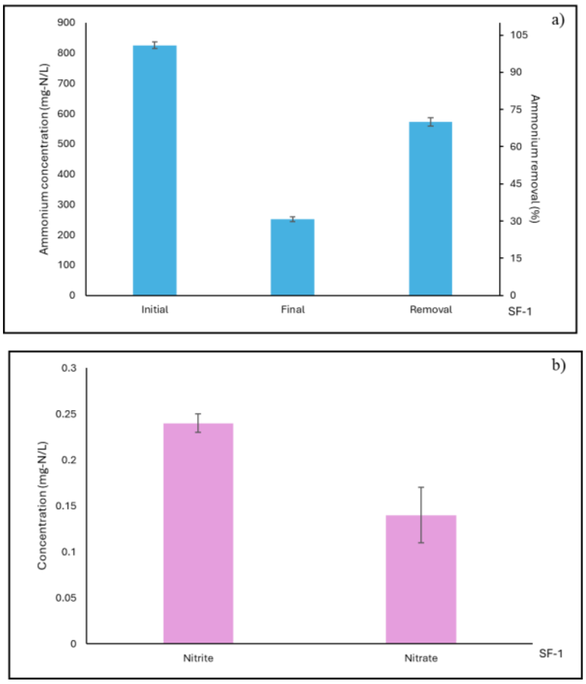

Figure 2. Nitrogen removal efficiency of *B. vietnamensis* SF-1; a) Ammonium removal efficiency, b) Nitrite concentration (mg-N/L).

Ammonium sulfate was the most effective nitrogen source for B. vietnamensis SF-1 in the nitrogen source. This bacterial strain can remove ammonia for 46.15% (Figure 4). This investigation's results aligned with our previous study regarding *B. oceanisediminis* Ba9, which utilized sucrose and ammonium sulfate as carbon and nitrogen sources, respectively, with an ammonium reduction efficiency of 50.53% [27]. Yang et al. [30] reported the effect of ammonium sulfate as a nitrogen source and 4 different carbon sources (glucose, acetate, sodium acetate, and succinate) on the ability of *B. subtilis* A1 to remove ammonia. The study results showed that carbon sources did not affect the ammonia elimination efficiency of B. subtilis A1. Considering different nitrogen sources, Lu et al. [33] studied the ammonium removal of the bacterium *Alcaligenes* strain W14. According to the data, ammonium sulfate was very effective at reducing ammonium. *Alcaligenes* strain W1 consequently selected sodium citrate and ammonium sulfates as optimal carbon and nitrogen sources. Also, with other research, ammonium sulfate was optimal for *B. tropicalis* L2, which has ammonium removed within 24 hours to 95.08%, and the maximum ammonium removal of 98.37% was observed at 36 hours [37]. Consequently, the report agreed with this study that *B. vietnamensis* SF-1 preferred sucrose as a carbon source and ammonium sulfate as a nitrogen source.

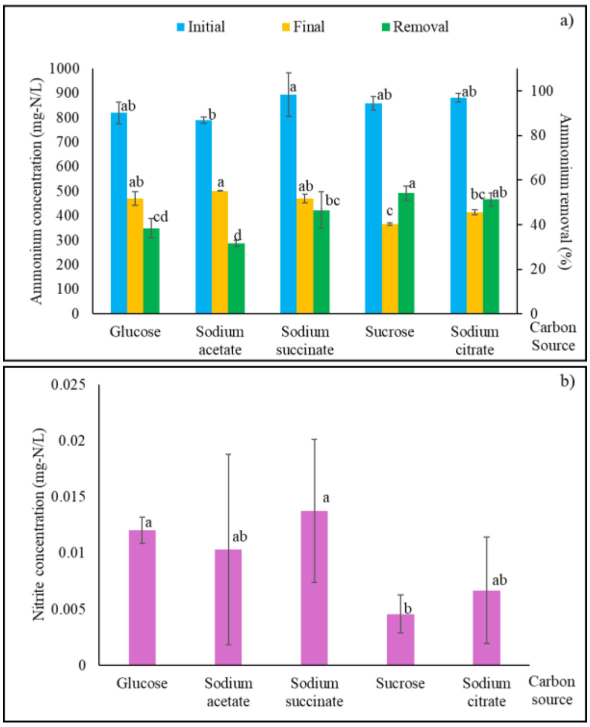

Figure 3. Optimal carbon source of *B. vietnamensis* SF-1, as well as a) ammonium removal efficiency and b) nitrite production.

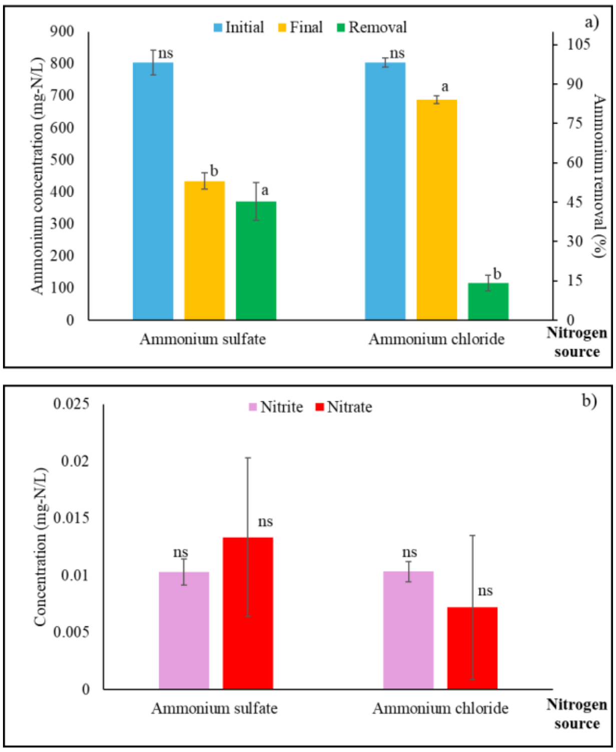

Figure 4. Optimal nitrogen source of *B. vietnamensis* SF-1; a) Ammonium removal, b) Nitrate production.

3.3.2 The optimal C/N ratio

The optimal C/N ratio is a significant regulator that has a major impact on the capability of heterotrophic nitrification-aerobic denitrification bacteria [38, 39]. Sucrose and ammonium sulfate were used as carbon and nitrogen sources for *B. vietnamensis* SF-1. The C/N ratio optimum of SF-1 was found to be 8, which can eliminate ammonia for 71.15%, subsequent by 4, 2, 16, and 0, which had ammonium removal of 65.93%, 62.09, 57.14, and 44.41%, respectively. Meanwhile, C/N ratio 4 has the highest production of nitrite and nitrate concentration (Figure 5). The C/N ratio at 0 showed the lowest ammonium removal. This result indicated carbon is important for heterotrophic nitrifying bacteria. The study has been related to the result that C/N at 9 was the most effective nitrogen removal condition for *B. tropicalis* L2 [37]. At a C/N ratio 5, *A. faecalis* NR demonstrated ammonium decreasing at 19.2 mg/L in 48 hours [34]. *Acinetobacter junii* YB showed a similar result, with ammonium being used at a C/N ratio of 5 [36], whereas *A. faecalis* no. 4 removed ammonia with good efficiency when the C/N ratio was 10 [32]. Furthermore, it became obvious that C/N ratios reached up to 10. The heterotrophic nitrifier needs carbon for development, comparable to biofloc production [40]. Furthermore, Xiao et al. [31] suggested that the most appropriate C/N ratio at 10 had the highest e ammonium removal efficiency by *B. subtillis* AYC. Another study revealed the mixer of *Pseudomonas geniculata* ATCC 19374 and *B. cereus* EC3 could remove ammonia of 99.84% at a C/N ratio of 12, which was higher than the C/N ratio 8 (92.8%) [41]. Research demonstrated effective nitrogen removal efficiency at a low C/N ratio, which is optimal for practical applications [42].

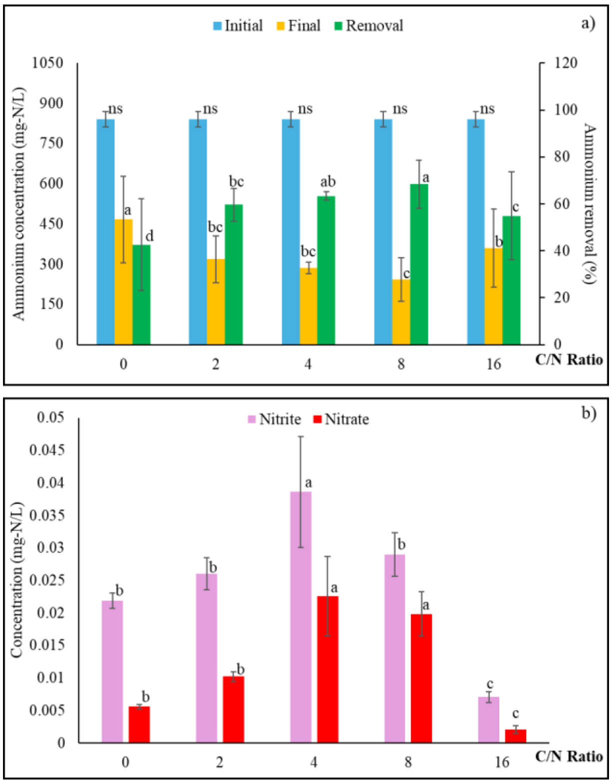

Figure 5. Optimal C/N of *B. vietnamensis* SF-1; a) Ammonium removal efficiency, b) Nitrite production.

3.3.3 Salt Requirement of B. vietnamensis **SF-1**

Salinity showed a major factor impacting nitrification; even strains grown in marine environments were inhibited by high salinity [43]. The optimum salinity test for *B. vietnamensis* SF-1 was studied at 9 different salinity levels from 0 to 4.0% NaCl (w/v). It demonstrated *that B. vietnamensis* SF-1 *can grow at the salinity range* from 2 to 4.0% NaCl (w/v) (Figure 6). According to Noguchi et al. [44], halotolerant *B. vietnamensis* 15-1 can reproduce in 15% NaCl, with 1% NaCl providing the best conditions for growth and development. *B. methylotrophicus* L7 could have been characterized as a halotolerant bacterium since it eliminated more than 58.70% of ammonium from 0-30% NaCl [35]. *B. oceanisediminis* is capable of developing at concentrations of salt between 0 and 13% NaCl (w/v), the optimal conditions being 0.5% NaCl (w/v) [45], *B. oceanisediminis* Ba9 grows thoroughly at 1.5-4.0% NaCl (w/v) (optimum 1.5-2.0% NaCl (w/v)) [27], while other reports suggested that *B. maritimus* may tolerate situation as high as 7% NaCl (w/v) (optimum at 5%), *B. aerius* NY6 can grow at up to 6% (optimum at 2%) [46, 47]. This salt-resistant property can effectively treat low-salinity and high-salinity aquaculture wastewater.

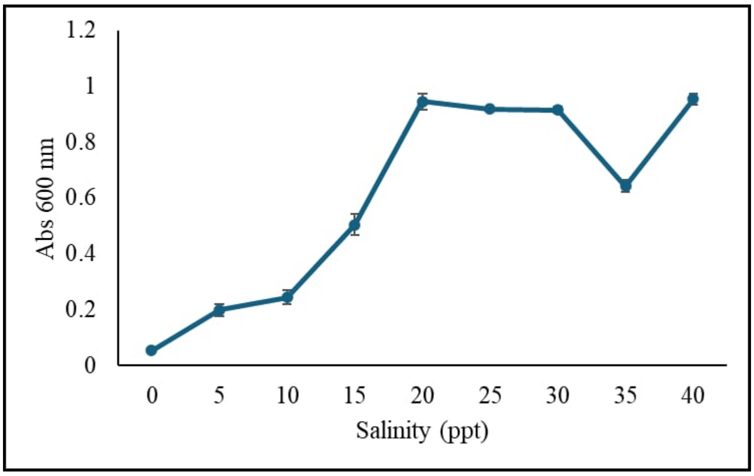

Figure 6. Growth profile of *B. vietnamensis* SF-1 at different salinity levels.

3.4 The efficiency of *B. vietnamensis* SF-1 for synthetic sewage treatment

The efficacy of ammonium removal in sterilizing sewage demonstrated that removing ammonia by *B. vietnamensis* SF-1 had a high ammonium removal efficiency (94.77%). Nitrite productivity dropped slightly from day 0 to day 7 (0.02-0.01 mg-N/L) and rose significantly from the 7 to 14 experiment date. From 0 to 14, the efficiency of nitrate production tends to increase with a quantity of 0.01-0.27 mg-N/L (Figure 8). The initially determined concentration of ammonium in the experiment to remove ammonium from shrimp aquaculture wastewater was around 191.38 mg-N/L, which was one-quarter of the initial concentration of ammonium in the flask-scale experiment (825 mg/L). According to Guo et al. [48], the initial ammonium demand significantly impacted the performance of heterotrophic bacteria in ammonium removal. For treating *B. oceanisediminis* Ba9 can remove ammonia for 96.87% (from 191.38 ± 0.02 mg-N/L to 5.99 ± 1.12 mg-N/L) and produce nitrite from 0.02 to 0.14 mg-N/L [27] when *B. methytotrophicus* L7 can decreased ammonia from 146.71 mg-N/L to 38.29 mg-N/L (41.02%) for 9 days [35]. *B. vietnamensis* SF-1, a heterotrophic nitrifier, showed higher ammonium removal efficiency at high ammonium concentrations than autotrophic nitrifying bacteria, as demonstrated by the nitrogen removal result [49].

The present investigation observed variances in nitrite and nitrate levels among treatment groups, which might indicate variation in the nitrification process. During the 14-day experiment, nitrite levels continuously got up and dropped, whereas the nitrate concentration progressively increased, corresponding to a decrease in ammonia levels. *B. vietnamensis* SF-1 efficiently converted ammonia to nitrite and continually nitrite to nitrate. In general terms, ammonium content can potentially be effectively oxidized by nitrification processes promoted by AOB (Ammonia-Oxidizing Bacteria), such as *Nitrosomonas* and *Nitrosospira.* AOB showed extraordinary ammonia oxidation potential. At the same time, the conversion of nitrite to nitrate is facilitated by nitrite-oxidizing bacteria (NOB). The NOB comprises *Nitrobacter winogradskyi, N. agilis, Nitrospira gracilis*, and *Nitrococcus mobilis*, all of which are members of this group. However, because the initial concentration of ammonia in this experiment was higher than the standard limit, the nitrification process that converts ammonia to nitrite could not have been completed [50, 51]. Kim et al. [52] found that combining B. subtilis PK8 and B. cereus PK5 led to 72% ammonium removal (initial ammonium 50.0 ± 1.5 mg-N/L). *Bacillus* sp. N31 can decrease ammonium, nitrite, and nitrate by 86.3, 89.3, and 89.4%, respectively (initial ammonium 250 mg-N/L) [38]. The nitrogen removal process can demonstrate that *B. vietnamensis* SF-1 belongs to the heterotrophic nitrifier.

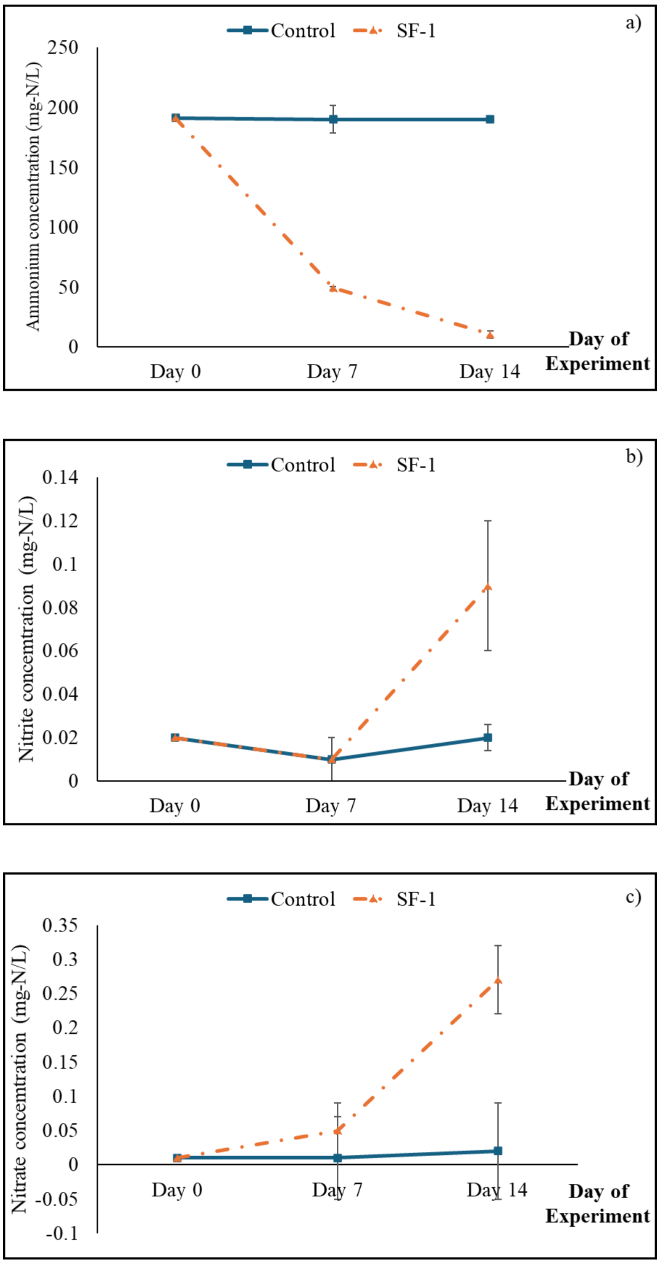

Figure 7. The efficiency of *B. vietnamensis* SF-1 removal in synthetic wastewater.

4. Conclusions

This study summarizes that *B. vietnamensis* SF-1 is an extraordinarily salt-tolerant heterotrophic nitrifying bacterium. It effectively reduces ammonia when sucrose is used as a carbon source and ammonium sulfate is used as a nitrogen source. Optimal C/N ratio of *B. vietnamensis* SF-1 is 8. *B. vietnamensis* SF-1 can grow over a wide salinity range. This study demonstrated by nitrogen removal efficiency studies that *B. vietnamensis* SF-1 was effective at oxidizing ammonium to nitrite and nitrate. As a result, there may be enormous prospects for expansion in sectors such as marine shrimp farming and saline wastewater treatment. In the future, *B. vietnamensis* SF-1 may be employed to sustain water quality for cultivating brackish and marine shrimp aquaculture. Controlling water quality by *B. vietnamensis* SF-1 will help reduce the cost of marine shrimp aquaculture.

5. Acknowledgements

We greatly thanked Miss Khiangkhwan Sakkayaphan and Miss Karnchanok Chiamsakul for their English proofing.

Author Contributions: Conceptualization, S.C. and Y.S.; methodology, S.C. and Y.S.; software, S.C.; validation, Y.S.; formal analysis, S.C. and Y.S.; investigation, S.C. and Y.S.; writing—original draft preparation, S.C. and Y.S.; writing—review and editing, S.C. and Y.S. All authors have read and agreed to the published version of the manuscript.

Funding: This research work was supported by budget revenue of the Agricultural Research Development Agency (Public Organization) (CRP6105020740).

References

[1] Song, T.; Zhang, X.; Li, J.; Wu, X.; Feng, H.; Dong, W. A review of research progress of heterotrophic nitrification and aerobic denitrification microorganisms (HNADMs). *Sci. Total Environ.* **2021**, *801*, 149319.

[2] Gupta, A. B.; Gupta, S. K. Simultaneous carbon and nitrogen removal from high strength domestic wastewater in an aerobic RBC biofilm. *Water Res.* **2001**, *35*, 1714–1722.

[3] Herrero, M.; Stuckey, D. C. Bioaugmentation and its application in wastewater treatment: a review. *Chemosphere* **2015**, *140*, 119–128.

[4] Zhao, B.; Tian, M.; An, Q.; Ye, J.; Guo, J. S. Characteristics of a heterotrophic nitrogen removal bacterium and its potential application on treatment of ammonium–rich wastewater. *Bioresour. Technol.* **2017**, *226*, 46–54.

[5] Chen, J.; Xu, J.; Zhang, S.; Liu, F.; Peng, J.; Peng, Y.; Wu, J. Nitrogen removal characteristics of a novel heterotrophic nitrification and aerobic denitrification bacteria, *Alcaligenes faecalis* strain WT14. *J. Environ. Manag.* **2021**, *282*, 111961.

[6] Kim, Y. M.; Park, D.; Lee, D. S.; Park, J. M. Inhibitory effects of toxic compounds on nitrification process for cokes wastewater treatment. *J. Hazard. Mater*. **2008**, *152*, 915–921.

[7] Zheng, H. Y.; Liu, Y.; Gao, X. Y.; Ai, G. M.; Miao, L. L.; Liu, Z. P. Characterization of a marine origin aerobic nitrifying–denitrifying bacterium. *J. Biosci. Bioeng.* **2012**, *114*, 33–37.

[8] Pan, Z.; Zhou, J.; Lin, Z.; Wang, Y.; Zhao, P.; Zhou, J.; Liu, S.; He, X. Effects of COD/TN ratio on nitrogen removal efficiency, microbial community for high saline wastewater treatment based on heterotrophic nitrification–aerobic denitrification process. *Bioresour. Technol.* **2020**, *301*, 122726.

[9] Iannacone, F.; Di Capua, F.; Granata, F.; Gargano, R.; Esposito, G. Shortcut nitrification–denitrification and biological phosphorus removal in acetate–and ethanol–fed moving bed biofilm reactors under microaerobic/aerobic conditions. *Bioresour. Technol.* **2021**, *330*, 124958.

[10] Duan, S.; Zhang, Y.; Zheng, S. Heterotrophic nitrifying bacteria in wastewater biological nitrogen removal systems: A review. *Crit. Rev. Env. Sci. Tec*. **2021**, *52*, 1–37.

[11] Thurlow, C. M.; Williams, M. A.; Carrias, A.; Ran, C.; Newman, M.; Tweedie, J.; Allison, E.; Jescovitch, L. N.; Wilson, A. E.; Terhune, J. S.; Liles, M. R. *Bacillus velezensis* AP193 exerts probiotic effects in channel catfish (*Ictalurus punctatus*) and reduces aquaculture pond eutrophication. *Aquaculture* **2019**, *503*, 347–356.

[12] Lalloo, R.; Ramchuran, S.; Ramduth, D.; Görgens, J.; Gardiner, N. Isolation and selection of *Bacillus* spp. as potential biological agents for enhancement of water quality in culture of ornamental fish. *J. Appl. Microbiol*. **2007,** *103*, 1471–1479.

[13] Song, Z. F.; An, J.; Fu, G. H.; Yang, X. L. Isolation and characterization of an aerobic denitrifying *Bacillus* sp. YX–6 from shrimp culture ponds. *Aquaculture* **2011**, *319*, 188–193.

[14] Nimrat, S.; Suksawat, S.; Boonthai, T.; Vuthiphandchai, V. Potential *Bacillus* probiotics enhance bacterial numbers, water quality and growth during early development of white shrimp (*Litopenaeus vannamei*). *Vet. Microbiol.* **2012**, *159*, 443–450.

[15] Xie, F.; Zhu, T.; Zhang, F.; Zhou, K.; Zhao, Y.; Li, Z. Using *Bacillus amyloliquefaciens* for remediation of aquaculture water. *SpringerPlus* **2013**, *2*, 119.

[16] Zokaeifar, H.; Babaei, N.; Saad, C. R.; Kamarudin, M. S.; Sijam, K.; Balcazar, J. L. Administration of *Bacillus subtilis* strains in the rearing water enhances the water quality, growth performance, immune

response, and resistance against *Vibrio harveyi* infection in juvenile white shrimp, *Litopenaeus vannamei*. *Fish Shellfish Immunol.* **2014**, *36*, 68–74.

[17] Hura, M. U. D.; Zafar, T.; Borana, K.; Prasad, J. R.; Iqbal, J. Effect of commercial probiotic *Bacillus megaterium* on water quality in composite culture of major carps. *Int. J. Curr. Agric. Sci.* **2018**, *8*, 268–273.

[18] Cha, J. H.; Rahimnejad, S.; Yang, S. Y.; Kim, K. W.; Lee, K. J. Evaluations of *Bacillus* spp. as dietary additives on growth performance, innate immunity and disease resistance of olive flounder (*Paralichthys olivaceus*) against *Streptococcus iniae* and as water additives. *Aquaculture*. **2013**, 402–403, 50–57.

[19] Das, A.; Nakhro, K.; Chowdhury, S.; Kamilya, D. Effects of potential probiotic *Bacillus amyloliquifaciens* FPTB16 on systemic and cutaneous mucosal immune responses and disease resistance of catla (*Catla catla*). *Fish Shellfish Immunol.* **2013**, *35*, 1547–1553.

[20] Saputra, F.; Shiu, Y. L.; Chen, Y. C.; Puspitasari, A. W.; Danata, R. H.; Liu, C. H.; Hu, S. Y. Dietary supplementation with xylanase–expressing *B. amyloliquefaciens* R8 improves growth performance and enhances immunity against *Aeromonas hydrophila* in Nile tilapia (*Oreochromis niloticus*). *Fish Shellfish Immunol.* **2016**, *58*, 397–405.

[21] Thy, H. T. T.; Tri, N. N.; Quy, O. M.; Fotedar, R.; Kannika, K.; Unajak, S.; Areechon, N. Effects of the dietary supplementation of mixed probiotic spores of *Bacillus amyloliquefaciens* 54A, and *Bacillus pumilus* 47B on growth, innate immunity and stress responses of striped catfish (*Pangasianodon hypophthalmus*). *Fish Shellfish Immunol.* **2017**, *60*, 391–399.

[22] Fei, H.; Lin, G. D.; Zheng, C. C.; Huang, M. M.; Qian, S. C.; Wu, Z. J.; Sun, C.; Shi, Z. G.; Li, J. Y.; Han, B. N. Effects of *Bacillus amyloliquefaciens* and *Yarrowia lipolytica* lipase 2 on immunology and growth performance of Hybrid sturgeon. *Fish Shellfish Immunol.* **2018**, *82*, 250–257.

[23] Zhang, F.; Xie, F.; Zhou, K.; Zhang, Y.; Zhao, Q.; Song, Z.; Cui, H. Nitrogen removal performance of novel isolated *Bacillus* sp. capable of simultaneous heterotrophic nitrification and aerobic denitrification. *Appl. Biochem. Biotech.* **2022**, *194*, 3196–3211.

[24] Noorak, S.; Rakkhiaw, S.; Limjirakhajornt, K.; Uppabullung, A.; Keawtawee, T.; Sangnoi, Y. Nitrite oxidizing bacteria for water treatment in coastal aquaculture system. IOP Conf. Ser.: *Earth Environ. Sci.* **2018**, *13*, 012005.

[25] Sangnoi, Y.; Chankaew, S.; O-Thong, S. Indigenous *Halomonas* spp., the potential nitrifying bacteria for saline ammonium wastewater treatment. *Pak. J. Biol. Sci.* **2017**, *20*, 52–58.

[26] Chankaew, S.; O-Thong, S.; Sangnoi, Y. Nitrogen removal efficiency of salt–tolerant heterotrophic nitrifying bacteria. *Chiang Mai. J. Sci.* **2018**, *45*, 11–20.

[27] Chankaew, S.; Sangnoi, Y. Exploring the efficacy of *Bacillus oceanisediminis* Ba9 from Asian seabass cage sediment in saline wastewater treatment. *ASEAN J. Sci. Tech. Report*. **2023**, *26*, 54–66.

[28] Strickland, J. D. H.; Parsons, T. R. A Practical Handbook of Seawater Analysis, 2nd ed.; The Alger Press Ltd.: Fishery Research Board, Canada, **1972**, 49–131.

[29] Purivirojkul, W.; Maketon, M.; Areechon, N. Probiotic properties of *Bacillus pumilus*, *Bacillus sphaericus* and *Bacillus subtilis* in Black tiger shrimp (*Penaeus monodon* Fabricius) culture. *Kasetsart Journal Natural Science* **2005**, *39*, 262–273.

[30] Yang, X. P.; Wang, S. M.; Zhang, D. W.; Zhou, L. X. Isolation and nitrogen removal characteristics of an aerobic heterotrophic nitrifying–denitrifying bacterium, *Bacillus subtilis* A1. *Bioresour. Technol*. **2011**, *102*, 854–862.

[31] Xiao, J.; Zhu, C.; Sun, D.; Guo, P.; Tian, Y. Removal of ammonium–N from ammonium–rich sewage using an immobilized *Bacillus subtilis* AYC bioreactor system. *J. Environ. Sci*. **2011**, *23*, 1279–1285.

[32] Joo, H. S.; Hirai, H.; Shoda, M. Characteristics of ammonium removal by heterotrophic nitrification–aerobic denitrification by *Alcaligenes faecalis* No. 4. *J. Biosci. Bioeng*. **2005**, *100*, 184–191.

[33] Lu, Y.; Wang, X.; Liu, B.; Liu, Y.; Yang, X. Isolation and characterization of heterotrophic nitrifying strain W1. *Chinese J. Chem. Eng.* **2012**, *20*, 995–1002.

[34] Zhao, B.; Tian, M.; An, Q.; Ye, J.; Guo, J. S. Characteristics of a heterotrophic nitrogen removal bacterium and its potential application on treatment of ammonium–rich wastewater. *Bioresour. Technol.* **2017**, *226*, 46–54.

[35] Zhang, Q. L.; Liu, Y.; Ai, G. M.; Miao, L. L.; Zheng, H. Y.; Liu, Z. P. The characteristics of a novel heterotrophic nitrification–aerobic denitrification bacterium, *Bacillus methylotrophicus* strain L7. *Bioresour. Technol.* **2012**, *108*, 35–44.

[36] Ren, Y. X.; Yang, L.; Liang, X. The characteristics of a novel heterotrophic nitrifying and aerobic denitrifying bacterium, *Acinetobacter junii* YB. *Bioresour. Technol.* **2014**, *171*, 1–9.

[37] Li, Q.; He, Y.; Wang, B.; Weng, N.; Zhang, L.; Wang, K.; Tian, F.; Lyu, M.; Wang, S. Heterotrophic nitrification–aerobic denitrification by *Bacillus* sp. L2: mechanism of denitrification and strain immobilization. *Water* **2024**, *16*, 416.

[38] Huang, F.; Pan, L. Q.; Lv, N.; Tang, X. Characterization of novel *Bacillus strain* N31 from mariculture water capable of halophilic heterotrophic nitrification–aerobic denitrification. *J. Biosci. Bioeng.* **2017**, *124*, 564–571.

[39] Wang, T.; Dang, Q.; Liu, C.; Yan, J.; Fan, B.; Cha, D.; Yin, Y.; Zhang, Y. Heterotrophic nitrogen removal by a newly–isolated alkalitolerant microorganism, *Serratia marcescens* W5. *Bioresour. Technol.* **2016**, *211*, 618–627.

[40] Xu, W. J.; Morris, T. C.; Samocha, T. M. Effects of C/N ratio on biofloc development, water quality, and performance of *Litopenaeus vannamei* juveniles in a biofloc–based, high–density, zero–exchange, outdoor tank system. *Aquaculture* **2016**, *453*, 169–175.

[41] Liu, L.; Gao, J.; Huang, Z.; Li, Y.; Shang, N.; Gao, J.; Zhang, J.; Cai, M. Potential application of a *Pseudomonas geniculata* ATCC 19374 and *Bacillus cereus* EC3 mixture in livestock wastewater treatment. *Waste Biomass Valori*. **2021**, *12*, 3927–3938.

[42] Gao, F.; Zhang, H. M.; Yang, F. L.; Qiang, H.; Li, H.; Zhang, R. Study of an innovative anaerobic (A)/oxic (O)/anaerobic (A) bioreactor based on denitrification–anammox technology treating low C/N municipal sewage. *Chem. Eng. J.* **2013**, *232*, 65–73.

[43] Finstein, M. S.; Bitzky, M. R. Relationships of autotrophic ammonium–oxidizing bacteria to marine salts. *Water Res*. **1972**, *6*, 31–36.

[44] Noguchi, H.; Uchino, M.; Shida, O.; Takano, K.; Nakamura, L. K.; Komagata, K. *Bacillus vietnamensis* sp. nov., a moderately halotolerant, aerobic, endospore–forming bacterium isolated from Vietnamese fish sauce. *Int. J. Syst. Evol. Microbiol.* **2004**, *54*, 2117–2120.

[45] Zhang, J.; Wang, J.; Fang, C.; Song, F.; Xin, Y.; Qu, L.; Ding, K. *Bacillus oceanisediminis* sp. nov., isolated from marine sediment. *Int. J. Syst. Evol. Microbiol.* **2010**, *60*, 2924–2929.

[46] Zhang, X.; Gao, J.; Zhao, F.; Zhao, Y.; Li, Z. Characterization of a salt–tolerant bacterium *Bacillus* sp. from a membrane bioreactor for saline wastewater treatment. *J. Environ. Sci.* **2014**, *26*, 1369–1374.

[47] Pal, D.; Kumar, R. M.; Kaur, N.; Kumar, N.; Kaur, G.; Singh, N. K.; Krishnamurthi, S.; Mayilraj, S. *Bacillus maritimus* sp. nov., a novel member of the genus *Bacillus* isolated from marine sediment. *Int. J. Syst. Evol. Microbiol.* **2017**, *67*, 60–66.

[48] Guo, Y.; Zhou, X.; Li, Y.; Li, K.; Wang, C.; Liu, J.; Yan, D.; Liu, Y.; Yang, D.; Xing, J. Heterotrophic nitrification and aerobic denitrification by a novel *Halomonas campisalis*. *Biotechnol. Lett.* **2013**, *35*, 2045–2049.

[49] Khin, T.; Annachhatre, A. P. Nitrogen removal in a fluidized bed bioreactor by using mixed culture under oxygen limited conditions. *Water Sci. Technol*. **2004**, *50*, 313–320.

[50] Bitton, G. Wastewater Microbiology. Wiley–Liss, Inc. USA. **1994**.

[51] Boyd, C. E. Water Quality in Ponds of Aquaculture. Alabama Agriculture Experiment Station, Auburn University. Alabama. **1990**.

[52] Kim, J. K.; Park, K. J.; Cho, K. S.; Nam, S. W.; Park, T. J.; Bajpai, R. Aerobic nitrification–denitrification by heterotrophic *Bacillus* strains. *Bioresour. Technol*. **2005**, *96*, 1897–1906.

ASEAN
Journal of Scientific and Technological Reports
Online ISSN:2773-8752

Research article

Film Development of Chitosan from Mussel Shells and Pacific White Shrimp Shells

Kanokkan Worawut[1*], Baramee Phungpis [2], Potchanee Kaewkumsan[3] and Pakin Noppawan [4]

[1] Department of Fisheries, Faculty of Natural Resources, Rajamangala University of Technology Isan Sakon Nakhon Campus, 47160, Thailand
[2] Department of Fisheries, Faculty of Natural Resources, Rajamangala University of Technology Isan Sakon Nakhon Campus, 47160, Thailand
[3] Department of Food Science and Technology, Faculty of Natural Resources, Rajamangala University of Technology Isan Sakon Nakhon Campus, 47160, Thailand
[4] Department of Chemistry, Faculty of Science, Mahasarakham University, 44150, Thailand
* Correspondence: kanokkan_pom@hotmail.co.th

Citation:
Worawut, K.; Phungpis, B.; Kaewkumsan, P.; Noppawan, P. Film Development of Chitosan from Mussel Shells and Pacific White Shrimp Shells. *ASEAN J. Sci. Tech. Report.* **2024**, *27*(4), e254066. https://doi.org/10.55164/ajstr.v27i4.254066

Article history:
Received: May 12, 2024
Revised: June 26, 2024
Accepted: June 27 2024
Available online: June 30, 2024

Abstract: The rapid expansion of Thailand's aquatic food processing industry has generated significant waste, prompting environmental concerns. This research aims to repurpose waste, specifically mussel and shrimp shells, to extract chitosan, a natural alternative to harmful chemicals. The primary goal is to create compostable packaging materials and preservation techniques while adding value to industry waste. The study investigated the properties of the extracted chitosan, optimized the chitosan films, and explored their use as paper coatings. The study thoroughly investigates mussel and shrimp shell-derived chitosan properties, including color value, pH, moisture, ash, and nitrogen content. Chitosan yield is 35% for mussel shells and 13.3% for shrimp shells, with a bright color and pH values of 7.32 and 7.26, respectively. Mussel shells have lower moisture (0.38%) and higher ash content (96.50%) compared to shrimp shells (4.07% moisture, 10.67% ash). Nitrogen content is 6.40% for mussel shells and 7.99% for shrimp shells. Regarding chitosan films, Method 4, a mixture of cassava starch and chitosan at a 1:0.6 ratio with 40% glycerol by weight, is identified as the optimal production method. The resulting chitosan-coated paper exhibits similar properties, making it suitable for sustainable packaging. Therefore, this research emphasizes repurposing waste from the aquatic food processing industry to promote sustainability and create livelihoods for farmers while addressing environmental challenges. Mussel shells are recommended as the primary raw material due to their larger volume and lower cost than shrimp shells. This research highlights chitosan's potential to address environmental issues and foster sustainable practices in the food processing industry.

Keywords: Chitosan; mussel shell; Pacific white shrimp shells; biodegradable film

1. Introduction

Thailand boasts aquatic food processing industries across all regions, a vital component of the country's economic framework. However, this industry generates significant waste during production, contributing to growing environmental concerns regarding non-biodegradable waste accumulation. Addressing this issue has spurred research efforts to repurpose these wastes into valuable products, presenting an alternative means of deriving value from food processing byproducts [1]. In parallel, there has been a shift in the consciousness of both citizens and aquaculture operators towards nature conservation and environmental preservation. This shift has led to innovative approaches in agriculture, replacing harmful chemicals with natural alternatives, such as chitin and chitosan, which can be extracted from waste materials such as crab, mussels, and shrimp shells [2].

Chitin, abundant in nature, is the second most common biopolymer after cellulose, with an estimated annual production of 10^{10}-10^{12} tons [3]. Structurally, chitin is similar to cellulose, with an acetamide group (-$NHCOCH_3$) at the C-2 position. Chitosan, derived from chitin through deacetylation, is a linear, polycationic heteropolysaccharide composed of β-1,4-2-deoxy-2-amino-D-glucopyranose and β-1,4-2-deoxy-2-acetamido-D-glucopyranose glycosidic linkages [4]. Chitin and chitosan possess unique physical, chemical, and biological properties, making them valuable in various applications, including immunostimulation, antimicrobial properties, and metal ion absorption in water treatment [5,6]. Chitosan is versatile and can undergo chemical modifications [7], finding application in pharmaceuticals, textiles, agriculture, cosmetics, food, and water treatment [8-14].

The widespread use of plastics in the food industry, including films, bags, and trays, has raised concerns about their detrimental effects on human health and the environment. Plastics are non-renewable and non-biodegradable, contributing to soil, water, and air pollution. Additionally, they release harmful gases when burned, leading to various health issues. The increasing demand for plastics, particularly in food packaging, exacerbates these problems [15]. To address these issues, there is a growing need for environmentally friendly alternatives, such as naturally degradable films and coatings derived from renewable sources like polysaccharides [16].

Chitosan's versatile applications extend to food preservation, which can be used as a coating for food items, vegetables, and fruits to prolong their freshness [17]. Additionally, research suggests that chitosan holds promise as a food packaging agent, primarily in the form of edible films derived from agricultural waste materials [18-21]. Chitosan's appeal stems from its renewable source and its environmental advantages, aligning with sustainability goals [22]. Recent research has focused on developing biodegradable films based on chitosan. Bajić et al. compared films with natural plant extracts like oak, hop, and brown algae, noting variations in moisture content, tensile strength, antibacterial activity, and optical properties [23]. Wrońska et al. explored chitosan-based films as alternatives to plastic packaging [24]. Nguyen and coworkers investigated edible films with extracts like *Piper Betle* L. and *Sonneratia ovata*, examining their effects on film color, surface morphology, and food preservation properties [25]. De Carli et al. enhanced chitosan films with propolis extract for improved antioxidant and antimicrobial activities [26]. In addition, Kamdem and coworkers created composite films with xylan and carvacrol, focusing on mechanical properties and thermogravimetric behavior [27]. Zehra et al. optimized films using response surface methodology, adjusting chitosan, glycerol, and drying temperatures [28]. Bhargavi and coworkers compared films with natural extracts, assessing their structural, physicochemical, and antibacterial properties [29]. These studies highlight the importance of chitosan in developing biodegradable films. Furthermore, investigations into chitosan's use as a coating for paper products have shown promise. This is because chitosan uniquely forms robust films and fibers with low oxygen gas permeability. When applied to paper, chitosan enhances mechanical properties and tear strength and renders the paper more opaque. However, it is important to note that chitosan does not effectively block water vapor [30].

Driven by this interest, the researcher has embarked on a project to explore and advance the creation of compostable packaging materials using waste derived from aquatic animal processing. This endeavor encompasses not only the development of packaging materials but also the establishment of preservation techniques. Central to this effort is the extraction of chitosan, a vital component found in mussel and white shrimp shells, employing chemical methods that yield the highest quantity and quality of chitosan, adhering to the standards used in Thailand's food production industry. The overarching goal is to produce high-quality packaging materials serving various stakeholders, including entrepreneurs, farmers, and the general public. By disseminating academic knowledge about chitin and chitosan extraction methods and using these extracts in packaging materials, the project aims to facilitate the creation of sustainable livelihoods for farmers. Additionally, it seeks to add value to the waste generated by the fisheries food processing sector and, in doing so, contribute to mitigating future environmental challenges associated with these industries. As such, this study aims to repurpose waste from Thailand's aquatic food processing industry, specifically mussel and shrimp shells, by extracting chitosan to create compostable packaging materials and preservation techniques.

The characterization of the extracted chitosan, the optimization of chitosan films, and their application as paper coatings were investigated.

2. Materials and Methods

2.1 Preparation of mussel and shrimp chitosan

Figure 1 illustrates the step-by-step process for preparing mussel chitosan and shrimp chitosan. First, mussel shells and shrimp shells were collected and cleaned. This involved separating the meat and fat from the shells and thoroughly washing the shells with clean water. Subsequently, the cleaned shells were left to dry in the sun until completely moisture-free. Once dry, the shells underwent further treatment. Initially, they were treated with 4% HCl at room temperature for four days to demineralize them. After this treatment, the demineralized shells were filtered, and any remaining impurities were washed away using distilled water. To remove protein from the sample, 4% NaOH was added to the dried demineralized shells at room temperature for four days. The resulting mixture was filtered to separate insoluble solids and washed with distilled water. The deproteinized shells were then immersed in 95% alcohol (1 g: 20 ml ratio) with continuous stirring for five minutes, followed by a thorough rinse with distilled water. They were subsequently dried in an oven at 80 °C. The deacetylation of chitin was accomplished by reacting the dried chitin with 40% NaOH, with the reaction mixture heated to 140 °C and stirred for 15 minutes. The alkali was drained, and the remaining material was washed repeatedly with distilled water until it reached a neutral pH of 7. Finally, the chitosan was dried in an oven at 100 °C for one hour. The chitosan was then ground into a fine, homogenized powder with a particle size of 4 mesh. The percentage yield of mussel chitosan and shrimp chitosan was determined as follows:

$$\text{chitosan yield (\%)} = \frac{\text{weight of extracted chitosan}}{\text{weight of starting shells}} \times 100$$

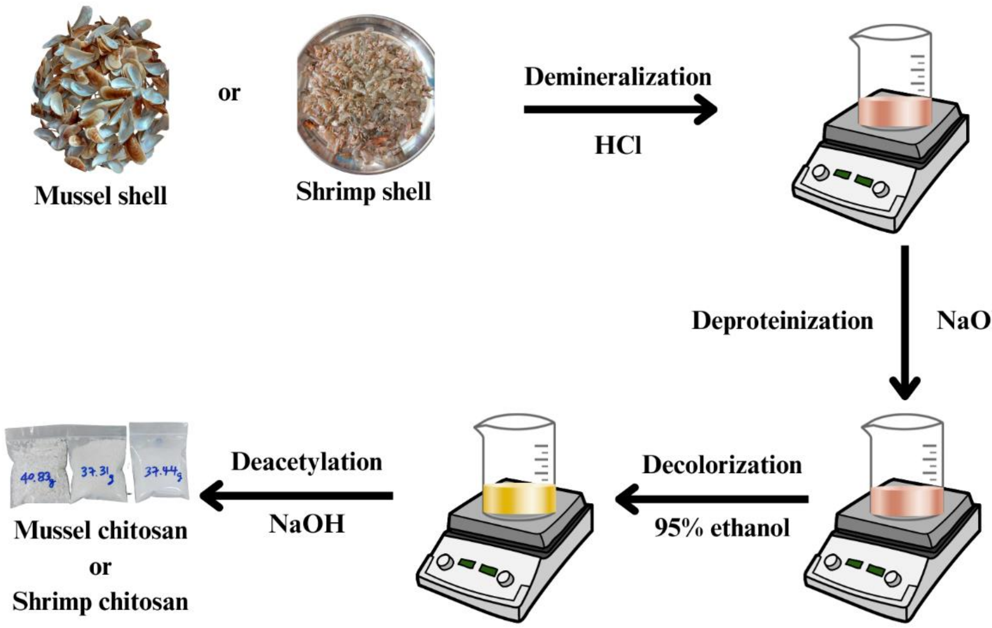

Figure 1. Extraction of chitosan from mussel and shrimp shells wastes.

2.2 Characterization of extracted chitosan

2.2.1 Color

The color of the chitosan samples was assessed using a HunterLab Colorimeter. One gram of each sample was placed on a plate. The Colorimeter measured the color value of the chitosan sample, which was then compared to a standard reference value to determine the color difference in terms of lightness (ΔL*), redness (Δa*), and yellowness (Δb*). The total color difference (ΔE) was calculated as follows:

$$\Delta E = (\Delta L^{*2} + \Delta a^{*2} + \Delta b^{*2})^{0.5}$$

2.2.2 pH

The chitosan powder was dissolved in distilled water at a concentration of 1% (w/v). The mixture was stirred for 30 minutes, and the pH was measured using a pH meter.

2.2.3 Moisture, ash and nitrogen content

These properties were assessed using the A.O.A.C. 2000 method [31].

For moisture content analysis, the empty dish and lid were dried in the oven at 105 °C for 3 hours and then transferred to a desiccator to cool. The empty dish and lid were weighed. Approximately 3 g of the sample were weighed and placed in the dish, ensuring uniform spread. The dish with the sample was placed in the oven and dried for 3 hours at 105 °C. After drying, the dish with the partially covered lid was transferred to the desiccator to cool. The dish and its dried sample were then reweighed. The moisture content was calculated as follows:

$$\text{Moisture content (\%)} = \frac{\text{weight of the sample before drying - the weight of the sample after drying}}{\text{weight of the sample before drying}} \times 100$$

For ash content analysis, the crucible and lid were placed in the furnace at 550 °C overnight to burn off any surface impurities. The crucible was then cooled in a desiccator for 30 minutes. The crucible and lid were weighed to three decimal places. Approximately 5 g of the sample was placed in the crucible, then heated over a low Bunsen flame with the lid half-covered. Once fumes were no longer produced, the crucible and lid were placed in the furnace and heated at 550 °C overnight without covering the lid during heating. After heating, the lid was placed on the crucible to prevent loss of fluffy ash. The crucible was cooled in the desiccator. The ash, crucible, and lid were weighed once the sample turned gray. If the sample had not turned gray, the crucible and lid were returned to the furnace for further ashing. The ash content was calculated as follows:

$$\text{Ash content (\%)} = \frac{\text{weight of ash}}{\text{weight of sample}} \times 100$$

For nitrogen content analysis, approximately 1 g of the sample was weighed in a digestion flask, with distilled water used as a blank. Five grams of Kjeldahl catalyst and 20 milliliters of concentrated H_2SO_4 were added. The flasks were placed in an inclined position and heated gently until frothing ceased, then boiled briskly until the solution cleared. After cooling, 50 ml of distilled water was cautiously added. The flask was immediately connected to a digestion bulb on the condenser, with the tip immersed in 40 ml of 4% w/v boric acid solution and mixed indicator solution in the receiver. The flask was rotated to mix the contents thoroughly, then heated while 40% w/v NaOH was added dropwise until all NH_3 had distilled. The receiver was removed, the condenser tip was washed, and the distillate was titrated with standard 0.02 N HCl solution. The nitrogen content was calculated as follows:

$$\text{Nitrogen content (\%)} = \frac{(\text{volume of HCl}_{\text{sample titration}} - \text{volume of HCl}_{\text{blank titration}}) \times \text{N of HCl} \times 1.4}{\text{weight of sample}} \times 100$$

2.3 Preparation of chitosan film

Films were prepared using previous methods with modifications [32,33]. To prepare the cassava starch solution, cassava starch was dissolved in distilled water to achieve a concentration of 5% (w/v). The mixture was heated to a temperature range of 70-80 °C while stirring with an electromagnetic stirrer until a clear gel formed. The solution was then allowed to cool to room temperature. Chitosan solutions at concentrations of 1%, 2%, 3%, 4%, and 5% (w/v) were prepared by dissolving chitosan in a 1% (v/v) acetic acid solution. This solution was stirred and heated to 70-80 °C until the chitosan was dissolved entirely. The solution was then filtered and collected using a vacuum filter set and allowed to cool to room temperature. Six methods were followed to create bioplastic films from cassava starch mixed with chitosan, with three repetitions each.

Method 1: cassava starch film without chitosan (1:0 ratio)
Method 2: cassava starch film mixed with chitosan at a ratio of 1:0.2
Method 3: cassava starch film mixed with chitosan at a ratio of 1:0.4
Method 4: cassava starch film mixed with chitosan at a ratio of 1:0.6
Method 5: cassava starch film mixed with chitosan at a ratio of 1:0.8
Method 6: cassava starch film mixed with chitosan at a 1:1 ratio

For each method, 100 ml of the 5% concentrated cassava starch solution was mixed with 100 ml of the corresponding concentrated chitosan solution. Glycerol was added at 40% by weight of solids [32] to enhance film flexibility. The solution was thoroughly stirred with a magnetic stirrer to avoid creating air bubbles. The mixture was then poured onto a tray to form a film and allowed to dry at room temperature. Once dry, the film was removed. The method that yielded the best results was selected to test the film's properties further.

2.4 Characterization of prepared chitosan film

2.4.1 Film thickness Following the ASTM D-645 and D-374 standards [34]. A film with a diameter of 9 cm was cut, and its thickness was measured with a micrometer at five different locations. The center and all four corners of the film were measured, and the average film thickness was calculated.

2.4.2 Oxygen transmission Following the ASTMD 3985 – 8 standard [34]. A film was removed from the desiccator and placed on the greased surface. The system was set to carrier purge mode to purge the air. The flow rate was then reduced to the desired value. After flushing the system with nitrogen, the sensor was inserted to divert the carrier gas, which had passed through both sides of the diffusion cell, into the sensor. Oxygen was switched into the test-gas side of the diffusion cell, an action automated in newer systems. The sensor output current gradually increased and stabilized at a constant value. The steady-state voltage value of the oxygen transmission rate was recorded.

2.4.3 Tensile strength and elongation Following the ASTMD 882-91 standard [34]. A film measuring 6.5 x 2.4 cm with a depth of 1.2 cm was cut into dumbbell shapes. The tensile strength and elongation percentage were measured using a Texture Analyzer model TA.XT. Plus, with the grip separation load distance set to 27 mm. The tensile strength (TS) and elongation percentage (%E) were calculated.

2.5 Preparation of chitosan-coated paper

Straw paper was coated with chitosan solution derived from mussel shells and another from shrimp shells, selected from the successful preparation of chitosan film. Ten milliliters of each solution were applied onto a sheet of straw paper measuring 29.5 × 21.0 cm and allowed to dry at room temperature. This coating process was repeated once more, and then the properties of the paper were tested.

2.6 Characterization of prepared chitosan-coated paper

2.6.1 Paper thickness Following the TAPPI T441-om97 standard [35].

2.6.2 Water adsorption Following the TAPPI T441 om-09 standard [36]. The water absorption capacity of the paper sheet was measured using Cobb's test, according to the TAPPI T441 om-09 standard, with a Cobb Sizing Tester (Kumagai Riki Kogyo Co. Ltd, Japan). The water absorption value was calculated as follows:

Water absorption = (weight of the paper after testing- weight of the paper before testing) x 100

2.7 Statistical analysis

Each measurement was conducted three times for accuracy. The data were presented as the mean ± standard deviation (SD) and analyzed using SPSS with analysis of variance (ANOVA). Statistical significance was determined at $p < 0.05$.

3. Results and Discussion

3.1 Extraction of mussel chitosan and shrimp chitosan

Chitosan derived from mussel shells resulted in a significantly higher percentage yield by dry weight than shrimp shells ($p < 0.05$). Specifically, the percentage yields were 35% for mussel shells and 13.3% for white shrimp shells (Table 1).

Table 1. Yield, pH, moisture, ash, and nitrogen content of the extracted chitosan from mussel and shrimp shell wastes.

Source	Yield	Chitosan composition*			
		pH	**Moisture content**	**Ash content**	**Nitrogen content**
Mussel shells	35.0	7.32 ± 0.06	0.38 ± 0.03	96.05 ± 0.01	6.40 ± 0.57
Shrimp shells	13.3	7.26 ± 0.07	4.07 ± 0.02	10.67 ± 0.03	7.99 ± 0.14

mean ± standard deviation (SD) from three times measurement

3.2 Characterization of mussel chitosan and shrimp chitosan

Tables 1 and 2 present the properties of chitosan obtained from mussel and shrimp shells. During the extraction process, it was observed that both chitosan samples from shrimp shells and mussel shells had a white appearance. Chitosan obtained from mussel shells exhibited a higher ΔL^* value than shrimp shells, while the Δa^* and Δb^* values tended to decrease. This color change is attributed to removing pigments while eliminating minerals and proteins from the shells. The Δa^* and Δb^* values may be influenced by carotenoids, with more pigments likely extracted from shrimp shells. However, the ΔL^* values for chitosan from shrimp shells and mussel shells did not differ significantly ($p < 0.05$), likely due to the minimal remaining pigments, resulting in a predominantly bright and white appearance.

Table 2. Color parameters of the extracted chitosan from mussel and shrimp shell wastes.

Source	Color parameters*			
	ΔL*	**Δa***	**Δb***	**ΔE**
Mussel shells	80.04 ± 0.64	1.07 ± 0.05	7.06 ± 0.34	80.34 ± 0.67
Shrimp shells	76.43 ± 0.13	1.90 ± 0.03	16.15 ± 0.08	78.14 ± 0.14

mean ± standard deviation (SD) from four times measurement

The pH measurement of the obtained chitosan was crucial to confirm the thorough removal of the solvent during the extraction process, ensuring the chitosan's neutrality. This step was essential to prevent adverse effects on the chitosan's subsequent applications. The pH values for chitosan obtained from white shrimp shells and mussel shells were found to be similar ($p > 0.05$), approximately 7.26 and 7.32, respectively, closely aligning with the pH of the distilled water used in the experiment (7.21).

The moisture content test results indicated that chitosan from shrimp shells contained more moisture than chitosan from mussel shells, with values of 4.07% and 0.38%, respectively. The ash content serves as an indicator of efficiency in removing calcium carbonate. Chitosan obtained from mussel shells had a higher ash content than that from shrimp shells, at 96.50% and 10.67%, respectively, possibly due to the presence of various minerals initially contained in shrimp and mussel shells, which are lost during the mineral removal process to produce chitosan.

Furthermore, the nitrogen content in chitosan obtained from white shrimp shells was higher than that from mussel shells, with values of 7.99% and 6.40%, respectively. This difference may be attributed to the loss of amine groups and potential contamination from other compounds like ash, which remains in the chitosan. Additionally, the chitosan produced in this experiment exhibited solubility in various organic acids, such as acetic acid and lactic acid. This suggests that removing the acetyl group enhances the presence of free amino groups, increasing the chitosan's positive charge and solubility [37].

From FT-IR spectra of chitin from mussel shells, the presence of the carbonyl (C=O) functional group in the amide molecule was detected at a wave number of 1655 cm^{-1}, along with the –N-H (bending) functional group at a wavenumber of 1554 cm^{-1}. Similarly, in the chitin portion derived from shells, the carbonyl functional group (C=O) of the amide molecule was identified at a wavenumber of 1655 cm^{-1}, while the –N-H (bending) functional group of the amide molecule was observed at a wavenumber of 1553 cm^{-1}. Moving on to the FT-IR spectra of chitosan from mussel shells, the amine molecule's functional group –N-H (bending) was detected at a wavenumber of 1589 cm^{-1}. Likewise, in the chitosan section obtained from shrimp shells, the amine molecule's functional group –N-H (bending) was also observed at a wavenumber of 1589 cm^{-1}.

3.3 Characterization of chitosan film

Cassava starch results in a hard and brittle film that is unsuitable for direct production into packaging material. To enhance the film's properties, making it stronger and more flexible, this experiment incorporated chitosan at various ratios and used glycerol as an additive. Research suggests that chitosan aids in the formation of cassava starch sheets and improves mechanical properties, particularly tensile strength [38]. Glycerol, on the other hand, enhances the film's flexibility and its resistance to water vapor permeability [39]. Glycerol is recognized as one of the most effective plasticizers for films. Compared to sorbitol and polyethylene glycol, it was selected as the preferred option at a concentration of 40% by weight of the solid material. This choice is based on reports indicating that glycerol contributes to superior film properties across various aspects [32].

The optimal process for producing chitosan film was Method 4, which involves creating a film by blending cassava starch and chitosan in a 1:0.6 ratio. The experimental findings revealed that this film could be easily formed into sheets, exhibiting flexibility that facilitated its removal from the acrylic mold. The resulting film was translucent, although it became slightly yellowish with higher chitosan content. Subsequently, various properties of the chitosan film, such as thickness, oxygen gas permeability, tensile strength, and elongation, were assessed, and the results are presented in Table 3.

Table 3. The thickness, oxygen transmission, tensile strength, and elongation of chitosan films from mussel and shrimp shell wastes.

Property	Chitosan film		
	No chitosan	**Mussel chitosan**	**Shrimp chitosan**
Thickness (mm)	0.28 ± 0.05	0.28 ± 0.07	0.29 ± 0.07
Oxygen transmission (cm^3/m^2/day)	1.35 ± 0.05	2.56 ± 0.07	2.61 ± 0.06
Tensile strength (kF/cm^2)	55.56 ± 0.79	120.8 ± 0.71	122.2 ± 0.56
Elogation (%)	70.59 ± 0.80	25.88 ± 0.93	23.71 ± 0.99

Table 3 indicates that the films without chitosan and those with chitosan derived from shrimp and mussel shells exhibit similar thicknesses: 0.282 mm, 0.288 mm, and 0.282 mm, respectively.

The oxygen transmission rate (OTR) assessment reveals that chitosan starch film exhibits excellent resistance to oxygen permeability, as indicated by OTR values less than 50 cm^3/m^2/day, in line with previous findings [40]. Specifically, the OTR values fall within the range of 2.56-2.61 cm^3/m^2/day due to the crystalline structure of the powder and the cohesive forces held within the molecule through hydrogen bonds. This structural arrangement results in limited gas permeability [41], increasing values as the chitosan content rises. Significantly different values ($p<0.05$) were observed as follows: Films with a starch-to-chitosan ratio of 1:0 and 1:0.6 exhibited OTR values of 1.35, 2.61 (Shrimp chitosan), and 2.56 (mussel chitosan) cm^3/m^2/day, respectively. This variation in OTR values can be attributed to the processing of chitosan-starch film, wherein heat and humidity potentially reduce the crystallinity of both starch and chitosan, creating more space within the molecules. Consequently, this allows for increased gas permeability.

Tensile Strength (TS) is significantly influenced by adding chitosan due to its capacity to enhance film strength, consistent with prior research findings [39]. Consequently, films containing chitosan exhibit higher tensile strength values. Specifically, films lacking chitosan had the lowest TS value of 55.56 kF/cm^2. In contrast, cassava starch films with a starch-to-chitosan ratio of 1:0.6, derived from mussel shells and white shrimp shells, demonstrated TS values of 120.8 kF/cm^2 (11.85 MPa) and 122.2 kF/cm^2 (11.98), respectively. These values are comparable to the TS of blended chitosan film with tapioca starch (10.87 MPa) reported by Chillo [39] and to blended films with natural extracts (5.5-12.7 MPa) reported by Bajić [23] and Nguyen [25] (4.8-18.1 MPa). Adding chitosan from both sources indicates a substantial increase in tensile strength.

The film's percentage elongation (E) exhibited a consistent decrease with an increase in the chitosan ratio. This phenomenon aligns with the behavior of tensile strength in the film; when a film possesses higher tensile strength, it tends to have a lower percentage of elongation or stretching capability. Notably, the starch film lacking chitosan displayed the highest E value at 70.59%. This difference was statistically significant ($p<0.05$), likely because starch molecules could interact effectively with glycerol without interfering with chitosan molecules. Glycerol contributed to improved film flexibility, enabling it to stretch well. Subsequently, the film made from cassava starch mixed with chitosan at a ratio of 1:0.6, combining starch with chitosan from mussel shells and chitosan from white shrimp, demonstrated E values of 25.88 and 23.71, respectively. These values did not significantly differ ($p<0.05$). The reduced elongation percentage can be attributed to increased interaction forces between starch and chitosan molecules, resulting in a stronger film with reduced stretchability [39]. However, these results are consistent with the report on blended films with natural extracts, which showed E values of 14-31%, as reported by Bajić [23] and 10-30% by Nguyen [25].

3.4 Characterization of chitosan-coated paper

After applying the chitosan solution from white shrimp shells and the chitosan solution from mussel shells to the paper, the paper's thickness was measured at 0.44 mm and 0.46 mm, respectively. Regarding water absorption, both exhibited similar values of 0.05 g/cm² and 0.04 g/cm², respectively. These results suggest no significant differences ($p>0.05$) in the properties of the two types of coated straw paper. This lack of differentiation could be attributed to the consistent solution applied to both types, which may not have significantly impacted the paper thickness, as depicted in Table 4.

Table 4. Physical properties of chitosan uncoated and coated papers.

Property	Paper type		
	Chitosan uncoated	**Mussel chitosan coated**	**Shrimp chitosan coated**
Thickness (mm)	0.21 ± 0.03	0.46 ± 0.02	0.44 ± 0.03
Water adsorption (g/cm²)	0.03 ± 0.003	0.04 ± 0.006	0.05 ± 0.005

4. Conclusions

The research findings demonstrate the successful extraction of chitosan from mussel and shrimp shells, yielding varying percentages. Characterization of the chitosan obtained from these sources has confirmed its neutrality, rendering it suitable for various applications. Furthermore, the research has shed light on the potential of chitosan-coated paper as a sustainable alternative to plastic packaging, boasting similar thickness and water absorption properties. In conclusion, this research underscores the significance of repurposing waste materials from aquatic food processing, such as shells, to harness the value of chitosan for sustainable packaging solutions. It addresses pressing environmental concerns and plays a pivotal role in fostering sustainable livelihoods and mitigating future challenges within the food processing industry, making it a substantial contribution to the field.

5. Acknowledgements

We want to express our deep appreciation for the generous research funding the National Research Council of Thailand (NRCT) provided and the unwavering support from the research facility at Rajamangala University of Technology Isan, Sakon Nakhon Campus.

Author Contributions: Conceptualization, K.W. and P.K.; methodology, K.W.; writing—original draft preparation, K.W.; writing—review and editing, K.W., P.N., and B.P. All authors have read and agreed to the published version of the manuscript.

Funding: This research received funding from the National Research Council of Thailand (NRCT).

Conflicts of Interest: The authors declare no conflict of interest.

References

[1] Avérous, L.; Fringant, C.; Moro, L. Plasticized starch–cellulose interactions in polysaccharides composites. *Polymer* **2001**, *42*, 6565-6572.

[2] Arancibia, M.Y.; Aleman, A.; Calvo, M.M.; Lopez-Caballero, M.E.; Montero, P.; Gomez-Guillen, M.C. Antimicrobial and antioxidant chitosan solutions enriched with active shrimp (*Litopenaeus vannamei*) waste materials. *Food Hydrocoll*. **2014**, *35*, 710-717.

[3] Je, J.Y.; Kim, S.K. Antimicrobial action of novel chitin derivative. *Biochimica et Biophysica Acta* **2006**, *1760*, 104-109.

[4] Costa, E.M.; Silva, S.; Pina, C.; Tavaria, F.K.; Pintado, M.M. Evaluation and insights into chitosan antimicrobial activity against anaerobic oral pathogens. *Anaerobe* **2012**, *18*, 305-309.

[5] Begin, A.; Calsteren, M.R.V. Antimicrobial films produced from chitosan. *Int. J. Biol. Macromol.* **1999**, *26*, 63-67.

[6] Ngo, D.-N.; Kim, M.-M.; Kim, S.-K. Chitin oligosaccharides inhibit oxidative stress in live cells. *Carbohydr. Polym*. **2008**, *74*, 228–234.

[7] Rinaudo, M. Chitin and chitosan: Properties and applications. *Prog. Polym. Sci*. **2006**, *31*, 603–632.

[8] Arvanitoyannis, I.S.; Nakayama, A.; Aiba, S.-I. Chitosan and gelatin based edible films: State diagrams, mechanical and permeation properties. *Carbohydr. Polym*. **1998**, *37*, 371–382.

[9] Elassal, M.; El-Manofy, N.Chitosan nanoparticles as drug delivery system for cephalexin and its antimicrobial activity against multiidrug resistent bacteria. *Int. J. Pharm. Sci*. **2019**, *11*, 14–27.

[10] Haque, T.; Chen, H.; Ouyang, W.; Martoni, C.; Lawuyi, B.; Urbanska, A. M.; Prakash, S. Superior cell delivery features of polyethylene glycol incorporated alginate, chitosan, and poly-L-lysine microcapsules. *Mol. Pharmaceutics* **2005**, *2*, 29–36.

[11] Kim, H.-J.; Chen, F.; Wang, X.; Rajapakse, N.C. Effect of chitosan on the biological properties of sweet basil (*Ocimum basilicum* L.). *J. Agric. Food Chem*. **2005**, *53*, 3696–3701.

[12] Verbeeck, R.M.H.; Haiben, M.; Thin, H.P.; Verbeek, F. Solubility and solution behaviour of strontium hydroxyapatite. *Zeitschrift für Physikalische Chemie* **1977**, *108*, 203–215.

[13] Yamada, K.; Akiba, Y.; Shibuya, T.; Kashiwada, A.; Matsuda, K.; Hirata, M. Removal of phenol compounds by the combined use of tyrosinase and chitosan. *Abstr. Pap. Am. Chem. Soc.* **2005**, *230*, U4039.

[14] Yen, M.-T.; Yang, J.-H.; Mau, J.-L. Physicochemical characterization of chitin and chitosan from crab shells. *Carbohydr. Polym*. **2009**, *75*, 15–21.

[15] Mollah, M.Z.I.; Akter, N.; Quader, F.B.; Sultana, S.; Khan, R.A. Biodegradable Colour Polymeric Film (Starch-Chitosan) Development: Characterization for Packaging Materials. *Open J. Org. Polym. Mater*. **2016**, *6*, 11-24.

[16] Dai, H.; Chang, P.R.; Yu, J.; Ma, X. *N,N*-Bis(2-hydroxyethyl)formamide as a New Plasticizer for Thermoplastic Starch. *Starch* **2008**, *60*, 676-684.

[17] Klinsoda, J. Edible coating and film for vegetables and fruits. *Food J*. 2016, 46, 33-37.

[18] Fan. W.; Sun, J.; Chen, Y.; Zhang, Y.; Chi, Y. Effect of chitosan coating on quality and shelf life of silver carp during frozen storage. *Food Chem.* **2009**, *115*, 66-70.

[19] Suman, S.P.; Mancini, R.A.; Joseph, P.; Ramanathan, R.; Konda, M.K.R.; Dady, G.; Yin, S. Packaging-specific influence of chitosan on color stability and lipid oxidation in refrigerated ground beef. *Meat Sci.* **2010**, *86*, 994-998.

[20] Petrou, S.; Tsiraki, M.; Giatrakou, V.; Savvaidis, I.N. Chitosan dipping or oregano oil treatments, singly or combined on modified atmosphere packaged chicken breast meat. *Int. J. Food Microbiol.* **2012**, *156*, 264-271.

[21] Imsombut, T.; Tansupo, P.; Pholhan, D. Preparation and characterization of chitosan/silk sericin blend films for use as drug delivery. *Research report* **2014**, pp. 5-8.

[22] Tapia-Blácido, D.; Sobral, P.J.A.; Menegalli, F.C. Development and characterization of edible films based on amaranth flour (*Amaranthus caudatus*). *J. Food Eng*. **2005**, *67*, 215–223.

[23] Bajić, M.; Ročnik, T.; Oberlintner, A.; Scognamiglio, F.; Novak, U.; Likozar, B. Natural plant extracts as active components in chitosan-based films: A comparative study. *Food Packaging Shelf*. **2019**, *21*, 100365.

[24] Wrońska, N.; Katir, N.; Nowak-Lange, M.; El Kadib, A.; Lisowska, K. Biodegradable chitosan-based films as an alternative to plastic packaging. *Foods*. **2023**, *12*, 3519.

[25] Nguyen, T.T.; Pham, B-T.T.; Le, H.N.; Bach, L.G.; Thuc, C.N.H. Comparative characterization and release study of edible films of chitosan and natural extracts. *Food Packaging Shelf.* **2022**, *32*, 100830.

[26] De Carli, C.; Aylanc, V.; Mouffok, K.M.; Santamaria-Echart, A.; Barreiro, F.; Tomás, A.; Pereira, C.; Rodrigues, P.; Vilas-Boas, M.; Falcão, S.I. Production of chitosan-based biodegradable active films using bio-waste enriched with polyphenol propolis extract envisaging food packaging applications. *Int. J. Biol. Macromol.* **2022**, *213*, 486-497.

[27] Kamdem, D.P.; Shen, Z.; Nabinejad, O.; Shu, Z. Development of biodegradable composite chitosan-based films incorporated with xylan and carvacrol for food packaging application. *Food Packaging Shelf.* **2019**, *21*, 100344.

[28] Zehra, A.; Wani, S.M.; Jan, N.; Bhat, T.A.; Rather, S.A.; Malik, A.R.; Hussain, S.Z. Development of chitosan-based biodegradable films enriched with thyme essential oil and additives for potential applications in packaging of fresh collard greens. *Sci. Rep.* **2022**, *12*, 16923.

[29] Bhargavi, U.; Keerthi, S.; Behera, P.; Sushmitha, M.; Padma, M. Development of biodegradable film from chitosan and lemongrass essential oil for food packaging applications. *Indian J. Ecol.* **2023**, *50*, 1563-1568.

[30] Khwaldia K.; Arab-Tehrany, E.; Desobry, S. Biopotymer coatings on paper packaging materials. *Compr. Rev. Food Sci. Food Saf.* **2010**, *9*, 82-91.

[31] AOAC. *Official Methods of Analysis*, 17th Ed.; The Association of Official Analytical Chemists, Gaithersburg, MD, USA. **2000**.

[32] Bourtoom, T. Plasticizer effect on the properties of biodegradable blend film from rice starch-chitosan. *Songklanakarin J. Sci. Technol.* **2008**. *30*, 149-165.

[33] Bourtoom, T.; Chinan M.S. Preparation and properties of rice starch-chitosan blend biodegradable film. *LWT - Food Sci. Technol.* **2008**, *41*, 1633-1641.

[34] ASTM. *Standard Test Methods for Tensile Properties of Thin Plastic Sheeting, Method D882-00*; American Society for Testing and Materials, Philadelphia, **2000**.

[35] The Technical Association of the Pulp and Paper Industry (TAPPI). Thickness (caliper) of paper, paperboard, and combined board, T411-om97, Georgia, **1997**.

[36] The Technical Association of the Pulp and Paper Industry (TAPPI). Water absorptiveness of sized (non-bibulous) paper, paperboard, and corrugated fiberboard (Cobb test), T411-om09, Georgia, **2013**.

[37] Roberts, G. A. F. Chitosan production routes and their role in determining the structure and properties of the product.- In Proceedings of International conference; 7th, Chitin and chitosan. Lyon. France. 1st January 1997. Domard, A., Roberts, G. A. F., Varum, K. M. (Eds.). Publisher: Jacques Andre, **1997**.

[38] Liu, L. Bioplastics in food packaging: Innovative technologies for biodegradable packaging. *San Jose State University Packaging Engineering* **2006**, *13*, 1348–1368.

[39] Chillo, S.; Flores, S.; Mastromatteo, M.; Conte, A.; Gerschenson, L.; Del Nobile, M.A. Influence of glycerol and chitosan on tapioca starch-based edible film properties. *J. Food Eng.* **2008**, *88*, 159-168.

[40] Selleh, E.; Muhamad, I.I.; Khairuddin, N. Structural Characterization and Physical Properties of Antimicrobial (AM) Starch-Based Films. *World Academy of Science, Engineering and Technology, International Journal of Biological, Biomolecular, Agricultural, Food and Biotechnological Engineering* **2009**, *3*, 352-360.

[41] Vartiainen, J.; Harlin, A. Crosslink as an Efficient Tool for Decreasing Moisture Sensitivity of Biobased Nanocomposite Films. *Materials Sciences and Applications* **2011**, *2*, 346-354.

ASEAN
Journal of Scientific and Technological Reports
Online ISSN:2773-8752

Research article

Valorization of Agro-industrial Solid Waste by Two-stage Anaerobic Digestion for Biohythane Production

Jetsada Tawantum[1,2], Nantakan Muensit[3,4*], Ponsit Sathapondecha[5], and Chonticha Mamimin[2]

[1] Division of Science for Industry, Faculty of Science, Prince of Songkhla University, Songkhla, 90110, Thailand
[2] Bio4gas (Thailand) Company Limited, Phatthalung, 93210, Thailand
[3] Division of Physical Science (Physics), Faculty of Science, Prince of Songkhla University, Songkhla, 90110, Thailand
[4] Center of Excellence in Nanotechnology for Energy (CENE), Songkhla, 90110, Thailand
[5] Division of Molecular Biotechnology and Bioinformatics, Faculty of Science, Prince of Songkhla University, Songkhla, 90110, Thailand
* Corresponding authors: nantakan.m@psu.ac.th

Citation:
Tawantum, J., Muensit, N., Sarhapondecha, P., Mamimin, C. Valorization of agro-industrial solid waste by two-stage anaerobic digestion for biohythane production. *ASEAN J. Sci. Tech. Report.* **2024**, *27*(4), e253769. https://doi.org/10.55164/ajstr.v27i4.253769

Article history:
Received: April 21, 2024
Revised: May 20, 2024
Accepted: May 21, 2024
Available online: June 30, 2024

Abstract: This study investigated the valorization of agro-industrial solid waste for biohythane production through a two-stage anaerobic digestion process. Seventeen waste samples were characterized, revealing diverse physico-chemical properties suitable for anaerobic digestion. The highest biohythane yields were obtained from waste-activated sludge (WAS) from a frozen convenience food wastewater treatment plant (895.63 mL/g VS), WAS from a processed chicken wastewater treatment plant (835.73 mL/g VS), and WAS from a municipal wastewater treatment plant (830.79 mL/g VS). Kinetic analysis using the modified Gompertz model provided insights into the biohythane production potential, with predicted yields ranging from 0 to 111.85 mL/g VS and production rates from 0 to 21.37 mL/d. The comparative analysis highlighted the superior biohythane production potential of the studied waste materials compared to other substrates, such as food waste (180.5 mL/g VS) and sugarcane bagasse (165.2 mL/g VS). The highest hydrogen and methane contents in the produced biohythane were 26.57% and 67.85%, respectively. The techno-economic assessment of scaled-up biohythane production demonstrated the economic feasibility, with a payback period of 2.05 years for a plant capacity of 100 ton waste/day, a biohythane yield of 500 m^3/ton waste, and a biohythane production of 50,000 m^3/day. The capital cost was estimated at 15 million USD, with an operating cost of 0.2 USD/m^3 biohythane and a revenue of 0.6 USD/m^3 from biohythane sales. The results of this study demonstrate the high potential of agro-industrial solid waste valorization for biohythane production and its contribution to sustainable waste management and renewable energy production.

Keywords: Agro-industrial solid waste; Biohythane; Waste valorization; Sustainable energy; Circular economy

1. Introduction

The rapid growth of the global population, urbanization, and industrialization has led to an increasing demand for energy and the generation of vast amounts of waste. The world's energy consumption is expected to increase by nearly 50% between 2018 and 2050, with fossil fuels continuing to dominate the energy mix [1]. However, the reliance on fossil fuels has resulted in numerous environmental problems, such as greenhouse gas emissions, air pollution, and climate change [2]. Moreover, the improper management of waste, particularly in developing countries, has caused severe environmental and public health issues, including water and soil contamination, air pollution, and the spread of diseases [3]. In response to these challenges, there has been a growing interest in the development of sustainable and renewable energy sources, as well as the implementation of effective waste management strategies. Anaerobic digestion (AD) has emerged as a promising technology for valorizing organic waste, as it can simultaneously address waste management and renewable energy production [4]. AD is a biological process in which microorganisms break down organic matter in the absence of oxygen, producing biogas, which primarily consists of methane (CH_4) and carbon dioxide (CO_2) [5]. Agro-industrial solid waste, generated from various agricultural and industrial activities, represents a significant portion of the global waste stream. The world is estimated to generate approximately 1.3 billion tons of agro-industrial solid waste annually, with a large portion disposed of in landfills or left to decay in the open environment [6]. This waste, however, contains a substantial amount of organic matter and nutrients, making it a suitable feedstock for AD [7].

Conventional AD processes produce methane-rich biogas, which can be used for heat and electricity generation. However, recent advancements in AD technology have led to the developing of two-stage AD systems, which produce biohythane, a mixture of hydrogen (H_2) and methane [8]. A two-stage AD system separates the process into two distinct stages: hydrogen and methane production. During the first stage, hydrogen-producing bacteria, such as Clostridium and Enterobacter, convert the organic matter into hydrogen and volatile fatty acids (VFAs). In the second stage, methanogens convert the VFAs and remaining organic matter into methane [9]. The production of biohythane through two-stage AD offers several advantages over conventional single-stage AD. First, biohythane has a higher energy content compared to methane-rich biogas, as hydrogen has a higher calorific value (122 kJ/g) than methane (50 kJ/g) [10]. Second, separating the hydrogen and methane production stages allows for optimizing process conditions, such as pH and hydraulic retention time (HRT), for each stage, improving overall process efficiency [11]. Third, hydrogen production in the first stage can enhance the biodegradability of the substrate, as it helps in the hydrolysis of complex organic compounds, making them more accessible for methanogens in the second stage [12]. Despite the promising potential of biohythane production from agro-industrial solid waste, challenges still need to be addressed. One of the main challenges is the variability in the composition and characteristics of the waste, which can affect the performance and stability of the AD process [4]. Another challenge is the optimization of process parameters, such as substrate concentration, inoculum ratio, and temperature, to maximize biohythane yield and quality [7]. Moreover, the scale-up and economic viability of biohythane production systems needs to be evaluated to ensure their successful implementation in real-world applications [8]. Several studies have investigated the potential of biohythane production from various agro-industrial solid waste streams. For example,[4] studied the co-digestion of pig manure and rice straw for biohythane production and achieved a maximum biohythane yield of 333.5 mL/g volatile solids (VS) with a hydrogen content of 38.6%. [7] investigated the use of palm oil mill effluent (POME) and oil palm empty fruit bunches (EFB) for biohythane production and obtained a maximum biohythane yield of 181.9 mL/g VS with a hydrogen content of 28.4%. [9] explored the potential of food waste for biohythane production and reported a maximum biohythane yield of 254.7 mL/g VS with a hydrogen content of 35.6%.

Therefore, this study aims to investigate the valorization of agro-industrial solid waste streams, including waste-activated sludge (WAS) from different wastewater treatment plants, expired seasoning powder, and plant residues, for biohythane production through a two-stage AD process. The specific objectives of this study are to characterize the physicochemical properties of the agro-industrial solid waste samples and evaluate their suitability for biohythane production, to investigate the biohythane production potential of the waste samples through a two-stage AD process, and determine the optimal process parameters for maximum biohythane yield and quality, to perform a kinetic analysis of the biohythane production.

2. Materials and Methods

2.1 Characterization of agro-industrial solid waste


1.WAS from sugar and starch products wastewater treatment plant
2.WAS from tapioca starch wastewater treatment plant
3.WAS from frozen convenience food wastewater treatment plant
4.WAS from soft drink wastewater treatment plant
5.WAS from processed chicken wastewater treatment plant
6.expired seasoning powder
7.WAS from chemical product wastewater treatment plant
8.WAS from municipal wastewater treatment plant
9.WAS from cleaning solution product wastewater treatment plant
10.WAS from condiments processing wastewater treatment plant
11.WAS from the chemical product from the wastewater treatment plant
12.plans residue
13.WAS from sugar and starch products wastewater treatment plant
14.WAS from feedstuff wastewater treatment plant
15.WAS from processed chicken wastewater treatment plant
16.expired lime flavor seasoning powder
17.WAS from sugar and starch products wastewater treatment plant

Figures 1. Variety of agro-industrial solid waste materials

Solid waste materials were sourced from various agro-industrial sectors, including waste-activated sludge from sugar and starch products wastewater treatment plant, Purac (Thailand) Co., Ltd. (sample 1), waste-activated sludge from tapioca starch wastewater treatment plant, Ingredion (Thailand) Co., Ltd. (sample 2), waste activated sludge from frozen convenience food wastewater treatment plant, McKey Food Services (Thailand) Ltd. (sample 3), waste activated sludge from soft drink wastewater treatment plant, Suntory PepsiCo Beverage (Thailand) Co., Ltd. (sample 4), waste activated sludge from processed chicken wastewater treatment plant, GFPT Nichirei (Thailand) Co., Ltd. (sample 5), expired seasoning powder, Ajinomoto (Thailand) Co., Ltd. (sample 6), waste activated sludge from chemical product wastewater treatment plant, TPT Petrochemicals Public Co., Ltd. (sample 7), waste activated sludge, from municipal wastewater treatment plant, Pankornwattanakit Ltd., Part. (sample 8), waste-activated sludge from cleaning solution product wastewater treatment plant, Colgate Palmolive (Thailand) Ltd. (sample 9), waste-activated sludge from condiments processing wastewater treatment plant, Cofco Biochemical (Thailand) Co., Ltd. (sample 10), waste-activated sludge from the chemical product from the wastewater treatment plant, BBGI Biodiesel Co., Ltd. (sample 11), plans residue, McCormick (Thailand) Co., Ltd. (sample 12), waste activated sludge from sugar and starch products wastewater treatment plant, Purac (Thailand) Co., Ltd. (sample 13), waste activated sludge from feedstuff wastewater treatment plant, CPF (Thailand) Public Co., Ltd. (sample 14), waste activated sludge from processed chicken wastewater treatment plant, Sun Food International Co., Ltd. (sample 15), expired lime flavor seasoning powder, Ajinomoto (Thailand) Co., Ltd. (sample 16), waste activated sludge from sugar and starch products wastewater treatment plant, Purac (Thailand) Co., Ltd.

(sample 17). The visualization of solid waste is shown in Figure 1. All samples were collected from each source using sterile containers and stored at 4°C until further analysis. The chemical and physical composition of the waste materials was determined using standard methods. Total solids, volatile solids, moisture, and ash content were determined according to [13]. Carbohydrate content, protein, total sugar, oil, and grease were analyzed using standard methods for examining water and wastewater [13]**.** The cellulose, hemicellulose, and lignin were analyzed following the protocol described by Van Soest et al. [14]. Volatile fatty acids (VFAs) were analyzed using a gas chromatograph (GC).

2.2 Preparation of inoculum for hydrogen and methane production

Seed sludge for hydrogen and methane production was collected from a local anaerobic digester and pretreated by the load-shock method to remove unwanted materials and enhance microbial activity [15]. Briefly, the sludge was mixed with a nutrient solution containing glucose (10 g/L), yeast extract (2 g/L), and peptone (5 g/L) and incubated at 40°C for 24 hours to activate the hydrogen-producing bacteria. For methane production, methane-producing microorganisms were obtained from the biogas production system and mixed with POME as a substrate at a ratio of 4:1 (v/v). The mixture was adjusted to a pH range of 7-8 using 1M NaOH and 1M HCl. The alkalinity was maintained at 5 g/kg of $CaCO_3$. The inoculum was incubated at 40°C for two weeks in a 1 L anaerobic reactor. Biogas production was monitored daily using a gas counter. Biogas composition was analyzed weekly using gas chromatography with a thermal conductivity detector (GC-TCD) (Gas Chromatography, CG-8A, Shimadzu). The inoculum was considered ready for use when it achieved a stable biogas production rate and a microbial sludge concentration of at least 50 g/L [7]. The microbial communities of inoculum, sampling each inoculum, were extracted for DNA using PowerSoil DNA kit (MO BIO, Carlsbad, CA, USA) and were analyzed with 16s rRNA sequencing using MiSeq technology in the V3–V4 regions of the bacterial and archaeal 16S rRNA gene fragments as described by [16].

2.3 Evaluation of hydrogen and methane production potential

The potential of various solid waste materials to produce hydrogen and methane was evaluated using a two-step fermentation process. Each solid waste material was mixed with the hydrogen-producing inoculum at a 4:1 VS basis ratio with a working volume of 200 mL in a 500 mL fermentation bottle. The bottles were purged with N_2:CO_2 (80:20) to maintain the anaerobic condition and sealed with silicone and aluminum caps using a hand crimper. The bottles were incubated at 40°C for 7 days, and the volume of biogas produced was measured daily using the water displacement method [15]. After the hydrogen fermentation step, the effluent from each bottle was mixed with the methane-producing inoculum at a 2:1 VS basis ratio. The bottles were purged with N_2:CO_2 (80:20), sealed, and incubated at 40°C for 45 days. Biogas production was monitored daily, and biogas composition was analyzed weekly using GC-TCD. All experiments were conducted in triplicate, and the results were expressed as mean± standard deviation.

2.4 Analytical methods

The contents of cellulose, hemicellulose, and lignin in wastes were determined following the protocol described by [14]. Alkalinity, chemical oxygen demand (COD), pH, total solids (TS), and volatile solids (VS) were determined following the standard methods described by [13]. The volume of biogas produced in the headspace of the fermentation bottles was measured daily using the water displacement method. The volume of gas produced was equivalent to the amount of water displaced in the cylinder. Continuous biogas volume was measured via a digester headspace connection to the gas counter using the water displacement method [17]. Biogas composition was analyzed by gas chromatography (GC-8A Shimadzu) equipped with Thermal Conductivity Detectors (GC-TCD) and fitted with a 2.0 m packed column (Shin-Carbon ST 100/120 Restek). Argon was used as a carrier gas at a flow rate of 15 mL min^{-1}. The injection port, oven, and detector temperatures were set at 120 ºC, 50 ºC, and 100 ºC, respectively [18]. Gas samples of 0.5 mL were injected in duplicate. The temperature of the injection port was 230 ºC. The chromatography program was as follows: 70 ºC for 1 min, ramping from 70 to 180 ºC at a rate of 20 ºC $min^{-1,}$ and holding at 180 ºC for 6 min. The detector temperature was 250 ºC. Gas measurements were reported under STP conditions (standard temperature and pressure, 273 K, 1.01325 Pa). Volatile fatty acids (VFAs) were analyzed using a Gas Chromatograph (GC) equipped with a Flame Ionization Detector (FID). The GC system was an Agilent 7890A (Agilent Technologies, USA) fitted with a DB-FFAP capillary column (30 m × 0.25 mm ID × 0.25 µm film thickness; J&W Scientific, USA).

2.5 Kinetic model and determination of hydrolysis constant

The kinetics of biogas production were described using a first-order kinetic model, as reported in a previous study. The first-order kinetic model is given by Equation 1

$$ln\frac{B_{\infty}-B}{B_{\infty}} = -K_h t \quad (1)$$

Where K_h is the constant biogas rate (d^{-1}), B_{∞} is the final methane production value, *B* is the methane produced at a given time, and *t* is the production time. To determine the hydrolysis constant (K_h), the experimental data of cumulative methane production (B) at different time points (t) were fitted to Equation 1 using linear regression. The slope of the linear regression line represents the hydrolysis constant (K_h). The lag phase before the start of methane production was determined using the modified Gompertz equation, as described in a previous study. The modified Gompertz equation is given by Equation 2:

$$M = P \cdot exp\left\{-exp\left[\frac{R_m \cdot e}{P}(\lambda - t) + 1\right]\right\} \quad (2)$$

Where M is the cumulative methane production, P is the methane production potential, Rmax is the maximum methane production rate, λ is the lag phase, t is the time, and e is the mathematical constant (exp (1) = 2.7183). The experimental data of cumulative methane production (M) at different time points (t) were fitted to Equation 2 using non-linear regression analysis in SigmaPlot ® 11.0 software [19]. The model parameters (P, R_{max}, and λ) were estimated by minimizing the sum of squared errors between the experimental data and the model predictions. The goodness of fit of the first-order kinetic model and the modified Gompertz model was evaluated using the coefficient of determination (R^2) and the root mean square error (RMSE). A p-value less than 0.05 was considered statistically significant. All statistical analyses were done using SigmaPlot ® 11.0 software [19].

3. Results and Discussion

3.1 Composition and characteristics of agro-industrial solid waste

The composition and characteristics of the agro-industrial and agricultural solid waste samples varied significantly, as shown in Table 1. The total solids (TS) content ranged from 10.04% to 95.81%, with samples 6, 12, and 15 having the highest TS values of 95.81%, 93.23%, and 95.78%, respectively. The volatile solids (VS) content also varied widely, from 7.94% to 83.97%, with samples 6, 12, and 15 exhibiting the highest VS values of 58.15%, 76.65%, and 83.97%, respectively. The high TS and VS contents in these samples indicate a higher organic matter content, which is advantageous for biogas production through anaerobic digestion [20]. The moisture content of the samples ranged from 4.19% to 89.96%, with most samples having moisture content above 70%. High moisture content is typical for agro-industrial and agricultural waste materials, and it can affect the performance of anaerobic digestion processes [21]. The ash content varied from 1.05% to 37.66%, with sample 6 having the highest ash content of 37.66%. High ash content can lead to operational problems in anaerobic digesters, such as reduced practical volume and clogging [22]. The carbohydrate content of the samples ranged from 0.05 g/L to 700 g/L, with samples 12 and 16 having the highest values of 645 g/L and 700 g/L, respectively. Carbohydrates are essential for biogas production, as they are readily biodegradable and can be converted into volatile fatty acids (VFAs) by acidogenic bacteria [5]. The protein content also varied significantly, from 50.25 g/L to 398.69 g/L, with samples 6 and 12 having the highest protein content of 330.69 g/L and 398.69 g/L, respectively. Proteins can contribute to biogas production, but their degradation can also lead to the formation of ammonia, which can inhibit the anaerobic digestion process at high concentrations [23]. The VFA content of the samples ranged from 0.10 g/L to 18.70 g/L, with sample 15 having the highest VFA content of 18.70 g/L. VFAs are intermediate products in the anaerobic digestion process and are essential for the stability and efficiency of the process [24]. The total sugar content varied from 0.36 g/L to 481.73 g/L, with sample 16 having the highest total sugar content of 481.73 g/L. Sugars are readily biodegradable and can contribute significantly to biogas production [25]. The oil and grease content of the samples ranged from 1.77% to 63.73%, with samples 5 and 8 having the highest values of 56.84% and 63.73%, respectively. High oil and grease content can inhibit the anaerobic digestion process by limiting the mass transfer of substrates and metabolites and causing flotation of biomass [26]. The composition of the agricultural solid waste samples varied significantly, with some samples having high organic matter content (e.g., samples 6, 12, and 15), while others had high moisture content (e.g., samples 4, 14, and 17).

3.2 Microbial community of inoculum

The microbial community analysis of the hydrogen production stage inoculum for biohydrogen production in a two-stage anaerobic digestion system revealed a diverse consortium of bacteria (Figure 2). The most abundant microorganisms were *Pseudoramibacter* sp. (19.64%), *Actinobacteria* sp. (11.70%), *Syntrophobacter sulfatireducens* (11.14%), *Syntrophus aciditrophicus* (11.14%), and *Prevotella* sp. (10.72%). Other notable members of the community included *Ruminococcaceae* bacterium (5.29%), *Clostridium tyrobutyricum* (3.76%), *Clostridium butyricum* (3.62%), and *Clostridium luticellarii* (3.06%). The remaining microorganisms had relative abundances ranging from 0.42% to 2.51%. The results of the microbial community analysis provide valuable insights into the complex interplay of bacteria involved in the dark fermentation stage of a two-stage anaerobic digestion system for biohydrogen production. The presence of a diverse range of bacteria highlights their crucial roles in the efficient production of hydrogen. *Pseudoramibacter* sp., the most abundant microorganism in the community, is known to be involved in the fermentation of carbohydrates and the production of hydrogen [28]. Its high abundance suggests it plays a key role in dark fermentation. *Actinobacteria* sp., the second most abundant microorganism, is also involved in the fermentation of various organic compounds and hydrogen production [29]. *Syntrophobacter sulfatireducens* and *Syntrophus aciditrophicus*, both equally abundant in the community (11.14%), are known to engage in syntrophic relationships with hydrogen-utilizing microorganisms [30,31]. These bacteria are capable of degrading complex organic compounds into simpler substrates, such as acetate and hydrogen, which can be utilized by other microorganisms in the community. The high abundance of these syntrophic bacteria highlights their crucial role in the efficient functioning of the dark fermentation stage. *Prevotella* sp., the fifth most abundant microorganism (10.72%), is known to be involved in the fermentation of carbohydrates and the production of hydrogen [32]. Its presence suggests that it contributes significantly to the overall hydrogen production in the dark fermentation stage. The presence of various *Clostridium* sp., such as *C. tyrobutyricum* (3.76%), *C. butyricum* (3.62%), and *C. luticellarii* (3.06%), is not surprising, as these bacteria are well-known hydrogen producers [33] [34]. Their presence further supports the importance of hydrogen production in the dark fermentation stage. Other bacteria, such as *Fermentimonas caenicola* (2.51%), *Ruminococcaceae bacterium* (5.29%), and *Bacteroidales bacterium* 6E (0.84%), are likely involved in the fermentation of complex organic matter into simpler compounds that the hydrogen-producing bacteria can utilize [35,36,37].

Table 1. Physico-chemical characteristics of agro-industrial solid waste samples

Sample	Total Solids (%)	Volatile Solids (%)	Moister (%)	Ash (%)	Carbo hydrate (g/L)	Protein (g/L)	Volatile fatty acids (g/L)	Total Sugar (g/L)	Oil and Grease (%)
1	33.46 ± 0.23	9.85 ± 0.03	66.54 ± 0.20	23.61 ± 0.23	0.64 ± 0.02	71.94 ± 0.22	2.20 ± 0.07	0.70 ± 0.00	7.70 ± 1.55
2	15.65 ± 0.94	15.65 ± 0.94	84.35 ± 0.13	13.46 ± 0.36	2.85 ± 0.09	50.25 ± 0.15	2.10 ± 0.06	1.93 ± 0.09	7.84 ± 1.22
3	17.63 ± 1.50	15.33 ± 0.04	82.37 ± 0.33	2.31 ± 1.50	0.05 ± 0.06	139.63 ± 0.42	2.54 ± 0.08	0.36 ± 0.00	48.66 ± 0.34
4	10.76 ± 1.08	7.94 ± 0.80	89.24 ± 0.27	2.82 ± 1.08	0.14 ± 0.01	150.25 ± 0.45	0.46 ± 0.01	0.58 ± 0.03	6.51 ± 0.24
5	15.37 ± 1.21	14.31 ± 1.14	84.63 ± 0.07	1.05 ± 1.21	0.06 ± 0.00	142.63 ± 0.43	0.39 ± 0.01	3.47 ± 0.06	56.84 ± 0.41
6	95.81 ± 0.14	58.15 ± 0.77	4.19 ± 0.78	37.66 ± 0.14	220.00 ± 0.00	330.69 ± 0.99	11.52 ± 0.35	290.42 ± 0.03	1.77 ± 0.15
7	16.66 ± 0.91	10.83 ± 0.75	83.34 ± 0.70	5.83 ± 0.91	0.25 ± 0.02	191.38 ± 0.57	0.11 ± 0.00	0.46 ± 0.03	3.74 ± 0.22
8	27.02 ± 0.40	25.59 ± 0.47	72.98 ± 0.09	1.43 ± 0.40	0.42 ± 0.03	179.63 ± 0.54	0.75 ± 0.02	2.31 ± 0.25	63.73 ±0.64
9	21.45 ± 0.80	13.27 ± 0.43	78.55 ± 0.37	8.18 ± 0.80	1.57 ± 0.02	82.88 ± 0.25	0.30 ± 0.01	1.85 ± 0.00	18.86 ± 0.48
10	17.59 ± 1.55	10.69 ± 0.71	82.41 ± 0.84	6.90 ± 1.55	5.60 ± 0.28	367.50 ± 1.10	0.18 ± 0.01	1.24 ± 0.21	7.10 ± 0.57
11	16.10 ± 2.08	14.20 ± 1.71	83.90 ± 0.26	1.90 ± 2.08	0.74 ± 0.04	184.38 ± 0.55	0.10 ± 0.00	1.08 ± 0.13	4.93 ± 1.16
12	93.23 ± 0.33	76.65 ± 0.12	6.77 ± 0.16	16.58 ± 0.33	645.00 ± 1.41	398.69 ± 1.20	0.60 ± 0.02	18.55 ± 0.07	2.27 ± 2.09
13	13.38 ± 0.38	9.92 ± .12	86.62 ± 0.26	3.45 ± 0.38	0.29 ± 0.03	210.50 ± 0.63	0.17 ± 0.01	0.47 ± 0.01	3.07 ± 2.29
14	10.41 ± 0.71	9.24 ± 0.60	89.59 ± 0.12	1.18 ± 0.71	193.50 ± 2.12	185.63 ± 0.56	0.11 ± 0.00	1.47 ± 0.01	3.41 ± 1.50
15	95.78 ± 0.02	83.97 ± 0.51	4.22 ± 0.49	11.81 ± 0.02	168.00 ± 1.41	303.50 ± 0.91	18.70 ± 0.56	1.54 ± 0.00	9.96 ± 0.37
16	12.74 ± 0.33	8.87 ± 0.20	87.26 ± 0.13	3.88 ± 0.33	700.00 ± 0.00	62.44 ± 0.19	17.68 ± 0.53	481.73 ± 0.00	8.31 ± 0.38
17	10.04 ± 0.20	8.94 ± 0.14	89.9 6± 0.06	1.10 ± 0.20	168.00 ± 1.41	111.00 ± 0.33	0.37 ± 0.01	1.21 ± 0.000	14.83 ± 2.33

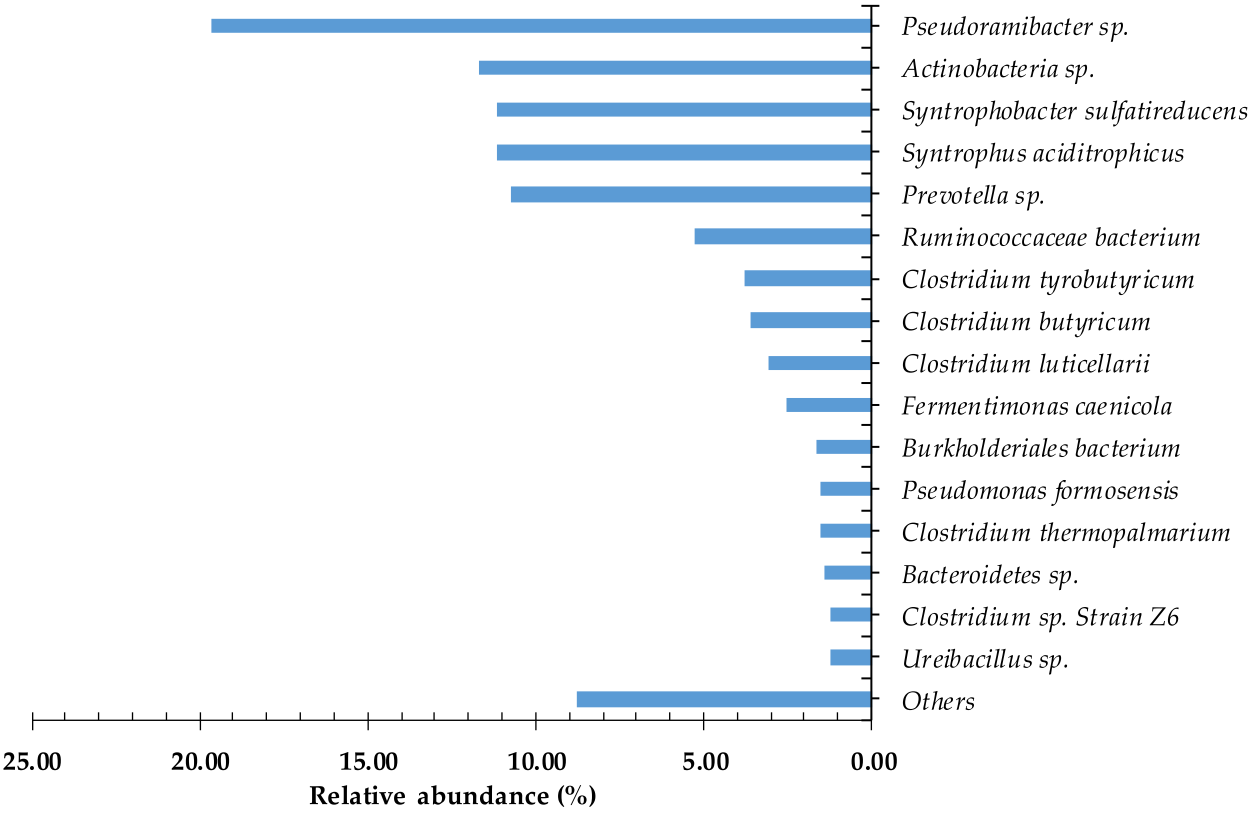

Figures 2. Taxa relative abundance in the species of the hydrogen-producing inoculum

The microbial community analysis of inoculum for the methane production stage in a two-stage anaerobic digestion system revealed a diverse consortium of archaea and bacteria (Figure 3). The most abundant microorganisms were *Methanothrix* sp. (21.60%), *Methanosarcina* sp. (15.39%), *Bipolaricaulis anaerobius* (14.41%), and *Syntrophus aciditrophicus* (14.37%). Other notable members of the community included *Atribacteria* sp. (8.51%), *Fermentimonas caenicola* (6.47%), and *Pelotomaculum* sp. (2.27%). The remaining microorganisms had relative abundances ranging from 0.08% to 1.93%. The results of the microbial community analysis provide valuable insights into the complex interplay of microorganisms involved in the methane production stage of a two-stage anaerobic digestion system. The presence of both archaea and bacteria highlights the importance of their synergistic interactions in the efficient production of methane. *Methanothrix* sp. and *Methanosarcina* sp., the most abundant microorganisms in the community, are methanogenic archaea known for utilizing acetate as a substrate for methane production [38] [39]. Their high abundance suggests that acetate is a key intermediate in methane production. The presence of *Methanobacterium formicicum* (1.85%) and *Methanosaeta harundinacea* (0.49%), also known as methanogens, further supports the importance of methanogenesis in this stage of anaerobic digestion [40]. *Bipolaricaulis anaerobius* and *Syntrophus aciditrophicus*, the third and fourth most abundant microorganisms, are known to engage in syntrophic relationships with methanogens [30] [31]. These bacteria can degrade complex organic compounds into simpler substrates, such as acetate and hydrogen, which the methanogens can utilize for methane production. The abundance of these syntrophic bacteria highlights their crucial role in the efficient functioning of the methane production stage. The presence of *Atribacteria* sp. (8.51%), *Fermentimonas caenicola* (6.47%), and *Pelotomaculum* sp. (2.27%) suggests that fermentative bacteria also play a significant role in the methane production process. These bacteria are likely involved in the fermentation of complex organic matter into simpler compounds that syntrophic bacteria and methanogens can utilize [41,42]. Other bacteria, such as *Aminicenantes* sp. (1.66%), *Pelobacter acetylenicus* (1.51%), and *Petrimonas mucosa* (1.13%), are known to be involved in the degradation of various organic compounds, further contributing to the overall efficiency of the methane production process [43,44].

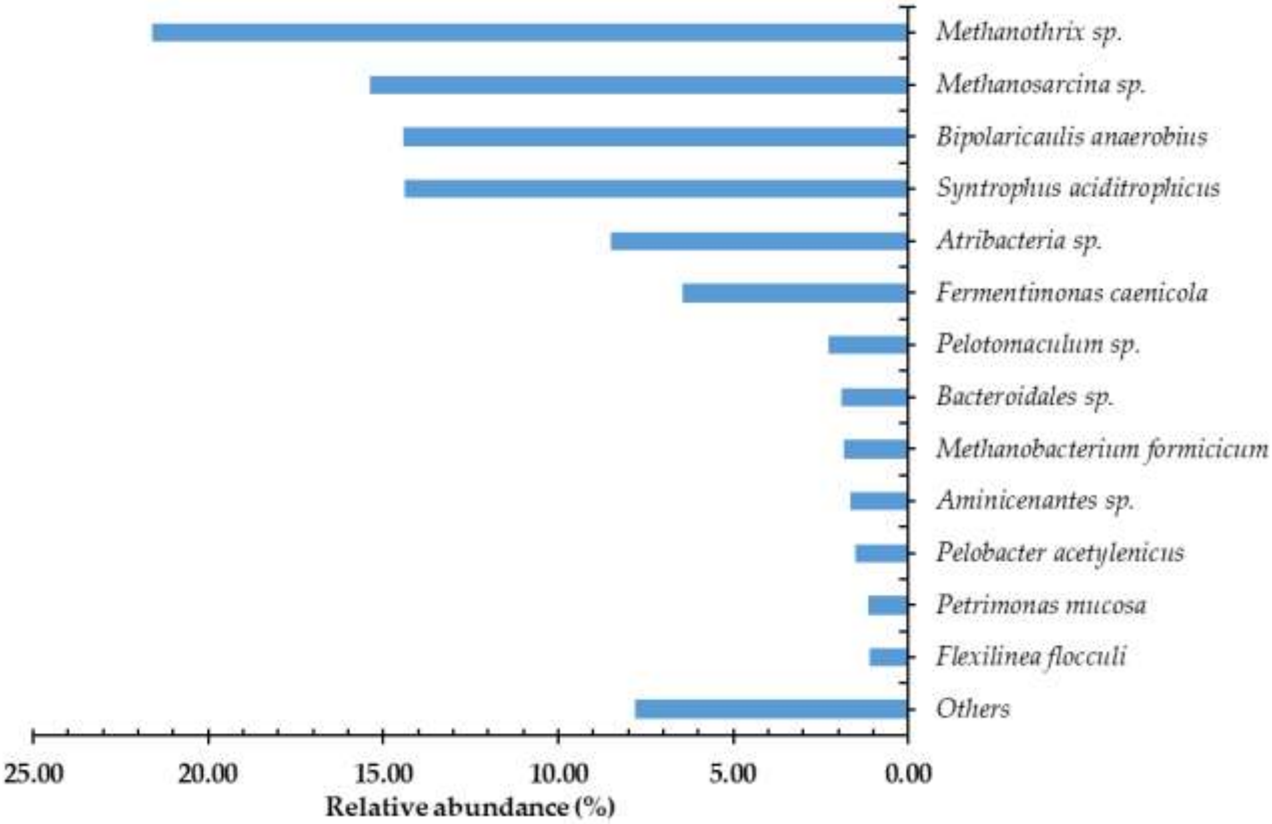

Figures 3. Taxa relative abundance in species in methane-producing inoculum

3.3 Performance of hydrogen production stage

Table 2 summarizes the hydrogen production performance from various agro-industrial solid waste samples. The hydrogen yield varied significantly among the samples, ranging from 0 to 28.46 mL H_2/g VS. Sample 6 exhibited the highest hydrogen yield of 28.46 mL H_2/g VS, followed by Sample 12 with 20.86 mL H_2/g VS and Sample 15 with 2.34 mL H_2/g VS. The remaining samples showed negligible or no hydrogen production, with yields below 2.10 mL H_2/g VS. The hydrogen concentration in the produced biogas also varied considerably, ranging from 0% to 15.27%. Sample 6 had the highest hydrogen concentration of 15.27%, followed by Sample 12 with 11.06% and Sample 9 with 2.33%. The low hydrogen concentrations in most samples indicate the presence of other gases, such as carbon dioxide, which can be attributed to the activity of non-hydrogen-producing microorganisms [45]. The hydrogen production per ton of waste ranged from 0 to 16.55 m^3/ton, with Sample 6 showing the highest production of 16.55 m^3/ton, followed by Sample 12 with 15.99 m^3/ton and Sample 15 with 1.96 m^3/ton. The low hydrogen production in most samples can be attributed to the low hydrogen yields and non-biodegradable components, such as lignin and cellulose, limiting fermentable substrates' availability [46]. Figure 4 presents the time course of hydrogen yield from the various agro-industrial solid waste samples. Samples 6 and 12 exhibited rapid hydrogen production, reaching their maximum yields within 1 and 4 days, respectively. This rapid hydrogen production can be attributed to readily fermentable substrates, such as sugars and carbohydrates, quickly consumed by hydrogen-producing bacteria [12]. In contrast, Sample 15 showed a slower hydrogen production rate, possibly due to more complex substrates requiring longer hydrolysis times [47]. The decomposition time for hydrogen production varied from 1 to 4 days, with most samples achieving complete decomposition within 2 days. The short decomposition times indicate the rapid activity of hydrogen-producing bacteria, such as *Clostridium* sp. and *Enterobacter* sp., which are known to convert fermentable substrates into hydrogen [48] efficiently. The hydrogen production performance varied significantly among the agro-industrial solid waste samples, with Sample 6 and Sample 12 exhibiting the highest hydrogen yields, concentrations, and production rates. The low hydrogen production in most samples can be attributed to the presence of non-biodegradable components and the activity of non-hydrogen-producing microorganisms. The rapid decomposition times in most samples highlight the potential for fast hydrogen production from readily fermentable substrates. However, pretreatment methods may be necessary to improve the biodegradability of complex substrates and enhance hydrogen production from these waste materials [49].

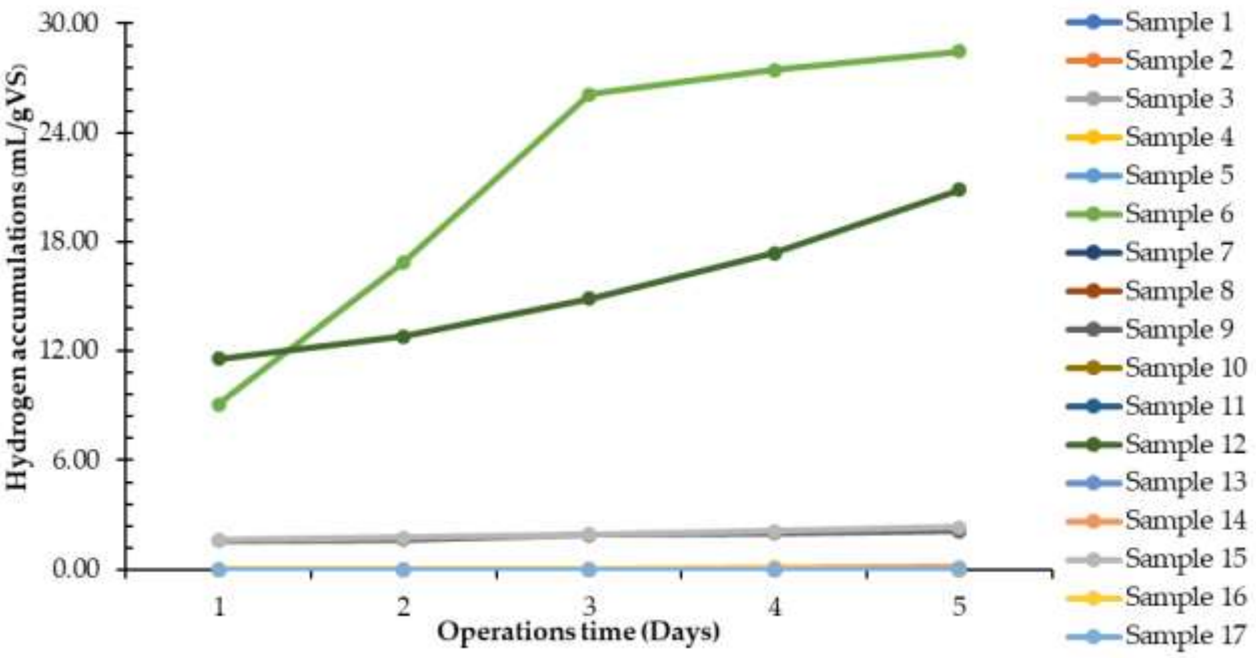

Figures 4. Time crouse for yield hydrogen from various agro-industrial solid waste.

Table 3 presents the kinetic parameters for hydrogen production from various agro-industrial solid waste samples using the modified Gompertz model. The model coefficients, including the hydrogen production potential (Kh), predicted hydrogen yield, hydrogen production rate, and lag time, were determined to evaluate the hydrogen production kinetics of each sample. The hydrogen production potential (Kh) varied significantly among the samples, ranging from 0 to 0.6754 days. Sample 6 exhibited the highest Kh value of 0.6754 days, followed by Sample 7 with 0.5274 days and Sample 4 with 0.5267 days. The high Kh values in these samples indicate their potential for extended hydrogen production periods, which can be attributed to the presence of slowly biodegradable substrates or the efficient activity of hydrogen-producing bacteria [45]. The predicted hydrogen yield ranged from 0 to 326.9316 mL H_2/g-VS, with Sample 6 showing the highest expected yield of 326.9316 mL H_2/g VS, followed by Sample 12 with 229.0055 mL H_2/g-VS and Sample 15 with 45.5818 mL H_2/g-VS. These predicted hydrogen yields are consistent with the experimental results presented in Table 2, confirming the accuracy of the modified Gompertz model in describing the hydrogen production kinetics [50]. The hydrogen production rate varied from 0 to 9.7385 mL H_2/d, with Sample 12 exhibiting the highest production rate of 9.7385 mL H_2/d, followed by Sample 6 with 9.2789mL H_2/d and Sample 15 with 2.8996 mL H_2/d.

The high hydrogen production rates in these samples can be attributed to readily fermentable substrates, such as sugars and carbohydrates, which are rapidly consumed by hydrogen-producing bacteria [12]. The lag time represents the initial adaptation period of the hydrogen-producing bacteria to the substrate and environmental conditions. Most samples exhibited no lag time, indicating the rapid initiation of hydrogen production. However, Samples 3, 5, and 1 showed lag times of 19.7097, 13.9578, and 8.5884 days, respectively, suggesting the presence of more complex substrates or the need for a more extended adaptation period for the hydrogen-producing bacteria [51]. The coefficient of determination (R^2) values ranged from 0.000 to 0.9998, indicating a moderate to good fit of the modified Gompertz model to the experimental data. The relatively low R^2 values in some samples may be attributed to the complexity of the substrate composition and the presence of non-biodegradable components, which can affect the hydrogen production kinetics [47]. The modified Gompertz model's kinetic analysis provided valuable insights into the agro-industrial solid waste samples' hydrogen production potential, predicted yield, production rate, and lag time. Samples 6, 12, and 15 exhibited the highest hydrogen production potential and predicted yields, consistent with their experimental performance. The high hydrogen production rates in Samples 6, 12, and 15 highlight their potential for rapid hydrogen production from readily fermentable substrates. The kinetic parameters obtained from this analysis can be used to optimize the design and operation of hydrogen production systems using these waste materials.

Table 2. A summary of the study on hydrogen gas production from agro-industrial solid waste

Samples of agro-industrial solid waste	**Hydrogen yield ($mL-H_2/g-VS$)**	**Hydrogen concentration (%)**	**Hydrogen production (m^3/ton of waste)**	**Decomposition time (Days)**
Sample 1	0.00	0.21	0.00	1
Sample 2	0.15	0.89	0.02	2
Sample 3	0.00	0.05	0.00	1
Sample 4	0.00	0.20	0.00	1
Sample 5	0.00	0.05	0.00	1
Sample 6	28.46	15.27	16.55	1
Sample 7	0.00	0.15	0.00	3
Sample 8	0.00	0.27	0.00	3
Sample 9	2.10	2.33	0.28	1
Sample 10	0.04	0.48	0.00	1
Sample 11	0.00	0.27	0.00	1
Sample 12	20.86	11.06	15.99	4
Sample 13	0.04	0.44	0.00	1
Sample 14	0.14	0.42	0.01	1
Sample 15	2.34	2.29	1.96	1
Sample 16	0.00	0.00	0.00	-
Sample 17	0.02	0.40	0.00	3

Table 3. Kinetic parameters for hydrogen production from agro-industrial solid waste using the modified Gompertz model

Agro-industrial solid waste	Gompertz coefficients of Hydrogen stage				K_h (days)
	Predicted hydrogen yield (ml-H_2/g VS)	Hydrogen production rate (ml-H_2/d)	Lag time (days)	Rsqr (R^2)	
Sample 1	0.2378	0.0000	8.5884	0.0000	0.4322
Sample 2	6.2869	1.3003	0.3493	0.9884	0.4925
Sample 3	0.1954	0.0000	19.7097	0.0000	0.4683
Sample 4	2.1446	0.329	0.0000	0.9966	0.5267
Sample 5	0.2683	0.0000	13.9578	0.0000	0.4978
Sample 6	326.9316	9.2789	0.0000	0.4357	0.6754
Sample 7	1.8781	0.2457	0.0000	0.9959	0.5274
Sample 8	2.3332	0.3179	0.2456	0.9997	0.4592
Sample 9	34.6487	2.9713	0.0000	0.9995	0.4728
Sample 10	5.6475	0.8613	0.0000	0.997	0.5222
Sample 11	4.8602	0.443	0.0000	0.999	0.4928
Sample 12	229.0055	9.7385	0.0000	0.7649	0.3838
Sample 13	5.6019	0.7602	0.0000	0.9974	0.5148
Sample 14	6.3411	0.7087	0.0000	0.9971	0.551
Sample 15	45.5818	2.8996	0.0000	0.9998	0.4334
Sample 16	0.0000	0.0000	0.0000	0.0000	0.0000
Sample 17	4.9685	0.7222	0.0000	0.9982	0.5419

3.4 Performance of methane production stage

Table 4 summarizes the methane production performance from various agro-industrial solid waste samples. The methane yield varied widely among the samples, ranging from 0 to 895.63 mL CH_4/g VS. Sample 3 exhibited the highest methane yield of 895.63 mL CH_4/g VS, followed by Sample 5 with 835.73 mL CH_4/g VS and Sample 8 with 830.79 mL CH_4/g VS. Samples 12 and 16 showed no methane production, indicating the presence of inhibitory compounds or the absence of readily biodegradable substrates [5]. The methane concentration in the produced biogas ranged from 8.16% to 76.68%, with most samples having methane concentrations above 65%. Sample 9 had the highest methane concentration of 76.68%, followed by Sample 6 at 73.93% and Sample 3 at 73.91%. The high methane concentrations in most samples indicate the efficient conversion of organic substrates into methane by methanogenic archaea [52]. The methane production per ton of waste varied significantly, ranging from 0 to 451.65 m^3/ton. Sample 15 showed the highest methane production of 451.65 m^3/ton, followed by Sample 6 with 429.23 m^3/ton and Sample 8 with

212.61 m^3/ton. The high methane production in these samples can be attributed to readily biodegradable substrates, such as carbohydrates and proteins, which are efficiently converted into methane during anaerobic digestion [53]. Figure 5 presents the time course of methane production yield from the agro-industrial solid waste samples. Most samples exhibited a rapid increase in methane yield during the first 10-15 days of the digestion process, followed by a gradual plateau as the readily biodegradable substrates were depleted. This pattern is consistent with the typical methane production kinetics observed in anaerobic digestion systems [54]. Sample 9 showed a slower methane production rate than other samples, possibly due to more complex substrates or the slow growth of methanogenic archaea [55]. The decomposition time for methane production varied from 17 to 48 days, with most samples achieving complete decomposition within 25 days. Sample 9 had the longest decomposition time of 48 days, indicating the presence of slowly biodegradable or recalcitrant substrates requires longer retention times for complete conversion [56]. The shorter decomposition times observed in Samples 3, 5, and 8 suggest the presence of readily biodegradable substrates and the efficient activity of methanogenic archaea [56]. The methane production performance varied significantly among the agro-industrial solid waste samples, with Samples 3, 5, and 8 exhibiting the highest methane yields, concentrations, and production rates. The high methane production in these samples can be attributed to readily biodegradable substrates and the efficient activity of methanogenic archaea. The rapid methane production rates observed in most samples highlight the potential for efficient methane recovery from these waste materials. However, pretreatment methods may be necessary to enhance the biodegradability of complex substrates and improve methane production from samples with lower yields [57].

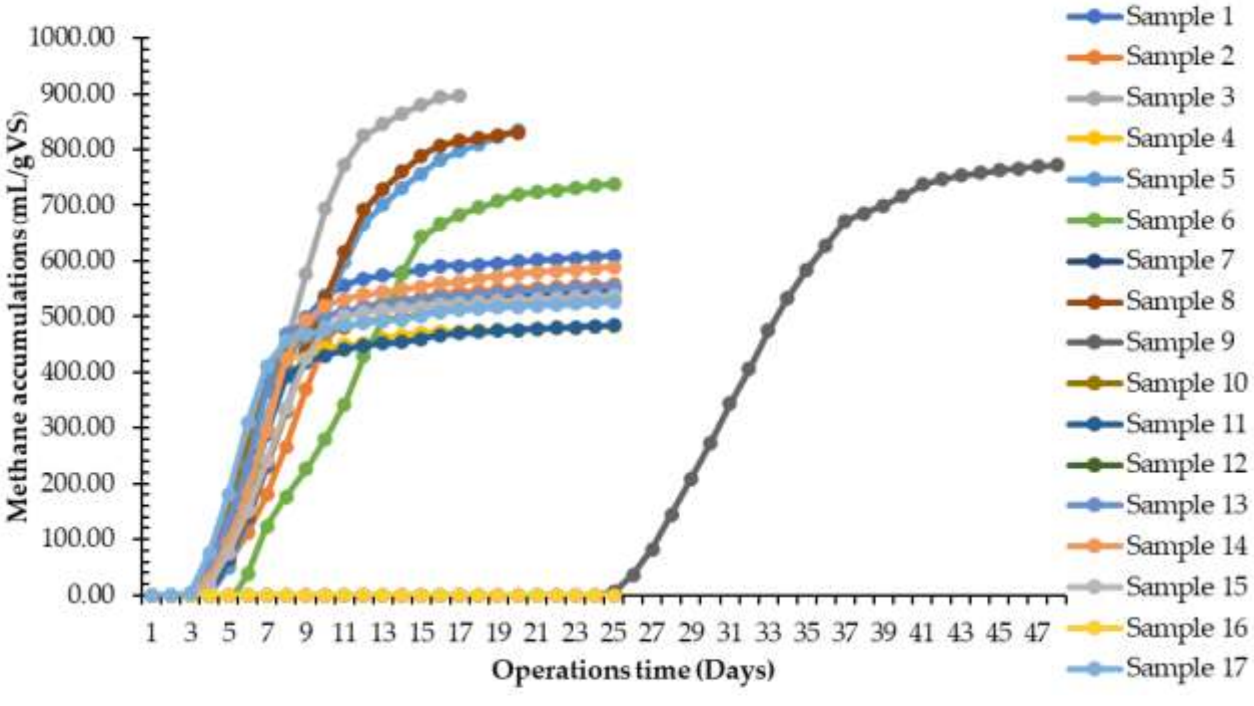

Figures 5. The time crouse methane production yield from agro-industrial solid waste

Table 4. A summary of methane gas production from agro-industrial solid waste

Samples of agro-industrial solid waste	Methane yield (mL-CH_4/g-VS)	Methane concentration (%)	Methane production (m^3/ton of waste)	Decomposition time (Days)
Sample 1	609.46	69.96	60.05	25
Sample 2	558.26	71.81	75.15	25
Sample 3	895.63	73.91	137.27	17
Sample 4	483.24	69.21	38.35	25
Sample 5	835.73	68.91	119.62	20
Sample 6	738.11	73.93	429.23	25
Sample 7	548.45	67.26	59.40	25
Sample 8	830.79	66.72	212.61	20
Sample 9	771.46	76.68	102.38	48
Sample 10	531.00	67.98	56.75	25
Sample 11	484.15	69.72	68.75	20
Sample 12	0.00	24.26	0.00	25
Sample 13	554.42	68.62	55.02	25
Sample 14	589.07	69.75	54.41	25
Sample 15	537.86	70.88	451.65	25
Sample 16	0.00	8.16	0.00	25
Sample 17	526.91	68.01	47.12	25

Table 5 presents the kinetic parameters for methane production from various agro-industrial solid waste samples using the modified Gompertz model. The model coefficients, including the methane production potential (Kh), predicted methane yield, methane production rate, and lag time, were determined to evaluate the methane production kinetics of each sample. The methane production potential (Kh) varied significantly among the samples, ranging from 0.0036 to 0.2782 days. Sample 3 exhibited the highest Kh value of 0.2782 days, followed by Sample 7 with 0.2384 days and Sample 5 with 0.2165 days. The high Kh values in these samples indicate their potential for extended methane production periods, which can be attributed to the presence of slowly biodegradable substrates or the efficient activity of methanogenic archaea [5]. The predicted methane yield ranged from 0 to 895.63 mL CH_4/g VS, with Sample 3 showing the highest expected yield of 895.63mL CH_4/g VS, followed by Sample 5 with 835.73 mL CH_4/g VS and Sample 8 with 830.79 mL CH_4/g VS. These predicted methane yields are consistent with the experimental results presented in Table 3, confirming the accuracy of the modified Gompertz model in describing the methane production kinetics [58]. The methane production rate varied from 0.2763 to 111.8479mL CH_4/d, with Sample 17 exhibiting the highest production rate of 111.8479mL CH_4/d, followed by Sample 7 with 111.3935 mL CH_4/d and Sample 4 with 110.0220 mL CH_4/d. The high methane production rates in these samples can be attributed to readily biodegradable substrates, such as carbohydrates and proteins, which are efficiently converted into methane by methanogenic archaea [53]. The lag time represents the initial adaptation period of the methanogenic archaea to the substrate and environmental conditions. Most samples exhibited lag times close to 2 days, indicating a relatively short adaptation period. However, Samples 9, 12, and 6 showed lag times of 21.3680, 8.5653, and 3.4864 days, respectively, suggesting the presence of readily biodegradable substrates or the rapid adaptation of methanogenic archaea to these waste materials [59]. The coefficient of determination (R^2) values ranged from 0.4384 to 0.9987, indicating a relatively poor fit of the modified Gompertz model to the experimental data. The low R^2 values may be attributed to the complexity of the substrate composition, the presence of inhibitory compounds, or the variability in the microbial community structure, which can affect the methane production kinetics [56]. The modified Gompertz model's kinetic analysis provided insights into the agro-industrial solid waste samples' methane production potential, predicted yield, production rate, and lag time. Samples 3, 8, and 5 exhibited the highest methane production potential, while Samples 17 , 7 , and 4 showed the highest predicted methane yields. The high methane production rates in Samples 9, 12, and 6 highlight their potential for efficient methane recovery from these waste materials.

Table 5. Kinetic parameters for methane production from agro-industrial solid waste using the modified Gompertz model

Agro-industrial solid waste	Gompertz coefficients of Methane stage				K_h (days)
	Predicted methane yield (ml-CH_4/gVS)	Methane production rate (ml-CH_4/d)	Lag time (days)	Rsqr (R^2)	
Sample 1	609.46	103.7757	2.1080	0.9947	0.2160
Sample 2	558.26	89.8765	2.5656	0.9936	0.2315
Sample 3	895.63	21.4057	0.0000	0.4384	0.2782
Sample 4	483.24	110.0220	1.7380	0.9934	0.2357
Sample 5	835.73	101.4742	2.8306	0.9987	0.2165
Sample 6	738.11	76.8701	3.4864	0.9952	0.1310
Sample 7	548.45	111.3935	1.8502	0.9932	0.2384
Sample 8	830.79	24.2655	0.0000	0.5854	0.2326
Sample 9	771.46	57.9625	21.3680	0.9893	0.0036
Sample 10	531.00	104.1500	1.6456	0.9936	0.1981
Sample 11	484.15	106.8100	2.5368	0.9936	0.2265
Sample 12	0.00	6.6126	8.5653	0.9648	0.0236
Sample 13	554.42	108.0634	1.8591	0.9903	0.2296
Sample 14	589.07	101.2926	2.0477	0.9907	0.2197
Sample 15	537.86	94.1521	2.2042	0.9936	0.2411
Sample 16	0.00	0.2763	1.3097	0.9973	0.0624
Sample 17	526.91	111.8479	1.5967	0.9923	0.2181

3.5 Overall biohythane production and process efficiency

Table 6 presents the overall biohythane production performance and process efficiency from various agro-industrial solid waste samples. The biohythane yield, composition, production per ton of waste, and decomposition time were evaluated to assess the feasibility and potential of these waste materials for biohythane production. The biohythane yield varied significantly among the samples, ranging from 0 to 895.63 mL/g VS. Sample 3 exhibited the highest biohythane yield of 895.63 mL/g VS, followed by Sample 5 with 835.73 mL/g VS and Sample 8 with 830.79 mL/g VS. The high biohythane yields in these samples can be attributed to readily biodegradable substrates, such as carbohydrates and proteins, which are efficiently converted into hydrogen and methane during the two-stage anaerobic digestion process [60]. The composition of the produced biohythane varied among the samples, with hydrogen content ranging from 0.07% to 26.57%, methane content ranging from 16.99% to 67.85%, and carbon dioxide content ranging from 31.97% to 82.94%. Sample 6 exhibited the highest hydrogen content of 26.57%, followed by Sample 12 with 21.04% and Sample 9 with 6.55%. The high hydrogen content in these samples indicates the efficient activity of hydrogen-producing bacteria and the presence of readily fermentable substrates (Sivagurunathan et al., 2017). Sample 1 showed the highest methane content of 67.85%, followed by Sample 3 at 63.37% and Sample 5 at 60.75%, suggesting the efficient conversion of organic acids and hydrogen into methane by methanogenic archaea [8]. The biohythane production per ton of waste ranged from 0 to 453.62 m^3/ton, with Sample 15 exhibiting the highest production of 453.62 m^3/ton, followed by Sample 6 with 445.78 m^3/ton and Sample 8 with 212.61 m^3/ton. The high biohythane production in these samples highlights their potential for large-scale biohythane production and the significant energy recovery from these waste materials [46].

The decomposition time for the overall biohythane production process varied from 18 to 49 days, with most samples achieving complete decomposition within 30 days. Sample 9 had the longest decomposition time of 49 days, indicating the presence of slowly biodegradable substrates or the need for process optimization to enhance the biohythane production efficiency [4]. Figure 6 illustrates the distribution of biohythane potential from the agro-industrial solid waste samples. The figure reveals that a significant portion of the samples (35%) exhibited biohythane yields between 500 and 750 mL/g VS, while 29% of the samples had yields above 750 mL/g VS. This distribution highlights the high biohythane production potential of the studied waste materials and the opportunity for their valorization through the two-stage anaerobic digestion process [7]. The overall biohythane production performance and process efficiency varied significantly among the agro-industrial solid waste samples. Samples 3, 5, and 8 exhibited the highest biohythane yields and production per ton of waste, indicating their potential for biohythane large-scale output. The composition of the produced biohythane varied, with some samples showing high hydrogen content (Samples 6, 12, and 9) and others exhibiting high methane content (Samples 1, 3, and 5). The decomposition time for most samples was within 30 days, suggesting the feasibility of the two-stage anaerobic digestion process for biohythane production from these waste materials. The distribution of biohythane potential highlights the significant opportunities for valorizing agro-industrial solid waste through biohythane production and the need for further research to optimize the process efficiency and scale up the technology.

3.6 Comparison with other studies and potential for scale-up

Table 7 compares the biohythane production performance of the agro-industrial and agricultural waste materials investigated in this study with those reported in other studies. The main parameters for comparison were the biohythane yield, hydrogen content, and methane content. The biohythane yields obtained in this study for WAS from a frozen convenience food wastewater treatment plant (Sample 3, 895.63 mL/g VS), WAS from processed chicken wastewater treatment plant (Sample 5, 835.73 mL/g VS), and WAS from municipal wastewater treatment plant (Sample 8, 830.79 mL/g VS) were significantly higher than those reported for food waste (180.5 mL/g VS) [9], wheat straw (143.7 mL/g VS) [10], sugarcane bagasse (165.2 mL/g VS) [4], dairy manure (120.8 mL/g VS) [61], and sewage sludge (98.6 mL/g VS) [62]. This comparative analysis highlights the superior biohythane production potential of the studied waste materials and their suitability for large-scale biohythane production.

The hydrogen content in the produced biohythane varied among the studies, with the expired seasoning powder (Sample 6) from this study exhibiting the highest hydrogen content of 26.57%, followed by sugarcane bagasse (22.4%) [4] and wheat straw (18.9%) [10]. The high hydrogen content in these waste materials indicates their potential for producing hydrogen-rich biohythane, which can be used as a clean and efficient fuel for various applications, such as electricity generation and transportation [8]. The methane content in the produced biohythane ranged from 36.05% to 65.8%, with dairy manure (Yin et al., 2017) and WAS from frozen convenience food wastewater treatment plant (Sample 3) from this study showing the highest methane contents of 65.8% and 63.37%, respectively. The high methane content in these waste materials suggests their potential for producing methane-rich biohythane, which can be used as a substitute for natural gas in various industrial and domestic applications [46]. The comparative analysis also reveals the potential for scale-up and commercialization of biohythane production from the studied waste materials. This study's high biohythane yields, hydrogen content, and methane content demonstrate the feasibility of developing large-scale biohythane production plants using these waste materials as feedstock. The scale-up of the technology can be achieved by optimizing the process parameters, such as substrate concentration, inoculum ratio, and reactor design, to maximize the biohythane production efficiency and minimize the operational costs [4]. Moreover, the successful implementation of biohythane production from agro-industrial and agricultural waste materials can contribute to developing a circular bioeconomy, where waste is valorized as a resource for renewable energy production (Suksong et al., 2017). Integrating biohythane production with existing waste management infrastructure and renewable energy systems can provide multiple benefits, such as reducing greenhouse gas emissions, enhancing energy security, and creating new employment opportunities [60]. The comparative analysis with other studies highlights the superior biohythane production potential of the agro-industrial and agricultural waste materials investigated in this study.

Table 6. Potential for biohythane production from agro-industrial solid waste

Samples of agro-industrial solid waste	Biohythane yield (mL/g-VS)	Biohythane composition (%)			Biohythane production (m^3/ton of waste)	Decomposition time (Days)
		%H_2	%CH_4	%CO_2		
Sample 1	609.46	0.18	67.85	31.97	60.05	26
Sample 2	558.41	2.47	56.26	41.27	75.17	27
Sample 3	895.63	0.15	63.37	36.48	137.27	18
Sample 4	483.24	0.58	57.92	41.50	38.35	26
Sample 5	835.73	0.17	60.75	39.08	119.62	21
Sample 6	766.57	26.57	36.05	37.38	445.78	26
Sample 7	548.45	0.43	55.58	43.99	59.40	28
Sample 8	830.79	0.97	60.55	38.48	212.61	23
Sample 9	773.56	6.55	59.00	34.44	102.66	49
Sample 10	531.04	1.31	53.93	44.76	56.75	26
Sample 11	484.15	0.66	59.89	39.45	68.75	21
Sample 12	20.86	21.04	18.52	60.44	15.99	29
Sample 13	554.46	1.18	54.92	43.90	55.02	26
Sample 14	589.21	1.12	57.86	41.02	54.42	26
Sample 15	540.20	5.73	57.71	36.56	453.62	26
Sample 16	0.00	0.07	16.99	82.94	0.00	26
Sample 17	526.93	1.08	52.12	46.80	47.12	28

Table 7. Comparison of biohythane production from agro-industrial and agricultural waste materials in different studies

Waste Material	Biohythane yield (mL/g VS)	H_2 Content (%)	CH_4 Content (%)	Reference
Food waste	180.5	15.2	60.3	Liu et al. (2009) [9]
Wheat straw	143.7	18.9	55.6	Zhang et al. (2020) [10]
Sugarcane bagasse	165.2	22.4	52.1	Nguyen et al. (2017) [4]
Dairy manure	120.8	10.5	65.8	Yin et al. (2017) [61]
Sewage sludge	98.6	8.2	58.3	Wang et al. (2018) [62]
WAS from a frozen convenience food wastewater treatment plant (sample 3)	895.63	0.15	63.37	This study
WAS from a processed chicken wastewater treatment plant (sample 5)	835.73	0.17	60.75	This study
WAS from a municipal wastewater treatment plant (Sample 8)	830.79	0.97	60.55	This study
expired seasoning powder (Sample 6)	766.57	26.57	36.05	This study
WAS from cleaning solution product wastewater treatment plant (Sample 9)	773.56	6.55	59.00	This study

Table 8 presents the techno-economic assessment of a scaled-up biohythane production plant using agro-industrial solid waste as feedstock. The evaluation was performed based on the experimental results obtained in this study and reasonable assumptions regarding the plant capacity, capital cost, operating cost, and revenue from biohythane sales. The plant capacity was assumed to be 100 tons of waste/day, a realistic scale for a commercial biohythane production facility [4]. The biohythane yield was estimated to be 500 m3/ton waste, which is an average value based on the high-yielding samples from this study, such as WAS from a frozen convenience food wastewater treatment plant (Sample 3), WAS from a processed chicken wastewater treatment plant (Sample 5), and WAS from municipal wastewater treatment plant (Sample 8). With these assumptions, the estimated biohythane production is 50,000 m^3/day, highlighting the potential for large-scale biohythane production from agro-industrial solid waste. The capital cost of the biohythane production plant was assumed to be 15 million USD, including land acquisition, reactor construction, equipment installation, and infrastructure development [8]. The operating cost was estimated to be 0.2 USD/m^3 biohythane, which covers the expenses related to waste transportation, pretreatment, utilities, labor, and maintenance [46]. The revenue from biohythane sales was assumed to be 0.6 USD/m3, based on the current market prices of renewable energy and the potential use of biohythane as a substitute for natural gas [60]. The payback period, which is the time required to recover the initial capital investment through the net annual profits, was calculated to be approximately 2.05 years. This relatively short payback period indicates the economic feasibility and attractiveness of scaled-up biohythane production from agro-industrial solid waste [7]. The short payback period can be attributed to the high biohythane yield, the low operating cost, and the significant revenue potential from biohythane sales. However, it should be noted that the techno-economic assessment presented in Table 8 is based on assumptions and may vary depending on the specific context, location, and market conditions of the biohythane production plant. Factors such as waste availability, transportation costs, energy prices, and government incentives can significantly influence the economic viability of the project [9]. Therefore, a more detailed and site-specific techno-economic analysis should be conducted before a large-scale biohythane production plant is implemented. Moreover, successfully implementing scaled-up biohythane production from agro-industrial solid waste requires a holistic approach that considers environmental, social, and policy aspects and technical and economic factors [61]. Integrating biohythane production with existing waste management and renewable energy systems, developing supportive policies and regulations, and engaging stakeholders is crucial for the long-term sustainability and success of the project [10].

Table 8. Techno-economic assessment of scaled-up biohythane production from agro-industrial solid waste

Parameter	Value	Unit
Plant capacity	100	ton waste/day
Biohythane yield	500	m^3/ton waste
Biohythane production	50,000	m^3/day
Capital cost	15	million USD
Operating cost	0.2	USD/m^3 biohythane
Revenue from biohythane sale	0.6	USD/m^3
Payback period	2.05	years

4. Conclusions

This study investigated the valorization of agro-industrial solid waste for biohythane production through a two-stage anaerobic digestion process. The results demonstrated the high potential of various waste materials, such as WAS from frozen convenience food wastewater treatment plants, WAS from processed chicken wastewater treatment plants, and WAS from municipal wastewater treatment plants for biohythane production. The physicochemical characterization of the agro-industrial solid waste samples revealed their diverse composition and suitability for anaerobic digestion. The high volatile solids content and readily biodegradable components, such as carbohydrates and proteins, indicated the potential for efficient biohythane production. The two-stage anaerobic digestion process, consisting of a hydrogen production stage followed by a methane production stage, effectively converted the agro-industrial solid waste into biohythane. The highest biohythane yields were obtained from WAS from a frozen convenience food wastewater treatment plant (895.63 mL/g VS), WAS from a processed chicken wastewater treatment plant (835.73 mL/g VS), and WAS from a municipal wastewater treatment plant (830.79 mL/g VS). The modified Gompertz model's kinetic analysis provided valuable insights into the biohythane production potential, predicted yield, production rate, and lag time of the agro-industrial solid waste samples. The model coefficients can be used to optimize the design and operation of biohythane production systems. The comparative analysis with other studies highlighted the superior biohythane production potential of the agro-industrial solid waste investigated in this study. This study's high biohythane yields, hydrogen content, and methane content demonstrate the feasibility of developing large-scale biohythane production plants using these waste materials as feedstock. The techno-economic assessment of scaled-up biohythane production from agro-industrial solid waste demonstrated this technology's economic feasibility and attractiveness. The high biohythane yield, low operating cost, and significant revenue potential from biohythane sales resulted in a relatively short payback period of approximately 2.05 years.

5. Acknowledgements

I sincerely thank the Higher Education for Industry Consortium (Hi-FI) for their generous support of this research project through the Experiential Learning Program, Office of The Permanent Secretary (OPS), Ministry of Higher Education, Science, Research, and Innovation.

Author Contributions: J.T.; methodology, conducted the research, analyzed the data, and wrote the paper; N.M., P.S., C.M., methodology, Proofread, funding, validated the results, and reviewed a manuscript.

Funding: This research was supported by the Higher Education for Industry Consortium (Hi-FI) Under the Experiential Learning Program, Office of The Permanent Secretary (OPS), Ministry of Higher Education, Science, Research, and Innovation.

References

[1] U.S. Energy Information Administration. International Energy Outlook 2019. **2019**. https://www.eia.gov/outlooks/ieo/

[2] Intergovernmental Panel on Climate Change. Global Warming of 1.5°C. An IPCC Special Report on the impacts of global warming of 1.5°C above pre-industrial levels and related global greenhouse gas emission pathways, in the context of strengthening the global response to the threat of climate change, sustainable development, and efforts to eradicate poverty. **2018**. https://www.ipcc.ch/sr15/

[3] World Bank. What a Waste 2.0: A Global Snapshot of Solid Waste Management to 2050. **2018**. https://openknowledge.worldbank.org/handle/10986/30317

[4] Nguyen, D. D.; Chang, S. W.; Cha, J. H.; Jeong, S. Y.; Yoon, Y. S.; Lee, S. J.; Tran, M. C.; Ngo, H. H. Dry Semi-Continuous Anaerobic Digestion of Food Waste in the Mesophilic and Thermophilic Modes: New Aspects of Sustainable Management and Energy Recovery in South Korea. *Energy Convers. Manag.* **2017**, *135*, 445–452. https://doi.org/10.1016/j.enconman.2016.12.030.

[5] Mao, C.; Feng, Y.; Wang, X.; Ren, G. Review on Research Achievements of Biogas from Anaerobic Digestion. *Renew. Sustain. Energy Rev.* **2015**, *45*, 540–555. https://doi.org/10.1016/j.rser.2015.02.032.

[6] Jenkins, W.; Tucker, M. E.; Grim, J. *Routledge Handbook of Religion and Ecology*; 2016. https://doi.org/10.4324/9781315764788.

[7] Suksong, W.; Kongjan, P.; Prasertsan, P.; Imai, T.; O-Thong, S. Optimization and Microbial Community Analysis for Production of Biogas from Solid Waste Residues of Palm Oil Mill Industry by Solid-State Anaerobic Digestion. *Bioresour. Technol.* **2016**, *214*, 166–174. https://doi.org/10.1016/j.biortech.2016.04.077.

[8] Ghimire, A.; Frunzo, L.; Pirozzi, F.; Trably, E.; Escudie, R.; Lens, P. N. L.; Esposito, G. A Review on Dark Fermentative Biohydrogen Production from Organic Biomass: Process Parameters and Use of by-Products. *Appl. Energy* **2015**, *144* (April), 73–95. https://doi.org/10.1016/j.apenergy.2015.01.045.

[9] Liu, G.; Zhang, R.; El-Mashad, H. M.; Dong, R. Effect of Feed to Inoculum Ratios on Biogas Yields of Food and Green Wastes. *Bioresour. Technol.* **2009**, *100*(21), 5103–5108. https://doi.org/10.1016/j.biortech.2009.03.081.

[10] Zhang, T.; Jiang, D.; Zhang, H.; Jing, Y.; Tahir, N.; Zhang, Y.; Zhang, Q. Comparative Study on Bio-Hydrogen Production from Corn Stover: Photo-Fermentation, Dark-Fermentation and Dark-Photo Co-Fermentation. *Int. J. Hydrogen Energy* **2020**, *45* (6), 3807–3814. https://doi.org/10.1016/j.ijhydene.2019.04.170.

[11] Nathao, C.; Sirisukpoka, U.; Pisutpaisal, N. Production of Hydrogen and Methane by One and Two Stage Fermentation of Food Waste. *Int. J. Hydrogen Energy* **2013**, *38*(35), 15764–15769. https://doi.org/10.1016/j.ijhydene.2013.05.047.

[12] Sivagurunathan, P.; Anburajan, P.; Park, J. H.; Kumar, G.; Park, H. D.; Kim, S. H. Mesophilic Biogenic H2 Production Using Galactose in a Fixed Bed Reactor. *Int. J. Hydrogen Energy* **2017**, *42*(6), 3658–3666. https://doi.org/10.1016/j.ijhydene.2016.07.203.

[13] APHA. Standard Methods for the Examination of Water and Wastewater. **2012**, 1496.

[14] Van Soest, P. J. Development of a Comprehensive System of Feed Analyses and Its Application to Forages. *J. Anim. Sci.* **1967**, *26*(1), 119–128. https://doi.org/10.2527/jas1967.261119x.

[15] Mamimin, C.; Kongjan, P.; O-Thong, S.; Prasertsan, P. Enhancement of Biohythane Production from Solid Waste by Co-Digestion with Palm Oil Mill Effluent in Two-Stage Thermophilic Fermentation. *Int. J. Hydrogen Energy* **2019**, *44*(32), 17224–17237. https://doi.org/10.1016/j.ijhydene.2019.03.275.

[16] Suksong, W.; Wongfaed, N.; Sangsri, B.; Kongjan, P.; Prasertsan, P.; Podmirseg, S. M.; Insam, H.; O-Thong, S. Enhanced Solid-State Biomethanisation of Oil Palm Empty Fruit Bunches Following Fungal Pretreatment. *Ind. Crops Prod.* **2020**, *145* (January), 112099. https://doi.org/10.1016/j.indcrop.2020.112099.

[17] Boshagh, F.; Rostami, K. A Review of Measurement Methods of Biological Hydrogen. *Int. J. Hydrogen Energy* **2020**, *45*(46), 24424–24452. https://doi.org/10.1016/j.ijhydene.2020.06.079.

[18] Hniman, A.; Prasertsan, P.; O-Thong, S. Community Analysis of Thermophilic Hydrogen-Producing Consortia Enriched from Thailand Hot Spring with Mixed Xylose and Glucose. *Int. J. Hydrogen Energy* **2011**, *36*(21), 14217–14226. https://doi.org/10.1016/j.ijhydene.2011.05.087.

[19] Trzcinski, A. P.; Stuckey, D. C. Determination of the Hydrolysis Constant in the Biochemical Methane Potential Test of Municipal Solid Waste. *Environ. Eng. Sci.* **2012**, *29*(9), 848–854. https://doi.org/10.1089/ees.2011.0105.

[20] Raposo, F.; De La Rubia, M. A.; Fernández-Cegrí, V.; Borja, R. Anaerobic Digestion of Solid Organic Substrates in Batch Mode: An Overview Relating to Methane Yields and Experimental Procedures. *Renew. Sustain. Energy Rev.* **2012**, *16*(1), 861–877. https://doi.org/10.1016/j.rser.2011.09.008.

[21] Zhang, C.; Su, H.; Baeyens, J.; Tan, T. Reviewing the Anaerobic Digestion of Food Waste for Biogas Production. *Renew. Sustain. Energy Rev.* **2014**, *38*, 383–392. https://doi.org/10.1016/j.rser.2014.05.038.

[22] Maamri, S.; Amrani, M. Biogas Production from Waste Activated Sludge Using Cattle Dung Inoculums: Effect of Total Solid Contents and Kinetics Study. *Energy Procedia* **2014**, *50*, 352–359. https://doi.org/10.1016/j.egypro.2014.06.042.

[23] Chen, Y.; Cheng, J. J.; Creamer, K. S. Inhibition of Anaerobic Digestion Process: A Review. *Bioresour. Technol.* **2008**, *99* (10), 4044–4064. https://doi.org/10.1016/j.biortech.2007.01.057.

[24] Ahring, B. K.; Sandberg, M.; Angelidaki, I. Volatile Fatty Acids as Indicators of Process Imbalance in Anaerobic Digestors. *Appl. Microbiol. Biotechnol.* **1995**, *43*(3), 559–565. https://doi.org/10.1007/s002530050451.

[25] Gunaseelan, V. N. Anaerobic Digestion of Biomass for Methane Production: A Review. *Biomass and Bioenergy* **1997**, *13* (1–2), 83–114. https://doi.org/10.1016/S0961-9534(97)00020-2.

[26] Cirne, D. G.; Paloumet, X.; Björnsson, L.; Alves, M. M.; Mattiasson, B. Anaerobic Digestion of Lipid-Rich Waste-Effects of Lipid Concentration. *Renew. Energy* **2007**, *32*(6), 965–975. https://doi.org/10.1016/j.renene.2006.04.003.

[27] Fernandes, T. V.; Klaasse Bos, G. J.; Zeeman, G.; Sanders, J. P. M.; van Lier, J. B. Effects of Thermo-Chemical Pre-Treatment on Anaerobic Biodegradability and Hydrolysis of Lignocellulosic Biomass. *Bioresour. Technol.* **2009**, *100*(9), 2575–2579. https://doi.org/10.1016/j.biortech.2008.12.012.

[28] Ling, Z., Wang, Y., Jian, S., Chen, Y., & Zou, S. Microbial Community Analysis and Performance of a Microbial Electrolysis Cell-Anaerobic Membrane Bioreactor with Different COD/SO42- Ratios. Bioresource Technology,. *Bioresour. Technol.* **2017**, 244, 905-915.

[29] Mohammadi, P., Ibrahim, S., Annuar, M. S. M., & Ghafari, S. Kinetic Study of the Fermentative Hydrogen Production by the Bacterium Clostridium Acetobutylicum. Bioprocess and Biosystems Engineering. *Bioprocess Biosyst. Eng.* **2016**, 39(7), 1103-1115.

[30] McInerney, M. J.; Sieber, J. R.; Gunsalus, R. P. Syntrophy in Anaerobic Global Carbon Cycles. *Curr. Opin. Biotechnol.* **2009**, *20*(6), 623–632. https://doi.org/10.1016/j.copbio.2009.10.001.

[31] Ziels, R. M.; Sousa, D. Z.; Stensel, H. D.; Beck, D. A. C. DNA-SIP Based Genome-Centric Metagenomics Identifies Key Long-Chain Fatty Acid-Degrading Populations in Anaerobic Digesters with Different Feeding Frequencies. *ISME J.* **2018**, *12*(1), 112–123. https://doi.org/10.1038/ismej.2017.143.

[32] Zhou, Y.; Zhang, Z.; Nakamoto, T.; Li, Y.; Yang, Y.; Utsumi, M.; Sugiura, N. Influence of Substrate-to-Inoculum Ratio on the Batch Anaerobic Digestion of Bean Curd Refuse-Okara under Mesophilic Conditions. *Biomass and Bioenergy* **2011**, *35*(7), 3251–3256. https://doi.org/10.1016/j.biombioe.2011.04.002.

[33] Masset, J.; Calusinska, M.; Hamilton, C.; Hiligsmann, S.; Joris, B.; Wilmotte, A.; Thonart, P. Fermentative Hydrogen Production from Glucose and Starch Using Pure Strains and Artificial Co-Cultures of Clostridium Spp. *Biotechnol. Biofuels* **2012**, *5*, 1–15. https://doi.org/10.1186/1754-6834-5-35.

[34] Jiang, L., Wu, H., Xu, H., & Zhao, G. A Two-Stage Process for Hydrogen and Methane Production from the Organic Fraction of Municipal Solid Waste. *Int. J. Hydrogen Energy* **2018**, 43(30), 13808-13817.

[35] Kato, S.; Yoshida, R.; Yamaguchi, T.; Sato, T.; Yumoto, I.; Kamagata, Y. The Effects of Elevated CO2 Concentration on Competitive Interaction between Aceticlastic and Syntrophic Methanogenesis in a Model Microbial Consortium. *Front. Microbiol.* **2014**, *5*(OCT), 1–8. https://doi.org/10.3389/fmicb.2014.00575.

[36] Dyksma, S.; Jansen, L.; Gallert, C. Syntrophic Acetate Oxidation Replaces Acetoclastic Methanogenesis during Thermophilic Digestion of Biowaste. *Microbiome* **2020**, *8*(1), 1–14. https://doi.org/10.1186/s40168-020-00862-5.

[37] Sun, L.; Liu, T.; Müller, B.; Schnürer, A. The Microbial Community Structure in Industrial Biogas

Plants Influences the Degradation Rate of Straw and Cellulose in Batch Tests. *Biotechnol. Biofuels* **2016**, *9*(1), 1–20. https://doi.org/10.1186/s13068-016-0543-9.

[38] Smith, K. S.; Ingram-Smith, C. Methanosaeta, the Forgotten Methanogen? *Trends Microbiol.* **2007**, *15*(4), 150–155. https://doi.org/10.1016/j.tim.2007.02.002.

[39] De Vrieze, J.; Hennebel, T.; Boon, N.; Verstraete, W. Methanosarcina: The Rediscovered Methanogen for Heavy Duty Biomethanation. *Bioresour. Technol.* **2012**, *112*, 1–9. https://doi.org/10.1016/j.biortech.2012.02.079.

[40] Yenigün, O.; Demirel, B. Ammonia Inhibition in Anaerobic Digestion: A Review. *Process Biochem.* **2013**, *48*(5–6), 901–911. https://doi.org/10.1016/j.procbio.2013.04.012.

[41] Nobu, M. K.; Narihiro, T.; Rinke, C.; Kamagata, Y.; Tringe, S. G.; Woyke, T.; Liu, W. T. Microbial Dark Matter Ecogenomics Reveals Complex Synergistic Networks in a Methanogenic Bioreactor. *ISME J.* **2015**, *9*(8), 1710–1722. https://doi.org/10.1038/ismej.2014.256.

[42] Kouzuma, A.; Kato, S.; Watanabe, K. Microbial Interspecies Interactions: Recent Findings in Syntrophic Consortia. *Front. Microbiol.* **2015**, *6* (MAY), 1–8. https://doi.org/10.3389/fmicb.2015.00477.

[43] Luo, G.; De Francisci, D.; Kougias, P. G.; Laura, T.; Zhu, X.; Angelidaki, I. New Steady-State Microbial Community Compositions and Process Performances in Biogas Reactors Induced by Temperature Disturbances. *Biotechnol. Biofuels* **2015**, *8* (1), 1–10. https://doi.org/10.1186/s13068-014-0182-y.

[44] Schmidt, A.; Müller, N.; Schink, B.; Schleheck, D. A Proteomic View at the Biochemistry of Syntrophic Butyrate Oxidation in Syntrophomonas Wolfei. *PLoS One* **2013**, *8*(2). https://doi.org/10.1371/journal.pone.0056905.

[45] Elbeshbishy, E.; Dhar, B. R.; Nakhla, G.; Lee, H. S. A Critical Review on Inhibition of Dark Biohydrogen Fermentation. *Renew. Sustain. Energy Rev.* **2017**, *79*(May), 656–668. https://doi.org/10.1016/j.rser.2017.05.075.

[46] Khan, M. A.; Ngo, H. H.; Guo, W. S.; Liu, Y.; Nghiem, L. D.; Hai, F. I.; Deng, L. J.; Wang, J.; Wu, Y. Optimization of Process Parameters for Production of Volatile Fatty Acid, Biohydrogen and Methane from Anaerobic Digestion. *Bioresour. Technol.* **2016**, *219*, 738–748. https://doi.org/10.1016/j.biortech.2016.08.073.

[47] Bundhoo, M. A. Z.; Mohee, R.; Hassan, M. A. Effects of Pre-Treatment Technologies on Dark Fermentative Biohydrogen Production: A Review. *J. Environ. Manage.* **2015**, *157*, 20–48. https://doi.org/10.1016/j.jenvman.2015.04.006.

[48] Saady, N. M. C. Homoacetogenesis during Hydrogen Production by Mixed Cultures Dark Fermentation: Unresolved Challenge. *Int. J. Hydrogen Energy* **2013**, *38*(30), 13172–13191. https://doi.org/10.1016/j.ijhydene.2013.07.122.

[49] Ren, N. Q.; Zhao, L.; Chen, C.; Guo, W. Q.; Cao, G. L. A Review on Bioconversion of Lignocellulosic Biomass to H2: Key Challenges and New Insights. *Bioresour. Technol.* **2016**, *215*, 92–99. https://doi.org/10.1016/j.biortech.2016.03.124.

[50] Lay, C. H.; Sen, B.; Chen, C. C.; Wu, J. H.; Lee, S. C.; Lin, C. Y. Co-Fermentation of Water Hyacinth and Beverage Wastewater in Powder and Pellet Form for Hydrogen Production. *Bioresour. Technol.* **2013**, *135*, 610–615. https://doi.org/10.1016/j.biortech.2012.06.094.

[51] Wang, J.; Wan, W. Kinetic Models for Fermentative Hydrogen Production: A Review. *Int. J. Hydrogen Energy* **2009**, *34*(8), 3313–3323. https://doi.org/10.1016/j.ijhydene.2009.02.031.

[52] Goswami, R.; Chattopadhyay, P.; Shome, A.; Banerjee, S. N.; Chakraborty, A. K.; Mathew, A. K.; Chaudhury, S. An Overview of Physico-Chemical Mechanisms of Biogas Production by Microbial Communities: A Step towards Sustainable Waste Management. *3 Biotech* **2016**, *6*(1), 1–12. https://doi.org/10.1007/s13205-016-0395-9.

[53] Li, W.; Siddhu, M. A. H.; Amin, F. R.; He, Y.; Zhang, R.; Liu, G.; Chen, C. Methane Production through Anaerobic Co-Digestion of Sheep Dung and Waste Paper. *Energy Convers. Manag.* **2018**, *156* (May 2017), 279–287. https://doi.org/10.1016/j.enconman.2017.08.002.

[54] Kafle, G. K.; Kim, S. H.; Sung, K. I. Ensiling of Fish Industry Waste for Biogas Production: A Lab Scale Evaluation of Biochemical Methane Potential (BMP) and Kinetics. *Bioresour. Technol.* **2013**, *127*, 326–336. https://doi.org/10.1016/j.biortech.2012.09.032.

[55] Mudhoo, A. Biogas Production: Pretreatment Methods in Anaerobic Digestion. *Biogas Prod. Pretreat. Methods Anaerob. Dig.* **2012**. https://doi.org/10.1002/9781118404089.

[56] Goux, X.; Calusinska, M.; Lemaigre, S.; Marynowska, M.; Klocke, M.; Udelhoven, T.; Benizri, E.; Delfosse, P. Microbial Community Dynamics in Replicate Anaerobic Digesters Exposed Sequentially to Increasing Organic Loading Rate, Acidosis, and Process Recovery. *Biotechnol. Biofuels* **2015**, *8*(1), 1–18. https://doi.org/10.1186/s13068-015-0309-9.

[57] Carrere, H.; Antonopoulou, G.; Affes, R.; Passos, F.; Battimelli, A.; Lyberatos, G.; Ferrer, I. Review of Feedstock Pretreatment Strategies for Improved Anaerobic Digestion: From Lab-Scale Research to Full-Scale Application. *Bioresour. Technol.* **2016**, *199*, 386–397. https://doi.org/10.1016/j.biortech.2015.09.007.

[58] Kafle, G. K.; Chen, L. Comparison on Batch Anaerobic Digestion of Five Different Livestock Manures and Prediction of Biochemical Methane Potential (BMP) Using Different Statistical Models. *Waste Manag.* **2016**, *48*, 492–502. https://doi.org/10.1016/j.wasman.2015.10.021.

[59] Zhen, G.; Lu, X.; Kobayashi, T.; Kumar, G.; Xu, K. Anaerobic Co-Digestion on Improving Methane Production from Mixed Microalgae (Scenedesmus Sp., Chlorella Sp.) and Food Waste: Kinetic Modeling and Synergistic Impact Evaluation. *Chem. Eng. J.* **2016**, *299*, 332–341. https://doi.org/10.1016/j.cej.2016.04.118.

[60] Mamimin, C.; Singkhala, A.; Kongjan, P.; Suraraksa, B.; Prasertsan, P.; Imai, T.; O-Thong, S. Two-Stage Thermophilic Fermentation and Mesophilic Methanogen Process for Biohythane Production from Palm Oil Mill Effluent. *Int. J. Hydrogen Energy* **2015**, *40*(19), 6319–6328. https://doi.org/10.1016/j.ijhydene.2015.03.068.

[61] Yin, Y.; Liu, Y. J.; Meng, S. J.; Kiran, E. U.; Liu, Y. Enzymatic Pretreatment of Activated Sludge, Food Waste and Their Mixture for Enhanced Bioenergy Recovery and Waste Volume Reduction via Anaerobic Digestion. *Appl. Energy* **2016**, *179*, 1131–1137. https://doi.org/10.1016/j.apenergy.2016.07.083.

[62] Wang, Y.; Li, G.; Chi, M.; Sun, Y.; Zhang, J.; Jiang, S.; Cui, Z. Effects of Co-Digestion of Cucumber Residues to Corn Stover and Pig Manure Ratio on Methane Production in Solid State Anaerobic Digestion. *Bioresour. Technol.* **2018**, *250*(September 2017), 328–336. https://doi.org/10.1016/j.biortech.2017.11.055.

ASEAN
Journal of Scientific and Technological Reports
Online ISSN:2773-8752

Research article

Stabilization of Sandy Soil with High Salinity Conditions using Rice Husk Ash and Gypsum to Improve Physical and Mechanical Properties

Nur Ayu Diana[1]*, Teguh Widodo[2], and Nurhidayanti Dewi Saputri[3]

[1] Department of Civil Engineering, Janabadra University, Indonesia
[2] Department of Civil Engineering, Janabadra University, Indonesia
[3] Department of Civil Engineering, Janabadra University, Indonesia
* Correspondence: nurayu@janabadra.ac.id

Citation:
Diana, N.A.; Widodo, T.; Saputri, N.D. Stabilization of sandy soil with high salinity conditions using rice husk ash and gypsum to improve physical and mechanical properties. *ASEAN J. Sci. Tech. Report.* **2024**, *27*(4), e252961. https://doi.org/10.55164/ajstr.v27i4.252961

Article history:
Received: February 26, 2024
Revised: July 2, 2024
Accepted: July 4. 2024
Available online: July 8, 2024

Publisher's Note:
This article is published and distributed under the terms of the Thaksin University.

Abstract: Sandy soil is a non-cohesive type with no binding force among particles. Non-cohesive soils have loose grains and are not solid. In high-water level conditions, the sandy soil changes its properties to liquid, causing the cohesion value between grains and its shear strength to be lost. This condition can damage civil structures, such as collapse and construction failure. Therefore, soil improvement is carried out by adding rice husk ash and gypsum, which contain SiO_2 and $CaSO_4.2H_2O$, to bind sand grains. Soil samples were tested by comparing the magnitudes of the cohesion values and the internal shear angles through direct shear tests. The mixing percentages for rice husk ash were 5%, 10%, and 15%, and for adding gypsum was 5%, with curing times of 3 days, 7 days, and 14 days (about 2 weeks). The soil sample used was sandy soil from Congot Beach, Yogyakarta, which has poorly graded sand. The optimal content for improving sandy soil was to use 5% gypsum and add 10% rice husk ash, which was proven to increase the carrying capacity of the soil. This improvement was evidenced by an increase in cohesion from the initial value of 0.029 to 0.061 and a change in shear angle from 19.82° to 29.18° in the sample taken after 14 days (about 2 weeks). The bonding observed due to stabilization was confirmed using the results of X-ray diffraction (XRD) and scanning electron microscopy (SEM).

Keywords: Gypsum; Rice husk ash; Saline soil; Soil stabilization

1. Introduction

The sandy soil at Glagah Beach, located east of Congot Beach, shows that Glagah Beach sand belongs to group S with a poor gradation classification and contains few fines, with a percentage of soil that passes sieve no 200 of 0.058%. The sampling location was on the coast, with the highest salinity level of 3.4%. Sandy soil is a type of soil that is non-cohesive (cohesionless soil) [1]. Non-cohesive soils, such as sandy soils, do not have the binding power among particles [2]. According to [3], in the technical sense of the term, soil carrying capacity is the ability of the soil to carry or resist settlement due to loading, namely the shear resistance spread by the soil along its shear planes.

The magnitude of the shear-bearing capacity of a layer of soil is affected by the soil cohesion value, the internal shear angle, the soil's unit weight, and the soil's pore pressure [4]. Non-cohesive soil with loose granules and not dense in high water conditions can act as a viscous liquid. Liquefaction transforms granular materials from solid to liquid due to increased pore water pressure and loss of effective stress [2]. When the soil is loose, and a loss of soil shear strength will accompany changes, this condition can cause damage to civil structures, such as building collapse [5]. Soil stabilization is a soil engineering method that aims to improve and maintain specific soil properties to meet technical requirements. Stabilization in sandy soil is carried out to increase sand's bearing capacity and shear strength [6, 7]. In previous research, no one has discussed the effect of salinity on stabilization tests with rice husk ash. This research aims to find out how salinity affects soil strength after stabilization because the sample location is on the south coast of Yogyakarta.

2. Materials and Methods

Rice husk ash is formed through the carbonization of husks, and for optimal bonding, it requires an additional step known as activation [6, 8]. Several factors, such as the activating agent and immersion time, influence the chemical activation process. Adding the activating agent helps remove impurities and enhance the absorbent quality. During the burning of rice husks, compounds like hemicellulose and cellulose are converted into CO_2 and H_2O. The resulting ash is whitish due to the burning process of rice husks. The primary component of husk ash is silica, but it also contains other compounds, as shown in Table 1.

Table 1 Chemical components of rice husk ash

Components	Percentage content (%)
SiO_2	94,4
Al_2O_3	0,61
Fe_2O_3	0,03
CaO	0,83
MgO	1,21
K_2O	1,06
Na_2O	0,77
SO_3	-

Source: Folleto (2006)

Gypsum is calcium sulfate hydrate ($CaSO_4$ $2(H_2O)$), a sulfate mineral found on the earth [9, 10]. Gypsum can enhance soil stability as it contains calcium, which binds organic matter and increases the water seepage rate. Moreover, gypsum can be readily hydrated by rice husk ash, the residue from burning rice husk, which has a high silicate element with a pozzolanic activity index of 87%, enhancing the permeability of the soil mixture. In this research, 5% gypsum was added to all samples.

The sampling was at Congot Beach in Jangkaran Village, Temon District, Kulon Progo Regency. The location for taking sand samples was at coordinates 7.9026197 110.0397730, with a sampling undisturbed depth of 20 cm (about 7.87 in) from the surface. The sampling location can be seen in Figure 1.

Rice husk ash, on the other hand, was subjected to various percentages within the mix, specifically 5%, 10%, and 15% of the weight of sandy soil. These different ratios of rice husk ash were systematically employed to investigate how they influenced the overall composition and performance of the soil mixture. By varying the amount of rice husk ash, researchers aimed to understand the optimal ratio that would enhance the desired properties and characteristics of the mix, ultimately contributing valuable insights for various applications in construction [11, 12].

The soil stabilization process involved mixing the initial sand soil sample with a predetermined percentage of gypsum and rice husk ash, with an initial water content of 6.12%. The rice husk ash was sifted using a No. 50 sieve to achieve a finer particle size, facilitating the effective filling of pore cavities in sandy soils. Adding gypsum and rice husk ash for each variation aims to achieve uniform mix content. The sand, gypsum, and rice husk ash were combined based on calculated weights for each mixture percentage, followed by aging in a sealed container for 3 days, 7 days, and 14 days (about 2 weeks). For each condition, 3 samples of test objects were made, and then the average test results was taken. Figure 3 illustrates the mixing and curing procedure.

Figure 1 Congot Beach, in Jangkaran Village, Temon District, Kulon Progo Regency

a) b) c)

Figure 2 Mixed material for sand soil stabilization experiments sandy soil, b) rice husk ash, c) gypsum powder

a) b)

Figure 3 The mixing process for the sand soil stabilization experiment, a) the process of mixing the stabilizing agent and b) Curing the specimen

The process of stabilization mixing, as depicted in Figure 3, was carried out using the water content determined to be optimal through the Proctor test. The optimum water content (OMC) value was 26%. Subsequently, the sample underwent a curing treatment at a room temperature of 25°C.

A direct shear test was conducted on sandy soils to determine the soil's cohesion value and shear angle under study. The standard used in this direct shear test was SNI 03-3420-2016, "Method of Direct Shear Strength Test of Unconsolidated and Undrained Soil" [13]. A direct shear test was carried out on each specimen for each mixture percentage. Initially, the test object was molded into the ring, and then the weight of the ring + the test object was measured by pressing the ring into the test object, which can be seen in Figure 4. After that, it should be assembled into the direct shear testing box and loaded [14].

Figure 4 Direct shear test

3. Results and Discussion

3.1 Direct Shear

The analysis of the direct shear initial soil test results showed that the initial soil cohesion value was 0.029 kg/cm^2, and the internal shear angle was 19.82°. Following curing for 3, 7, and 14 days (approximately 2 weeks), the results indicated an increase in cohesion and shear angle.

Based on Figure 5, the addition of varying levels of rice husk ash and gypsum has been shown to increase the carrying capacity of the soil, as seen from the increase in the soil cohesion value. There was a slow increase in the variation of the mixture of 5% rice husk ash + 5% gypsum, followed by the rise in the mix of 10% rice husk ash + 5% gypsum. However, the variation in the content of the mixture of 15% rice husk ash + 5% gypsum began to decrease, based on strength cohesion and shear angle test.

The increase in cohesion value observed in this context can be attributed to the cementation reaction during the curing time. As the soil matures, a chemical reaction occurs between the calcium (Ca) present in gypsum and the silicate (SiO_2) and aluminum (Al_2O_3) in rice husk ash. This reaction was graphically represented, illustrating a noticeable surge in the soil's cohesion value post-curing time [11].

This reaction's significance lies in enhancing the soil's structural integrity. Calcium, silicate, and aluminum combine to form stable compounds that effectively bind the soil particles, increasing cohesion. This improved cohesion is vital for various applications, such as construction and geotechnical engineering, where the strength and stability of the soil are critical factors. In summary, the cementation reaction between gypsum, silicate, and aluminum in rice husk ash is pivotal in enhancing soil cohesion, making it a valuable process for soil improvement and engineering. Regarding the testing after 14 days (about 2 weeks) of age, there may still be an increase in the shear strength of the soil, but the humidity level will further decrease, causing cracks in the sample and resulting in a decrease in strength when the sample becomes too brittle. This prompts a need for further research to carry out tests with a longer curing age of 14 days (about 2 weeks) and determine the brittle point of the sample.

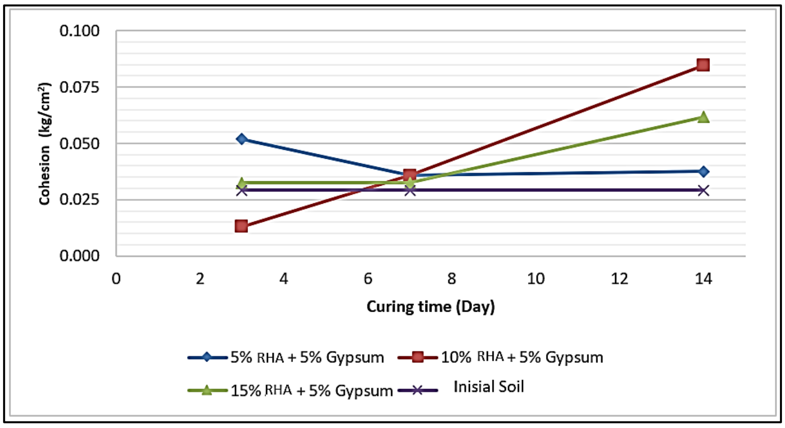

Figure 5 Graph of the effect of curing time on the cohesion value in the direct shear test

The percentage of added rice husk ash and gypsum significantly affected the increase in soil strength. A large percentage of the mixture did not necessarily result in the highest growth in cohesion, as shown in the percentage addition of 15% rice husk ash + 5% gypsum. This condition happened because the effect of the lime (Ca) reaction on the silicate (SiO_2) and aluminum (Al_2O_3) content was insufficient to support the pozzolanic reaction. Low calcium (Ca) gypsum levels made the bonds between granules not optimal [7].

The opposite occurred with the percentage of the mixture of 5% rice husk ash + 5% gypsum at different levels. The mixture did not increase the highest cohesion value because the silicate (SiO2) and aluminum (Al2O3) content in the rice husk ash was too low to react with lime in the gypsum.

The optimal mix level variation occurred at the percentage addition of 10% rice husk ash + 5% gypsum. The balanced calcium, silicate, and aluminate content reacted well with a mixture of 10% rice husk ash and 5% gypsum. It was aged for 14 days (about two weeks) so that the contents in rice husk ash and gypsum could bind soil particles better, and soil strength increased, as shown in Figure 6.

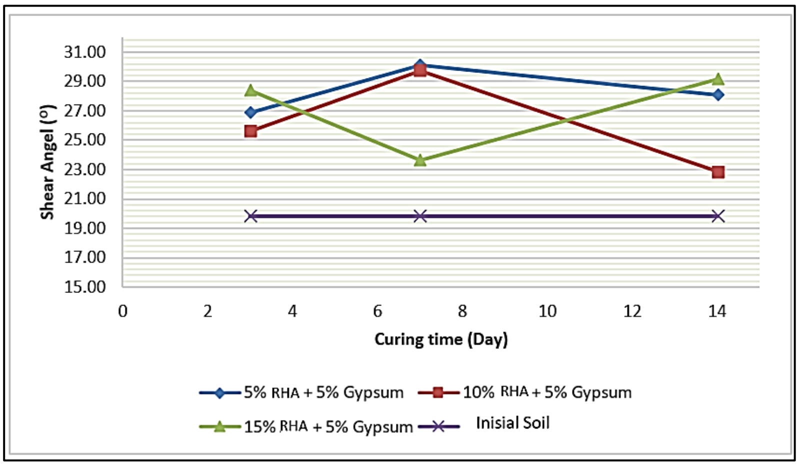

Figure 6 Graph of the effect of curing time on the internal shear angle in the direct shear test

Determining the amount of mixture percentage and the length of curing time was carried out using the trial-and-error method with variations in the mixture percentage based on previous journals regarding combinations of variations in mixing for stabilization [15][16]. A slow increase occurred in the variation of the mixture of 5% rice husk ash + 5% gypsum, and then it increased in the variation of the mix of 10% rice husk ash + 5% gypsum. However, the variation in the content of the mixture of 15% rice husk ash + 5% gypsum began to decrease based on strength cohesion and shear angle test. It can be concluded that adding husk ash can increase the binding force between particles because in rice husks, SiO2 is 94.4%. The table of normal stress and shear stress for each mixture in sandy soil is shown in Table 2 below.

Table 2 Table of average shear stress to normal stress on direct shear testing of native soil with the addition of rice husk ash and gypsum

Day	**Variation**	**Shear Stress (kg/cm^2)**		
		0,25	**0,50**	**1,00**
		Normally Stress (kg/cm^2)		
3 Day	Initial Soil	0,097	0,188	0,370
	Initial Soil + 5% RHA + 5% gypsum	0,182	0,305	0,565
	Initial Soil + 10% RHA + 5% gypsum	0,084	0,266	0,461
	Initial Soil + 15% RHA + 5% gypsum	0,123	0,253	0,539
7 Day	Initial Soil	0,097	0,188	0,370
	Initial Soil + 5% RHA + 5% gypsum	0,162	0,318	0,604
	Initial Soil + 10% RHA + 5% gypsum	0,149	0,305	0,591
	Initial Soil + 15% RHA + 5% gypsum	0,143	0,247	0,474
14 Day	Initial Soil	0,097	0,188	0,370
	Initial Soil + 5% RHA+ 5% gypsum	0,136	0,335	0,552
	Initial Soil + 10% RHA + 5% gypsum	0,156	0,344	0,526
	Initial Soil + 15% RHA + 5% gypsum	0,195	0,351	0,617

Figure 7 shows the normal stress relationship with the shear stress of the initial sandy soil and sandy soil with a mixture of rice husk ash and gypsum at each curing time.

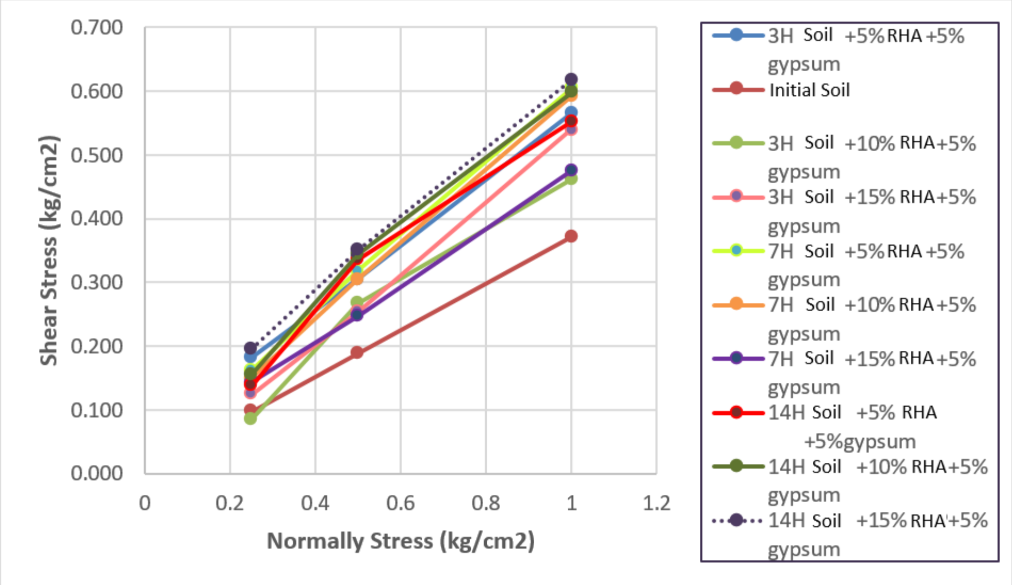

Figure 7 Graph of the effect of curing time on the internal shear angle in the direct shear test

The data presented in Figure 7 highlights a notable trend in the normal stress versus shear stress of various mixture combinations. Specifically, an increase is observed across all mixtures over time. However, the most substantial increase is observed in the mixtures featuring 5% gypsum and 15% rice husk ash.

3.2 XRD and SEM Test Result

The samples in the XRD test were taken from the highest test results with a combination of the initial soil + 15% RHA + 5% gypsum in curing for 14 days (about 2 weeks). This shows that the level of chemical bond performance has occurred optimally, resulting in the soil having the highest shear strength. Besides the elemental composition, knowing the crystallinity of SiO_2 is necessary because it is related to the synthesis process. Crystallinity analysis was performed with an X-ray diffraction instrument. The following is a diffractogram of the results analysis by X-ray diffraction shown in Figure 8.

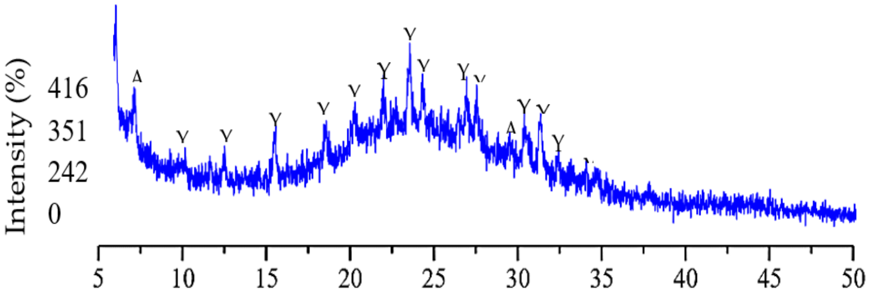

Figure 8 XRD test result

The SiO_2 diffractogram from rice husk ash with peaks in the 2ø range of 20 – 30° had low intensity, indicating that the SiO_2 phase from rice husk ash was amorphous. Amorphous silica has an arrangement of atoms and molecules in random and irregular patterns, making it more reactive than crystalline silica under various conditions [10, 12]. Therefore, rice husk ash silica can be used as a source of silica in the synthesis of Y nano zeolite [17].

Based on Figure 8 of the synthesized Y nano zeolite with variations in curing time, the crystallinity was higher the longer the curing time. At 14 days (about 2 weeks) of curing time, the synthesized Y nano zeolite had a high purity of 100%. The highest purity of Y nano zeolite was produced at 14 days (about 2 weeks) with 100% purity, but the resulting peak intensity was low. Therefore, there was a possibility of forming zeolite A and zeolite Y from the cementation. The formation of nano zeolite A was due to the synthesis of zeolite Y, which was very sensitive to pH; an increase in relatively high pH can cause the formation of zeolite A [12].

SEM characterized the surface morphology of the Y nano zeolite crystals formed. The SEM characterization results of the Y nano zeolite at curing times of 7 and 14 days (approximately 2 weeks) are illustrated in Figure 9.

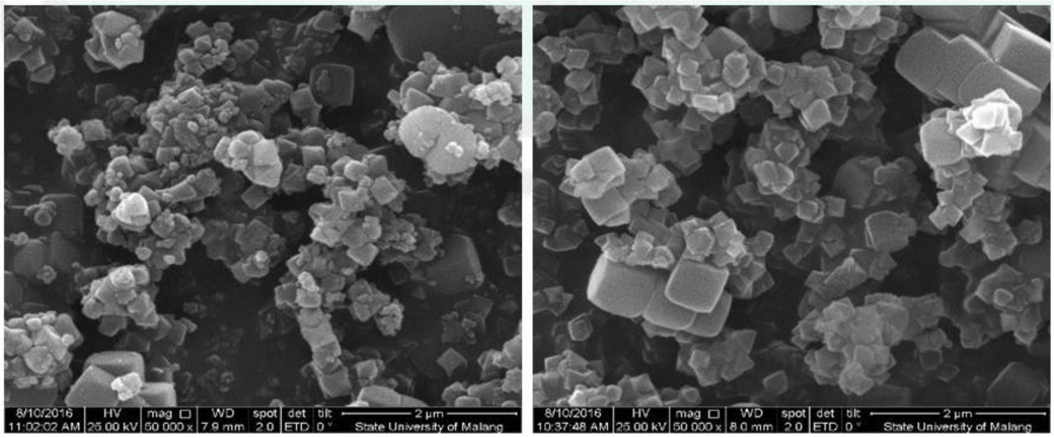

a) b)

Figure 9 SEM test result 7- and 14-days curing, a) zoom 25000x, b) zoom 50000x

SEM characterization in Figure 9 showed the presence of cubic crystals for a curing time of 7 days and 14 days (approximately 2 weeks). At 7 days of curing, the size of the cubic crystals was smaller. It appeared more homogeneous, while at 14 days (approximately 2 weeks) of curing, the size of the cubic crystals was more significant and appeared slightly less homogeneous. This was also supported by the XRD results, where the crystallinity peak was lower at 7 days of curing time, and the particle size was smaller than 14 days (approximately 2 weeks). The size of the cubic crystals at 7 days of curing was calculated using the Debye Scherrer equation and ranged from 26 - 42 nm, while at 14 days (approximately 2 weeks) of curing, it ranged from 20-95 nm [18].

4. Conclusions

The SEM characterization in Figure 9, at both 7 and 14 days (approximately 2 weeks) of curing time, revealed the presence of cubic crystals. At 7 days of curing, the cubic crystals appeared smaller and more homogeneous, whereas at 14 days (approximately 2 weeks), the crystals were more extensive and slightly less homogeneous. These observations were consistent with the XRD results, indicating a lower crystallinity peak at 7 days of curing and a smaller particle size than at 14 days (about 2 weeks). Calculations using the Debye-Scherrer equation estimated the size of the cube crystals to range from 26 to 42 nm at 7 days of curing and 20 to 95 nm at 14 days (approximately 2 weeks) of curing. At 14 days (about 2 weeks) of curing time, the synthesized Y nano zeolite exhibited a high purity of 100%. The highest purity of Y nano zeolite was achieved at 14 days (about 2 weeks) of age with 100% purity, but the resulting peak intensity was low. Consequently, there was a possibility of forming zeolite A and zeolite Y from SBU. The formation of nano zeolite A was attributed to the synthesis of zeolite Y, which was highly sensitive to pH; a relatively high increase in pH can lead to the formation of zeolite A. SEM characterization revealed the presence of cubic crystals at both 7 days and 14 days (about 2 weeks) of curing time. At the 7-day curing time, the size of the cubic crystals was smaller and more homogeneous, whereas at the 14-day curing time, the size of the cubic crystals was larger and relatively more homogeneous. These observations corresponded to XRD results, which showed lower crystallinity peaks at 7 days of curing and smaller particle sizes than at 14 days (about 2 weeks). The size of the cubic crystals at 7 days of curing was estimated using the Debye Scherrer equation to be within the range of 26 - 42 nm, while at 14 days of curing, it ranged from 20-95 nm.

References

[1] Mizan, M. H. *Study on the behavior of soft soil reinforced with rice husk ash Study on the behavior of soft soil reinforced with rice husk ash.* **2020**. no. July 2016, pp. 3–8.

[2] Ahmad, D. *The Characteristics and Engineering Properties of Soft Soil at Cyberjaya c ::: J*, no. November 2015, **2010**.

[3] Ma'Ruf, M. A.; Yulianto, F. E.; Wardani, M. K.; Iswinarti.; Firmansyah, Y. K. Utilization of Lime and Rice Husk Ash for Peat Soil Stabilization in Different Water Content Condition. *IOP Conf. Ser. Earth Environ. Sci.* **2022**. *999*(1). doi: 10.1088/1755-1315/999/1/012028

[4] Muntohar, A. S.; Widianti, A.; Hartono,E.; Diana, W. Engineering Properties of Silty Soil Stabilized with Lime and Rice Husk Ash and Reinforced with Waste Plastic Fiber, *J. Mater. Civ. Eng.* **2013**, *25*(9), 1260–1270, doi: 10.1061/(asce)mt.1943-5533.0000659

[5] Nugroho, S. A.; Fatnanta, F.; Ongko, A.; Ihsan, A. R. Behavior of High-plasticity Clay Stabilized with Lime and Rice Husk Ash. *Makara J. Technol.* **2021**. *25*(3). doi: 10.7454/mst.v25i3.3580

[6] Rahil, F. H.; Al-Soudany, K. Y. H.; Abbas, N. S.; Hussein, L. Y. Geotechnical Properties of Clayey Soils Induced by the Presence of Sodium Chloride. *IOP Conf. Ser. Mater. Sci. Eng.* **2019**, *518*(2). doi: 10.1088/1757-899X/518/2/022064

[7] Wibowo, D. E.; Ramadhan, D. A.; Endaryanta.; Prayuda, H. Soil stabilization using rice husk ash and cement for pavement subgrade materials. *Rev. la Constr.* **2023**, *22*(1), 192–202. doi: 10.7764/RDLC.22.1.192

[8] Qasim, M.; Bashir, A.; Tanvir, M.; Anees, M. M. Effect of Rice husk on soil stabilization. *Bull. Energy Econ.* **2015**, *3*(1), 10–17, [Online]. Available: http://www.tesdo.org/JournalDetail.aspx?Id=4

[9] Adedeji. Soil stabilization using rice husk ash. *Intech.* **2016**, i, no. tourism, 13. [Online]. Available: https://www.intechopen.com/books/advanced-biometric-technologies/liveness-detection-in-biometrics

[10] Kumar, B. S.; Preethi, T. V. Behavior of Clayey Soil Stabilized with Rice Husk Ash & Lime. *Int. J. Eng. Trends Technol.* **2014**, *11*(1), 44–48. doi: 10.14445/22315381/ijett-v11p209

[11] Pham, V. P.; Tran, V. T. Rice Husk Ash Burnt in Simple Conditions for Soil Stabilization. *Lect. Notes Civ. Eng.* **2020**, *62*, 717–721. doi: 10.1007/978-981-15-2184-3_93

[12] Al-azzawi, A. A. Effect of Silica Fume Addition on the Behavior of Silty-Clayey Soils. *J. Eng. Dev.* **2012**, *16*(1), 92–105.

[13] Adefemi, B. A.; Olufemi, A. S.; Tajudeen, O. A. Influence of compactive efforts on lateritic soil stabilized with rice husk ash. *Int. J. Appl. Eng. Res.* **2014**, *9*(21), 9639–9654.

[14] Alhassan, M.; Mustapha, A. M. Effect of Rice Husk Ash on Cement Stabilized Laterite. *Leonardo Electronic Journal of Practices and Technologies* **2007**, *11*, 47–58.

[15] Abdurrozak, M. R.; Mufti, D. N. Stabilisasi Tanah Lempung Dengan Bahan Tambah Abu Sekam Padi Dan Kapur Pada Subgrade Perkerasan Jalan. *J. Tek.* **2017**, XXII(2), 416–424.

[16] Diana, N. A.; Ekaputri, J. J.; Satrya, T. R.; Warnana, D. D. Biocementing Process to Improve the Physical and mechanical properties of saline soils that have the potential for liquefaction. **2024**.

[17] Adajar, M. A. Q.; Aquino, C. J. P.; dela Cruz, J. D.; Martin, C. P. H.; Urieta, D. K. G. Investigating the effectiveness of rice husk ash as stabilizing agent of expansive soil. *Int. J. GEOMATE.* **2019**, *16*(58), 33–40. doi: 10.21660/2019.58.8123

[18] Sarapu, D. POTENTIALS OF RICE HUSK ASH FOR SOIL STABILIZATION' Department of Civil Engineering Presented by : Divyateja Sarapu 'POTENTIALS OF RICE HUSK ASH FOR SOIL STABILIZING. **2016**.

ASEAN
Journal of Scientific and Technological Reports
Online ISSN:2773-8752

Research article

Physiotherapy Assistance for Patients Using Human Pose Estimation With Raspberry Pi

Khasim Vali Dudekula[1], Mukkoti Maruthi Venkata Chalapathi[2], Yellapragada Venkata Pavan Kumar[3], Kasaraneni Purna Prakash[4], Challa Pradeep Reddy[5*], Dhiren Gangishetty[6], Manaswita Solanki[7], and Rohith Singhu[8]

[1] School of Computer Science and Engineering, VIT-AP University, Amaravati 522237, Andhra Pradesh, India
[2] School of Computer Science and Engineering, VIT-AP University, Amaravati 522237, Andhra Pradesh, India
[3] School of Electronics Engineering, VIT-AP University, Amaravati 522237, Andhra Pradesh, India
[4] Department of Computer Science and Engineering, Koneru Lakshmaiah Education Foundation, Vaddeswaram, 522502, Andhra Pradesh, India
[5] School of Computer Science and Engineering, VIT-AP University, Amaravati 522237, Andhra Pradesh, India
[6] School of Computer Science and Engineering, VIT-AP University, Amaravati 522237, Andhra Pradesh, India
[7] School of Computer Science and Engineering, VIT-AP University, Amaravati 522237, Andhra Pradesh, India
[8] School of Computer Science and Engineering, VIT-AP University, Amaravati 522237, Andhra Pradesh, India
* Correspondence: pradeep.ch@vitap.ac.in

Citation:
Dudekula, K.V.; Chalapathi, M.M.V.; Kumar, Y.V.P.; Prakash, K.P.; Reddy, C.P.; Gangishetty, D.; Solanki, M.; Singhu R. Physiotherapy assistance for patients using human pose estimation with raspberry pi. *ASEAN J. Sci. Tech. Report.* **2024**, 27(4), e251096. https://doi.org/10.55164/ajstr.v27i4.251096

Article history:
Received: September 28, 2023
Revised: June 28, 2024
Accepted: June 29, 2024
Available online: July 11, 2024

Publisher's Note:
This article is published and distributed under the terms of Thaksin University.

Abstract: In this work, we employed a device that utilizes Raspberry Pi 4, a camcorder constituent, and a set of audio apparatus to provide real-time assistance to patients during rehabilitation exercises. A person's lifestyle and physical activity explicitly influence their cerebral health. Exercise routines are crucial for maintaining a proper hormone level and physical fitness. Therefore, the workout routine must be constantly examined and adjusted if any changes are needed. With the help of this device, patients may perform their exercises without a physiotherapist. A physiotherapist can show how to perform the exercises during the first few appointments; after that, the patient can utilize the system to track their routines. This will prevent injuries caused by performing exercises inaccurately when not under the guidance of a medical practitioner. The device monitors how frequently a certain exercise is performed and guides the patient in performing the exercises correctly, promoting quicker recovery. The voice generated also helps the patients analyze and correct the exercises if needed. When detecting a slump, an alarm is triggered to alert the individual. We focused on human pose detection using the OpenCV and MediaPipe libraries to capture and dissect in real-time accurately. OpenCV and MediaPipe libraries were used to capture and detect poses accurately in real time.

Keywords: Camcorder; OpenCV; Physiotherapy; Raspberry Pi 4; Real-time assistance; Voice generation

1. Introduction

Due to the present development and popularity of Virtual and Augmented Reality, human pose estimation technology is expanding quickly. Numerous applications, such as human-computer interaction, activity detection, motion analysis, augmented reality, sports and fitness, and robotics, have made use of human posture estimation [1]. Multifarious therapeutic treatments are accustomed in the medical specialty of physiotherapy to treat deformities, diseases, and injuries. These methods include massage, heat therapy, exercise, and electrotherapy. In the process of recovering from serious injuries or surgeries, people typically turn to physiotherapy, and they attend the sessions to get rid of the discomfort that limits their strength and movement. Our goal is to incorporate the idea of human position estimates with physiotherapy. This simple-to-create and simple-to-use gadget monitors a patient's movement as they carry out physiotherapy exercises. Based on the input provided, the system considers the coordinates of a body part during an exercise and counts the instances in which a certain movement is recorded [2]. According to medical data, there are just 0.59 physiotherapists for every 10,000 people in India [3]. There is a significant necessity for physiotherapists in India. The thrust for assistance while carrying out therapies is the need of the hour and will be highly appreciated. The need and urge for proper posture maintenance has also surged among people due to the rise in cases of musculoskeletal problems [4]. During the pandemic in 2019, people had no choice but to work from home and they suffered from postural problems [5]. People have suffered from numerous disorders [6] because they have been forced to sit at their desks for long hours while working. The Raspberry Pi is as small as a credit card and is an inexpensive single-board computer [7]. Its compact size and low power consumption make it suitable for portable applications such as wearable devices for human pose estimation. The Raspberry Pi is equipped with a powerful GPU and CPU that can manage the image processing tasks required for human posture evaluation. It is suitable for real-time applications since it can effectively process pictures or video streams from cameras. The Raspberry Pi has a variety of connectivity choices, such as USB, Wi-Fi, and Bluetooth, allowing integration with cameras, sensors, or other devices required for human posture estimation jobs. With this versatility, unique setups can be made to meet certain pose estimation needs [8]. A 30 MP camera was used and was instrumental in capturing high-resolution images and video streams for estimating human pose. Due to the high quality of the images, it was straightforward to identify and analyze important details and landmarks connected to human positions. Ground-truth validations [9] and recordings were done in line and processed by the frameworks as mentioned earlier.

1.1 Related Work

This microscopic comprehension of contemporary contributors describes the recent developments in the said area. Numerous individuals are ignorant of Therapeutic treatment since COVID-19 is under lockdown. To address this issue, Yeo et al. developed a real-time posture sensor for mobile activity using the Body Discovery package. The Flutter SDK and the Dart programming language were used to produce the operation. They showed its utility by precisely recognizing the stoner's position [10]. Nishchal et al. proposed a vision-based human fall detection system The Raspberry Pi and the YOLO algorithm, which defines a computer vision system, are used in this exploration to develop a mortal fall discovery system. The input is a real-time videotape captured by a camera. This technology has the potential to enhance the well-being of older adults and individuals with disabilities by offering safety and security measures, thereby improving their overall quality of life. To identify the human fall, they employed the YOLO method, Alpha-pose estimation, and ST-CGN skeletal pose action recognition [11]. Gregory et al., on the other hand, focused on a new gamified recovery system for those who have had total knee replacement surgery that uses a dereliction detector placed on the knee. When a case detects activity, a one-of-a-kind, single-light, moveable, and extremely low-cost detector with an Inertial Measurement Unit, IMU is mounted to the case's bottom leg to capture its exposure in space in real-time [12]. By using the Raspberry and Pose Net models, Kosei et al. proposed a human posture recognition system involving a single-board computer, and a posture recognition system was created. Their approach uses the disguised Pose Net model to identify several important body parts from the camera module. The proposed system may recognize six different postures and four different movement types [7]. The proposed approach for assessing yoga positions utilizes disguise discovery to help individuals in tone-literacy yoga. The system begins by relating a yoga disguise using a multi-part discovery from the PC camera. Later, it calculates the variation in body angles. However, Maybel et al.'s system provides corrective feedback if the difference exceeds a destined threshold [13]. Navjot et al. focused on the edge device grounded on the Raspberry Pi, the Mini-Xception Deep Network, due to its superior computational effectiveness, allowing for faster processing compared to other networks. This device has successfully achieved a 100-delicacy rate for real-time face discovery, surpassing the delicacy reported in the state-of-the-art approaches using the FER 2013 dataset by reaching 68 delicacies [14]. By exercising a coral USB accelerator, Ryberg et al. successfully linked and navigated toward a specified object, flaunting effective performance across all tested control systems using the Raspberry Pi. This opens up possibilities for exploring the eventuality of real-time object identification in briskly-paced scripts [15]. Raspberry Pi-based sleep posture recognition system using an AIoT technique by Pei-Jarn. The study introduces an IoT-grounded sleep monitoring system that operates without physical contact, exercising a Jeer Pi 4 Model B and RFID markers bedded in bed wastes. This low-cost and energy-effective microsystem incorporates a Random Forest Bracket (RFC) to identify different sleep positions. The sleep position data is also transmitted via Wi-Fi to a garçon database and displayed on a computer [16].

1.2 Paper Contribution

From the above-described literature works, it is observed that several papers discussed different applications of human pose estimation using various algorithms and frameworks. There has been no such work that presents real-time and quality physiotherapy assistance to patients. Further, lightweight technology like Raspberry Pi wasn't being used for the processing of all the landmarks on the human body. With this motivation, this paper proposes a system that uses body landmark detection frameworks: MediaPipe and OpenCV to accurately capture the exercises being performed by the users and provide guidance.

The major contributions of the proposed work can be summed up as follows.

- The frameworks were modified, and new models utilizing MediaPipe, OpenCV, and PyGame were created and applied on live video streams as well as pre-captured video data.
- These models provide a count of the exercise and in addition to this, a proper system will guide the users at home through audio and visual feedback.
- This process was performed based on the average joint angles calculated and based on the matching of these angles, filtering was done and output was given.

The remaining sections of the paper are organized as follows. Section 2 presents the description of the datasets that are used in this paper. Section 3 presents the description and implementation of the proposed methodology. Section 4 presents the comparative results and discussion between the methods used and other existing frameworks. Section 5 summarizes the outcomes of the paper. It also mentions the proposed work's limitations and potential future directions.

2. Description of Datasets

Datasets of participants performing various physiotherapy exercises related to spinal exaggeration and cardiovascular fitness. The dataset included both recorded videos and real-time video streams captured through the camera module.

- Uploading pre-recorded videos: Participants could upload previously recorded videos of themselves performing the exercises.
- Live camera feed: Participants could opt to use the live camera feed from the camera module to perform the exercises and have real-time feedback.

The two different kinds of data put to use for developing the models are described in sections 2.1 and 2.2.

2.1 Pre-recorded video data

The pre-recorded video data is sourced from the University of Idaho's Physical Rehabilitation Movement Data (UI-PRMD) collection. This freely available dataset contains movements associated with common exercises performed by patients in physical rehabilitation programmes. For data collection, ten healthy volunteers repeated ten different physical therapy motions. Motion was captured using a Vicon optical tracker and a Microsoft Kinect sensor, which provided the locations and angles of all full-body joints. This dataset provides a solid foundation for the mathematical modeling of therapeutic movements and for creating performance metrics to assess patient consistency in carrying out prescribed rehabilitation activities [17]. Using this professionally gathered dataset ensures the quality and reliability of our ground truth data.

2.2 Live-camera feed

Video capture option is enabled and the user's video is used to capture the various landmarks. This is being done using a camera module that is connected to the Raspberry Pi directly for fast execution.

The details of five different users and the exercises being performed by them in the case of pre-recorded videos are given in Table 1. The columns related to the data are 'User ID', 'Exercise Performed', 'Area of issue', 'Duration of exercise', and 'Video'. The column 'Exercise Performed' depicts the name of the exercise the respective user is performing, and 'Area of issue' represents the region of the user's body or part that requires physiotherapy assistance. The time spent by the user on any exercise is given in the column 'Duration of exercise'. The column related to the video data is 'Video' which holds the videos of exercises of the user.

Table 1. Description of recorded video data.

User ID	Exercise Performed	Area of Issue	Duration of exercise	Video
1001	▪ Partial Curl	▪ Spine, hip, neck	▪ 73s	▪ user1pc.mp4
	▪ Bridge	▪ Heart, knee, hip	▪ 102s	▪ user1b.mp4
	▪ Shoulder rolls	▪ Shoulder, heart	▪ 83s	▪ user1sr.mp4
	▪ Squats	▪ Spine, hip, knee	▪ 31s	▪ user1sq.mp4
	▪ Back extension	▪ Hip, spine	▪ 40s	▪ user1bck.mp4
1002	▪ Push Ups	▪ Heart, upper arm	▪ 17s	▪ user2pus.mp4
	▪ Squats	▪ Spine, hip, knee	▪ 35s	▪ user2sq.mp4
	▪ Bird dog	▪ Spine, knee, hip	▪ 42s	▪ user2bd.mp4
	▪ Back extension	▪ Hip, spine	▪ 33s	▪ user2bck.mp4
	▪ Bridge	▪ Heart, knee, hip	▪ 85s	▪ user2b.mp4
1003	▪ Shoulder Rolls	▪ Shoulder, heart	▪ 95s	▪ user3sr.mp4
	▪ Bridge	▪ Heart, knee, hip	▪ 120s	▪ user3b.mp4
	▪ Squats	▪ Spine, hip, knee	▪ 80s	▪ user3sq.mp4
	▪ Back extension	▪ Hip, spine	▪ 61s	▪ user3bck.mp4
	▪ Cat-cow stretch	▪ Spine, shoulder	▪ 72s	▪ user3cw.mp4
1004	▪ Partial Curl	▪ Spine, neck, hip	▪ 26s	▪ user4pc.mp4
	▪ Bird dog	▪ Spine, knee, hip	▪ 33s	▪ user4bd.mp4
	▪ Back extension	▪ Hip, spine	▪ 18s	▪ user4bck.mp4
	▪ Shoulder rolls	▪ Shoulder, heart	▪ 21s	▪ user4sr.mp4
	▪ Squats	▪ Spine, hip, knee	▪ 13s	▪ user4sq.mp4
1005	▪ Bridge	▪ Heart, knee, hip	▪ 36s	▪ user5b.mp4
	▪ Shoulder rolls	▪ Shoulder, heart	▪ 45s	▪ user5sr.mp4
	▪ Cat-cow stretch	▪ Spine, shoulder	▪ 28s	▪ user5cw.mp4
	▪ Bird dog	▪ Spine, knee, hop	▪ 60s	▪ user5bd.mp4
	▪ Push Ups	▪ Heart, upper arm	▪ 24s	▪ user5pus.mp4

3. Description and Implementation of the Proposed Methodology

OpenCV was utilized for video capture, image processing, and visualization of results and MediaPipe was used to detect the important body landmarks.

3.1. Mediapipe Framework

The posture estimating abilities of the MediaPipe framework can be used to detect exercises. The shoulders, elbows, wrists, hips, knees, and ankles are just a few of the body joints that may be estimated using the MediaPipe Pose model in 2D. Exercise patterns and motions can be identified by tracking the spatial correlations and movements of these key points throughout time. This framework can be used to represent several elements of a perceptual pipeline graphically, such as model inference, media processing algorithms, and data conversions [18]. The values from all the modalities are optimally merged during the pipeline process. Also using the improved MediaPipe framework the Z value of the joint point is corrected for the human tilt angle through statistics and a better accuracy in the curves could be generated [19]. Various inbuilt attributes were used to detect the landmarks for body parts, such as the nose, wrists, elbows, and shoulders. These landmarks' locations are then employed for additional computations and analysis, like calculating joint angles and counting [20].

3.2. OpenCV

OpenCV provides a real-time optimized Computer Vision library, tools, and hardware. By simply adding z dimension to the prediction in 3D pose estimation, it is possible to convert a 2D image into a 3D image, which aids in the correct prediction of the spatial placement of a depicted item [21].

3.3. Preprocessing

The recorded videos were processed using OpenCV [22] for uploaded videos. Frames from the videos were extracted, and the resolution was standardized to 640x480 pixels to ensure consistent input size for subsequent processing steps. Image enhancement techniques were also applied to improve the quality and reduce frame noise. OpenCV was utilized for the live camera feed to capture and preprocess the video frames in real-time [23]. The frames were resized and enhanced for optimal processing.

MediaPipe and OpenCV were combined to process the chosen video stream. Both submitted films and live camera feeds may be processed without issues due to the integration.

3.4. Landmark Detection

The pose estimation algorithm detected and localized key body landmarks, such as joints and key points, using the trained model. These landmarks were crucial for analyzing the participants' body postures during the exercises. OpenCV was utilized to visualize the estimated poses and landmarks on the frames [24]. The detected landmarks were overlaid onto the frames using OpenCV's drawing functions. This provided real-time visual feedback to the participants, enabling them to observe and adjust their body postures during the exercises. Metrics such as joint angles and distances between specific body parts were calculated based on the detected landmarks [25]. These metrics provided objective measurements for evaluating the correctness and effectiveness of the performed exercises.

If the average joint angle is below the threshold (indicating the start of an exercise), increment the exercise count accordingly. When the angle exceeds the threshold (indicating the completion of an exercise), the current count is displayed, and the auditory feedback is activated. The Raspberry Pi board was configured using a VNC server with the help of the VNC Viewer application. A headless operation through VNC was deployed to access the Raspberry Pi's desktop remotely. Python code files and video datasets were internally stored on a 16 GB SD card. The implementation flow of the system design is shown in Figure 1.

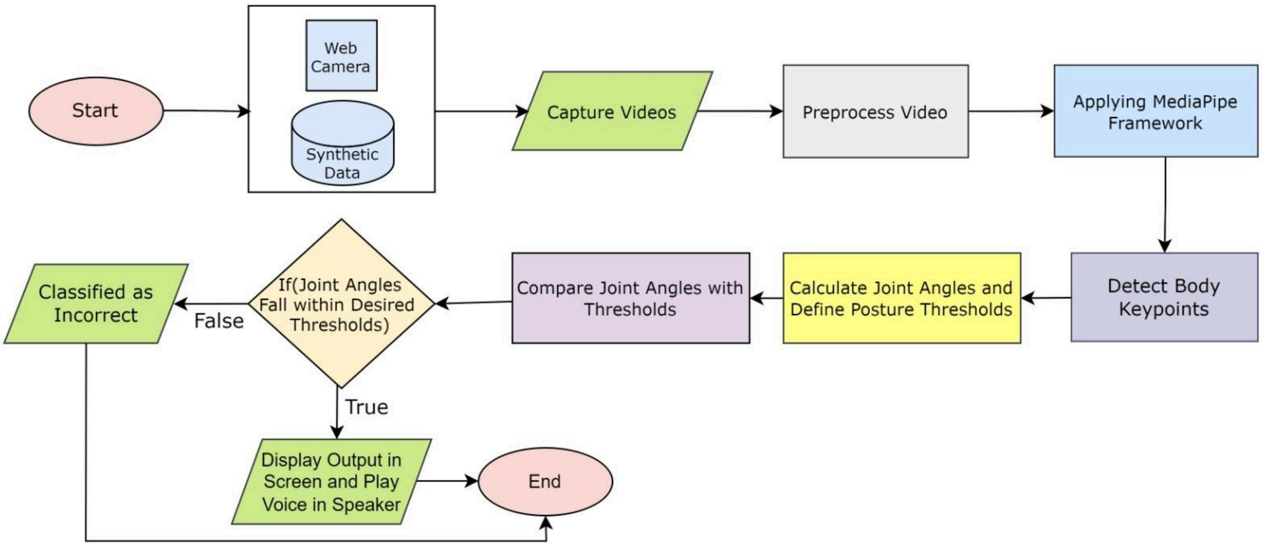

Figure 1. Conceptual working flow implementation of the physiotherapy exercise analysis.

The process starts by using the data already stored in the memory (or) by capturing the user's live video data. The data preprocessing is done to standardize the resolution and reduce noise in the frames. The proposed human pose estimation frameworks are then applied, and the body landmarks are detected. The average joint angles of the input data are calculated and compared with the prescribed angles (threshold levels). If these angles lie within the range, output is presented- the voice output through the speakers and count on the monitor display. If the algorithm cannot detect any landmarks, then the video is considered incorrect. Steps for an automated exercise counting algorithm using OpenCV and Mediapipe for real-time tracking are given in Algorithm 1.

Algorithm 1. Automated exercise counting algorithm using OpenCV and Mediapipe for real-time tracking.

```
Steps
Input: Video stream or recorded video file containing human poses
Output: Displayed video frames with annotated landmarks and exercise count, Text-to-speech announcements, and corrections
Start
Initialize the video capture to obtain the input video stream or load the recorded video
Create an instance of the pose estimation model using MediaPipe
while frames available in the video do
    Read the next frame from the video
    Resize the frame to a standardized size
    Process into pose estimation model and obtain landmarks
    Extract specific landmarks - wrists, shoulders, waist
    Calculate the average joint angle ( j )
        if j < threshold value then
            exercise_count ← 1
        else if exercise_count ← 1 AND j > threshold value
            exercise_count ← exercise_count + 1
        else
            exercise_count ← 0
    Display video frame with landmarks and update count
    if exercise_count reaches a specific milestone (e.g. 10,20) then
        Use text-to-speech to announce the milestone
end while
end
```

The algorithm is implemented to monitor exercise repetitions and joint angles using MediaPipe's pose estimation model. It starts by initializing the video capture and creating a pose estimation model. The algorithm then iterates through each video frame, resizing it for consistent processing. The pose estimation model extracts landmarks such as wrists, shoulders, and waist. The video frame is displayed with the extracted landmarks and the exercise count is updated accordingly. If the exercise count reaches a specific milestone (e.g., 10, 20), a text-to-speech feature can be used to announce the milestone.

This algorithm provides a framework for real-time exercise monitoring and feedback based on joint angle analysis. It can be customized with specific threshold values and milestones based on the desired exercise goals. By incorporating pose estimation techniques and utilizing MediaPipe, the algorithm offers a robust solution for exercise tracking and performance evaluation. The average joint angle can be calculated using equation (1).

$$y = \frac{\sum_{i=1}^{n} xi}{n}\ , i = 1, 2. \ldots . n \qquad (1)$$

where y= average joint angle calculated; x_i = joint angle in the i^{th} repetition of the exercise; n = number of repetitions of exercise performed by the user

The sum of the angles at a particular joint is calculated and divided by the number of times the exercise is performed, resulting in a quantitative measure of the average joint movement or position observed during the exercise. This is a useful metric to evaluate the consistency and effectiveness of the exercise performance.

While many existing systems use basic angle thresholds to count exercise repetitions, our designed system integrates real-time visual and audio feedback mechanisms, which is a significant improvement. With the help of this, users may adjust their posture in real time and receive quick feedback on how they are performing their exercises. This is very important in physiotherapy settings, where precise motions are essential for successful recovery outcomes. In contrast to the simple counting methods available on many websites, our system uses newly developed and revised body landmark recognition models from MediaPipe and OpenCV. These modifications provide more reliable and precise position estimation, improving the feedback's accuracy and usefulness. Our system counts repetitions and stands out as a useful resource for physiotherapists and patients who need dependable, in-the-moment exercise execution advice because of its comprehensive approach.

3.5. Real-time Feedback Mechanism

This real-time feedback loop is essential for physiotherapy to be effective, where precise motions are required for recovery. OpenCV's drawing functions are employed to overlay important spots and skeleton lines onto video frames to provide visual feedback. When the system determines that the participant's posture is improper, it highlights the exact joints or body regions that require modification. This is accomplished by altering the color of the landmarks or adding extra markers, such as arrows or bounding boxes, around the areas that require rectification. The monitor's real-time display allows participants to see their posture instantly and make any needed modifications. Audio warnings give participants quick audio feedback when their posture deviates from the proper form or when an activity repeat is tallied. The Raspberry Pi board uses a simple Python audio module to create these alarms. This is accomplished using the pygame library, which is well-known for its simple use for playing sound files. Pre-recorded audio messages or tones are broadcast over Raspberry Pi-connected speakers to assist the participant. For example, if the participant's joint angles go outside the allowed range, an alarm may sound, suggesting that they should adjust their posture.

4. Results and Discussion

The total count of the exercise being done during the live video or live camera session is displayed. The joint angles are calculated by considering the positions of relevant body joints in the captured 3D space [26]. For each exercise, joint angles are extracted at relevant time intervals (e.g., at the starting position, during the downward motion, at the lowest point, during the upward motion, and at the ending position). The average joint angle is calculated by summing up the joint angles for each exercise and dividing by the total count. The actual ground truth data was matched with the detected count. Here, in total, five counts are considered. The prescribed average joint angles in five types of spinal exercise are given in Table 2. And, the prescribed average joint angles in five types of cardiovascular exercises are given in Table 3.

Table 2. Prescribed average joint angles in five types of spinal exercise.

Physiotherapy Exercise Name	Prescribed Average Joint Angle (for 5 counts)
Cat-cow Stretch	▪ Spine flexion: 38.5° ▪ Spine extension: 27.8° ▪ Knee flexion: 5.6° ▪ Shoulder protraction: 14.9° ▪ Shoulder retraction: 14.8°
Partial Curl	▪ Spine flexion: 32.9° ▪ Hip extension: 16.86°
Bird dog	▪ Spine extension: 10.6° ▪ Hip extension: 16.88° ▪ Shoulder flexion: 20° ▪ Knee flexion: 11.2°

Squats	Ankle dorsiflexion: 31° Hip flexion: 81° Spine extension: 2.2° Knee flexion: 90°
Back extension	Facet joint: 2.2° Sacroiliac joint: 0.6° Hip joint: 83.5° Shoulder joint: 1.7°

Table 3. Prescribed average joint angles in five types of cardiovascular exercises.

Physiotherapy Exercise Name	Prescribed Average Joint Angle (for 5 counts)
Push Ups	Shoulder protraction: 11.5° Shoulder retraction: 15.5° Elbow flexion: 118.7° Elbow extension: 1.7° Spine: 0°(neutral position)
Bridge	Ankle dorsiflexion: 12.2° Ankle plantar-flexion: 5.4° Knee flexion: 89° Knee extension: 1.7° Spinal extension: 22.4° Hip flexion: 41° Hip extension: 0.8°
Shoulder Rolls	Shoulder abduction: 33.5° Shoulder internal rotation: 25.9° Shoulder external rotation: 26°

By calculating the average joint angles, insights are gained into the form, technique, and alignment of the body, and the correctness of a pose is evaluated. When joint angles deviate from the prescribed range, it may be a sign of incorrect form or compensatory movements, which might lead to injuries or lessen the efficiency of the exercise. This method accurately tracked key body landmarks in varying lighting conditions or during complex body poses. Certainly, there is a limitation when an occlusion occurs during an exercise. Real-time feedback and guidance are provided to users, facilitating proper form and technique. The back extension exercise is shown in Figure 2.

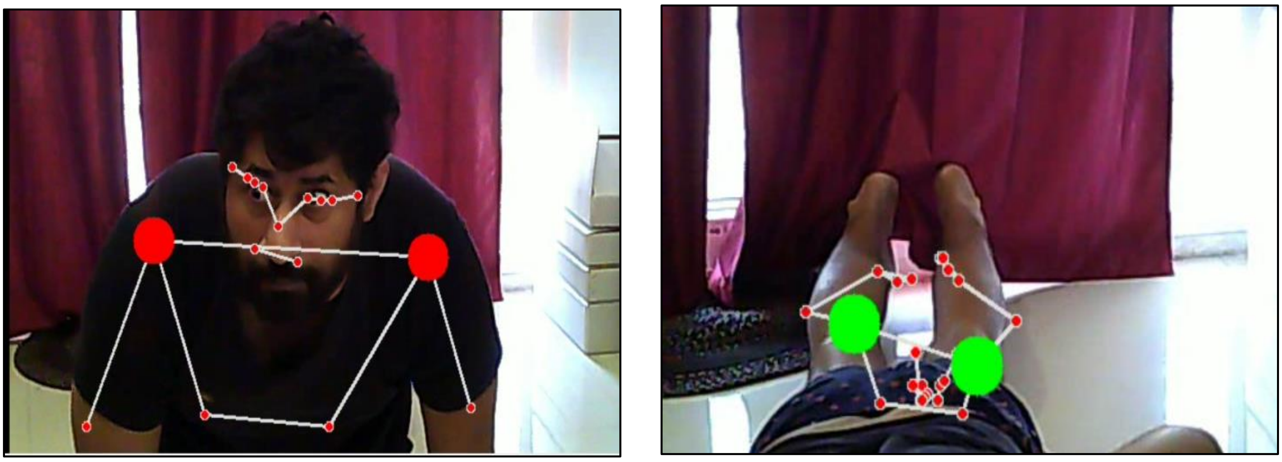

Figure 2. Back extension exercise being performed.

All the exercises and their respective joint angles are shown in the following figures in the form of graphs. The exercises related to the spine are shown in Figures 3 to 7. All the joint angles involved while performing the Cat-cow stretch exercise are shown in Figure 3. The parts involved in this exercise are the spine, shoulder, and knee. This figure shows the subplots for five iterations of the exercise. All angles in these subplots are in degrees.

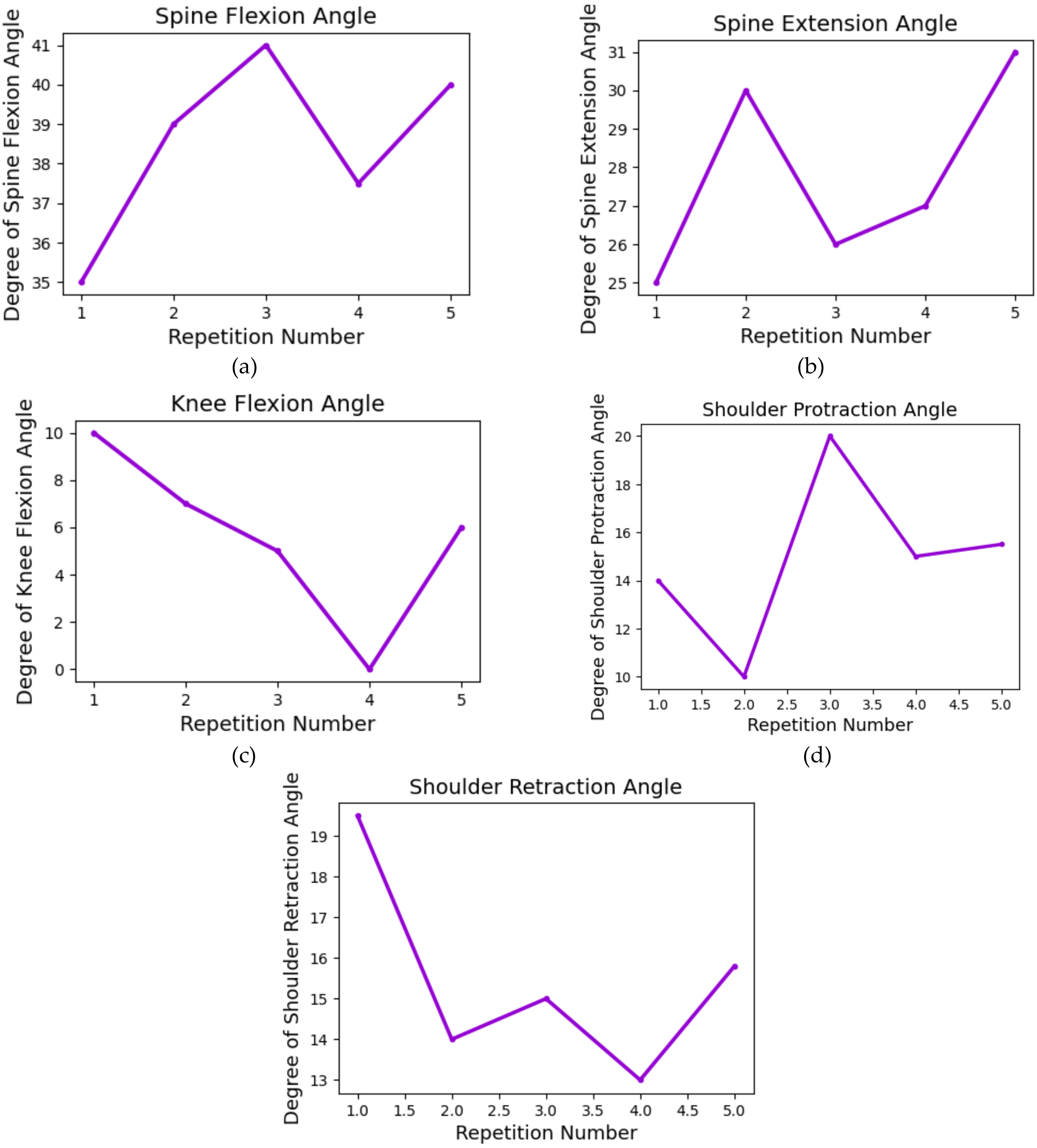

(a) (b)

(c) (d)

(e)

Figure 3. Different kinds of angles are involved in the cat-cow stretch exercise.

All the joint angles involved in the partial curl exercise are shown in Figure 4. The parts involved are the hip and spine. This figure shows the subplots for five iterations of the exercise. All angles in the subplots are in degrees. All the joint angles involved in the bird-dog exercise are shown in Figure 5. The parts involved are the spine, knee, and shoulder. This figure shows the subplots for five iterations of the exercise. All angles in the subplots are in degrees.

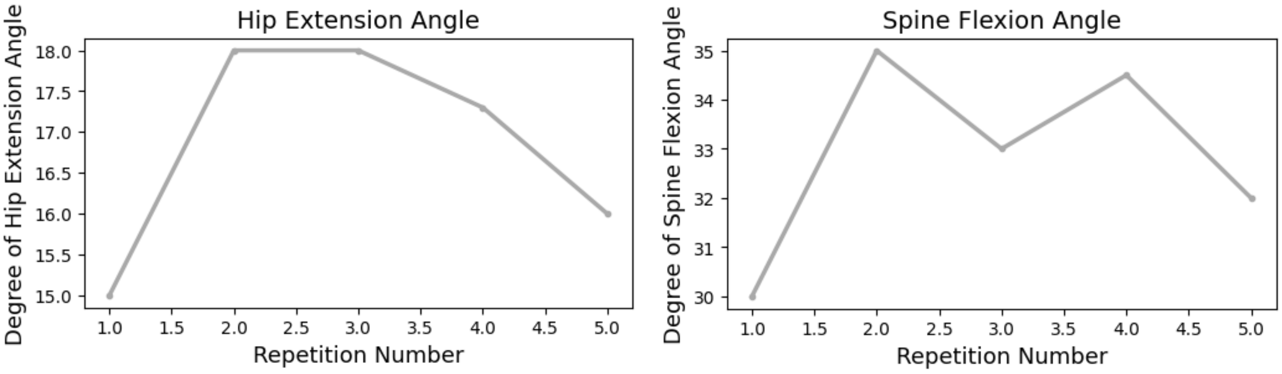

(a) (b)

Figure 4. Different kinds of angles involved in the partial curl stretch exercise.

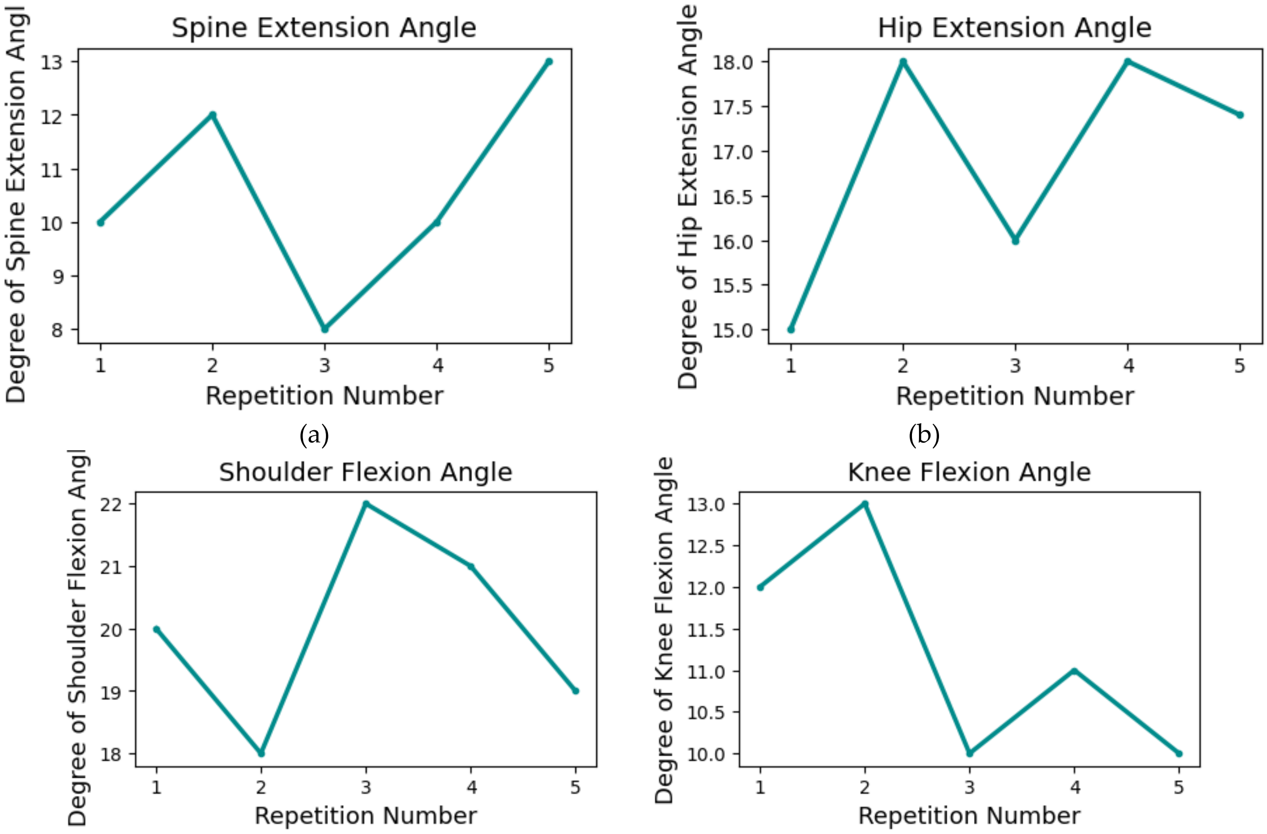

(a) (b)

(c) (d)

Figure 5. Different kinds of angles are involved in bird dog exercise.

The angles related to the cardiovascular exercises are shown in Figures 6 and 7. All the joint angles involved in the push-up exercise are shown in Figure 6. The parts involved are the shoulder and elbow. This figure shows the subplots for five iterations of the exercise. All angles in the subplots are in degrees. All the joint angles involved in the bridge exercise are shown in Figure 7. The parts involved are the knee, ankle, spine, and hip. This figure shows the subplots for five iterations of the exercise. All angles in the subplots are in degrees.

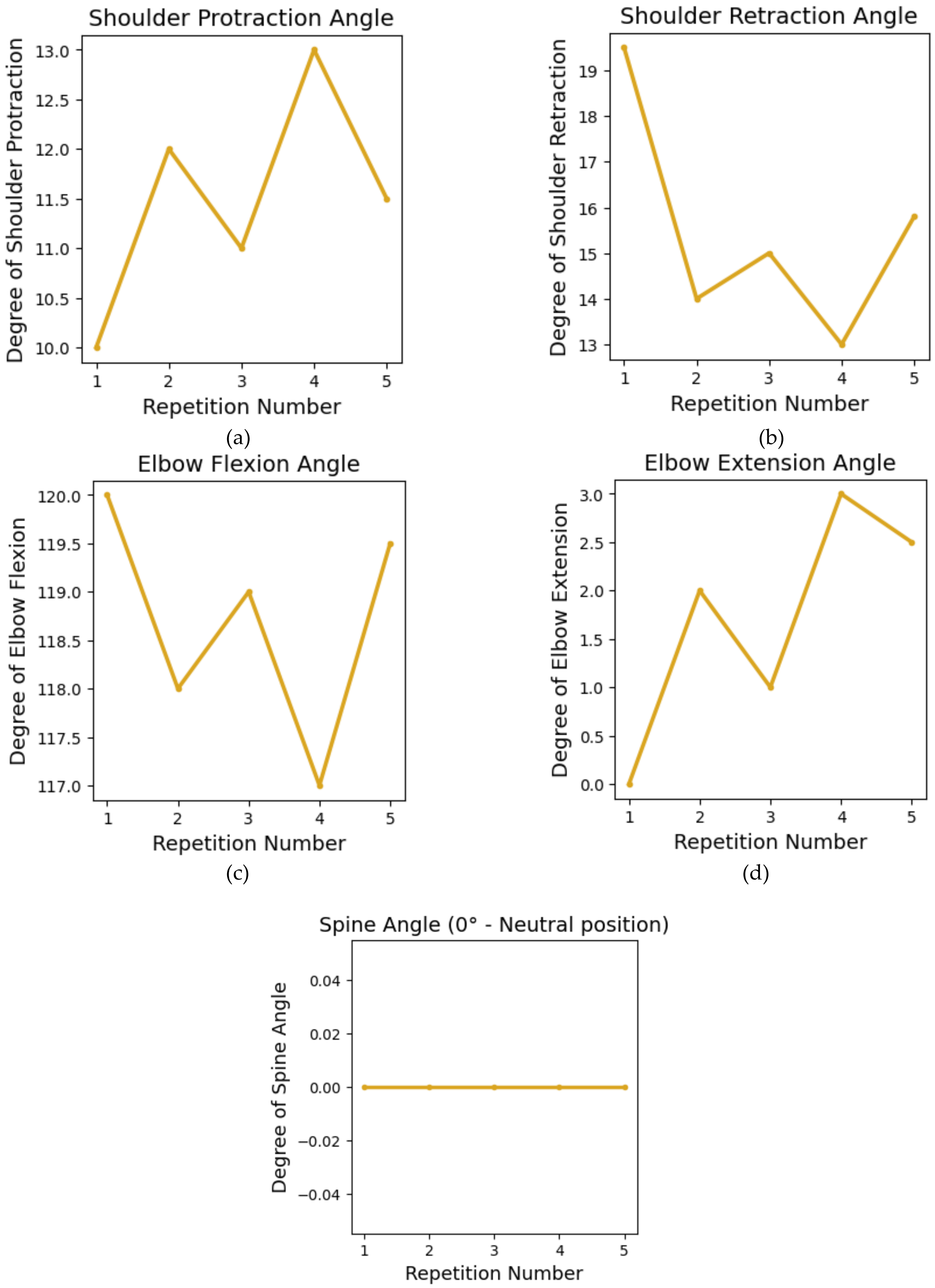

(a) (b)

(c) (d)

(e)

Figure 6. Different kinds of angles are involved in push-up exercises.

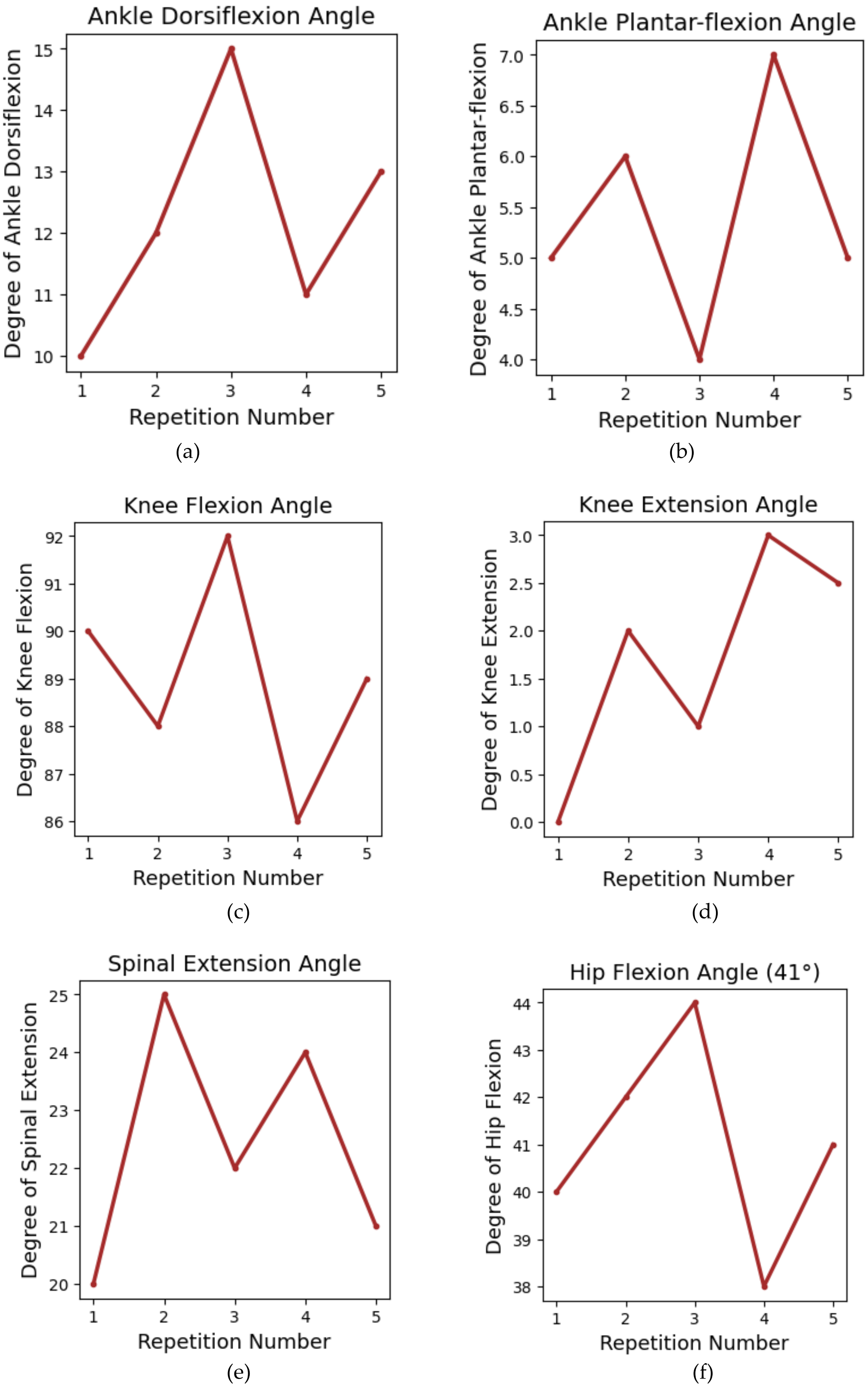

(a) (b)

(c) (d)

(e) (f)

Figure 7. Different kinds of angles are involved in bridge exercise.

In addition to tracking exercise repetitions, our system offers instant feedback on how well each action is performed. Joint angles are calculated and compared to predetermined criteria to do this. For instance, the system determines the angle at which the torso and upper arm form during a shoulder raise exercise. The device instantly gives the user visual and audio feedback if the angle goes outside of the advised range, assisting them in correcting their form.

The comparison between OpenPose and OpenCV is given in Table 4. This table shows how an OpenCV framework is superior to the OpenPose framework regarding flexibility, integration, and performance. The obtained accuracy while the users performed spinal exercises is shown in Figure 8. From this figure, the accuracy obtained for the back extension physiotherapy exercise is the maximum compared to other spinal exercises. The accuracy obtained is 93.2% for back extension, 85.6% for squats, 85% for a bird dog, 90% for partial curl, and 89.5% for cat-cow stretch exercises, respectively.

Table 4. Comparison between OpenPose and OpenCV.

OpenPose	**OpenCV**
▪ OpenPose is built on deep learning models. It employs intricate neural network topologies, like multi-stage convolutional networks, to find and localize human key points.	▪ OpenCV is a comprehensive computer vision library that provides a wide range of pre-built functions and algorithms for various tasks, including pose estimation. In comparison to OpenPose, it provides a simpler and more user-friendly API.
▪ It may require additional effort and expertise to adapt it to specific use cases.	▪ With its diverse set of functions and algorithms, it offers more flexibility and easier integration.
▪ Computationally intensive, it requires substantial processing power, memory, and high-end GPU.	▪ Less resource-intensive compared to the deep learning models used in OpenPose, often optimized for efficient execution on various hardware platforms.
▪ Limited flexibility and customization. The customization of the network architecture might be challenging.	▪ OpenCV and Mediapipe provide flexibility in terms of customization, adjusting parameters, and adding more computer vision algorithms if necessary.

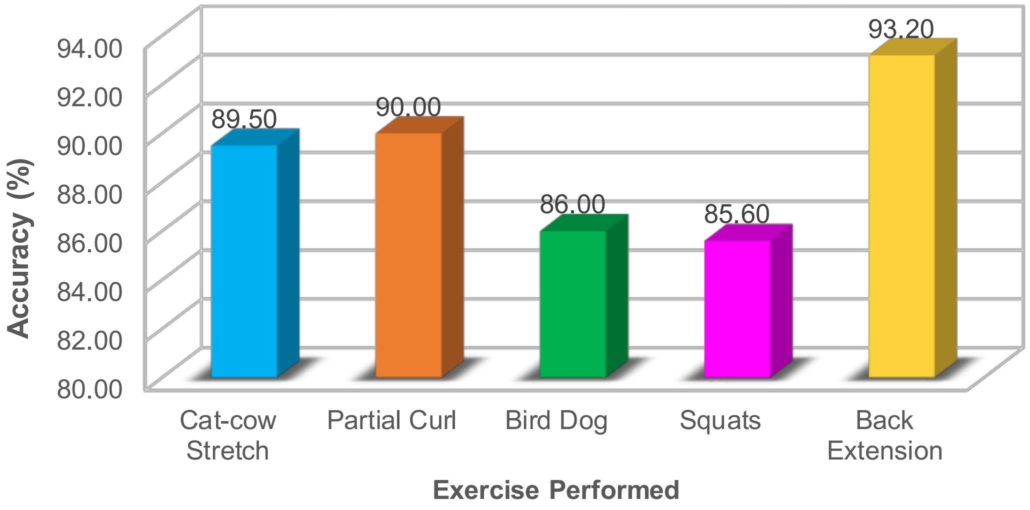

Figure 8. Obtained accuracy while the users performed spinal exercises.

The obtained accuracy while the users performed cardiovascular exercises is shown in Figure 9. This figure shows that the accuracy obtained for the push-up physiotherapy exercise is the maximum when compared to other cardiovascular exercises. The accuracy obtained is 96.5% for push-ups, 88% for bridge, and 85.98% for shoulder roll exercises, respectively.

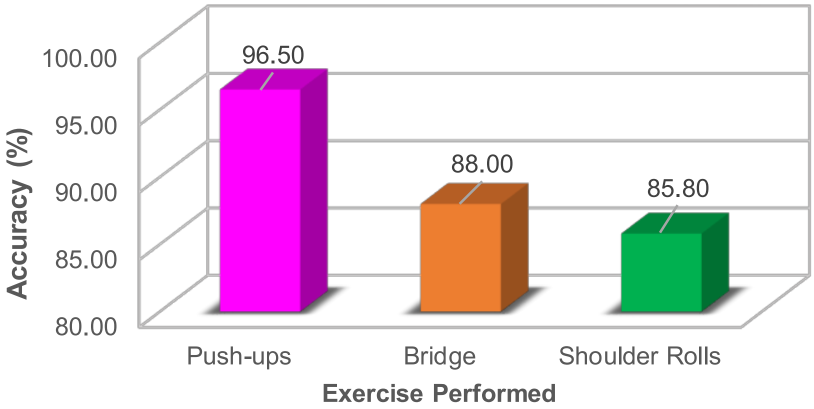

Figure 9. Obtained accuracy while the users performed cardiovascular exercises.

5. Conclusions

In this study, a system was developed to estimate human postures utilizing OpenCV and MediaPipe. The system's tracking and detection capabilities were thoroughly evaluated to assess its accuracy in accurately identifying human stances. The successful monitoring of important human body landmarks achieved real-time, highly accurate human pose estimation. OpenCV and MediaPipe offered several advantages over. The system showed superior accuracy and robustness, making it a favorable choice for physiotherapy-related tasks. Also, the voice acknowledgment makes the system more user-friendly. Additionally, the user's ability to choose between live camera feeds and video uploads increased the usefulness and scenario adaptability of the system. This system can also be used for fitness monitoring, rehabilitation exercises, and sports performance analysis. We can also incorporate a gesture recognition system here.

5.1. Ethical Considerations

The research was conducted following ethical standards, which guaranteed participant informed permission and upheld the privacy and confidentiality of their data. The study was carried out under all applicable laws and ethical guidelines.

5.2. Limitations

The project focuses on a specific set of physiotherapy exercises. However, numerous other exercises and movement patterns could benefit rehabilitation or fitness. The scope of the project may not cover all possible exercises. Moreover, although the UI-PRMD dataset provided a solid foundation, its generalizability to all physiotherapy exercises and patient demographics may be limited. Environmental factors such as lighting conditions, background clutter, and camera angles may affect the system's accuracy. Adverse conditions or distractions in the surroundings could impact the accuracy of joint angle calculations and exercise detection. Future iterations should address these limitations by integrating adaptive algorithms and enhancing dataset diversity to improve overall effectiveness in clinical and home-based physiotherapy settings.

5.3. Future Scope

This work can be extended further using the newly developed frameworks like AlphaPose and EfficientPose. The purpose of the AlphaPose [27, 28] framework is to provide precise joint localization and detailed pose information. It employs deep learning models and advanced algorithms to achieve highly accurate pose estimation results. Also, it can handle challenging pose estimation scenarios, including occlusions and complex poses. EfficientPose [29, 30] is a pose estimation framework known for its efficient and lightweight architecture. It is developed to offer a decent balance between speed and precision. For applications where real-time performance and minimal computational demands are essential, the EfficientPose framework is more suitable.

Author Contributions: Conceptualization, K.V.D. and R.S.; methodology, M.M.V.C. and Y.V.P.K.; software, K.P.P. and D.G.; validation, C.P.R. and M.S.; formal analysis, K.V.D.; investigation, M.M.V.C.; resources, C.P.R.; data curation, Y.V.P.K.; writing—original draft preparation, K.P.P.; writing—review and editing, D.G.; visualization, M.S.; supervision, C.P.R.; project administration, R.S.. All authors have read and agreed to the published version of the manuscript.

Funding: This research received no external funding.

Conflicts of Interest: The authors declare no conflict of interest.

References

[1] Kertesz, C. Physiotherapy Exercises Recognition Based on RGB-D Human Skeleton Models. *2013 European Modelling Symposium, Manchester, United Kingdom* **2013**, 21–29. https://doi.org/10.1109/EMS.2013.4

[2] Herbert, R. D.; Maher, C. G.; Moseley, A. M.; Sherrington, C. Regular review: Effective physiotherapy. *British Medical Journal* **2001**, *323*(7316), 788–790. https://doi.org/10.1136/bmj.323.7316.788

[3] Rucha, G. (2023, September 9). India. *Physiopedia*. https://www.physio-pedia.com/India

[4] Piñero-Fuentes, E.; Canas-Moreno, S.; Rios-Navarro, A.; Domínguez-Morales, M.; Sevillano, J. L.; Linares-Barranco, A. A Deep-Learning Based Posture Detection System for Preventing Telework-Related Musculoskeletal Disorders. *Sensors* **2021**, *21*(15), 5236. https://doi.org/10.3390/s21155236

[5] Khan, Rushina., Deogiri Inst of Engg. Management Studies. Telecommunting: The Problems Challenges During Covid-19. *International Journal of Engineering Research and Technology* **2020**, *V9*(07), IJERTV9IS070432. https://doi.org/10.17577/IJERTV9IS070432

[6] Nag, P. K. Musculoskeletal Disorders: Office Menace. In P. K. Nag, *Office Buildings*. 105–126. Springer Singapore **2019**. https://doi.org/10.1007/978-981-13-2577-9_4

[7] Yamao, K.; Kubota, R. Development of Human Pose Recognition System by Using Raspberry Pi and PoseNet Model. *2021 20th International Symposium on Communications and Information Technologies (ISCIT), Tottori, Japan* **2021**, 41–44. https://doi.org/10.1109/ISCIT52804.2021.9590593

[8] Kulkarni, K. M.; Shenoy, S. *Table Tennis Stroke Recognition Using Two-Dimensional Human Pose Estimation* **2021**. https://doi.org/10.48550/ARXIV.2104.09907

[9] Zhang, Y.; You, S.; Karaoglu, S.; Gevers, T. Multi-person 3D pose estimation from a single image captured by a fisheye camera. *Computer Vision and Image Understanding* **2022**, 222, 103505. https://doi.org/10.1016/j.cviu.2022.103505

[10] Yeo, N. Posture detection for physical therapy application. Final Year Project (FYP), *Nanyang Technological University, Singapore* **2023**. https://hdl.handle.net/10356/166826

[11] Nishchal, K. A.; Prajwal, R. V.; Prakruthi, B. M.; Venika, S.; Anil, K. C. Vision Based Human Fall Detection System. *International Research Journal of Modernization in Engineering Technology and Science* **2023**. https://doi.org/10.56726/IRJMETS37625

[12] Kontadakis, G.; Chasiouras, D.; Proimaki, D.; Halkiadakis, M.; Fyntikaki, M.; Mania, K. Gamified platform for rehabilitation after total knee replacement surgery employing low cost and portable inertial measurement sensor node. *Multimedia Tools and Applications* **2020**. *79*(5–6), 3161–3188. https://doi.org/10.1007/s11042-018-6572-6

[13] Thar, M. C.; Winn, K. Z. N.; Funabiki, N. A Proposal of Yoga Pose Assessment Method Using Pose Detection for Self-Learning. *2019 International Conference on Advanced Information Technologies (ICAIT)* **2019**, 137–142. https://doi.org/10.1109/AITC.2019.8920892

[14] Rathour, N.; Khanam, Z.; Gehlot, A.; Singh, R.; Rashid, M.; AlGhamdi, A. S.; Alshamrani, S. S. Real-Time Facial Emotion Recognition Framework for Employees of Organizations Using Raspberry-Pi. *Applied Sciences* **2021**, *11*(22), 10540. https://doi.org/10.3390/app112210540

[15] Ryberg, S.; Jansson, J. *Real-time object detection robot control: Investigating the use of real time object detection on a Raspberry Pi for robot control (Dissertation).* Retrieved from https://urn.kb.se/resolve?urn=urn:nbn:se:kth:diva-320969. **2022**.

[16] Chen, P.-J.; Hu, T.-H.; Wang, M.-S. Raspberry Pi-Based Sleep Posture Recognition System Using AIoT Technique. *Healthcare* **2022**, *10*(3), 513. https://doi.org/10.3390/healthcare10030513

[17] Yalin, L.; Aleksandar, V.; Min, X. A Deep Learning Framework for Assessing Physical Rehabilitation Exercises. *IEEE Transactions on Neural Systems and Rehabilitation Engineering* **2020**, *28*(2), 468-477. https://doi.org/10.1109/TNSRE.2020.2966249

[18] Lugaresi, C.; Tang, J.; Nash, H.; McClanahan, C.; Uboweja, E.; Hays, M.; Zhang, F.; Chang, C.-L.; Yong, M. G.; Lee, J.; Chang, W.-T.; Hua, W.; Georg, M.; Grundmann, M. MediaPipe: A Framework for Building Perception Pipelines (arXiv:1906.08172). arXiv. **2019.** http://arxiv.org/abs/1906.08172

[19] Lin, Y.; Jiao, X.; Zhao, L. Detection of 3D Human Posture Based on Improved Mediapipe. *Journal of Computer and Communications*, **2023**, *11*(02), 102–121. https://doi.org/10.4236/jcc.2023.112008

[20] On-device machine learning for everyone *MediaPipe*. **2023**. https://developers.google.com/mediapipe

[21] Podduturi, H. V. R.; Varla, C.; Gopaldinne, K. R.; Bhukya, N.; Reddy Nallagondu, R. K.; Bapiraju, G. S. Smart Trainer using OpenCV. *2023 International Conference on Innovative Data Communication Technologies and Application (ICIDCA), Uttarakhand, India* **2023**, 477–480. https://doi.org/10.1109/ICIDCA56705.2023.10099780

[22] Mahato, A. (2023, September 9). Getting started with Image Processing Using OpenCV. Retrieved from Analytics Vidhya website: https://www.analyticsvidhya.com/blog/2023/03/getting-started-with-image-processing-using-opencv/

[23] Naveenkumar, M.; Vadivel, A. OpenCV for Computer Vision Applications [Conference session]. Conference: *Proceedings of National Conference on Big Data and Cloud Computing (NCBDC'15), Trichy, India* **2015**. https://www.researchgate.net/publication/301590571_OpenCV_for_Computer_Vision_Applications#fullTextFileContent

[24] Xiangxin, Zhu.; Ramanan, D. Face detection, pose estimation, and landmark localization in the wild. *2012 IEEE Conference on Computer Vision and Pattern Recognition* **2012**, 2879–2886. https://doi.org/10.1109/CVPR.2012.6248014

[25] Sunil, D. K.; Nipun, K.; Kumbhkarn, Sumit, K.; Atharva, K.; Shreyash, K. Posture Detection and Comparison of Different Physical Exercises Based on Deep Learning Using Media Pipe, Opencv. *International Journal of Scientific Research in Engineering and Management (IJSREM)* **2023**. https://ijsrem.com/download/posture-detection-and-comparison-of-different-physical-exercises-based-on-deep-learning-using-media-pipe-opencv/

[26] Alwani, A. A.; Chahir, Y.; Goumidi, D. E.; Molina, M.; Jouen, F. 3D-Posture Recognition Using Joint Angle Representation. In A. Laurent, O. Strauss, B. Bouchon-Meunier, R. R. Yager (Eds.), *Information Processing and Management of Uncertainty in Knowledge-Based Systems* **2014**, *443*, 106–115. Springer International Publishing. https://doi.org/10.1007/978-3-319-08855-6_12

[27] Fang, H.-S.; Li, J.; Tang, H.; Xu, C.; Zhu, H.; Xiu, Y.; Li, Y.-L.; Lu, C. AlphaPose: Whole-Body Regional Multi-Person Pose Estimation and Tracking in Real-Time. *IEEE Transactions on Pattern Analysis and Machine Intelligence* **2023**, *45*(6), 7157–7173. https://doi.org/10.1109/TPAMI.2022.3222784

[28] Machine Vision and Intelligence Group @ SJTU. (2023, September 9). Real-Time and Accurate Full-Body Multi-Person Pose Estimation and Tracking System. Retrieved from https://github.com/MVIG-SJTU/AlphaPose

[29] Bukschat, Y.; Vetter, M. EfficientPose: An efficient, accurate and scalable end-to-end 6D multi object pose estimation approach (arXiv:2011.04307). arXiv. **2020**. http://arxiv.org/abs/2011.04307

[30] Ybkscht. (2023, September 9). EfficientPose. Retrieved from https://github.com/ybkscht/EfficientPose

ASEAN
Journal of Scientific and Technological Reports

Online ISSN:2773-8752

ASEAN
Journal of Scientific and Technological Reports
Online ISSN: 2773-8752

Article type

Type of the Paper (Article, Review, Communication, etc.)about 8,000 words maximum

Title (Palatino Linotype 18 pt, bold)

Firstname Lastname[1], Firstname Lastname[2] and Firstname Lastname[2*]

[1] Affiliation 1; e-mail@e-mail.com
[2] Affiliation 2; e-mail@e-mail.com
* Correspondence: e-mail@e-mail.com; (one corresponding authors, add author initials)

Citation:
Lastname, F.; Lastname, F.; Lastname, F. Title. *ASEAN J. Sci. Tech. Report.* **2023**, *26*(X), xx-xx. https://doi.org/10.55164/ajstr.vxxix.xxxxxx

Article history:
Received: date
Revised: date
Accepted: date
Available online: date

Abstract: A single paragraph of about 400 words maximum. Self-contained and concisely describe the reason for the work, methodology, results, and conclusions. Uncommon abbreviations should be spelled out at first use. We strongly encourage authors to use the following style of structured abstracts, but without headings: (1) Background: Place the question addressed in a broad context and highlight the purpose of the study; (2) Methods: briefly describe the main methods or treatments applied; (3) Results: summarize the article's main findings; (4) Conclusions: indicate the main conclusions or interpretations.

Keywords: keyword 1; keyword 2; keyword 3 (List three to ten pertinent keywords specific to the article yet reasonably common within the subject discipline.)

1. Introduction

The introduction should briefly place the study in a broad context and highlight why it is crucial. It should define the purpose of the work and its significance. The current state of the research field should be carefully reviewed and critical publications cited. Please highlight controversial and diverging hypotheses when necessary. Finally, briefly mention the main aim of the work. References should be numbered in order of appearance and indicated by a numeral or numerals in square brackets—e.g., [1] or [2, 3], or [4–6]. See the end of the document for further details on references.

2. Materials and Methods

The materials and methods should be described with sufficient details to allow others to replicate and build on the published results. Please note that your manuscript's publication implicates that you must make all materials, data, computer code, and protocols associated with the publication available to readers. Please disclose at the submission stage any restrictions on the availability of materials or information. New methods and protocols should be described in detail, while well-established methods can be briefly described and appropriately cited.

Interventional studies involving animals or humans, and other studies that require ethical approval, must list the authority that provided approval and the corresponding ethical approval code.

2.1 Subsection

2.1.1. Subsubsection

3. Results and Discussion

This section may be divided by subheadings. It should provide a concise and precise description of the experimental results, their interpretation, as well as the experimental conclusions that can be drawn.Authors should discuss the results and how they can be interpreted from previous studies and the working hypotheses. The findings and their implications should be discussed in the broadest context possible. Future research directions may also be highlighted.

3.1. Subsection

3.1.1. Subsubsection

3.2. Figures, Tables, and Schemes

All figures and tables should be cited in the main text as Figure 1, Table 1, etc.

Figure 1. This is a figure. Schemes follow the same formatting.

Table 1. This is a table. Tables should be placed in the main text near the first time they are cited.

Title 1	**Title 2**	**Title 3**
entry 1	data	data
entry 2	data	data [1]

[1] Table may have a footer.

3.3. Formatting of Mathematical Components

This is example 1 of an equation:

$$a = 1, \tag{1}$$

The text following an equation need not be a new paragraph. Please punctuate equations as regular text. This is example 2 of an equation:

$$a = b + c + d + e + f + g + h + i + j + k + l + m + n + o + p + q + r + s + t + u \tag{2}$$

The text following an equation need not be a new paragraph. Please punctuate equations as regular text. The text continues here.

4. Conclusions

Concisely restate the hypothesis and most important findings. Summarize the significant findings, contributions to existing knowledge, and limitations. What are the future directions? Conclusions MUST be well stated, linked to original research question & limited to supporting results.

5. Acknowledgements

Should not be used to acknowledge funders – funding will be entered as a separate. As a matter of courtesy, we suggest you inform anyone whom you acknowledge.

Author Contributions: For research articles with several authors, a short paragraph specifying their individual contributions must be provided. The following statements should be used "Conceptualization, X.X. and Y.Y.; methodology, X.X.; software, X.X.; validation, X.X., Y.Y. and Z.Z.; formal analysis, X.X.; investigation, X.X.; resources, X.X.; data curation, X.X.; writing—original draft preparation, X.X.; writing—review and editing, X.X.; visualization, X.X.; supervision, X.X.; project administration, X.X.; funding acquisition, Y.Y. All authors have read and agreed to the published version of the manuscript." Please turn to the CRediT taxonomy for the term explanation. Authorship must be limited to those who have contributed substantially to the work reported.

Funding: Please add: "This research received no external funding" or "This research was funded by NAME OF FUNDER, grant number XXX" and "The APC was funded by XXX". Check carefully that the details given are accurate and use the standard spelling of funding agency names at https://search.crossref.org/funding. Any errors may affect your future funding.

Conflicts of Interest: Declare conflicts of interest or state "The authors declare no conflict of interest." Authors must identify and declare any personal circumstances or interest that may be perceived as inappropriately influencing the representation or interpretation of reported research results. Any role of the funders in the design of the study; in the collection, analyses or interpretation of data; in the writing of the manuscript, or in the decision to publish the results must be declared in this section. If there is no role, please state "The funders had no role in the design of the study; in the collection, analyses, or interpretation of data; in the writing of the manuscript, or in the decision to publish the results".

References

References must be numbered in order of appearance in the text (including citations in tables and legends) and listed individually at the end of the manuscript. We recommend preparing the references with a bibliography software package, such as EndNote, ReferenceManager to avoid typing mistakes and duplicated references. Include the digital object identifier (DOI) for all references where available.

Citations and references in the Supplementary Materials are permitted provided that they also appear in the reference list here.

In the text, reference numbers should be placed in square brackets [ ] and placed before the punctuation; for example [1], [1–3] or [1, 3]. For embedded citations in the text with pagination, use both parentheses and brackets to indicate the reference number and page numbers; for example [5] (p. 100), or [6] (pp. 101–105).

Using the American Chemical Society (ACS) referencing style

[1] Author 1, A.B.; Author 2, C.D. Title of the article. *Abbreviated Journal Name* Year, *Volume*, page range.

[2] Author 1, A.; Author 2, B. Title of the chapter. In *Book Title*, 2nd ed.; Editor 1, A., Editor 2, B., Eds.; Publisher: Publisher Location, Country. **2007**, Volume *3*, pp. 154–196.

[3] Author 1, A.; Author 2, B. *Book Title*, 3rd ed.; Publisher: Publisher Location, Country, **2008**, pp. 154–196.

[4] Author 1, A.B.; Author 2, C. Title of Unpublished Work. *Abbreviated Journal Name* stage of publication (under review; accepted; in press).

[5] Author 1, A.B. (University, City, State, Country); Author 2, C. (Institute, City, State, Country). Personal communication, 2012.

[6] Author 1, A.B.; Author 2, C.D.; Author 3, E.F. Title of Presentation. In Title of the Collected Work (if available), Proceedings of the Name of the Conference, Location of Conference, Country, Date of Conference; Editor 1, Editor 2, Eds. (if available); Publisher: City, Country, Year (if available); Abstract Number (optional), Pagination (optional).

[7] Author 1, A.B. Title of Thesis. Level of Thesis, Degree-Granting University, Location of University, Date of Completion.

[8] Title of Site. Available online: URL (accessed on Day Month Year).

Reviewers sugestion

1. Name, Address, e-mail
2. Name, Address, e-mail
3. Name, Address, e-mail
4. Name, Address, e-mail

URL link:

Notes for Authors >>
https://drive.google.com/file/d/1r0zegnIVeQqe4iLQyT1xDEIinNggINPD/view?usp=sharing
https://drive.google.com/file/d/1r0zegnIVeQqe4iLQyT1xDEIinNggINPD/view?usp=sharing

Online Submissions >> https://ph02.tci-thaijo.org/index.php/tsujournal/user/register

Current Issue >> https://ph02.tci-thaijo.org/index.php/tsujournal/issue/view/16516

AJSTR Publication Ethics and Malpractice >> https://ph02.tci-thaijo.org/index.php/tsujournal/ethics

Journal Title Abbreviations >> http://library.caltech.edu/reference/abbreviations

ASEAN
Journal of Scientific and Technological Reports
Online ISSN:2773-8752

ASEAN
Journal of Scientific and Technological Reports
Online ISSN:2773-8752

ASEAN Journal of Scientific and Technological Reports (AJSTR)
Institute of Research and Innovation, Thaksin University, Phatthalung Campus
222 Moo. 2, Baan Prao Sub-District, Papayom District, Phatthalung, 93210, Thailand
Tel. +668 1540 7304